Title
Searches for WIMPs and Axions with the XENON1T Experiment

Author
Ye, Jingqiang

Publication Date
2020

UNIVERSITY OF CALIFORNIA SAN DIEGO

Searches for WIMPs and Axions with the XENON1T Experiment

A dissertation submitted in partial satisfaction of the
requirements for the degree
Doctor of Philosophy

in

Physics

by

Jingqiang Ye

Committee in charge:

Professor Kaixuan Ni, Chair
Professor Tongyan Lin
Professor Vivek Sharma
Professor Dong Wang
Professor Frank Wuerthwein

2020

The dissertation of Jingqiang Ye is approved, and it is acceptable in quality and form for publication on microfilm and electronically:

Chair

University of California San Diego

2020

DEDICATION

To my parents

TABLE OF CONTENTS

Signature Page iii

Dedication iv

Table of Contents v

List of Figures viii

List of Tables xvi

Acknowledgements xvii

Vita and Publications xx

Abstract of the Dissertation xxii

Chapter 1 Dark Matter 1
- 1.1 Evidence of Dark Matter 1
  - 1.1.1 Galaxy Rotation Curve 1
  - 1.1.2 Bullet Cluster 3
  - 1.1.3 Cosmic Microwave Background 4
- 1.2 Dark Matter Candidates 7
  - 1.2.1 WIMP 7
  - 1.2.2 Axion 9

Chapter 2 Direct Detection with Xenon 13
- 2.1 Two-phase Liquid Xenon TPC 13
- 2.2 WIMP Detection 17
  - 2.2.1 WIMP-nucleon Elastic Scattering 17
  - 2.2.2 Annual Modulation 21
- 2.3 Axion Detection 22
  - 2.3.1 Axion Experiments 23
  - 2.3.2 Solar Axions 24
  - 2.3.3 Galactic ALPs 30

Chapter 3 Analyzing the XENON1T Data 33
- 3.1 The XENON1T Experiment 33
- 3.2 Energy and Position Corrections 34
  - 3.2.1 Energy Corrections 34
  - 3.2.2 Field Distortion Correction 41
- 3.3 Detector Calibrations 51
  - 3.3.1 Electronic Recoil Calibration 51

3.3.2 Nuclear Recoil Calibration 53
3.3.3 Energy Scale Calibration 55
3.4 Backgrounds 57
3.4.1 Electronic Recoil Backgrounds 58
3.4.2 Nuclear Recoil Backgrounds 58
3.4.3 Accidental Coincidences 60
3.4.4 Surface Background 61
3.5 Acknowledgements 72

Chapter 4 XENON1T WIMP Results 74
4.1 Heavy WIMP Search Results 74
4.1.1 SI WIMP-nucleon Scattering 76
4.1.2 SD WIMP-nucleon Scattering 77
4.1.3 Scalar WIMP-Pion Coupling 80
4.2 Light WIMP Search Results 82
4.2.1 S2-only Approach 82
4.2.2 Migdal and Bremsstrahlung Effects 84
4.3 Acknowledgements 88

Chapter 5 Search for Solar Axions with XENON1T 89
5.1 Data Selection 90
5.1.1 Effective Time of Data 90
5.1.2 Event Selection Critefria 90
5.1.3 Event Selection Efficiency 92
5.1.4 Fiducial Volume 94
5.2 Detector Response Modeling 96
5.2.1 Efficiency 97
5.2.2 Energy Resolution 99
5.2.3 Modeling 99
5.3 Backgrounds 100
5.3.1 β decay of ^{214}Pb 101
5.3.2 Time-dependent Backgrounds 102
5.3.3 Solar Neutrino Electron Elastic Scattering 106
5.3.4 Compton Scattering from Materials 106
5.3.5 Double β decay of xenon isotopes 106
5.4 Statistics Method 107
5.5 Results 111
5.5.1 Excess at Low Energies 111
5.5.2 Tritium Hypothesis 117
5.5.3 Solar Axions 120
5.6 Additional Checks and Discussion 126
5.6.1 Check on Science Run 2 126
5.6.2 Impact from β Spectral Shape 128

5.6.3 Efficiency Check with ^{220}Rn Calibration Data . . 130
5.6.4 Detection Threshold 132
5.6.5 S2-only Check 135
5.6.6 Time and Spatial Dependence 137
5.6.7 Tension with Astrophysical Constraints 140
5.7 Acknowledgements 141

Chapter 6 Searches for Other New Physics and Rare Processes 142
6.1 Neutrino Magnetic Moment 143
6.2 Bosonic Dark Matter 147
6.3 Leptophillic Dark Matter 151
6.4 Double Electron Capture of ^{124}Xe 154
6.5 Acknowledgements 156

Chapter 7 The XENONnT Experiment 157
7.1 Background Predictions 157
7.2 Projected WIMP Sensitivity 161
7.3 Discrimination Power on the XENON1T ER Excess . . . 162
7.4 Acknowledgements 164

Bibliography 165

LIST OF FIGURES

Figure 1.1: M33 rotation curve (points) compared with the best-fitting model (solid line), which consists of contributions from the dark matter halo (dot-dashed line), stellar disk (short-dashed line), and gas (long-dashed line). Figure from Ref. [4]. 2

Figure 1.2: Bullet cluster (1E 0667-56). The red population is from X-ray observation and blue clump is revealed from the weak-lensing mass map. Yellow and white blobs are galaxies determined from optical measurement. Figure from Refs. [5, 6]. 4

Figure 1.3: Temperature anisotropy in CMB from the latest Planck result [8]. Red and blue regions indicate relatively hot and cold regions, respectively. Figure from Ref. [8]. 5

Figure 1.4: CMB power spectrum. Red points are measurements from Planck [8] and blue curve is the fit result using ΛCDM model. Figure from Ref. [8]. 6

Figure 1.5: WIMP density in a comoving volume evolves with the cooling of the Universe. The solid line is the equilibrium abundance assuming the Universe is not expanding. 8

Figure 2.1: Illustration of working principle of two-phase time projection chamber. See details in the text. Figure from Ref. [22]. 15

Figure 2.2: Helm form factors $\mathcal{F}^2(q)$ as function of nuclear recoil energies for ^{131}Xe (blue), ^{73}Ge (red), and ^{40}Ar (green), respectively. . . . 20

Figure 2.3: Elastic scattering spectra for a $30\,\mathrm{GeV}/c^2$ WIMP with a spin-independent WIMP-nucleon cross section σ_N=$1 \times 10^{-47}\,\mathrm{cm}^2$ in target media of ^{131}Xe (blue), ^{73}Ge (red), and ^{40}Ar (green), respectively. 21

Figure 2.4: Illustration of the annual modulated WIMP signal. Figure from Ref. [31]. 22

Figure 2.5: Fluxes of ABC (blue), ^{57}Fe (purple), and Primakoff (orange) solar axions with the couplings of $g_{\mathrm{ae}} = 3.5 \times 10^{-12}$, $g_{\mathrm{an}}^{\mathrm{eff}} = 1 \times 10^{-6}$, and $g_{\mathrm{a}\gamma} = 2 \times 10^{-10}\,\mathrm{GeV}^{-1}$, respectively. Each flux scales with the square of the corresponding coupling. 26

Figure 2.6: Photoelectric cross section σ_{pe} for xenon atoms. The data points are from Ref. [51] and the dashed line is the interpolation. See text for more details. 28

Figure 2.7: Axio-electric cross section σ_{ae} as a function of axion mass m_{a} for three axion energies, including 1 keV (blue), 1.5 keV (red), and 2 keV (green), which are typical energies for solar axions. In all cases, σ_{ae} is constant for m_{a} below $100\,\mathrm{eV}/c^2$. 29

Figure 2.8: Solar axion spectra in a perfect xenon detector, i.e., without energy smearing and efficiency loss. The increase at $\sim 5\,\mathrm{keV}$ is due to the L-shell electrons of xenon atoms. 30

Figure 3.1: Illustration of the XENON1T TPC. It is built from materials selected for their low radioactivity, e.g., OFHC copper, stainless steel and PTFE. 35

Figure 3.2: S1 LCE map with respect to the mean of LCE across the XENON1T TPC using $^{83\mathrm{m}}$Kr data in SR1. The LCE is averaged out along the azimuthal angle. 36

Figure 3.3: Electron lifetime evolution in SR0 and SR1. The vertical colored bands indicate different calibrations. The electron lifetime measured from decays of $^{83\mathrm{m}}$Kr, ^{218}Po, and ^{222}Rn are illustrated in black, green, and red dots, respectively. 39

Figure 3.4: Correction maps for $S2$ signals in top (top) and bottom (bottom) PMT array from $^{83\mathrm{m}}$Kr calibration source. Both $S2$ light yiled are normalized to the average value in each map. See text for more details. 40

Figure 3.5: The observed positions of surface events (see Sec. 3.4.4), which happen in proximity with the TPC boundary indicated by the black line, are illustrated with different periods, including April 2017, September 2017, and January 2018. 43

Figure 3.6: Reconstructed xy position distribution of $^{83\mathrm{m}}$Kr events from neural network algorithms without field distortion correction. . 44

Figure 3.7: Illustration of radial position mapping in the data-driven 3D FDC from observed positions (left) to corrected positions (right) based on $^{83\mathrm{m}}$Kr data. The dashed and solid lines in the two plots correspond to each other. 46

Figure 3.8: Neutron generator event positions from data after 3D FDC (left) and MC simulations (right). 48

Figure 3.9: Corrected positions of surface events (see Sec. 3.4.4) after 3D FDC. Events from different periods are denoted with different colors and are all aligned with the TPC boundary (black dashed line) as expected. Figure adapted from Ref. [59]. 49

Figure 3.10: Position resolution of surface events from the top part (blue) of the detector are consistent with that of the same $S2$ size but from the bottom part (red) of the detector. 49

Figure 3.11: Radial position resolution σ_R at the TPC boundary as a function of $S2$ size, which is fit by the empirical formula Eq. (3.7) in the orange line. The $S2$ threshold (200 PE) used in the WIMP search is indicated by the gray dashed line. 50

Figure 3.12: ^{220}Rn decay chain. β decays of ^{212}Pb are used for ER calibration in XENON1T. Figure published in Ref. [67]. 52

Figure 3.13: ^{220}Rn calibration data in SR1. Blue solid and dashed lines are the ER band median and $\pm 2\sigma$ quantiles, respectively. The red line is the NR band median from Fig. 3.14. Gray lines show isoenergy contours in ER energy. 53

Figure 3.14: ^{241}AmBe and NG calibration data in SR1. Red solid and dashed lines are the NR band median and $\pm 2\sigma$ quantiles, respectively. The blue line is the ER band median from Fig. 3.13. Gray lines show isoenergy contours in NR energy. 54

Figure 3.15: A global fit to extract $g1$ and $g2_{\mathrm{b}}$ in SR1. Black points represent light and charge yields from different mono-energetic peaks which the red line fits to. The statistical uncertainties of light and charge yields, which are from the fitting, are too small to be visible. 57

Figure 3.16: Multiple scattered events in XENON1T. Left: Spatial distribution of events after FDC. Solid and empty circles represent energy depositions from neutrons, and the solid circle has the largest $S2$ size. 59

Figure 3.17: The distribution AC background in $(S1, S2)$ space. The ROI of DM search is between NR band median and NR band -2σ that are denoted by the red and black dashed lines, respectively. The projections in S1 and S2 directions are also provided. . . . 60

Figure 3.18: Charge loss in $^{83\mathrm{m}}$Kr calibration data, which are selected based on the unique two-S1 signature to ensure purity. 63

Figure 3.19: ^{222}Rn decay chain. The β decay of ^{214}Pb, a ^{222}Rn daughter, is the main background for XENON1T WIMP search. 64

Figure 3.20: The decay scheme of ^{210}Pb and its daughters. Figure from Ref. [86]. 65

Figure 3.21: Three α emitters in ^{222}Rn decay chain with notation on each population. The large spread of c$S2_{\mathrm{b}}$ for ^{210}Po events is due to charge loss. c$S1_{\alpha}$ is $S1$ signal after correction to account for its saturation in some PMTs. 66

Figure 3.22: Spatial distribution of ^{210}Po events selected from the orange rectangle in Fig. 3.21. The reconstructed positions are after the 3D FDC. 66

Figure 3.23: Radial distribution of surface events within a specific $S2$ range (257, 283) PE fitted by skew Gaussian (brown) and skew t (orange) functions, respectively. 68

Figure 3.24: The distributions in $S2$, c$S2_{\mathrm{b}}$, c$S1$, and z for surface events *reconstructed* inside (red) and outside (blue) the TPC in background data share similar shapes. The rates are normalized so as to compare the spectral shape. 70

Figure 3.25: Surface background event distribution in (c$S1$, c$S2_\mathrm{b}$) parameter space with probability density indicated by the color in the logarithm scale. 71

Figure 4.1: The best-fit of background plus a 200 GeV/c^2 WIMP to the data under the 3D (c$S1$, c$S2_\mathrm{b}$, R) likelihood. The observed events in ROI are denoted with pie charts, which are larger with a relatively larger WIMP possibility. 75

Figure 4.2: 90% confidence level upper limit on σ_SI from this work (thick black line) with the 1σ (green) and 2σ (yellow) sensitivity bands. Previous results from LUX [25] and PandaX-II [24] are shown for comparison. 77

Figure 4.3: Comparison of the WIMP-nucleus recoil spectra in the SD neutron-only, SD proton-only, and SI (scaled by 10^{-4}) cases in LXe for a 10 GeV/c^2 and 100 GeV/c^2 WIMP and a WIMP-nucleon cross section of 10^{-45} cm^2. 78

Figure 4.4: The neutron-only (top) and proton-only (bottom) cases for spin-dependent WIMP-nucleon cross section. The green (yellow) band is the 1 $(2)\sigma$ sensitivity band for XENON1T and the black line is the corresponding limit. 79

Figure 4.5: Comparison of the differential recoil spectrum for WIMP–nucleon (black) $\mathcal{F}_+^M$ versus WIMP–pion interactions (red) $\mathcal{F}_\pi$. Exemplarily shown are WIMP masses of 30 GeV/c^2 (full line) and 200 GeV/c^2 (dashed line) for the most abundant isotope ^{132}Xe. 80

Figure 4.6: Result on scalar WIMP-pion coupling from XENON1T. The green (yellow) band is the 1 $(2)\sigma$ sensitivity band and the black is the 90% C.L. upper limit. Figure published in Ref. [92]. . . . 81

Figure 4.7: Event rate in S2-only analysis. Several background components are denoted, including the regular ER background (blue), cathode events (red), and CEνNS (red). 83

Figure 4.8: The 90% C.L. upper limits (black lines with gray shading above) on DM-matter scattering or bosonic DM absorption for the models discussed in the text, with the DM mass m_χ on the horizontal axes. 85

Figure 4.9: Median effective exposures of ER signals after event selections as a function of recoil energy for the S1S2 data (black line) and S2-only data (red line). 86

Figure 4.10: Limits on the SI (upper panel), SD proton-only (middle panel), and SD neutron-only (lower panel) DM-nucleon interaction cross sections at 90% C.L. 87

Figure 5.1: Science data in SR1 used in this analysis. The accumulated live time of data used is indicated by the blue curve, amounting to a total of 226.9 days. 91
Figure 5.2: The cumulative selection efficiency in this analysis. The efficiency uncertainty includes both systematic and statistical uncertainty and is indicated by the band. 94
Figure 5.3: Top: The figure of merit (Eq. (5.2)) of 1T FV (red) and the most optimized FV (red). Both are in arbitrary units (A. U.). Bottom: The ratio between figure of merit in 1T FV and the one in the optimized FV. 96
Figure 5.4: Efficiency as a function of energy. The dashed (dotted) line refers to detection (selection) efficiency, while the blue curve and band illustrate the total efficiency and the associated 1-σ uncertainty, respectively. 98
Figure 5.5: Relative energy resolution $\sigma(E)/E$ as a function of energy. The energy resolution from mono-energetic peaks in XENON1T (black dots) with energies below 1500 keV are fitted with an empirical function given in Eq. (5.3) (black line). 98
Figure 5.6: The ABC (blue), Primakoff (orange), and ^{57}Fe (purple) spectrum before (unshaded) and after (shaded) considering the energy resolution and efficiency specific to XENON1T. The assumed axion couplings are indicated in the plot. 100
Figure 5.7: Rate evolution of events within $\pm 3\sigma$ region centered around 163.9 keV, which is dominated by $^{131\text{m}}$Xe events. 103
Figure 5.8: Distribution of predicted $^{131\text{m}}$Xe rates in SR1 from toyMC simulations is shown in the blue curve. The 1σ region (gray) predicts the $^{131\text{m}}$Xe rate to be (42310 ± 840) events/(t·y) without efficiency loss. 104
Figure 5.9: Fit to the SR1 data set using the likelihood framework described in Sec. 5.4 and the background model B_0 in Sec. 5.3. The plot shows the entire SR1 spectrum, while the best fit in each partition is shown in Fig. 5.10. 112
Figure 5.10: Fit to the SR1 data set using the likelihood framework described in Sec. 5.4 and the background model B_0 in Sec. 5.3. The top (bottom) panel shows SR1$_\text{a}$ (SR1$_\text{b}$), which contains more (less) neutron-activated backgrounds. 113
Figure 5.11: A zoomed-in and re-binned version of Fig. 5.9, where the data display an excess over the background model B_0. Figure from Ref. [134]. 114
Figure 5.12: Hypothesis test for tritium. The red and gray curves are the best-fits under alternate and null hypotheses, respectively. The tritium component under alternate hypothesis is denoted by the orange dashed line. Figure adapted from Ref. [134]. 118

Figure 5.13: Significance of the solar axion hypothesis. The blue curve is the null distribution of log-likelihood ratio q of solar axion hypothesis fit to simulated data from toyMC simulations using background model B_0. 120
Figure 5.14: Hypothesis test for solar axions. The red and gray curves are the best-fits under alternate and null hypotheses, respectively. Each component of solar axion under alternate hypothesis is denoted with corresponding colored dashed line. 121
Figure 5.15: Constraints on the axion-electron g_{ae} and axion-photon $g_{\mathrm{a\gamma}}$ couplings from a search for solar axions. 122
Figure 5.16: Constraints on the axion-electron g_{ae}, axion-photon $g_{\mathrm{a\gamma}}$, and effective axion-nucleon $g_{\mathrm{an}}^{\mathrm{eff}}$ couplings from a search for solar axions.123
Figure 5.17: Hypothesis test for solar axions, with an unconstrained tritium component added in both alternate and null hypotheses. The red and gray curves are the best-fits under alternate and null hypotheses, respectively. 125
Figure 5.18: A fit to SR2 data if tritium is treated as a signal. The red (gray) line is the fit with (without) tritium in the background model. Figure from Ref. [134]. 127
Figure 5.19: The log likelihood ratio curve for the tritium rate in SR2. The orange line and band indicate the best-fit and $1\,\sigma$ uncertainty for the tritium rate in SR1. The SR2 fit result is consistent with SR1, but with a large uncertainty due to limited statistics. . . . 128
Figure 5.20: Low energy part of the β spectral shape of the ground-state to ground-state transition in ^{214}Pb decay. 130
Figure 5.21: Fit to ^{220}Rn *calibration* data with a theoretical β-decay mode (see the appendix in Ref. [134]) and the efficiency nuisance parameter, using the same unbinned profile likelihood framework described in Sec. 5.4. 131
Figure 5.22: Fitting of different hypotheses under different energy thresholds indicated inside the parenthesis. Top: ABC axion. Middle: Tritium. Bottom: ABC axion vs. Tritium. See text for more details. 133
Figure 5.23: Using S2-only approach in [103] to probe the main hypotheses for the excess, including solar axion (ABC), tritium, and neutrino magnetic moment (Sec. 6.1). The balck line is the background model in S2-only approach [103]. 135
Figure 5.24: The spatial distribution of events with energies between 1–7 keV. Events with relative probabilities of being solar axions larger than 25% are indicated with pie charts, the sizes of which increase with the relative probabilities. 138

Figure 6.1: Electronic recoils induced by solar neutrino assuming finite magnetic moment $\mu_\nu = 2.8 \times 10^{-11}\,\mu_{\mathrm{B}}$, excluding the contribution from neutrino elastic scattering off the electrons. 143
Figure 6.2: Hypothesis test for neutrino magnetic moment. The red and gray curves are the best-fits under alternate and null hypotheses, respectively. The green dashed line is the best-fit of the neutrino magnetic moment contribution to ER spectrum. 145
Figure 6.3: Constraints (90% C.L.) on the neutrino magnetic moment from this work using both S1 and S2 signals compared to experiments Borexino [210] and Gemma [215], along with astrophysical limits. 146
Figure 6.4: The detection rates for ALPs and Dark photon as function of mass, assuming all the local DM are made of them, respectively. The assumed axion-electron coupling $g_{\mathrm{ae}} = 1 \times 10^{-13}$ and the kinetic mixing parameter $\kappa = 1 \times 10^{-14}$. 148
Figure 6.5: Constraints on couplings for bosonic pseudoscalar ALP (top) and vector (bottom) dark matter, as a function of particle mass. The XENON1T limits (90% C.L.) are shown in black with the expected 1 (2) σ sensitivities in green (yellow). 149
Figure 6.6: Left: The log-likelihood ratio for different bosonic dark matter masses with respect to the best-fit mass at 2.3 keV/c^2. At each mass, we show the result for the best-fit coupling at that mass. 150
Figure 6.7: Momentum space wave functions in different xenon shells. . . . 152
Figure 6.8: Energy spectrum for a 200 GeV/c^2 WIMP coupled with electrons through axial-vector coupling of $\sigma^0_{\chi\mathrm{e}} = 1 \times 10^{-34}\,\mathrm{cm}^2$. The thick black curve is the total energy spectrum while the various thin curves represent the contribution from different xenon shells. 152
Figure 6.9: Spectra for WIMP-electron scattering via axial-vector coupling for different WIMP masses with $\sigma^0_{\chi\mathrm{e}} = 1 \times 10^{-34}\,\mathrm{cm}^2$. The detection threshold (1 keV) in XENON1T is indicated by the right bound of the shaded region. 153
Figure 6.10: 90% C.L. upper limit on the cross section $\sigma^0_{\chi\mathrm{e}}$ for WIMPs coupling to electrons through axial-vector interactions, along with the 1 (2)σ sensitivity bands indicated by the green (yellow) region. 154
Figure 6.11: Best-fit of the background model plus the signal of two-neutrino double electron capture (2νECEC) of ^{124}Xe to the measured energy spectrum. The shaded region was blinded before the event selection and background model were finalized. 155

Figure 7.1: The CAD rendering of the two cryostat vessels, as well as the XENONnT TPC, which has a diameter of 1.3 m and a height of 1.5 m. A total of 253 and 241 PMTs are deployed in the top and bottom PMT arrays, respectively. Figure from Ref. [55]. . . 158

Figure 7.2: Left: Projected ER backgrounds in XENONnT. The solid lines are the true energy spectra, i.e. excluding efficiency or energy resolution. The dashed lines are ^{124}Xe peaks after considering XENON1T energy resolution [144]. 159
Figure 7.3: XENONnT experiment projected sensitivity of SI WIMP-nucleon cross section. The 1 (2)σ sensitivity band is shown in green (yellow) region and the median of sensitivity band is denoted with the black line. 161
Figure 7.4: Top: The rejection power of solar axion hypothesis with coupling obtained from XENON1T [134] if the excess is completely gone in XENONnT. 163

LIST OF TABLES

Table 3.1: Kolmogorov–Smirnov test (KS test) results of $^{131\mathrm{m}}$Xe event distribution under 2D and 3D FDC, respectively. 47
Table 3.2: Surface background rates in several noble liquid detectors inferred from either ^{210}Pb or ^{210}Po isotopes. One of the rate in the LUX experiment is for the cathode surface events, which is indicated in the table. 67

Table 4.1: The best-fit to data under the hypothesis of a 200 GeV/c^2 WIMP in 1.3T FV in the full ROI. The fit results for each background components and the 200 GeV/c^2 WIMP are listed for the full ROI in 1.3T FV. 76

Table 5.1: Summary of components in the background model B_0 with expected and fitted number of events in the 0.65 tonne-year exposure of SR1. Both numbers are within the (1, 210) keV ROI and with efficiency loss. 111
Table 5.2: Key quantities for the estimation of ^{37}Ar rate due to a constant leak. 115
Table 5.3: Total efficiencies, including detection and event selection efficiency, at several energies that were used as energy thresholds in this threshold study. 132
Table 5.4: Significances of solar axion and tritium hypotheses with different energy thresholds. 134
Table 5.5: 90% C.L. upper limit for each hypothesis using S2-only method, including the avarage tritium activity over SR1, the axion-electron coupling g_{ae} inferred from ABC solar axion only, and the neutrino magnetic moment μ_{ν}. 136

ACKNOWLEDGEMENTS

I would like to thank many people, without whom I could not finish this long journey.

First, I would like to thank my advisor, Prof. Kaixuan Ni, for his fast, consistent, inspiring feedback and guidance throughout the past five years. Kaixuan is patient, easy-going, and always available to talk to. He not only welcomed me into the lab when I switched from a completely different field but also sets me an example of being an extraordinary advisor in the future.

I thank members in Ni group, Dr. Yuehuan Wei, Jialing Fei, Dr. Francesco Lombardi, Yue Ma, Jianyang Qi, and Min Zhong, for the useful discussion and casual chat. Special thanks go to Dr. Yuehuan Wei, who I worked with most in the lab and in the analysis of XENON1T. I also appreciate all the group activities, such as group barbeque, kayaking, and numerous hiking in the sunny San Diego.

I want to express my gratitude to members in the XENON Collaboration. I am grateful to my collaborators, Alexey Elykov, Dr. Alexander Fieguth, Dr. Michelle Galloway, and Dr. Evan Shockley. Especially I should thank Dr. Galloway and Dr. Shockley, without whom the study of the low-energy excess would never be completed. I would like to thank Dr. Jelle Aalbers, Prof. Patrick de Perio, Prof. Fei Gao, Prof. Shingo Kazama, and Prof. Qing Lin for their help in analysis, during the remote telecons and in-person analysis workshops. Thank Prof. Patrick Decowski and Prof. Luca Grandi for being wonderful editors for the excess paper. I also thank Prof. Elena Aprile for making the XENON project possible.

I would like to thank all my friends for their support during these years. Special thanks go to Bili Dong, Dr. Jiuyuan Nie, Dr. Yinming Shao, Kaiyue Yang, Yidan Yin, Dr. Shu Zhang for outdoor activities, roadtrips, and countless lunch and dinner together. Those are the moments I will treasure forever.

Lastly but more importantly, I want to thank my parents, Qinghua Ye and Fenlan Zhai, for their unconditional support. I left home and studied in a different place when I was 11, and the distance from home keeps growing over years. I am more than grateful for your understanding, support, and encouragement for me to pursue my dream of being a physicist. This dissertation is for you.

Chapter 3, in part, includes material from the following publications. (1) XENON Collaboration, “The XENON1T dark matter experiment”, Eur. Phys. J. C 77, 881 (2017). (2) XENON Collaboration, “XENON1T Dark Matter Data Analysis: Signal Reconstruction, Calibration and Event Selection”, Phys. Rev. D 100, 052014 (2019). (3) XENON Collaboration, “XENON1T dark matter data analysis: Signal and background models and statistical inference”, Phys. Rev. D 99, 112009 (2019). The dissertation author is an author of those publications.

Chapter 4, in full, is a summary of the following publications. (1) XENON Collaboration, “Dark matter search results from a one ton-year exposure of XENON1T”, Phys. Rev. Lett. 121, 111302 (2018). (2) XENON Collaboration, “Constraining the Spin-Dependent WIMP-Nucleon Cross Sections with XENON1T”, Phys. Rev. Lett. 122, 141301 (2019). (3) XENON Collaboration, “First Results on the Scalar WIMP-Pion Coupling, Using the XENON1T Experiment”, Phys. Rev. Lett. 122, 071301 (2019). (4) XENON Collaboration, “Light Dark Matter Search with Ionization Signals in XENON1T”, Phys. Rev. Lett. 123, 251801 (2019). (5) XENON Collaboration, “Search for Light Dark Matter Interactions Enhanced by the Migdal Effect or Bremsstrahlung in XENON1T”, Phys. Rev. Lett. 123, 241803 (2019). The dissertation author is an author of those publications.

Chapters 5 and 6, in part, are accepted for publication as they should appear soon in Phys. Rev. D, 2020, XENON Collaboration and Xavier Mougeot, “Excess Electronic Recoil Events in XENON1T”. The dissertation author is one of the corresponding authors of this publication. Chapter 6 also contains results from XENON Collaboration, “Observation of two-neutrino double electron capture in ^{124}Xe with XENON1T”, Nature 568, 532-535 (2019). The dissertation author is an author of this publication.

Chapter 7, in part, is accepted for publication and will appear soon in Journal of Cosmology and Astroparticle Physics, 2020, XENON Collaboration, “Projected WIMP Sensitivity of the XENONnT Dark Matter Experiment”. The dissertation author is an author of this publication.

VITA

2014	Bachelor of Science, Department of Physics, Zhejiang University, Hangzhou, China
2020	Doctor of Philosophy, Department of Physics, University of California San Diego, La Jolla, United States

PUBLICATIONS

XENON Collaboration, ^{222}Rn emanation measurements for the XENON1T experiment, arXiv: 2009.13981

Y. Wei, J. Long, F. Lombardi, Z. Jiang, J. Ye and K. Ni, Development of a Sealed Liquid Xenon Time Projection Chamber with a Graphene-Coated Electrode, arXiv: 2007.16194

XENON Collaboration, Projected WIMP Sensitivity of the XENONnT Dark Matter Experiment, arXiv: 2007.08796

XENON Collaboration and Xavier Mougeot, Excess Electronic Recoil Events in XENON1T, arXiv: 2006.09721

XENON Collaboration, Energy resolution and linearity in the keV to MeV range measured in XENON1T, Eur. Phys. J. C 80, 785 (2020)

A. Bernstein, M. Clark, R. Essig, M. Fernanderz-Serra, A. Kopec, R. F. Lang, J. Long, K. Ni, S. Pereverzev, J. Qi, P. Sorensen, Y. Wei, J. Xu, J. Ye, C. Zhen, LBECA: A Low Background Electron Counting Apparatus for Sub-GeV Dark Matter Detection, Journal of Physics: Conference Series 1468, 01203 (2020)

XENON Collaboration, Search for Light Dark Matter Interactions Enhanced by the Migdal Effect or Bremsstrahlung in XENON1T, Phys. Rev. Lett. 123, 241803 (2019)

XENON Collaboration, Light Dark Matter Search with Ionization Signals in XENON1T, Phys. Rev. Lett. 123, 251801 (2019)

XENON Collaboration, XENON1T Dark Matter Data Analysis: Signal Reconstruction, Calibration and Event Selection, Phys. Rev. D 100, 052014 (2019)

XENON Collaboration, XENON1T dark matter data analysis: Signal and background models and statistical inference, Phys. Rev. D 99, 112009 (2019)

XENON Collaboration, The XENON1T data acquisition system, JINST 14, P07016 (2019)

XENON Collaboration, Observation of two-neutrino double electron capture in 124Xe with XENON1T, Nature 568, 532-535 (2019)

XENON Collaboration, Constraining the Spin-Dependent WIMP-Nucleon Cross Sections with XENON1T, Phys. Rev. Lett. 122, 141301 (2019)

XENON Collaboration, First Results on the Scalar WIMP-Pion Coupling, Using the XENON1T Experiment, Phys. Rev. Lett. 122, 071301 (2019)

XENON Collaboration, Dark matter search results from a one ton-year exposure of XENON1T, Phys. Rev. Lett. 121, 111302 (2018)

XENON Collaboration, Signal yields of keV electronic recoils and their discrimination from nuclear recoils in liquid xenon, Phys. Rev. D 97, 092007 (2018)

XENON Collaboration, Intrinsic backgrounds from Rn and Kr in the XENON100 experiment, Eur. Phys. J. C 78, 132 (2018)

XENON Collaboration, The XENON1T dark matter experiment, Eur. Phys. J. C 77, 881 (2017)

XENON Collaboration, Search for bosonic super-WIMP interactions with the XENON100 experiment, Phys. Rev. D 96, 122002 (2017)

XENON Collaboration, Online ^{222}Rn removal by cryogenic distillation in the XENON100 experiment, Eur. Phys. J. C 77, 358 (2017)

XENON Collaboration, Search for WIMP inelastic scattering off xenon nuclei with XENON100, Phys. Rev. D 96, 022008 (2017)

XENON Collaboration, Removing krypton from xenon by cryogenic distillation to the ppq level, Eur. Phys. J. C 77, 275 (2017)

XENON Collaboration, First Dark Matter Search Results from the XENON1T Experiment, Phys. Rev. Lett. 119, 181301 (2017)

XENON Collaboration, Search for Electronic Recoil Event Rate Modulation with 4 Years of XENON100 Data, Phys. Rev. Lett. 118, 101101 (2017)

XENON Collaboration, Results from a Calibration of XENON100 Using a Source of Dissolved Rndon-220, Phys. Rev. D 95, 072008 (2017)

XENON Collaboration, Effective field theory search for high-energy nuclear recoils using the XENON100 dark matter detector, Phys. Rev. D 96, 042004 (2017)

XENON Collaboration, Search for magnetic inelastic dark matter with XENON100, JCAP 1710 (2017) 039

ABSTRACT OF THE DISSERTATION

Searches for WIMPs and Axions with the XENON1T Experiment

by

Jingqiang Ye
Doctor of Philosophy in Physics

University of California San Diego, 2020

Professor Kaixuan Ni, Chair

Numerous evidence suggests that the majority of matter in the Universe is made of a rarely interacting, non-luminous component, termed dark matter. The XENON1T experiment, utilizing a two-phase liquid xenon time projection chamber, was primarily designed to search for Weakly Interacting Massive Particles (WIMPs), one of the most promising dark matter candidates. With one tonne-year exposure, XENON1T placed the most stringent upper limits of WIMP interaction strength for a large range of WIMP masses and a variety of interaction types. The unprecedented low background in XENON1T also enabled competitive searches for electronic recoil signals. An excess was observed above the known background at low energies and is most prominent between 2 and 3 $\mathrm{keV_{ee}}$. This excess favors solar axions over backgrounds at 3.4σ, a hypothetical particle arising from the Peccei-Quinn theory to solve the strong CP problem. The resulting axion couplings, however, are in strong tension with astrophysical constraints. The excess can also be explained by β decays of tritium at 3.2σ with a trace amount, which can neither be confirmed nor be rejected with the current knowledge of its production and mitigation mechanisms. If an unconstrained tritium component is added to both alternate and null hypotheses, the significance of the solar axion hypothesis is reduced to 2.0σ. This search also includes other electronic recoil signals, such as an enhanced neutrino magnetic moment, bosonic dark matter, and leptophilic dark matter. The prospect of XENONnT, the next-generation experiment that is expected to take science data in 2021, is also discussed in the context of searching for WIMPs and deciphering the excess observed in XENON1T, respectively.

Chapter 1

Dark Matter

Dark matter (DM) is the non-luminous, stable, and weakly-interacting matter that consists of 85% matter in the Universe. So far physicists only have limited knowledge of the nature of dark matter, but its existence has been supported by numerous evidence that motivates a variety of dedicated experiments to hunt for this elusive matter. This chapter is organized as follows. In Sec. 1.1, several leading evidence for DM are presented, including galaxy rotation curve, bullet cluster, and the CMB observation. In Sec. 1.2, two promising DM candidates, i.e. WIMPs and axions, are discussed.

1.1 Evidence of Dark Matter

1.1.1 Galaxy Rotation Curve

The dynamical observation has a longer history than people usually think; in fact, even scientists working in this field are not necessarily aware of the full history. In 1884, Lord Kelvin made the first attempt to estimate the amount of DM in the Milky Way by assuming the stars acting like a gas of particles and subsequently studying the relation between the system size and velocity dispersion of the stars. He concluded that "Many of our stars, perhaps a great majority of them, may be dark bodies" [1]. In 1906, Henri Poincaré argued that Lord Kelven's calculation is comparable with the results given by telescope and the majority is still the shining matter [2]. In this paper, Poincaré coined the term "dark matter", which is 27 years earlier than Fritz Zwicky who is apocryphally considered to devise the name. Lots of observations started then but none of them was convincing until 1970s, when Vera Rubin, Albert Bosma as well as many other astronomers made observations in a collection of galaxies through optical measurement and radio observation of the 21-cm Hydrogen line. A detailed history can be found in Ref. [3].

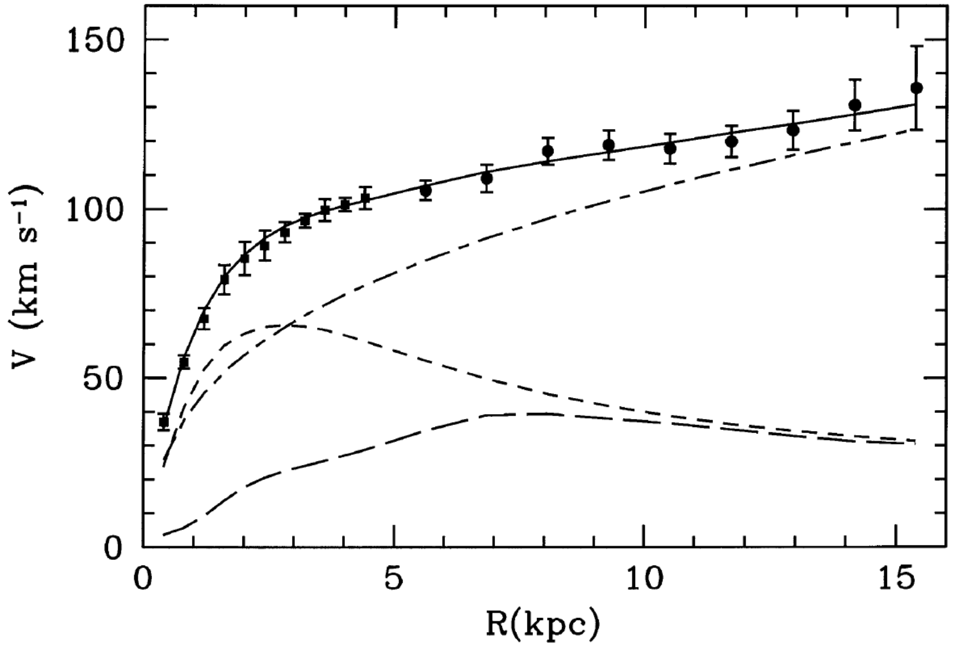

Figure 1.1: M33 rotation curve (points) compared with the best-fitting model (solid line), which consists of contributions from the dark matter halo (dot-dashed line), stellar disk (short-dashed line), and gas (long-dashed line). Figure from Ref. [4].

In Newtonian dynamics, an object orbiting around the central astrophysical object with a larger distance to the center would have a smaller velocity. However, discrepancies are found between the expectation and observation, for which the nearby galaxy M33 is illustrated in Fig. 1.1 as an example. The predicted velocity from the visible stellar disk and gas quickly falls down after the radius of 3 kpc while the observed data keep rising to the last measured point. This discrepancy is observed in many galaxies and thus suggests two possibilities:

1. The law of gravity fails in large scale and has to be modified.
2. Most matter in the Universe is made up by a non-luminous component, which cannot be observed via electromagnetic radiation but can interact gravitationally.

The former one leads to the hypothesis of Modification Newtonian Dynamics (MOND) while the latter points to the existence of DM.

1.1.2 Bullet Cluster

Bullet cluster is deemed as one of the most compelling evidence for DM. In 1E 0667-56, one of most hot and X-ray luminous galaxy clusters, a sub-cluster passed through the main cluster from the left, as illustrated in Fig. 1.2. A bullet-like pink clump was observed by Chandra using X-rays, which was emitted by the baryonic matter as they got heated in the collision. The blue population is revealed by utilizing the weak-lensing effect, which is an effect that light ray would be bent when passing by object with large mass and is thus related to the gravitation. In Fig. 1.2, the pink clump is clearly lagged compared to the blue region. It follows that, the center of gravity and the center of baryonic matter do not coincide in this cluster. It is one of observations that cannot be resolved by the MOND theory but

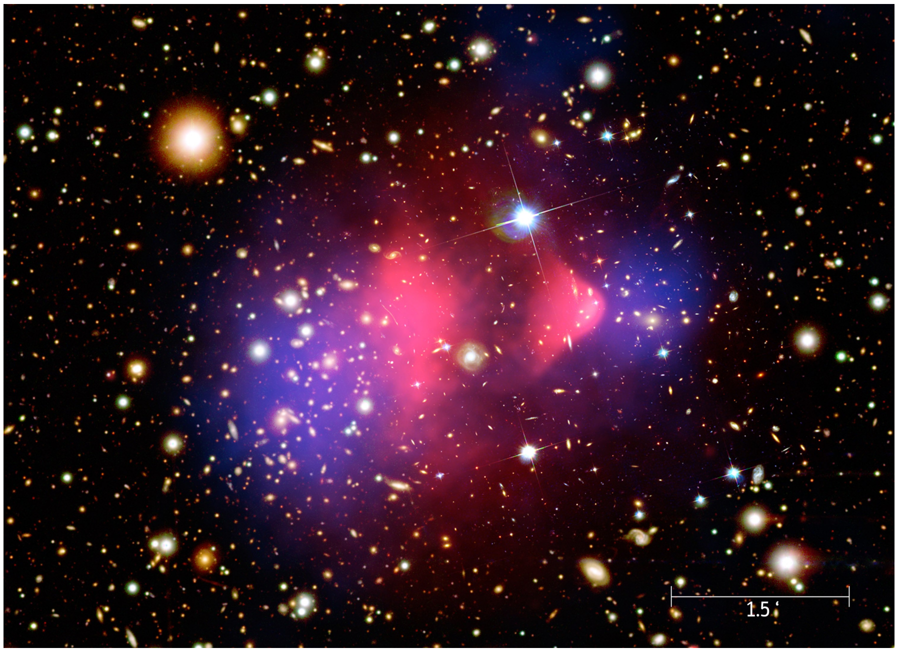

Figure 1.2: Bullet cluster (1E 0667-56). The red population is from X-ray observation and blue clump is revealed from the weak-lensing mass map. Yellow and white blobs are galaxies determined from optical measurement. Figure from Refs. [5, 6].

can be easily explained by DM.[1] Since DM interacts weakly with either baryonic matter or itself, it can go through collisionlessly; on the contrary, baryonic matter will lag behind due to the collisional interaction. In the scenario of DM, the large deviation between the center of gravitation and that of baryonic matter suggests that DM makes up the majority of mass in this galaxy cluster.

1.1.3 Cosmic Microwave Background

Cosmic microwave background (CMB) is the remnant from around 380,000 years after the Big Bang. Prior to this point, the temperature of the Universe was so high that everything in the Universe was in the plasma state, i.e. the state of being charged particles like proton and electron, thereby photons could

---

[1] There are also a plenty of other things that cannot be explained by the MOND theory. For example, in 2018 researchers found a galaxy lacking DM [7], which is contradictory to the MOND theory that should be observed everywhere.

not travel far due to the frequent Thompson scattering and absorption by charged particles. As the Universe cools down with time, protons were finally able to combine with electrons and form neutral hydrogen atoms around 380,000 years after the Big Bang, which is remarked as the start of the *recombination epoch*. As a consequence, the mean free path of photons became approximately the size of the Universe and the emitted photons imprinted in the cosmos at the start of recombination epoch are now observed as CMB.

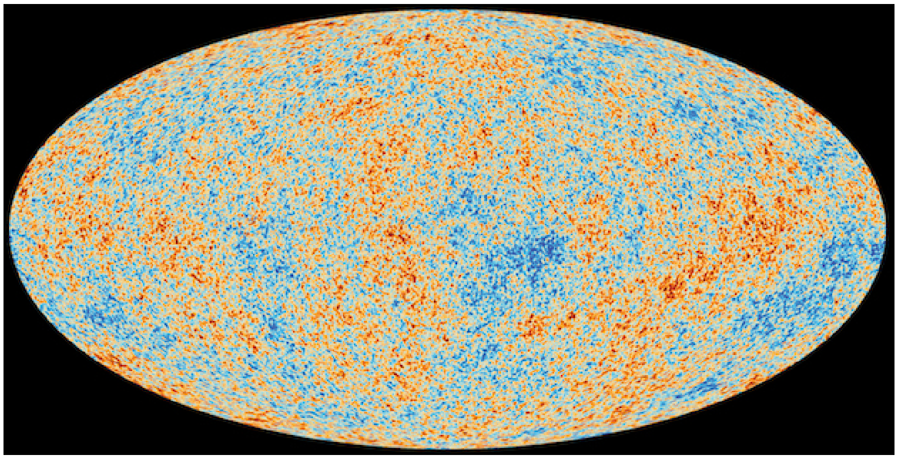

Figure 1.3: Temperature anisotropy in CMB from the latest Planck result [8]. Red and blue regions indicate relatively hot and cold regions, respectively. Figure from Ref. [8].

CMB was first observed by Penzias and Wilson in 1964 when calibrating their radio telescope [9]. They found an isotropic and time-independent "noise" which was later proved to be an important evidence for the Big Bang Theory. A series of scientific satellites, including COBE [10], WMAP [11], and Planck [8], have been launched to measure CMB with improved precision and the latest result from Planck suggests the CMB temperature of $(2.722 \pm 0.027)\,\mathrm{K}$. Yet scientists found imperfection in CMB isotropy — a tiny fluctuation of $\sim 250\,\mu\mathrm{K}$ — as illustrated in Fig. 1.3. The red spots are slightly hotter and the blue are colder.

There are many ways to infer the DM percentage of all the matter in the

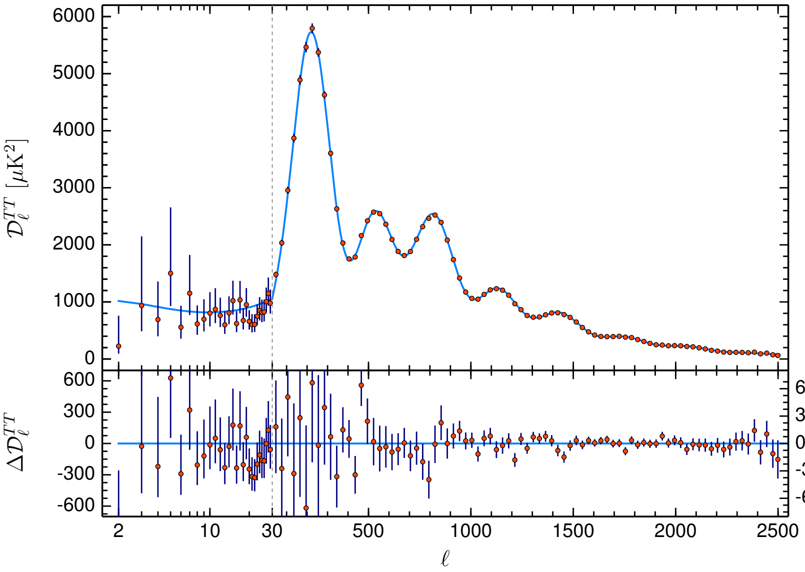

Figure 1.4: CMB power spectrum. Red points are measurements from Planck [8] and blue curve is the fit result using ΛCDM model. Figure from Ref. [8].

Universe, such as the gravitational lensing effect, the galaxy rotation curve, etc. Among them, the most accurate approach is to make use of the CMB anisotropy. In ΛCDM model, the Standard Model of cosmology, baryonic matter, DM, and dark energy contribute to the anisotropy differently.[2] By fitting ΛCDM model to the CMB power spectrum shown in Fig. 1.4, we have $\Omega_b h^2 = 0.0224 \pm 0.0001$, $\Omega_c h^2 = 0.120 \pm 0.001$, and $\Omega_\Lambda h^2 = 0.6847 \pm 0.0073$, where $h = H_0/100$ is the reduced Hubble constant, $\Omega_b h^2$, $\Omega_c h^2$, and $\Omega_\Lambda h^2$ are the density of baryonic matter, DM, and dark energy, respectively. This result translates to a composition of the Universe with ~27% DM, ~5% baryonic matter, and ~68% dark energy.

---

[2] Radiation is relatively small and thus is ingored here.

1.2 Dark Matter Candidates

Lots of physics models have been proposed to solve the DM mystery. In this section, two DM candidates that are most promising and relevant to this thesis are introduced: WIMPs and axions. Each candidate is well-motivated and has led to enormous experimental efforts. It is noteworthy to mention that axions can not only solve the DM puzzle, but also solve the so-called strong CP problem, abnormal cooling of stars, as well as the matter-antimatter asymmetry [12].

1.2.1 WIMP

The Weakly Interacting Massive Particle (WIMP) is a class of hypothetical particles that have been the leading candidate of DM for decades. The main reason for the popularity is that it can naturally explain the DM relic density.

The standard assumption of WIMP production is the thermal production. WIMPs could be generated through the collision between Standard Model (SM) particles in the radiation dominated age, which is before the Big Bang Nucleosynthesis (BBN) and is able to generate WIMPs due to the extremely high temperature. At the same time, WIMPs can annihilate with each other into SM particles through the reverse reaction, the flux of which is given by

$$\Gamma_{\mathrm{ann}} = \langle \sigma_{\mathrm{A}} v \rangle \, n, \tag{1.1}$$

where σ_{A} is the annihilation cross section, v is the WIMP velocity, and n is the WIMP density. An equilibrium can be achieved between the production and annihilation.

The temperature drops as the Universe expands, and only SM particles at the

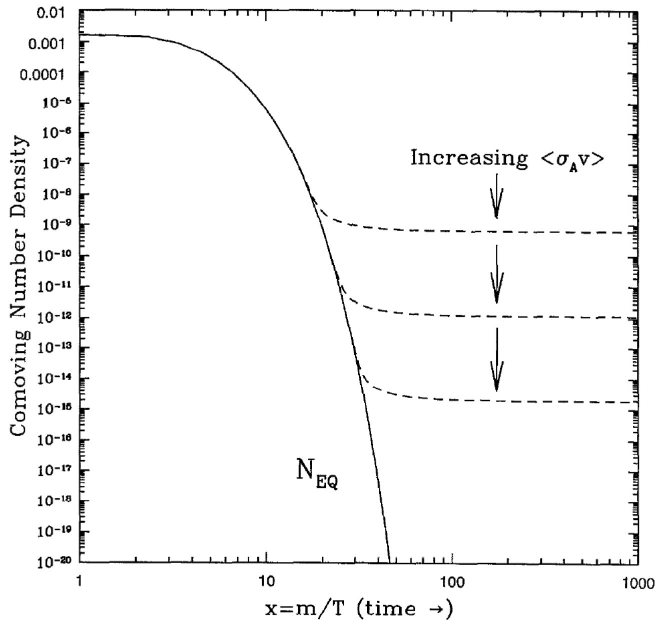

Figure 1.5: WIMP density in a comoving volume evolves with the cooling of the Universe. The solid line represents the equilibrium abundance assuming the Universe is not expanding. The dash lines are the actual abundance considering the expansion of the Universe with different annihilation cross sectons $\langle\sigma_{\mathrm{A}} v\rangle$. Figure from Ref. [13].

tail of Boltzmann distribution are energetic enough to produce WIMPs. Given that the production and annihilation are in equilibrium, WIMP density decreases by e^{-T/m_χ}, where T is the Universe temperature and m_χ is the WIMP mass. When the annihilation rate (or production rate, as they are in equilibrium) is even smaller than the expansion rate of Universe, both production and annihilation are deemed to cease due to the low temperature of the Universe and the low WIMP density, respectively. At this point, the production and annihilation are not in equilibrium and WIMP relic density is constant in a comoving volume to account for the Universe expansion. This WIMP density evolution is referred to as freeze-out and is illustrated by Fig. 1.5. The solid line is from production and annihilation equilibrium without taking universe expansion into account while the dashed lines consider the actual abundance assuming different $\langle \sigma_\mathrm{A} v \rangle$. With a larger $\langle \sigma_\mathrm{A} v \rangle$, it will stay in the equilibrium line longer until the annihilation rate is lower than the expansion rate, leading to a smaller final abundance. The relic density of WIMPs is given as [14]

$$\Omega_\mathrm{c} h^2 \simeq \frac{3 \times 10^{-27}\ \mathrm{cm}^3\,\mathrm{s}^{-1}}{\langle \sigma_\mathrm{A} v \rangle}. \tag{1.2}$$

1.2.2 Axion

Axion is a hypothetical particle arising from the Peccei-Quinn theory [15], which is proposed to solve the so-called strong CP problem. Physicists used to assume conjugation (C) and parity (P) symmetry for elemental processes, respectively, but changed their mind in 1960s due to evidences from both theories and experiments. Later, the combination of charge conjugation and parity symmetry was observed to not conserve either in the weak interaction, i.e. the CP violation. Naturally, people expected the same violation in the strong interaction. The neutron electric dipole moment (nEDM), however, was found to be very close to zero with improved accuracy over decades, which turned out to be a strong evidence for CP conservation in the strong interaction. This problem is known as the strong CP problem. Many theories were proposed to solve the problem and perhaps the most cogent solution is the Peceei-Quinn theory. In this theory, the key parameter θ, which has to be manually put as zero to conserve CP in other theories, is instead introduced as a field of vaccum angle $\bar{\theta}$ that is associated with the vaccum potential, and $\bar{\theta}$ would be zero naturally to minimize the energy. While solving the problem, the spontaneous symmetry breaking of the $\bar{\theta}$ field would introduce a pseudoscalar Nambu-Goldstone boson, which is known as the axion.[3]

Generally, axions can be categorized into quantum chromodynamics (QCD) axions and axion-like particles (ALPs). For QCD axions, the mass m_a is related to the decay constant f_a via

$$m_\mathrm{a} = \frac{z^{1/2}}{1+z}\frac{f_\pi m_\pi}{f_\mathrm{a}} \simeq \frac{6 \times 10^6\ \mathrm{GeV}}{f_\mathrm{a}}\ \ \mathrm{eV}/c^2, \tag{1.3}$$

where $z = m_\mathrm{u}/m_\mathrm{d}$ is the ratio between the masses of up and down quarks, $f_\pi = 92\,\mathrm{MeV}$ is the pion decay constant, and m_π is the pion mass. Since axion couplings are inversely proportional to f_a, it follows that the couplings are proportional to m_a for QCD axions. Reciprocally, ALPs do not necessarily satisfy Eq. (1.3), therefore the axion couplings and masses are decoupled for ALPs.

Axions are also well-motivated DM candidates. At the time of the Big Bang, axions could be created via thermal mechanism and non-thermal mechanisms, e.g. the misalignment mechanism. For QCD axions, the preferred mass region is μeV–meV owing to the following reasons. The lower bound comes from the

---

[3] Axion is named by Frank Wilczek after a laundry detergent since it can clean up the strong CP problem with an axial current.

axion cosmology. As the relic density of axions produced through the vaccum misalignment mechanism can be expressed as [16]

$$\Omega_{\mathrm{a}} \sim (\frac{5\,\mu\mathrm{eV}}{m_{\mathrm{a}}})^{7/6}, \tag{1.4}$$

m_{a} has to be larger than $\mathcal{O}(\mu\mathrm{eV})$ to avoid a closed universe ($\Omega_{\mathrm{a}} > 1$). The upper bound of m_{a} is placed by axion searches in particle and nuclear experiment, as well as astrophysical observation that will be described in the next paragraphs [17]. The ALP DM, on the other hand, does not have such a tight restriction of mass as its mass and coupling are not related.

The axion could not only be a viable DM candidate in cosmology, but also play a pivot role in the star evolution in astrophysics. The standard channels of star cooling are neutrino emission and surface photon radiation. However, many stars are found to cool faster than the prediction from the two standard channels. For example, a Red Giant (RG) star will ignite the helium core and become a Horizontal Branch (HB) star after reaching the required temperature; however, the R parameter, the ratio of the number of HB over that of RG stars, is found to be smaller than expected, indicating extra cooling channels of RG stars which lead to the delayed ignition of the helium in RG stars. Similarly, several pulsating White Dwarfs (WDs), the cooling speed of which can be obtained by the changing rate of rotating speed, also show that their actual cooling are faster than the prediction from the standard channels.

These disagreements can be resolved by introducing axion as an extra channel for star cooling. The production of axion in stars is viable through several mechanisms and the emission of axion is unhindered in the star due to its feeble interaction. The strongest axion source in the sky is the Sun. Details of the axion produced in the Sun, i.e. solar axions, can be found in Sec. 2.3.2.1. We do emphasize that the production of QCD axions or ALPs in astrophysical objects are largely indistinguishable, therefore the derived constraints are in principle applicable for both. However, the axion flux is usually calculated under the massless assumption to be relativistic [18], thus the derived limits cannot be compared to the non-relativistic ALP DM limits without modification.

Chapter 2

Direct Detection with Xenon

This chapter focuses on the direction detection with liquid xenon based detectors and is organized as follows. In Sec. 2.1, we describe the working principle of the two-phase liquid xenon time projection chamber, including the signal detection, position/energy reconstruction, and event type identification. In Sec. 2.2, we present the expected signatures of WIMPs in the direct detection with xenon, including the energy spectrum and annual modulation. In Sec. 2.3, we briefly review the axion detection experiments and then discuss axion detection with experiments based on liquid xenon.

2.1 Two-phase Liquid Xenon TPC

Noble gas detectors have a long history.[1] Based on the phase of the target medium, they can be categorized into single-phase and two-phase detectors. Single-phase detectors can utilize either gaseous phase or liquid phase, while two-phase detectors make use of both. Time projection chambers (TPCs) can infer the event time information by its definition, commonly from the drift of ionized electrons.

---

[1] A brief history of noble gas detectors can be found in Ref. [19].

In this thesis, we will focus on two-phase TPC, which is one of the most promising technologies in all the possibilities and has consistently led in the direct detection of WIMPs and many other rare processes.

The working principle of two-phase TPC is illustrated in Fig. 2.1. An incoming particle excites and ionizes the xenon atoms at the same time. A fraction of the ionized atoms recombine with the liberated electrons and form xenon excimers, the emitted photons of which are recorded as the prompt scintillation signal together with the initial excimers in the direct excitation as the time scale of recombination process is comparable to the half-life of xenon excimers [20]. The rest of ionized electrons will drift upwards under the *drift electric field* established by the grounded gate and the cathode. When arriving at the liquid-gas interface, the electrons will be extracted into gaseous xenon (GXe) by the strong *extraction field* between the anode and gate, which is stronger in GXe than that in liquid xenon (LXe) due to the larger dielectric constant in LXe. As the electrons accelerate in the GXe, they produce a large number of xenon atom excimers due to the strong electric field and the relatively long mean free path. This amplification process is referred to as the electroluminescence and the resulting detected signal is called the delayed scintillation signal. The prompt and delayed scintillation signals are also referred to as light and charge signals, repectively, or symbolically, S1 and S2.[2] Both signals can be recorded by photosensors, such as photomultiplier tupess (PMTs) or silicon photomultipliers (SiPMs). The scintillation signal from a xenon excimer has a wavelength of 178 nm [21], which is transparent for the quartz window of PMTs. This is one advantage of LXe target as scintillation signal in the alternate detection media may need wavelength shifter to optimize the detection efficiency.

---

[2] The S1 signals would be symbolically represented by the upright S1, while the S1 size would be denoted by the italic $S1$ in the following text. So does the S2 signal.

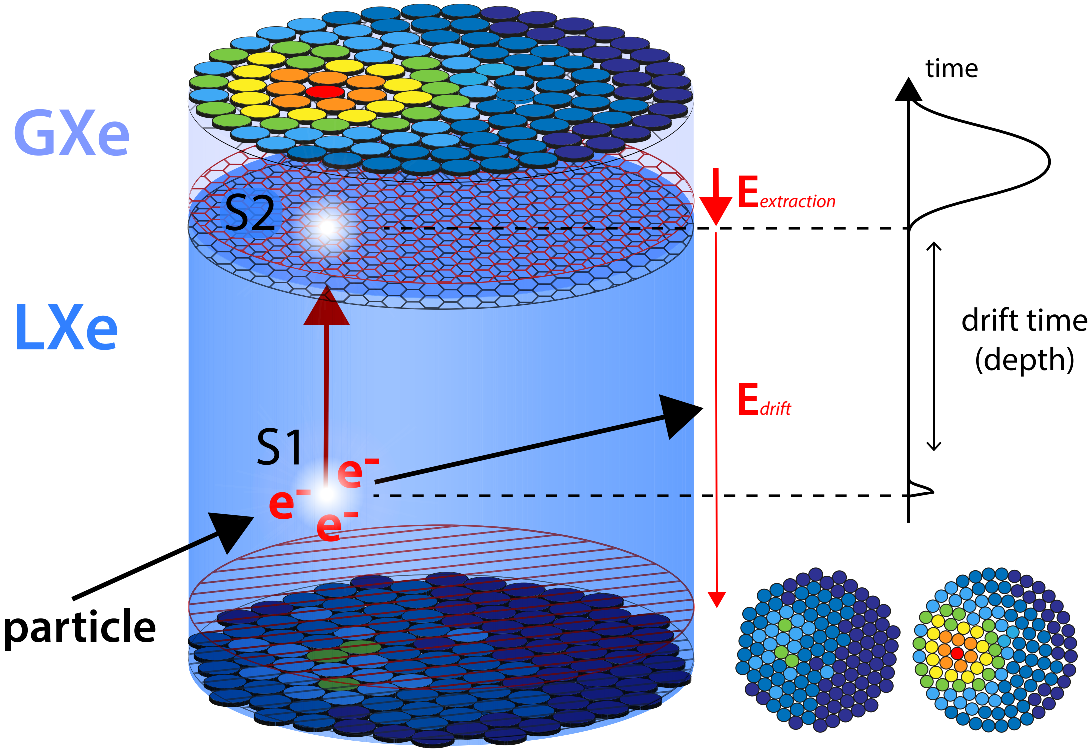

Figure 2.1: Illustration of working principle of two-phase time projection chamber. See details in the text. Figure from Ref. [22].

In general there are mainly two types of recoils in LXe detectors.The first type is the electronic recoil (ER), where the incoming particle interacts with the orbital electrons, such as βs and γs. The other one is the nuclear recoil (NR) which is induced from the interaction with a xenon nucleus; The interactions of neutrons and the hypothetical WIMPs in the xenon target fall in this category. In LXe, ER and NR events can be distinguished by different $S2/S1$ ratios, as ER events tend to ionize more electrons and thus have larger $S2$. By utilizing this feature, background events from βs and γs (ER) can be greatly suppressed in the search for WIMP signal (NR). Currently, the ER rejection power of more than 99.5% (with 50% NR acceptance) has been achieved [23–25].

Two-phase TPCs have good positioning capabilities. The time difference between S1 and S2 signals, defined as drift time, can be used to infer the depth (z position) of the event together with the electron drift velocity, which can be determined from the maximum drift time and the known TPC length.[3] The position in the horizontal plane (i.e. xy position), on the other hand, is reconstructed based on the unique pattern that S2 signals illustrate in the top PMT array. By comparing the observed pattern and the expected pattern from Monte Carlo (MC) simulations, one can reconstruct the most likely position of the event using algorithms based on either neural network or likelihood. The observed positions need further correction to account for the field distortion, of which more details can be found in Sec. 3.2.2. LXe is a good shielding medium with a large density of $\sim 2.9\,\mathrm{g/L}$, thus a good knowledge of event positions allows to reject the external backgrounds by fiducialization, such as those from the TPC or cryostat materials.

Unlike position reconstruction, the energy reconstruction is different for ER and NR events. The ER events deposit almost all the energy into S1 and S2 signals,

---

[3] For the same detection medium with a fixed density, electron drift velocity is mainly dependent on the drift field.

from which one can reconstruct the total deposited energy, see more details in Sec. 3.3.3. NR events not only deposit energies into the light and charge signals, but also lose a fraction to the heat due to the fact that the recoiled xenon atom transfers kinetic energy to its surrounding atoms. The fraction of lost energy to heat is know as the Lindhard factor [26] and is typically between 0.1–0.2 in LXe. The quenching effect must be accounted for to have proper energy reconstruction for NR events.

2.2 WIMP Detection

This section describes the WIMP detection in direct detection experiments, including the expected energy spectrum and annual modulation signature. The energy spectrum calculation is limited to the elastic scattering between WIMP and target medium; the inelastic scattering is beyond the scope of this thesis but a related experimental search with the XENON100 detector can be found in Ref. [27].

2.2.1 WIMP-nucleon Elastic Scattering

Assuming elastic scattering between WIMP and nucleon, the differential rate can be written as:

$$\frac{dR}{dE_\mathrm{r}} = \frac{\rho_0}{m_\chi} \int \frac{d\sigma}{dE_\mathrm{r} m_A} f(\boldsymbol{v}) |\boldsymbol{v}| d^3\boldsymbol{v}, \tag{2.1}$$

where ρ_0 is local WIMP density, m_χ the WIMP mass, m_A is the mass of target atoms, σ is the elastic scattering cross section between WIMP and target medium nucleus, E_r is the nuclear recoil energy, $\boldsymbol{v}$ is the WIMP velocity *relative to the detector*, and $f(\boldsymbol{v})$ is the WIMP velocity distribution. It is noteworthy that the differential rate provided by Eq. (2.1) is in the unit of counts per unit mass (not per atom), time, and recoil energy.

WIMP velocity In the standard halo model (SHM), WIMP velocity is usually considered to follow an isotropic and isothemal Boltzmann-Maxwellian distribution with respect to the *frame of the galaxy*,[4] with the most probable velocity $v_0 = \sqrt{2kT/m_\chi} \simeq 220\,\mathrm{km/s}$, the escape velocity $v_{\mathrm{esc}} = 544\,\mathrm{km/s}$, and the Earth velocity $v_{\mathrm{e}} = 232\,\mathrm{km/s}$. The velocity function is truncated at the escape velocity, as WIMPs that exceed the escape velocity are no longer gravitationally bounded in the galaxy. The velocity distribution is written as below:

$$f(\boldsymbol{v}) = \frac{4v^2}{v_0^3\sqrt{\pi}} \exp(-(\boldsymbol{v} - \boldsymbol{v}_{\mathbf{e}})^2/v_0^2). \tag{2.2}$$

As $\boldsymbol{v}$ is assumed to be isotropic, Eq. (2.2) can be rewritten in the scalar form $f'(v)$ from Ref. [14]:

$$f'(v) = \frac{v}{v_{\mathrm{e}} v_0 \pi} \left[\exp(-(v - v_{\mathrm{e}})^2/v_0^2) - \exp(-(v + v_{\mathrm{e}})^2/v_0^2)\right]. \tag{2.3}$$

Form factor The scattering cross section σ consists of contribution from spin-independent (SI) and spin-dependent (SD) interactions. As SD scattering will be discussed in Sec. 4.1.2, the calculation here is restricted to SI scattering, the differential cross section of which is given then by:

$$\frac{d\sigma}{dE_{\mathrm{r}}} = \frac{m_A}{2\mu_A^2 v^2} \sigma_0^{\mathrm{SI}} \mathcal{F}^2(q), \tag{2.4}$$

where μ_A is the WIMP-nucleus reduced mass, σ_0^{SI} is the SI WIMP-nucleus cross section with zero momentum transfer, $\mathcal{F}(q)$ is the form factor, and $q = \sqrt{2m_A E_{\mathrm{r}}}$ is the momentum transfer. When q increases to the extent that the De Brogile

---

[4] Note that a conversion of velocity is necessitated here as $\boldsymbol{v}$ in Eq. 2.1 is with respect to the detector.

wavelength $\lambda = \hbar/q$ becomes smaller than the nucleus radius, the coherence in the scattering is gone and consequently the effective cross section begins to decrease with an increasing q. This effect is accounted for by the form factor, which can be conveniently expressed in an analytic form, i.e. the Helm form factor [28]:

$$\mathcal{F}(q) = \frac{3j_1(qr_n)}{qr_n} \times e^{-(qs)^2/2}, \tag{2.5}$$

where r_n is the effective nucleus radius, s is a measure of nuclear skin thickness, and $j_1(qr_n)$ is the second spherical Bessel function of the first kind. It is recognized in Ref. [29] that the analytic Helm form factor (Eq. (2.5)) matches with the numerical calculation best with $r_n \simeq 1.14A^{1/3}\,\text{fm}$ and $s \simeq 0.9\,\text{fm}$, where A is the mass number of the target atom. This approximation was also found in a good agreement with a more dedicated shell-model calculation before the first minimum [30],[5] which covers the typical region of interest (ROI) for WIMP search in LXe experiment, e.g. (4.9, 40.9) keV_{nr} in XENON1T [23]. The form factors in three commonly used direct detection materials, including ^{131}Xe, ^{40}Ar, and ^{73}Ge, are shown in Fig. 2.2. The first minimum of form factor $\mathcal{F}(q)$ is set by the nucleus radius. Before the first minimum, the form factor $\mathcal{F}$ decreases faster for target medium with a larger mass number A, as it leads to a larger nucleus mass (larger q) and a larger radius (larger r_n).

Zero momentum transfer cross section The cross section at zero momentum transfer σ_0 in Eq. (2.4) is given by:

$$\sigma_0 = \sigma_N \frac{\mu_A^2}{\mu_N^2} \left(Z \cdot f^{\text{p}} + (A - Z) \cdot f^{\text{n}}\right)^2, \tag{2.6}$$

where σ_N is the SI WIMP-nucleon cross section, μ_N is the WIMP-nucleon reduced

---

[5] An alternate parameterization of s and r_n was used in Ref. [30], but the resulting difference in Helm form factor is negligible.

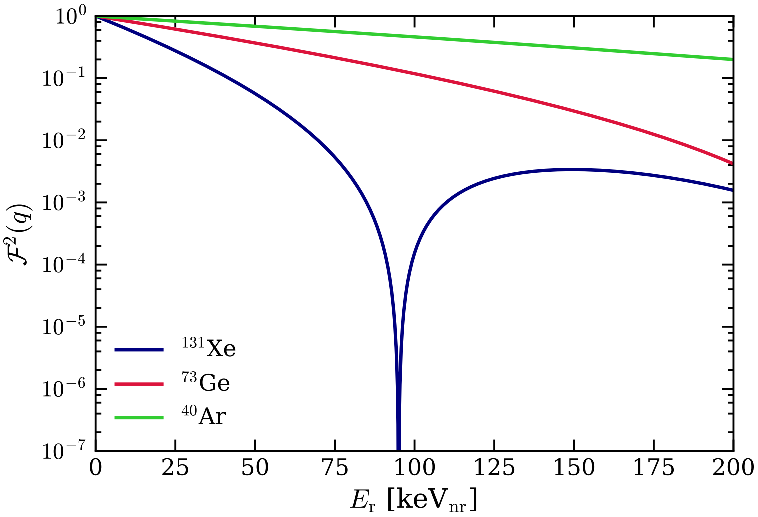

Figure 2.2: Helm form factors $\mathcal{F}^2(q)$ as function of nuclear recoil energies for ^{131}Xe (blue), ^{73}Ge (red), and ^{40}Ar (green), respectively.

mass, $f^{\mathrm{p/n}}$is the contribution of proton/neutron to the total coupling strength. Since a common practice is that assuming neutrons and protons contribute equally to the SI WIMP-nucleon scattering process ($f_{\mathrm{n}} \simeq f_{\mathrm{p}}$), σ_0^{SI} is then proportional to A^2, which indicates that heavier targets have larger discovery potential for SI scattering process. In the end, the differential rate dR/dE_{r} is proportional to the SI WIMP-nucleon cross section σ_N, thus this unknown parameter is used to set constraints as a function of WIMP mass.

Final calculation Combining Eq. (2.1, 2.4, 2.6), one can arrive at the following formula:

$$\frac{dR}{dE_{\mathrm{r}}} = \sigma_N \frac{\rho_0}{2m_\chi \mu_N^2} A^2 \mathcal{F}^2(\sqrt{2E_{\mathrm{r}} m_A}) \int_{v_{\mathrm{min}}}^{v_{\mathrm{esc}}} \frac{f'(v)}{v} dv, \tag{2.7}$$

where $\mathcal{F}$ and $f'(v)$ are given in Eq. (2.3, 2.5), respectively, and $v_{\mathrm{min}} = \sqrt{E_{\mathrm{r}} m_A/(2\mu_A^2)}$, the minimum required WIMP velocity to induce a nuclear recoil with energy of E_{r}. Eq. (2.7) not only reinstates the fact that the WIMP signal rate is higher for heavier target medium ($\propto A^2$), but also reveals the dependency of the event rate on E_r. The event rate decreases with increasing E_r mainly due to the falling form factor $\mathcal{F}(\sqrt{2E_\mathrm{r}m_A})$, but also partly from the resulting higher threshold of WIMP velocity v_min. The scattering signal spectra for the three aforementioned detection media are illustrated in Fig. 2.3, assuming a $30\,\mathrm{GeV}/c^2$ WIMP with a SI WIMP-nucleon cross section of $1 \times 10^{-47}\,\mathrm{cm}^2$.

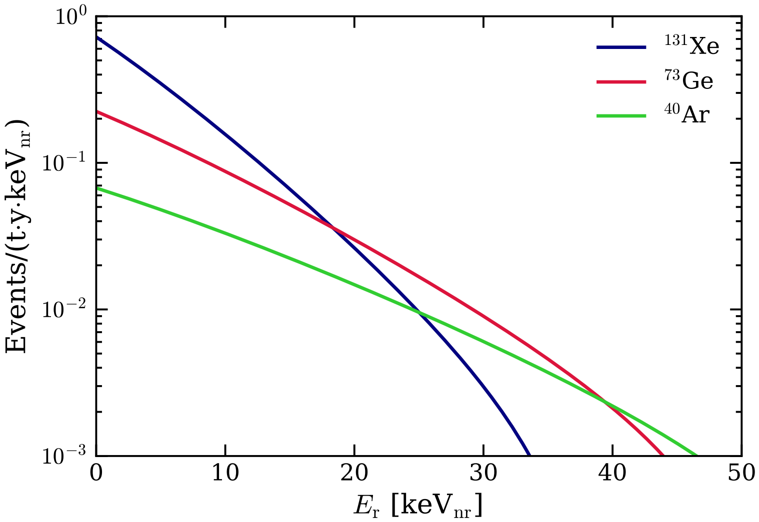

Figure 2.3: Elastic scattering spectra for a $30\,\mathrm{GeV}/c^2$ WIMP with a spin-independent WIMP-nucleon cross section σ_N=$1 \times 10^{-47}\,\mathrm{cm}^2$ in target media of ^{131}Xe (blue), ^{73}Ge (red), and ^{40}Ar (green), respectively.

2.2.2 Annual Modulation

The other signature of WIMP is the annually modulated pattern due to the Earth's orbiting around the Sun. As the Sun orbits in the Milky Way Galaxy, the relative velocity between the Sun and local WIMP is $\sim 320\,\mathrm{km/s}$; however, since the Earth also moves around the Sun, the local WIMP velocity observed on the Earth $\boldsymbol{v}$ (i.e. the WIMP velocity relative to the detector) varies with season. In June, when the Earth's velocity is in the same direction as the Sun's orbital velocity, $|\boldsymbol{v}|$ achieves the maximum; on the contrary, $|\boldsymbol{v}|$ is minimum in December.

Therefore, WIMP is expected to have the annual modulated signal with higher rate in the summer and lower rate in the winter, as illustrated in Fig. 2.4.

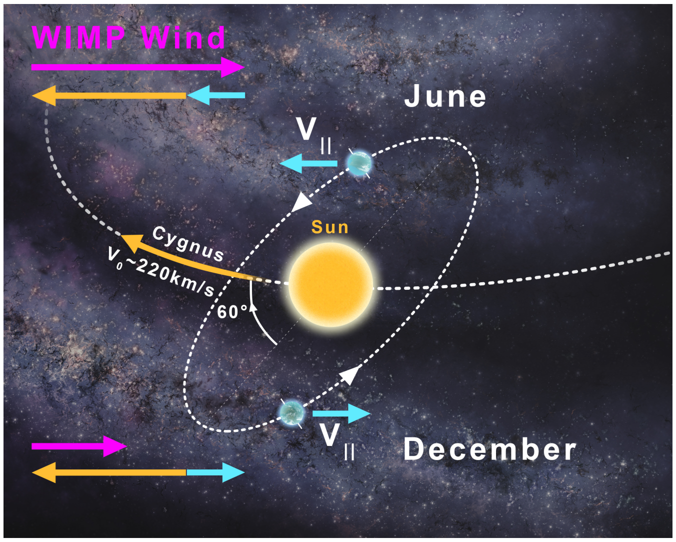

Figure 2.4: Illustration of the annual modulated WIMP signal. Figure from Ref. [31].

DAMA/LIBRA Collaboration claimed to detect WIMPs by this annual modulation method with NaI target [32, 33]. However, with the detected rate from the DAMA experiment, the possibilities of induced nuclear recoils or electronic recoils have been excluded by other experiments [34–37] with different target materials. To get rid of the model dependence, the SABRE experiment [38] employs the same NaI target in Laboratori Nazionali del Gran Sasso (LNGS), Italy, where the DAMA experiment was located, and another identical detector in Australia to account for the difference between hemispheres.

2.3 Axion Detection

The constraints on axion couplings are mainly from the direct detection experiments and astrophysical observation (stellar evolution). This section focuses on the axion search in direct detection experiments. Sec. 2.3.1 briefly summarize the dedicated axion searches with different types of experiments. Sec. 2.3.2 discusses the hunt for solar axions, while Sec. 2.3.3 focuses on the detection for ALP DM; both of them use xenon as the detection medium.

2.3.1 Axion Experiments

A variety of experiments have been deployed or under planning to search for axions. Based on the axion sources, they can be roughly categorized into laser-induced axion experiment (LSW), solar axion experiment (helioscope), or galactic DM axion experiment (haloscope). Most of them rely on two possible axion couplings — the axion-photon coupling (Primakoff effect) and the axion-electron coupling (axio-electric effect).

In the Light-Shining-through-a-Wall (LSW) experiments like ALPS [39], a strong laser is utilized to shine on the wall and a receiver is on the other for detection. Photons cannot penetrate the wall. However, the photon and axion can be converted to each other in the presence of external electric or magnetic fields if there is a finite coupling between axion and photon, which is known as the Primakoff effect.[6] By adding external magnetic fields on both sides, the photons emitted by the laser is possible to be converted into axions on the source side, which can "shine" through the wall due to its feeble interaction and be detected by the receiver when converted back to photons under the magnetic field on the detection side. The magnetic field are usually perpendicular to the axion/photon propagation direction to maximize the conversion probability.

The axion helioscope experiments, notably CAST [42] and its successor IAXO [43],

---

[6] Sometimes the effect of photons being converted into axions are called Primakoff effect and the other direction is referred to as inverse-Primakoff effect [40, 41].

mostly detect solar axions by the Primakoff effect. Solar axions can emerge with energies of $\mathcal{O}(\mathrm{keV})$ via several mechanisms (Sec. 2.3.2.1). In the CAST experiment, solar axions could be converted into X-rays within the 9T magnet directed towards the Sun with a probability of

$$P_{\mathrm{a}\to\gamma} = \left(g_{\mathrm{a}\gamma} B \frac{\sin(qL/2)}{q} \right)^2 , \tag{2.8}$$

where $q = m_{\mathrm{a}}^2/2E$ is the axion-photon momentum transfer in vacuum, and $L = 9.26\,\mathrm{m}$ for CAST. Therefore, the sensitivity for higher mass ($m_{\mathrm{a}} \gtrsim 10\,\mathrm{meV}/c^2$) is quickly reduced due to the suppressed axion-photon conversion probability.

The ADMX experiment [44], one of the most sensitive cold axion DM search experiments, use microwave cavity for axion detection. The cavity is permeated with magnetic field; if the cavity's resonant frequency matches with the axion field, an axion passing through the cavity would be converted into a photon and subsequently be detected with a sensitive microwave receiver. As the entire mass of an axion is converted to the energy of the photon, the preferred QCD axion mass between μeV and meV correspond to frequencies between 240 MHz and 240 GHz. The resonant frequency of the cavity is tunable by adjusting the size of the magnetic field and/or moving a dielectric tuning rod. The signature for a fixed-mass axion in the microwave cavity experiment is a quosi-chromatic signal at the expected $\mathcal{O}(\mathrm{GHz})$ frequency with an $\mathcal{O}(\mathrm{kHz})$ dispersion from the DM velocity distribution.

2.3.2 Solar Axions

2.3.2.1 Production

Axions can be produced in the Sun from its coupling with electrons, photons, and nucleons, respectively.

For coupling between electron and axion, solar axions are generated from three mechanisms: (1) Atomic deexcitation and recombination, (2) Bremsstrahlung, and (3) Compton Scattering, which are collectively referred to as ABC process [18]. The main contribution of ABC axion flux comes from the Bremsstrahlung process since the dominant matter in the Sun, i.e. hydrogen and helium, are fully ionized. Axion fluxes from Bremsstrahlung and Compton scattering are both continuous, as illustrated in Fig. 2.5 (blue), while the peaks above the continuum are from the atomic deexcitation and recombination. The ABC flux scales with the axion-electron coupling g_{ae} as

$$\Phi_{\mathrm{a}}^{\mathrm{ABC}} \propto g_{\mathrm{ae}}^2. \tag{2.9}$$

The Sun would also emit axions if there is a finite coupling between photons and axions. In this case, photons can be transformed into axions in external electric or magnetic fields. This axion emission process is known as the Primakoff process. The Primakoff flux is given by [16]

$$\begin{aligned} \frac{d\Phi_{\mathrm{a}}^{\mathrm{Prim}}}{dE_{\mathrm{a}}} = & \left(\frac{g_{\mathrm{a}\gamma}}{\mathrm{GeV}^{-1}}\right)^2 \left(\frac{E_{\mathrm{a}}}{\mathrm{keV}}\right)^{2.481} e^{-E_{\mathrm{a}}/(1.205\,\mathrm{keV})} \\ & \times 6 \times 10^{30} \quad \mathrm{cm}^{-2}\mathrm{s}^{-1}\mathrm{keV}^{-1}, \end{aligned} \tag{2.10}$$

where E_a is the axion energy and $g_{a\gamma}$ is the axion-photon coupling.

Lastly, axions can be emitted from the ^{57}Fe nuclear deexcitation. Special attention is devoted to ^{57}Fe instead of other isotopes due to two reasons: (1) ^{57}Fe is relatively abundant in the core of the Sun, which is $(9.0 \pm 1.2) \times 10^{19}\,\mathrm{cm}^{-3}$ [45] or 2.8×10^{-5} abundance by mass fraction [46]. (2) The lowest excited state of ^{57}Fe is 14.4 keV (M1 transition) and thus is possible to be thermally excited given that

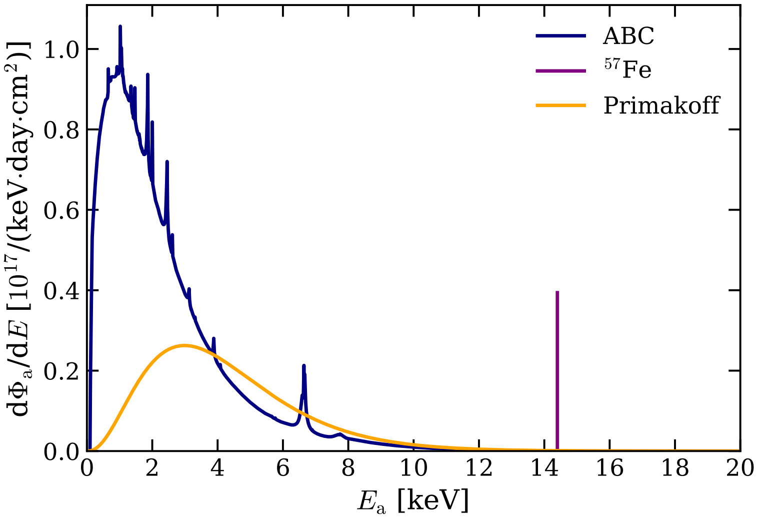

Figure 2.5: Fluxes of ABC (blue), ^{57}Fe (purple), and Primakoff (orange) solar axions with the couplings of $g_{ae} = 3.5 \times 10^{-12}$, $g_{an}^{\text{eff}} = 1 \times 10^{-6}$, and $g_{a\gamma} = 2 \times 10^{-10}\,\text{GeV}^{-1}$, respectively. Each flux scales with the square of the corresponding coupling. The ABC axion flux is obtained from Ref. [18].

the average temperature in the core of the Sun is $\sim 1.3\,\text{keV}$. The excited state of ^{57}Fe decays to the ground state by emitting γs; however, should axions are coupled to nucleons, the decay process can happen with emission of axions of 14.4 keV. In this case, the ^{57}Fe solar axion flux is given as [46, 47]

$$\Phi_a^{^{57}\text{Fe}} = \left(\frac{k_a}{k_\gamma}\right)^3 \times 4.56 \times 10^{23} (g_{an}^{\text{eff}})^2 \quad \text{cm}^{-2}\text{s}^{-1}, \tag{2.11}$$

where k_a and k_γ are the momenta of the produced axions and photons, respectively, g_{an}^{eff} is the effective axion-nucleon coupling and is defined as

$$g_{an}^{\text{eff}} = -1.19 g_{an}^0 + g_{an}^3, \tag{2.12}$$

where $g_{an}^{0/3}$ is the isoscalar/isovector coupling constant and -1.19 is a coefficient dependent on ^{57}Fe nuclear structure. With that said, the definition of g_{an}^{eff} is isotope-dependent and the definition of the effective axion-nucleon coupling g_{an}^{eff}

in Eq. (2.12) only works for axions emitted by ^{57}Fe. The three components of the solar axion flux are summarized in Fig. 2.5, with the assumed couplings as $g_{\mathrm{ae}} = 3.5 \times 10^{-12}$, $g_{\mathrm{an}}^{\mathrm{eff}} = 1 \times 10^{-6}$, and $g_{\mathrm{a}\gamma} = 2 \times 10^{-10}\,\mathrm{GeV}^{-1}$. We note that the all the derived solar axion fluxes are under the assumption that axion is massless so that the kinetic energy dominates the total axion energy; the calculation including a finite axion mass does not present much difficulties though [48].

2.3.2.2 Detection

Besides the dedicated axion experiments, which mainly employ the Priamokff effect for detection, liquid xenon detectors can also search for axions by the axio-electric effect, the axion analog of photoelectric effect. In the axio-electric effect, the total energy of axion is fully absorbed by the target medium. The energy threshold in liquid xenon experiments is usually $\mathcal{O}(\mathrm{keV})$, e.g. 1 keV detection threshold in XENON1T (Sec. 5.2.1), therefore the $\mathcal{O}(\mathrm{keV})$ solar axions are observable in liquid xenon detectors. Different from WIMP signals, axions would induce ER signals in the absorption process, with a cross section given by [47–50]:

$$\sigma_{\mathrm{ae}} = \sigma_{\mathrm{pe}} \frac{g_{\mathrm{ae}}^2}{\beta} \frac{3E_{\mathrm{a}}^2}{16\pi\alpha m_{\mathrm{e}}^2} \left(1 - \frac{\beta^{2/3}}{3}\right), \tag{2.13}$$

where σ_{pe} is the photoelectric cross section, g_{ae} is the axion-electron coupling, β and E_{a} are the velocity and energy of the axion, respectively, α is the fine structure constant, and m_{e} is the electron mass.

The photoelectric cross section σ_{pe} with xenon atoms, one of the key components to calculate the absorption cross section σ_{ae}, can be acquired from Ref. [51]. The obtained cross section σ_{pe} with a few discrete energies necessitates an interpolation, which is done in the logarithm of both energies and cross sections in the

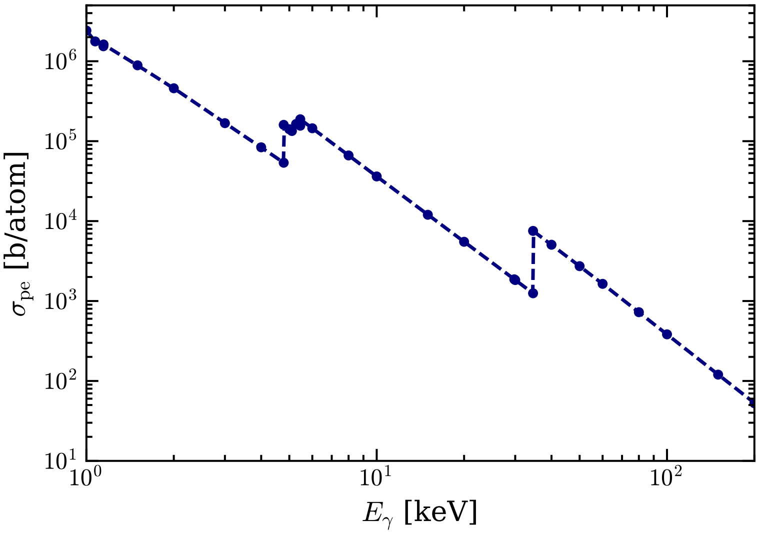

Figure 2.6: Photoelectric cross section $\sigma_{\rm pe}$ for xenon atoms. The data points are from Ref. [51] and the dashed line is the interpolation. See text for more details.

following way suggested by NIST [52]:

1. Linear interpolation in the log-log scale for each shell below K shell (34.5 keV for xenon atoms).
2. Cubic-spline interpolation in the log-log scale for energies above K shell.

Both data points and the interpolation are illustrated in Fig. 2.6, where the interpolated line follows the data points quite well. Reciprocally, a linear interpolation in the linear-linear scale would overestimate the cross section, as the true relationship between photon energies and $\sigma_{\rm pe}$ is more close to a convex function.

Since the massless assumption was used in the solar axion flux derivation, it was also applied in the detection for consistence. Eq. (2.13) is then simplified as

$$\sigma_{\rm ae} = \sigma_{\rm pe}\frac{g_{\rm ae}^2 E_{\rm a}^2}{8\pi\alpha m_{\rm e}^2}, \tag{2.14}$$

where the cross section $\sigma_{\rm ae}$ is mass-independent.[7] To determine a mass upper limit

---

[7] $E_{\rm a}$ does not equal $m_{\rm a}c^2$ as it is dominated by kinetic energy.

for the massless assumption, σ_{ae} from Eq. (2.13) for several fixed axion energies are depicted as the function of the axion mass m_{a} in Fig. 2.7, where we conservatively consider σ_{ae} is mass-independent for m_{a} below $100\,\mathrm{eV}/c^2$.

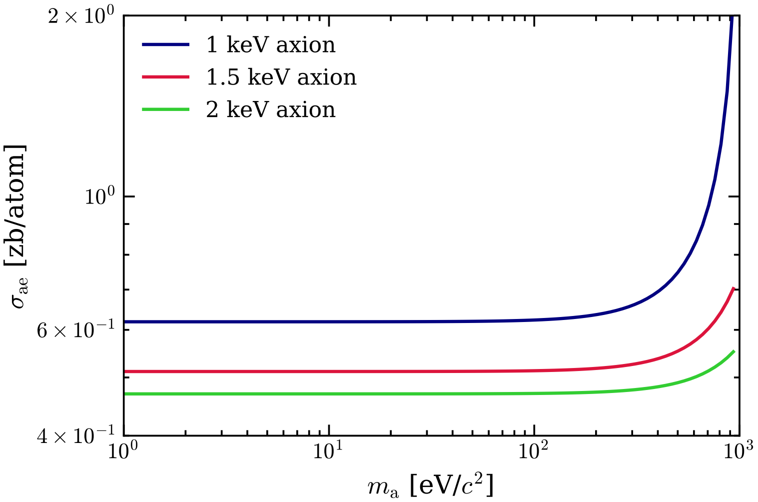

Figure 2.7: Axio-electric cross section σ_{ae} as a function of axion mass m_{a} for three axion energies, including 1 keV (blue), 1.5 keV (red), and 2 keV (green), which are typical energies for solar axions. In all cases, σ_{ae} is constant for m_{a} below $100\,\mathrm{eV}/c^2$. The assumed axion-electron coupling g_{ae} is 3.5×10^{-12}. $1\,\mathrm{zb} = 10^{-45}\,\mathrm{cm}^2$.

With the axio-electric cross section σ_{ae} given in Eq. (2.14) and solar axion flux shown in Fig. 2.5, we are able to compute the solar axion spectra for a perfect xenon detector, i.e., without energy smearing or effciency loss, as shown in Fig. 2.8. The sharp increases at ∼5 keV for both ABC and Primakoff axion spectra are due to the increased photoelectric cross section σ_{pe} from xenon L shell, resulting in "double-peak" features for both signals (more evident for the Primakoff axion). Since the flux of each component scales with the square of the corresponding coupling while σ_{ae} scales with g_{ae}^2, the ABC, Primakoff, and ^{57}Fe axion detection rates scale with g_{ae}^4, $g_{\mathrm{a}\gamma}^2 g_{\mathrm{ae}}^2$, and $(g_{\mathrm{an}}^{\mathrm{eff}})^2 g_{\mathrm{ae}}^2$, respectively, which holds for all solar axion experiments via the axio-electric detection channel. As previously discussed, the solar axion spectra in Fig. 2.8 hold for any axion mass below $100\,\mathrm{eV}/c^2$, therefore one does

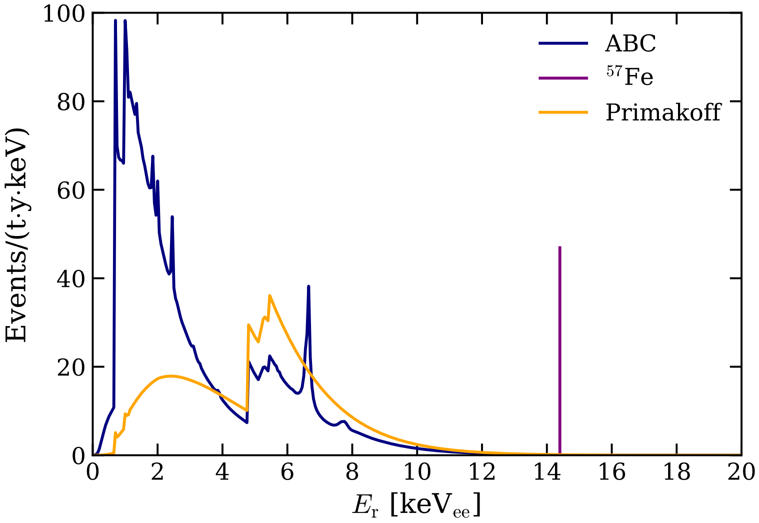

Figure 2.8: Solar axion spectra in a perfect xenon detector, i.e., without energy smearing and efficiency loss. The increase at $\sim 5\,\text{keV}$ is due to the L-shell electrons of xenon atoms. Since axio-electric cross section $\sigma_{\rm ae}$ scales with $g_{\rm ae}^2$, the ABC, Primakoff, and ^{57}Fe axion detection rates scale with $g_{\rm ae}^4$, $g_{\rm a\gamma}^2 g_{\rm ae}^2$, and $(g_{\rm an}^{\rm eff})^2 g_{\rm ae}^2$, respectively.

not need to take into account the look-else effect, which requires to include a trial factor due to multiple tests, if the considered axion mass is restricted to this region.

Recently, proposed in Refs. [40, 41], axions can also scatter with xenon atoms through the inverse-Primakoff process, which emits a photon and produce an electronic recoil. This new detection channel was not considered in the solar axion search in XENON1T but its potential impact is discussed in Sec. 5.6.7.

2.3.3 Galactic ALPs

ALPs, like QCD axions, are pseudoscalar bosons, but with decay constant and particle mass (Eq. (1.3)) decoupled from each other and instead taken as two independent parameters. This decoupling allows ALPs to take on higher masses than QCD axions; however, it also implies that ALPs do not solve the strong CP problem. ALPs are viable dark matter candidates [53], and could be absorbed in liquid xenon detectors via the axioelectric effect like their QCD counterparts. Therefore, the detection signature of ALP DM in the liquid xenon detectors is a mono-energetic peak centered around its rest mass, different from the continuous spectrum arising from solar axions.

Since the local DM velocity is non-relativistic, Eq. (2.13) can be approximated as

$$\sigma_{\mathrm{ae}} = \sigma_{\mathrm{pe}} \frac{g_{\mathrm{ae}}^2}{\beta} \frac{3m_{\mathrm{a}}^2}{16\pi\alpha m_{\mathrm{e}}^2}. \tag{2.15}$$

The detected rate of ALPs per atom is:

$$R = N_{\mathrm{A}} \frac{\rho_0}{m_{\mathrm{a}}} v, \tag{2.16}$$

where N_{A} is the Avogadro number, ρ_0, m_{a}, and v are the density, rest mass, and velocity of local ALP DM, respectively.[8] From Eq. (2.15, 2.16), the ALP detection rate is then:

$$\begin{aligned} \text{Rate} =& N_A \rho_0 c \frac{3}{16\pi\alpha m_e^2} \mathrm{kg} \cdot \mathrm{day} \cdot \mathrm{keV} \cdot \mathrm{b} \\ & \frac{(g_{\mathrm{ae}})^2}{A} \frac{m_{\mathrm{a}}}{\mathrm{keV}} \frac{\sigma_{\mathrm{pe}}}{\mathrm{b}} \mathrm{kg}^{-1} \mathrm{day}^{-1}, \end{aligned} \tag{2.17}$$

where A is the atom mass number. With known parameters plugged in, Eq. (2.17) can be simplified as

$$\text{Rate} \simeq \frac{1.5 \times 10^{19}}{A} g_{\mathrm{ae}}^2 \left(\frac{m_{\mathrm{a}}}{\mathrm{keV}/c^2} \right) \left(\frac{\sigma_{\mathrm{pe}}}{\mathrm{b}} \right) \mathrm{kg}^{-1} \mathrm{day}^{-1}. \tag{2.18}$$

The rate coefficient (1.5×10^{19}) from our calculation is consistent with Ref. [54]

---

[8] ALP DM velocity v does not enter the final rate as it cancels between cross section and flux.

for the DM density used in this work. One should resist concluding that the galactic ALP absorption rate in the detector increases with ALP mass m_{a} from Eq. (2.18), as the rate is also dependent on the photoelectric cross section σ_{pe}, which is evaluated at $m_{\mathrm{a}}c^2$ and thus leads to a generally decreasing detection rate for ALPs with higher masses. The ALP detection rate dependency on ALP mass will be discussed in Sec. 6.2.

Chapter 3

Analyzing the XENON1T Data

This chapter presents the XENON1T experiment with a focus on the data analysis and is organized as follows. Sec. 3.1 briefly introduces the XENON1T experiment. The corrections for signal and position reconstruction are given in Sec. 3.2. Various calibrations that were done in XENON1T to understand the detector response are detailed in Sec. 3.3. Sec. 3.4 discusses the background components in the context of the WIMP search with an emphasis of surface background that contributes substantially in the signal reference region.

3.1 The XENON1T Experiment

The XENON1T experiment was located at the Laboratori Nazionali del Gran Sasso (LNGS) with a depth of 3600 m water equivalent. The experiment utilized a two-phase xenon TPC and was primarily designed to search for DM, in particular the hypothetical WIMPs. The cylindrical TPC of 97 cm length and 96 cm diameter in XENON1T featured a LXe target of ~ 2 tonne and was confined by 24 polytetrafluoroethylene (PTFE) reflectors. In total there were ~ 3.2 tonne LXe inside the detector so as the other 1.2 tonne plays the pivot role of shielding backgrounds from detector materials, such as the radioactivities from cryostat vessels and flanges. 128 and 121 PMTs were deployed in the top and bottom array for signal detection, respectively. The XENON1T TPC is illustrated in Fig. 3.1.

The XENON1T experiment was operated from Nov. 2016 to Dec. 2018, which could be divided into three main science runs:

- **Science Run 0 (SR0)**: Nov. 22, 2016 – Jan. 18, 2017[1]
- **Science Run 1 (SR1)**: Feb. 2, 2017 – Feb. 8, 2018
- **Science Run 2 (SR2)**: Feb. 8, 2018 – Dec. 10, 2018

Both SR0 and SR1 data were used to search for DM and other rare processes while SR2 is more close to a R&D run where multiple tests were performed for the upgrade in XENONnT [55].

3.2 Energy and Position Corrections

After energy and position reconstruction mentioned in Sec. 2.1, both the signal sizes and reconstructed positions need further corrections, which are detailed in Sec. 3.2.1 and Sec. 3.2.2, respectively.

3.2.1 Energy Corrections

Both S1 and S2 signal sizes are dependent on the event positions and thus require correction.

$S1$ Correction Based on the detection method described in Sec. 2.1, the $S1$

---

[1] SR0 was interrupted by an Earthquake.

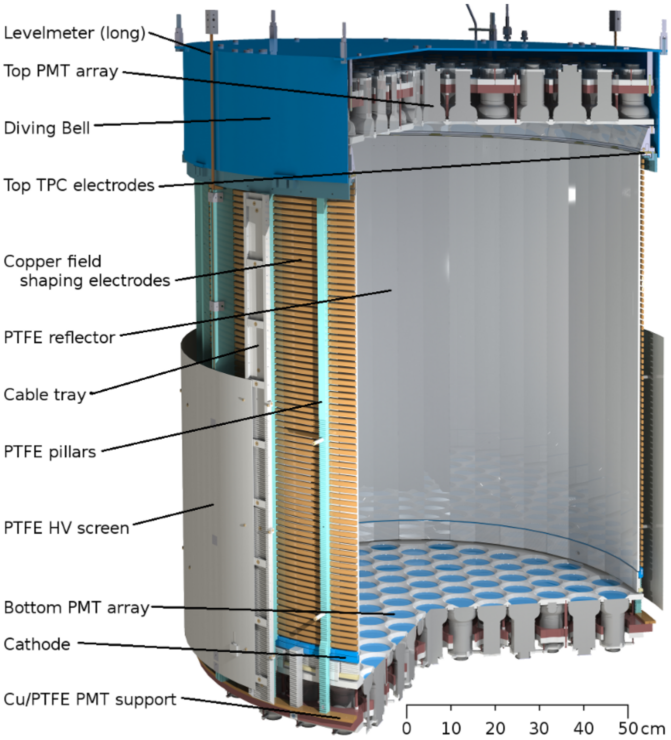

Figure 3.1: Illustration of the XENON1T TPC. It is built from materials selected for their low radioactivity, e.g., OFHC copper, stainless steel and PTFE. The top and bottom PMT arrays are instrumented with 127 and 121 Hamamatsu R11410-21 PMTs, respectively. Figure published in Ref. [56].

size can be expressed as:

$$S1 = n_{\text{ph}} \cdot \epsilon_{\text{LCE}}(x, y, z) \cdot (1 + p_{\text{DPE}}) \cdot \epsilon_{\text{QE}} \cdot \epsilon_{\text{CE}}, \tag{3.1}$$

where n_{ph} is the number of generated photons at the interaction site, ϵ_{LCE} is the number of photons that hit the PMT photocathode per generated photon at the interaction site and is referred to as S1 light collection efficiency (LCE), p_{DPE} is the probability of double photoelectron emission (DPE) effect [57, 58], where two photoelectrons are occasionally emitted when one photon hit the PMT photocathode, quantum efficiency ϵ_{QE} is the ratio between incident photons and emitted photoelectrons, and ϵ_{CE} is the collection efficiency of photoelectrons within the PMT.

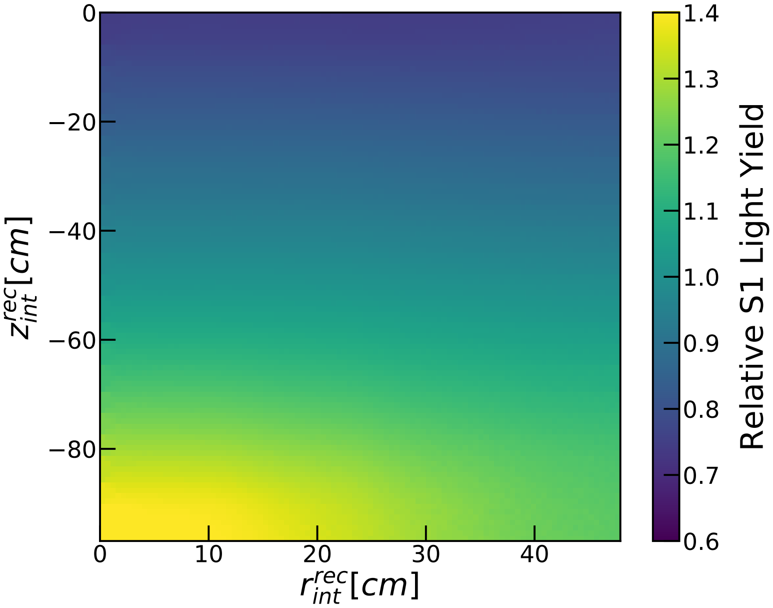

Figure 3.2: S1 LCE map with respect to the mean of LCE across the XENON1T TPC using $^{83\text{m}}$Kr data in SR1. The LCE is averaged out along the azimuthal angle.

From Eq. (3.1), it is apparent that the $S1$ spatial dependency is virtually introduced by ϵ_{LCE}.[2] The S1 LCE is mainly affected by two factors: the scintillation propagation length and the number of reflections. The scintillation light can be absorbed by impurities in LXe, mainly H_2O. As the refractive index of LXe for its intrinsic scintillation light at 180 nm is ∼1.57 [60], most photons would experience total reflection at the liquid-gas interface; therefore, a large fraction of S1 signal would be detected by the bottom PMT array. A large solid angle to the bottom PMT array means a shorter average distance for photons to reach the bottom PMTs and therefore a larger LCE. The reflectivity of PTFE is high but not 100%, thereby less number of reflections also leads to a larger S1 LCE.

To correct the spatial dependence, the 32.1 keV peak from $^{83\mathrm{m}}$Kr calibration data was used to map out the S1 LCE. $^{83\mathrm{m}}$Kr is an internal calibration source produced by ^{83}Rb in the xenon purification system and can mix homogeneously with LXe. $^{83\mathrm{m}}$Kr decays via a two-step scheme with the first decay of 32.1 keV that is easy to identify. The mapping result is illustrated in Fig. 3.2. The S1 LCE is maximum right above the center of cathode and is minimum at the corner of the top part of the TPC. $S1$ is then corrected to the mean of S1 LCE throughout the TPC, known as the corrected $S1$ (c$S1$). Therefore, Eq. (3.1) can be modified as:

$$cS1 = n_{\mathrm{ph}} \cdot \langle \epsilon_{\mathrm{LCE}} \rangle \cdot (1 + p_{\mathrm{DPE}}) \cdot \epsilon_{\mathrm{QE}} \cdot \epsilon_{\mathrm{CE}}, \tag{3.2}$$

where the spatial dependence is almost gone. The S1 LCE map obtained from $^{83\mathrm{m}}$Kr calibration source is applicable to all types of events except for those with large S1 signals that are saturated in the PMTs (e.g. α events, see Sec. 3.4.4.2).

***$S2$* Correction** Similarly, $S2$ can be written as:

---

[2] In fact, n_{ph} is also implicitly dependent on the positions as it is affected by the non-uniform electric field. This subdominant effect is beyond the scope of this thesis but was considered in the XENON1T analysis [59].

$$\begin{aligned} S2 = n_\mathrm{e} \cdot f(t) \cdot \epsilon_\mathrm{ext}(x,y) \cdot A_\mathrm{SE}(x,y) \cdot \epsilon_\mathrm{LCE}(x,y) \\ \cdot (1 + p_\mathrm{DPE}) \cdot \epsilon_\mathrm{QE} \cdot \epsilon_\mathrm{CE}, \end{aligned} \tag{3.3}$$

where n_e is the number of induced electrons at the interaction site, $f(t)$ accounts for the electron attachment along the drift in z direction with a drift time t, ϵ_ext is the extraction efficiency of electrons at the liquid-gas interface, single electron amplification A_SE is the number of generated photons in the electroluminescence process per extracted electron, ϵ_LCE is the number of photons reach the PMT photocathode per generated photons in the electroluminescence process and is denoted as S2 LCE, and the rest are the same as Eq. (3.1). A three-dimensional correction for $S2$ is clearly necessitated from Eq. (3.3).

The correction in z direction is relatively straightforward. When the induced electron cloud drifts upwards under the established drift field, a fraction of the electrons would be attached to electronegative impurities (mainly $\mathrm{O_2}$ dissolved in LXe) and thus is attenuated by the drift time. Therefore, $S2$ is related to its drift time t by:

$$S2(t) = S2_0 \exp(-t/\tau), \tag{3.4}$$

where τ is defined as the electron lifetime (EL), which can be extracted from any mono-energetic data using Eq. (3.4). The EL trend in SR0 and SR1 is shown in Fig. 3.3, where three mono-energetic peaks, $^{83\mathrm{m}}$Kr, ^{218}Po (α), and ^{222}Rn (α), were used to extract the EL. A discrepancy was found between the EL from $^{83\mathrm{m}}$Kr and that from two α emitters and is not understood yet [59]. Since the energy of $^{83\mathrm{m}}$Kr decays is closer to the ROI of DM search, the EL from $^{83\mathrm{m}}$Kr data was used for the correction in the following way. A dedicated EL temporal model [61] was fit to the measurements from α decays, which provides more continuous measurements, and was then scaled to $^{83\mathrm{m}}$Kr measurements.

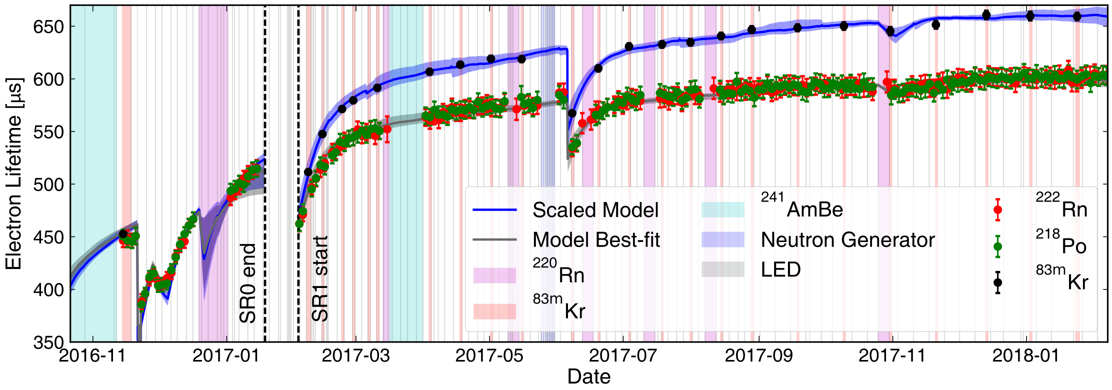

Figure 3.3: Electron lifetime evolution in SR0 and SR1. The vertical colored bands indicate different calibrations. The electron lifetime measured from decays of $^{83\mathrm{m}}$Kr, ^{218}Po, and ^{222}Rn are illustrated in black, green, and red dots, respectively. The gray line (band) is the best-fit ($\pm 1\sigma$) of an electron lifetime temporal model to the measurements from ^{218}Po and ^{222}Rn and the blue line (band) is the scaled the best-fit ($\pm 1\sigma$) based on $^{83\mathrm{m}}$Kr measurements. Figure published in Ref. [59].

After accounting for the electron attachment, $S2$ still have xy dependence resulting from ϵ_{ext}, A_{SE}, and S2 LCE. Under the electric attractive force between anode and gate, center region has a shorter distance between the two electrodes and thus a stronger extraction field than the edge, which is known as the electrode warping. As both ϵ_{ext} and A_{SE} increase with extraction field [62], the product of the two components, i.e. $S2$ amplification, is the largest at the center and decreases gradually to the edge. This electrode-warping effect has the same impact for S2 signals detected in the top and bottom PMT array; S2 LCE, on the contrary, has a distinct impact. Since the S2 signal generation site is between the liquid-gas interface and the anode, which is much closer to the top PMT array ($\sim$7.5 cm) than the bottom PMT array($\sim$1 m), the S2 LCE has a strong xy dependence in the

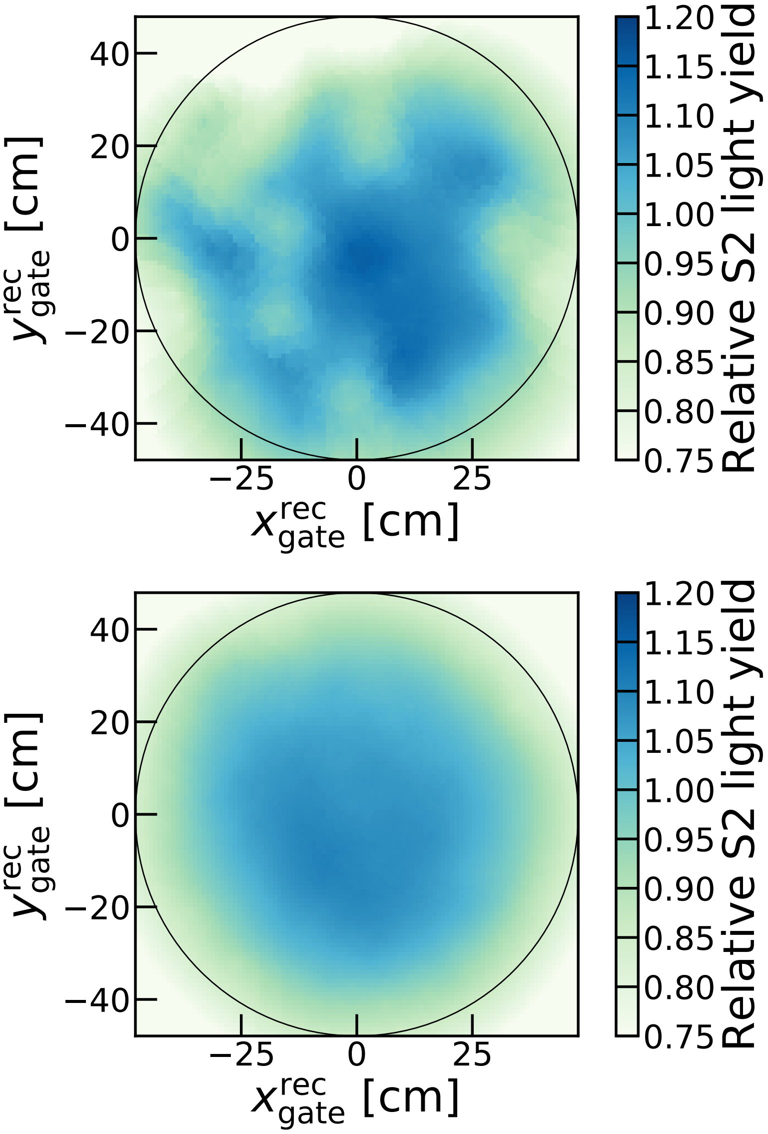

Figure 3.4: Correction maps for $S2$ signals in top (top) and bottom (bottom) PMT array from $^{83\mathrm{m}}$Kr calibration source. Both $S2$ light yiled are normalized to the average value in each map. See text for more details.

top PMT array but a negligible xy dependence in the bottom.[3] Consequently, the bottom PMT array is more resilient to non-functional PMTs due to the negligible xy variation of S2 LCE.The final $S2$ correction map is a multiplication of these two effects and is shown in Fig. 3.4. The $S2$ correction of the bottom PMT array decreases gradually from the center to the edge since it is mainly impacted by the electrode warping, whereas the correction map of the top PMT array has patchy structures due to the non-functional PMTs. As a result, $\mathrm{c}S2_{\mathrm{b}}$, the corrected $S2$ in the bottom PMT array, can be conveyed as

$$\begin{aligned}\mathrm{c}S2_{\mathrm{b}} = n_{\mathrm{e}} \cdot \langle \epsilon_{\mathrm{ext}} \rangle \cdot \langle A_{\mathrm{SE}} \rangle \cdot \langle \epsilon^{\mathrm{b}}_{\mathrm{LCE}} \rangle \\ \cdot (1 + p_{\mathrm{DPE}}) \cdot \epsilon_{\mathrm{QE}} \cdot \epsilon_{\mathrm{CE}},\end{aligned} \tag{3.5}$$

and was adopted in the DM search. It is important to note that the $S2$ correction is based on its observed position since that is where it is generated, while the $S1$ correction is based on its interaction position due to the same reason.

3.2.2 Field Distortion Correction

An uniform drift electric field is desirable in TPC for many benefits, including a good position reconstruction. However, the homogeneity of electric field is inevitably degraded by the edge effect, even with the presence of evenly-spaced copper rings (shaping rings) to shape the drift field. The distorted electric field necessitates a correction to the reconstructed position.

---

[3] To some extent, S2 LCE xy variations in the top and bottom PMT array are similar to the S1 LCE variation in the bottom and top parts in Fig. 3.2, respectively, due to the distance between the generation site and the detection PMT array.

3.2.2.1 Electric Field Distortion

Four *xy* positions that are related but slightly different should be distinguished:

- Interaction position, where the particle interacts with xenon atoms
- Gate position, where the ionized electrons are extracted at the liquid-gas interface
- Observed position, where the event is reconstructed based on observed pattern in the top PMT array
- Corrected position, which is further corrected from observed position to account for field distortion

Both interaction and gate positions are *true* positions; these two position are typically different as the drift trajectory is distorted from a vertical line by the electric field. The observed and corrected positions are the *reconstructed* positions corresponding to gate and interaction positions, respectively.

Typically, the gate position is pushed inwards due to the accumulated negative charge on the PTFE panels and the deviation increases with drift time. This effect is illustrated in Fig. 3.5. The interaction positions of surface events (see Sec. 3.4.4) are supposed to be in proximity with PTFE panel; the observed positions of background events, shown in Fig. 3.5, exhibit a larger inward tendency with an increasing depth.

The effect was already widely acknowledged by the community and was accounted for by applying field distortion correction (FDC) in two dimension, i.e. rz parameter space. Typically, this correction was based on 2D field simulations. We note that this method presumes an azimuthal-symmetry in xy gate positions.

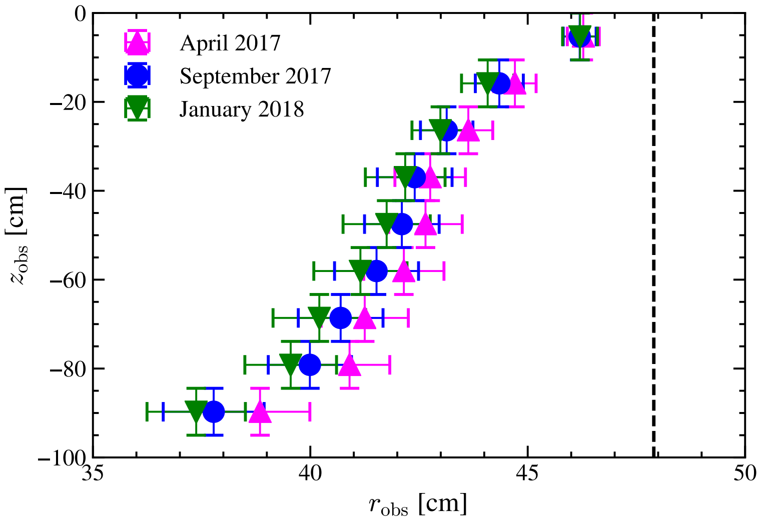

Figure 3.5: The observed positions of surface events (see Sec. 3.4.4), which happen in proximity with the TPC boundary (black line), are illustrated with different periods, including April 2017 (magenta), September 2017 (blue), and January 2018 (green). The horizontal uncertainties are the $1-\sigma$ resolution from the Gaussian fitting and vertical uncertainties reflect the chunk width in z direction. Figure adapted from Ref. [59].

$^{83\mathrm{m}}$Kr was also used for the field distortion correction. The relatively long half-life (~ 1.83 hour [63]) allows $^{83\mathrm{m}}$Kr source to be mixed homogeneously in the horizontal direction and thus we expect the interaction positions of $^{83\mathrm{m}}$Kr events to be uniform in xy plane. In Fig. 3.6, the observed positions of $^{83\mathrm{m}}$Kr are close to the 24 fixed panels that are connected to electrodes for the shaping rings but move inwards from the 24 sliding PTFE reflectors that are without electrode connections. The inward tendency for events near each sliding PTFE reflector is also different. This azimuthal-dependent field distortion motivates a position correction in three dimensions, i.e, (r, z, ϕ), where ϕ is the azimuthal angle in the horizontal plane.

Furthermore, a time-dependent field distortion was observed due to the charge accumulation on PTFE panels over time. In Fig. 3.5, the observed positions of surface events from January 2018 are further inwards than that from April 2017, necessitating a time-dependent FDC.

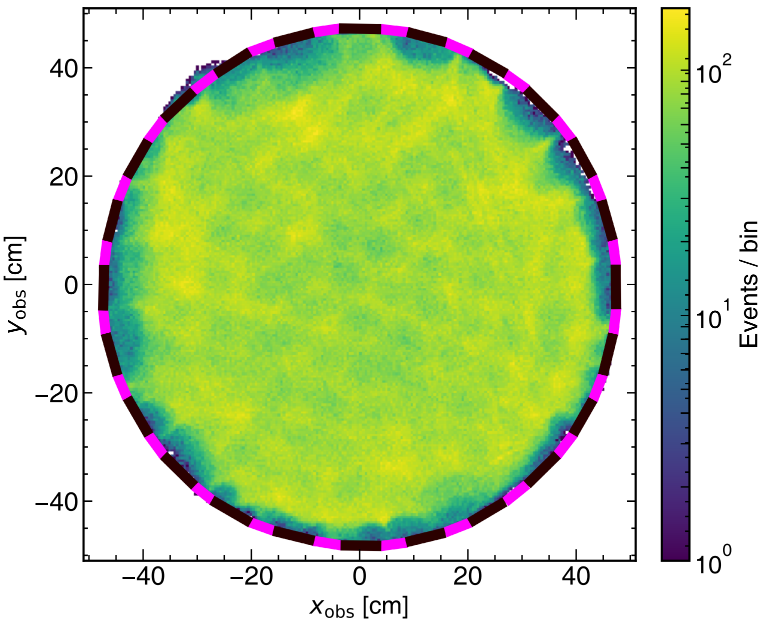

Figure 3.6: Reconstructed xy position distribution of $^{83\rm m}$Kr events from neural network algorithms without field distortion correction. The event distribution is away from the 24 sliding PTFE reflectors (black segments) that are not in contact with the electrodes and coincide with the fixed reflectors (magenta segements) that are connected to the electrodes. Figure published in Ref. [59].

3.2.2.2 Time-dependent 3D Field Distortion Correction

A natural idea is to use 3D field simulation to provide input for the fully-motivated 3D FDC. However, this was not used due to the expensive computing, and more importantly, the lack of a precise model for the charge accumulation on each panel and over time. Instead, we used a data-driven method based on $^{83\mathrm{m}}$Kr data that does not encounter either issue mentioned above.

The correction is based on two assumptions:

1. $^{83\mathrm{m}}$Kr 41.5 keV population is uniform in r^2 direction.[4]

2. Field distortion only shifts event positions in radial direction.

There is one additional requirement that the observed (or uncorrected) positions should be continuous in radial direction. Due to the second assumption, we can correct (r, z) positions instead of (x, y, z) since ϕ does not require correction.[5]

$^{83\mathrm{m}}$Kr data is divided into slices in both ϕ and z directions. Based on the uniformity assumption, $^{83\mathrm{m}}$Kr events within each small slice are shifted from observed positions to corrected positions such that these events are evenly spaced. For each corrected position, the corresponding observed position is found by quantile; the TPC boundary in observed position is defined as the 98% quantile in each slice due to smearing. For example, for the corrected position of 20 cm, the corresponding observed position would be $98\% \times (20^2/47.9^2) = 17.1\%$ in r^2, where 47.9 cm is the TPC radius. See the illustration in Fig. 3.7. After mapping out the correspondence between observed positions and corrected positions, the discrete mapping is then interpolated to be continuous. While the mapping provides r correction, the corrected z position is subsequently obtained using Pythagoras theorem under the

---

[4] This assumption is verified in Sec. 3.2.2.3.

[5] It is still a 3D correction as r and z corrections are based on 3 parameters, i.e. (r, z, ϕ).

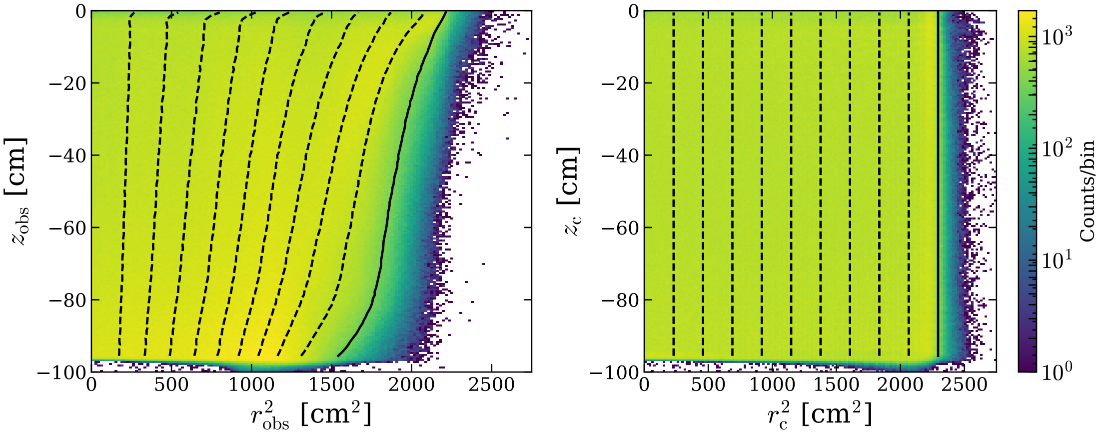

Figure 3.7: Illustration of radial position mapping from observed positions (left) to corrected positions (right) in $^{83\mathrm{m}}$Kr data based on the data-driven 3D FDC. The dashed and solid lines in the two plots correspond to each other. Left: Dashed lines represent 10%, 20%, ..., 90% quantiles in r^2_{obs} direction in each horizontal slice. The observed position of detector boundary is considered to be reconstructed at 98% quantile due to smearing and is denoted by the black solid line. Right: All the lines represent *true* positions. The black line is the TPC boundary at $r = 47.9\,\mathrm{cm}$, whereas the dashed lines show the nine deciles in r^2 within the TPC.

assumption that the electron drift trajectory is a straight line. Therefore, the r and z correction can be expressed as:

$$\begin{aligned} r_{\mathrm{c}} &= f(r_{\mathrm{obs}}, \phi_{\mathrm{obs}}, z_{\mathrm{obs}}) \\ z_{\mathrm{c}} &= -\sqrt{z^2_{\mathrm{obs}} - (r_{\mathrm{c}} - r_{\mathrm{obs}})^2}, \end{aligned} \tag{3.6}$$

where the observed positions are indicated by subscript “obs” and corrected positions are with subscript “c”.

To account for the time dependence, $^{83\mathrm{m}}$Kr calibration data was divided into 4 periods with equal calendar time, and the same correction procedure was repeated in each period. Due to less statistics in the last period, we have 30 and 120 slices in z and ϕ direction in this period, respectively, but 40 and 180 slices in the rest periods.

3.2.2.3 Correction Performance

The 3D FDC performance is tested by check corrected positions of uniform and non-uniform distributed events.

$^{131\mathrm{m}}$Xe, a metastable xenon isotope activated by fast neutrons, produces a mono-energetic peak at 163.9 keV via interval conversion (IC) with a half-life of 11.84 days [64]. $^{131\mathrm{m}}$Xe is considered to mix uniformly in LXe due to its long half-life, therefore the corrected positions of $^{131\mathrm{m}}$Xe should be homogeneously distributed if the 3D FDC works right. The uniformity of $^{131\mathrm{m}}$Xe corrected positions is measured by the Kolmogorov–Smirnov (KS) test [65, 66], which compares an observed distribution to an expected distribution by two metrics, KS test statistic and p-value. The KS test statistic means the largest difference of the cumulative density probability between the predicted distribution (uniform distribution in this case) and the observed distribution. The observed distribution is more similar to the predicted distribution when the KS test statistic is closer to 0. The p-value has the regular meaning that indicates how extreme the case is, and a tiny p-value suggests an unlikely scenario. The null hypothesis for the p-value is that the observed distribution follows the predicted distribution.

Table 3.1: Kolmogorov–Smirnov test (KS test) results of $^{131\mathrm{m}}$Xe event distribution under 2D and 3D FDC, respectively.

Method	KS test statistic	p-value
2D FDC	0.0231	0
3D FDC	0.0042	0.55

The KS test result for 3D FDC corrected positions is shown in Tab. 3.1, together with that from the traditional 2D correction. The KS test statistic for 3D FDC is less than 1/5 of that in 2D FDC, suggesting that 3D FDC outperforms 2D FDC. Furthermore, the good agreement between predicted and observed distribution in

3D FDC ($p = 0.55$) not only shows a good performance of 3D FDC for uniformly distributed events, but also verifies the assumption that $^{83\mathrm{m}}$Kr events are uniform in horizontal direction, otherwise the derived correction would make $^{131\mathrm{m}}$Xe events non-uniform. The good performance is further confirmed by another uniformly distributed source, ^{222}Rn, which yields a p-value of 0.07.

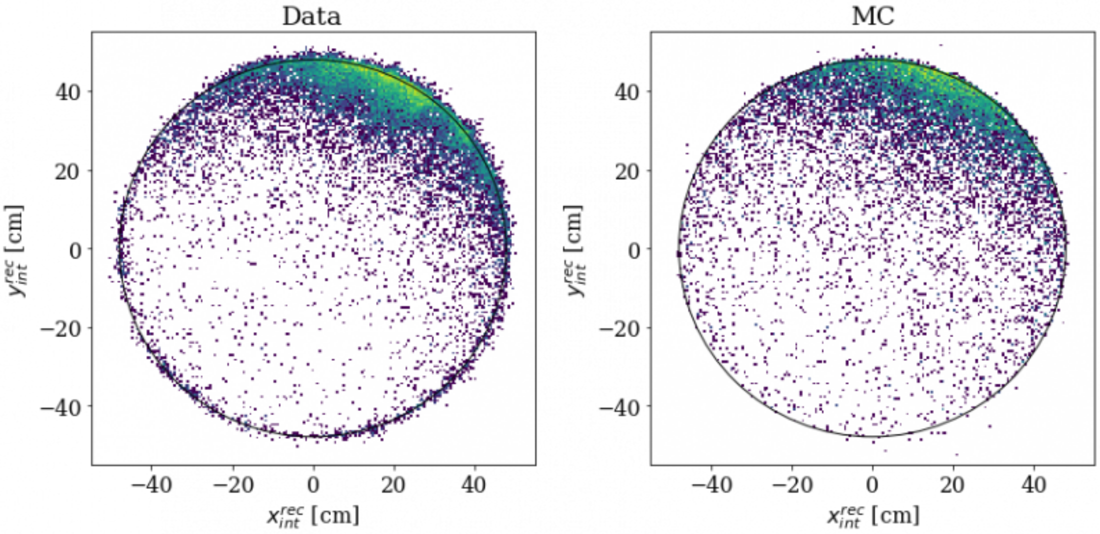

Figure 3.8: Neutron generator event positions from data after 3D FDC (left) and MC simulations (right).

Neutron generator (NG) events, on the other hand, have non-uniform distribution as they are from an external source. The predicted positions are provided by MC simulations and are used to compare with corrected positions in data after 3D FDC, as shown in Fig. 3.8, where an acceptable similarity is found. The gap in upper right region for 3D FDC in Fig. 3.8 (left) is due to the lack of ϕ correction. Since the FVs used in XENON1T are ϕ-independent, the small distortion in ϕ direction has negligible impact on the final results.

The surface events are used to check the time-dependence for 3D FDC. As illustrated in Fig. 3.9, the corrected positions of surface events from different periods are all close to the TPC boundary and do not exhibit a difference from each other;

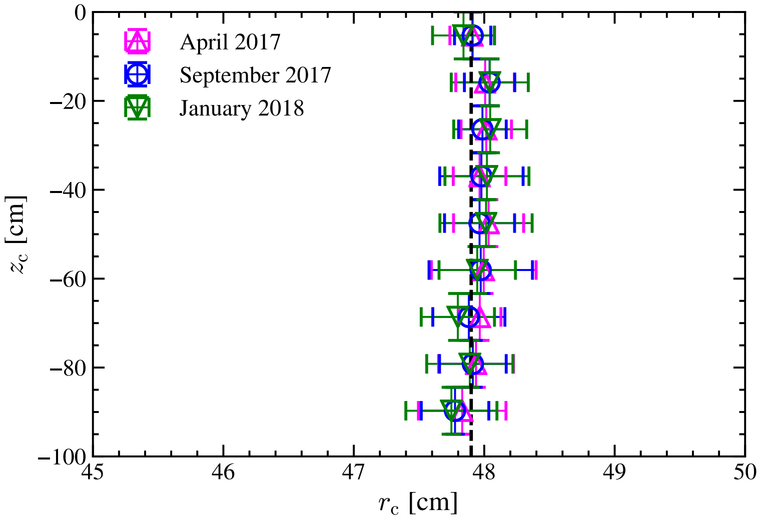

Figure 3.9: Corrected positions of surface events (see Sec. 3.4.4) after 3D FDC. Events from different periods are denoted with different colors and are all aligned with the TPC boundary (black dashed line) as expected. Figure adapted from Ref. [59].

therefore, we conclude that 3D FDC also gets rid of the time dependence that was observed in Fig. 3.5.

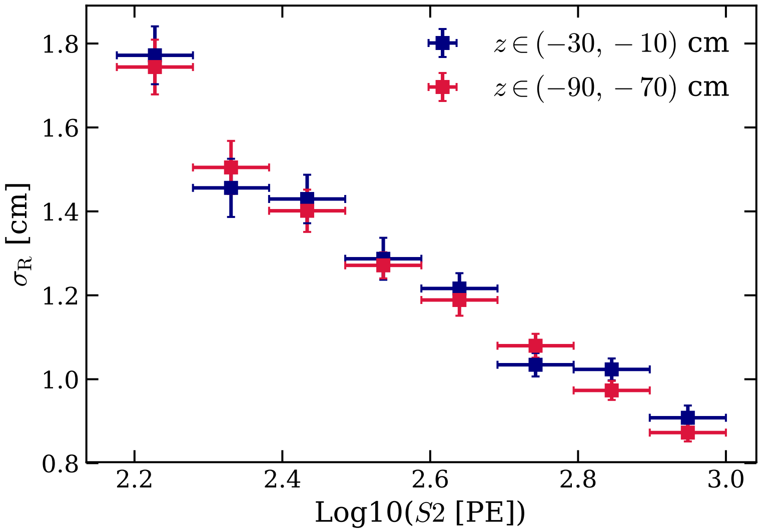

Figure 3.10: Position resolution of surface events from the top part (blue) of the detector are consistent with that of the same $S2$ size but from the bottom part (red) of the detector.

The improved position resolution can also be inferred by the surface events. Since the position reconstruction is based on the illuminated pattern of top patterns from S2 signals, it is natural to relate the position resolution to the $S2$ size. As shown in Fig. 3.10, surface events in the same $S2$ slice from the top and bottom part of the TPC have similar position resolution, indicating that the electron cloud diffusion in XENON1T has a negligible impact on the position reconstruction. Although position resolution is not dependent on the depth z, we note that depth may implicitly impact the position resolution as events from deeper z have smaller $S2$ due to the finite electron lifetime.

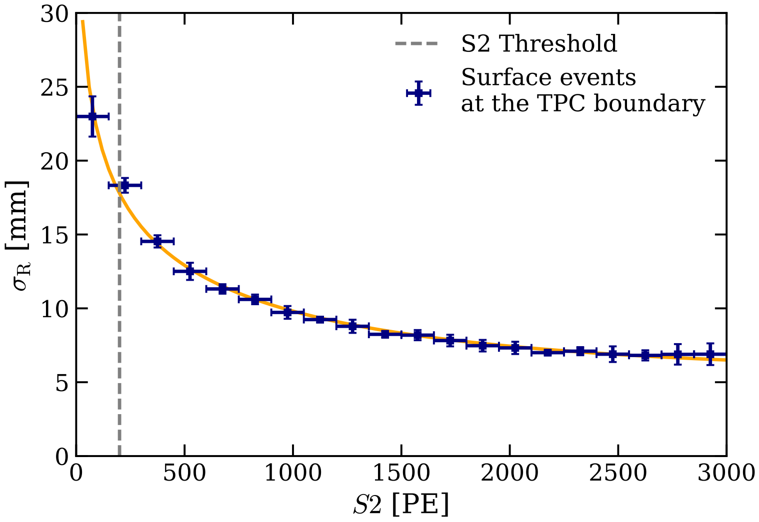

Figure 3.11: Radial position resolution σ_{R} at the TPC boundary as a function of $S2$ size, which is fit by the empirical formula Eq. (3.7) in the orange line. The $S2$ threshold (200 PE) used in the WIMP search is indicated by the gray dashed line. Figure adapted from Ref. [59].

Fig. 3.11 shows the position resolution in radial direction as a a function of $S2$ size, which follows an empirical formula:

$$\sigma_{\mathrm{R}} = a + b \log_{10}(S2/\mathrm{PE}) + c\sqrt{S2/\mathrm{PE}}, \tag{3.7}$$

with $a = (52 \pm 2)\,\mathrm{mm}$, $b = (-16.1 \pm 0.8)\,\mathrm{mm}$, $c = (0.19 \pm 0.03)\,\mathrm{mm}$. We emphasize that this is the position resolution of events happening near the TPC surface, which could be degraded compared to that in the center due to the fewer PMTs for receiving signals and the extra complexity of the reflection from the slanted PTFE in the electroluminescence region. It is remarkable to achieve position resolution below 1 cm with 3" PMTs (7.62 cm in diameter) for $S2$ larger than 1000 PE.

3.3 Detector Calibrations

Various sources were employed to calibrate different aspects of the XENON1T detector. ^{220}Rn calibration source was used to understand the detector response of ER events, while NG and ^{241}AmBe, both generating neutrons, were for NR events. Periodical LED calibrations were performed to measure and monitor the properties of PMTs, including the PMT gain that is critical for photoelectron (PE) conversion. Another calibration sources that were regularly taken is $^{83\mathrm{m}}$Kr, which can be utilized to characterize many important detector responses, such as S1 and S2 LCE correction (Sec. 3.2.1), position correction (Sec. 3.2.2), etc. This section will describe the ER calibration, NR calibration, and energy scale calibration in XENON1T.

3.3.1 Electronic Recoil Calibration

As mentioned in Sec. 2.1, the ER events and NR events can be discriminated by the different ratio of $S2/S1$, it is vital to calibrate their response in ($S1$, $S2$) parameter space.

^{220}Rn calibration source is used in XENON1T for several reasons. First, it is an internal source that can mix with the LXe. As XENON1T is a tonne-scale detector,

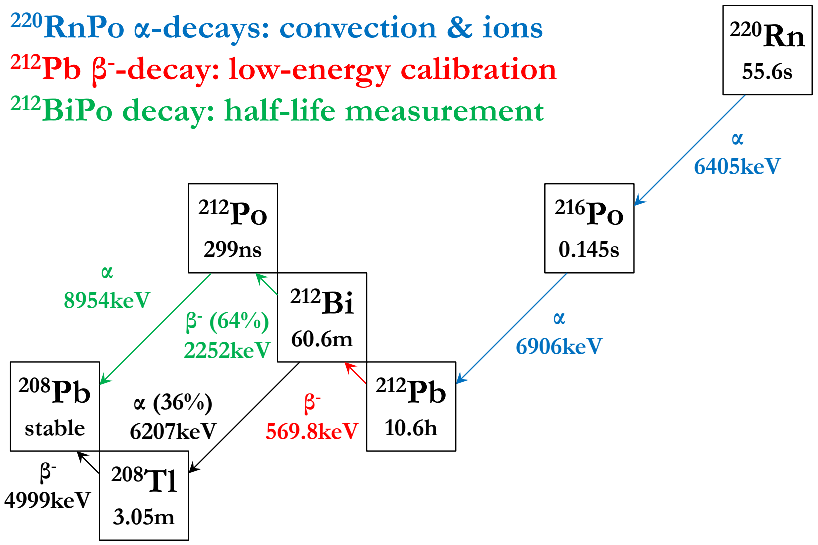

Figure 3.12: ^{220}Rn decay chain. β decays of ^{212}Pb are used for ER calibration in XENON1T. Figure published in Ref. [67].

internal calibration source is more desired than external calibration sources, such as ^{137}Cs which was used in the XENON100 detector [68]. Second, as shown in Fig. 3.12, the half-life of isotopes in the ^{220}Rn chain are relatively short and thus the injected radioactivity can naturally decay away within one week, which in this sense is better than the tritium source that requires a dedicated effort to remove [69, 70] otherwise would end up as an annoying background [24]. Third, it can produce ample single scatter events in low energy region ($< \sim 11\,\mathrm{keV_{ee}}$), which is the ROI for WIMP searches. Last but not least, ^{220}Rn decay chain is quite similar to ^{222}Rn decay chain. We can study ^{212}Pb to learn more about ^{214}Pb, a daughter of ^{222}Rn and one of the dominant backgrounds in XENON1T's WIMP search; in addition, the coincidence between ^{212}Bi and ^{212}Po, i.e. the so-called ^{212}BiPo tagging, can be studied and used in the similar ^{214}BiPo tagging to infer ^{214}Pb activities.

A total of six ^{220}Rn calibrations were done during SR0 and SR1 in XENON1T.

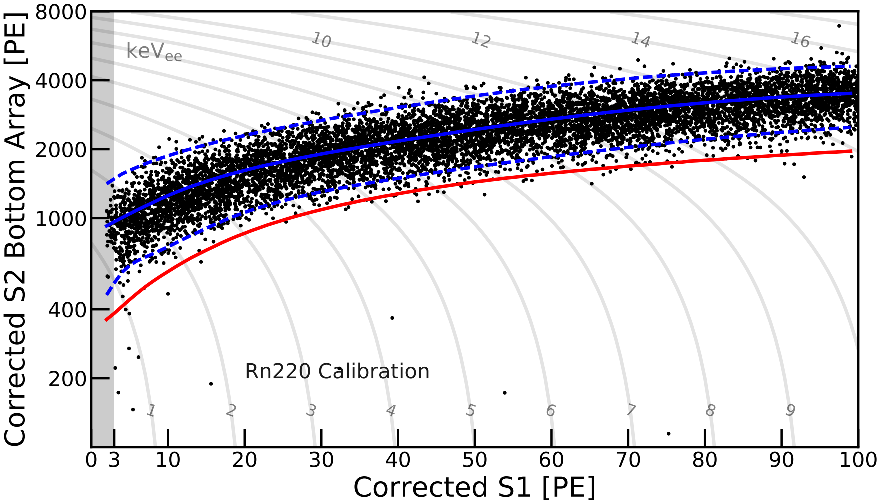

Figure 3.13: ^{220}Rn calibration data in SR1. Blue solid and dashed lines are the ER band median and $\pm 2\sigma$ quantiles, respectively. The red line is the NR band median from Fig. 3.14. Gray lines show isoenergy contours in ER energy.

A set of data quality cuts were then investigated based on this ER calibration data and most of the efficiency estimation are also from this data. It is important to note that these data quality selection are also applicable to NR events. The ER calibration data with good quality was then fed into a microphysics model [71] to simulate the event response in a similar way to NEST [72]; the distribution of ER events in ($S1$, $S2$) parameter space is referred to as ER band, as shown in Fig. 3.13. To avoid human bias, the data in signal reference region was blinded until everything is finalized; the blinding criterion is largely defined by the lower bound of ER band.

3.3.2 Nuclear Recoil Calibration

Two calibration sources were used for NR calibration in XENON1T: NG [73] and ^{241}AmBe [56]. Both produce neutrons for the NR calibration. ^{241}AmBe was used in the XENON100 and early period in XENON1T, and later was replaced by NG that demands shorter calibration time due to its high intensity, which can save more time for DM searches. Additionally, the intense neutron calibration can increase the purity of NR events over the persisting ER events from the background.

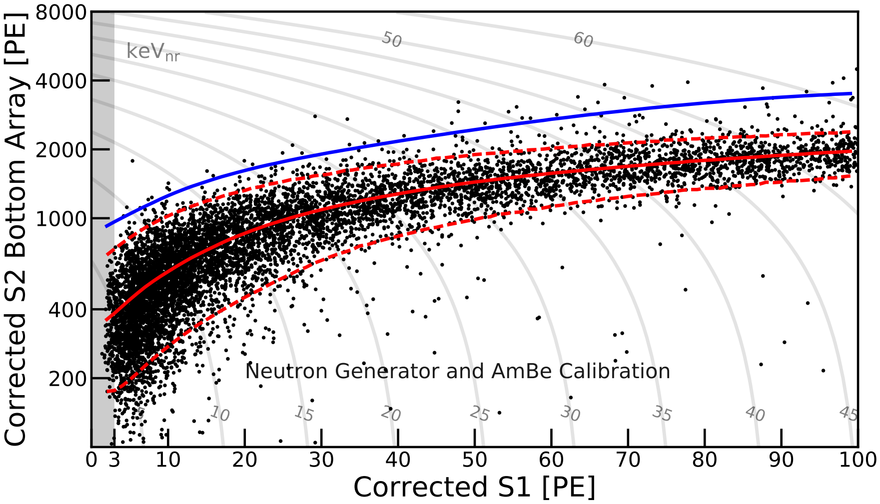

Figure 3.14: ^{241}AmBe and NG calibration data in SR1. Red solid and dashed lines are the NR band median and $\pm 2\sigma$ quantiles, respectively. The blue line is the ER band median from Fig. 3.13. Gray lines show isoenergy contours in NR energy.

Similarly to ER calibration, the NR calibration after quality selection was fit by the response model [71], which later is able to simulate the NR event distribution in ($S1$, $S2$) parameter space, i.e. the NR band, with sufficient statistics. The region between the NR band median and NR band -2σ from the model simulation is close to WIMP signal reference region with 50% acceptance of the signal, as illustrated in Fig. 3.14, but do notice that the reference regiones for WIMPs with different masses are slightly different. The *ER rejection power* is defined as the fraction of ER events that are above the signal reference region. ER rejection powers greater than 99.5% with 50% NR acceptance have been achieved in XENON1T and other xenon dual-phase detectors [23–25].

3.3.3 Energy Scale Calibration

ER events deposit almost all the energy into S1 and S2 signals; therefore, by combining the two signals, an improved energy resolution can be achieved as the recombination fluctuation will not enter [74]. The energy can be reconstructed as:

$$E = (n_{\mathrm{ph}} + n_{\mathrm{e}}) \cdot W = \left(\frac{\mathrm{c}S1}{g1} + \frac{\mathrm{c}S2_{\mathrm{b}}}{g2_{\mathrm{b}}} \right) \cdot W, \tag{3.8}$$

where n_{ph} and n_{e} are the number of generated photons and electrons, respectively. W is the effective energy to produce either a photon or electron; $W = 13.7 \pm 0.2\,\mathrm{eV}$ for LXe [75].[6] $g1 = \mathrm{c}S1/n_{\mathrm{ph}}$ is the average number of detected photoelectrons in all PMTs per generated photon at the interaction site, while $g2_{\mathrm{b}} = \mathrm{c}S2_{\mathrm{b}}/n_{\mathrm{e}}$ is the average number of detected photoelectrons in bottom PMTs per generated electron.[7] Combined with Eqs. (3.2, 3.5), $g1$ and $g2_{\mathrm{b}}$ can be rewritten as:

$$\begin{aligned} g1 &= \langle \epsilon_{\mathrm{LCE}} \rangle \cdot (1 + p_{\mathrm{DPE}}) \cdot \epsilon_{\mathrm{QE}} \cdot \epsilon_{\mathrm{CE}} \\ g2_{\mathrm{b}} &= \langle \epsilon_{\mathrm{ext}} \rangle \cdot \langle A_{\mathrm{SE}} \rangle \cdot \langle \epsilon^{\mathrm{b}}_{\mathrm{LCE}} \rangle \cdot (1 + p_{\mathrm{DPE}}) \cdot \epsilon_{\mathrm{QE}} \cdot \epsilon_{\mathrm{CE}}. \end{aligned} \tag{3.9}$$

From Eq. (3.9), one can found that $g1$ is dependent on the S1 LCE ϵ_{LCE} in the detector, while $g2_{\mathrm{b}}$ relies on S2 LCE $\epsilon^{\mathrm{b}}_{\mathrm{LCE}}$ and the extraction electric field, the latter of which will determine the amplification amplitude of an extracted electron A_{SE} as well as the extraction efficiency ϵ_{ext}. A more detailed discussion of $g2_{\mathrm{b}}$ can be found in Ref. [62]. Note that both $g1$ and $g2_{\mathrm{b}}$ are independent of the drift

---

[6] The recent measured W value in EXO experiment [76] is lower but does not impact the result here as (1) it is measured in much higher energy ($\mathcal{O}$(MeV)) and (2) it would only scale $g1$ and $g2$ while the energy resolution remains the same.

[7] The reason to use c$S2_{\mathrm{b}}$ over c$S2$ can be found in Sec. 3.2.1.

electric field and the energy of events, which can also be inferred from Eq. (3.9).

Eq. (3.8) can be rewritten as the following:

$$\frac{cS2_{\mathrm{b}}}{E} = -\frac{g2_{\mathrm{b}}}{g1}\frac{cS1}{E} + \frac{g2_{\mathrm{b}}}{W}, \tag{3.10}$$

where $cS1/E$ and $cS2_{\mathrm{b}}/E$ are the light yield and charge yield of one event, respectively. As mentioned above, $g1$ and $g2_{\mathrm{b}}$ would remain the same once the detector configuration — notably the extraction field — is fixed. From the anti-correlation of c$S1$ and c$S2_{\mathrm{b}}$ in Eq. (3.10), $g1$ and $g2_{\mathrm{b}}$ values can be inferred from a global fit with a variety of ($cS1/E$, $cS2_{\mathrm{b}}/E$). Assuming the interception with y-axis and the slope of the anti-correlation line is b and k, respectively, $g1$ and $g2_{\mathrm{b}}$ are subsequently given as

$$\begin{aligned} g1 &= bW \\ g2_{\mathrm{b}} &= -\frac{bW}{k}. \end{aligned} \tag{3.11}$$

The different ($cS1/E$, $cS2_{\mathrm{b}}/E$) pairs come from either different energies or different drift electric fields, the latter of which only change light and charge yields and do not impact $g1$ and $g2_{\mathrm{b}}$. Since the drift electric field is typically unchanged during a science run, a plenty of mono-energetic peaks are usually utilized to fulfill this purpose.

In SR1, 6 mono-energetic peaks were used to extract $g1$ and $g2_{\mathrm{b}}$, as illustrated in Fig. 3.15. The fitting result shows that in SR1:

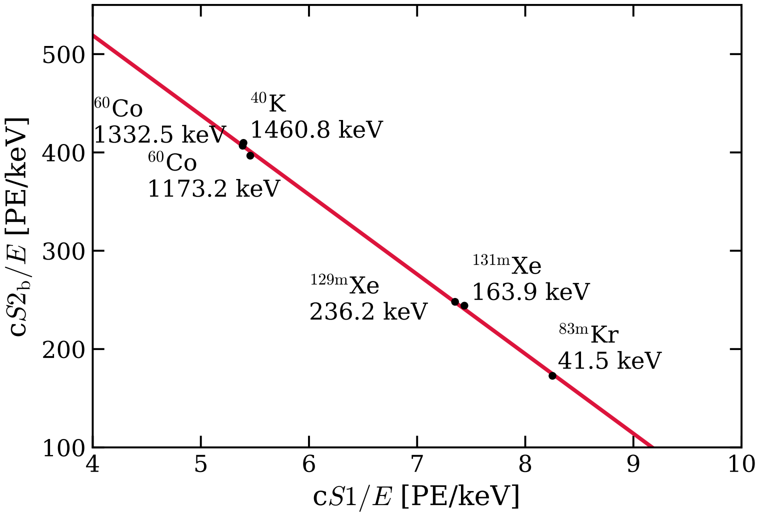

Figure 3.15: A global fit to extract $g1$ and $g2_\mathrm{b}$ in SR1. Black points represent light and charge yields from different mono-energetic peaks which the red line fits to. The statistical uncertainties of light and charge yields, which are from the fitting, are too small to be visible.

$$\begin{aligned} g1 &= (0.1426 \pm 0.0001)\,\mathrm{PE/ph} \\ g2_\mathrm{b} &= (11.55 \pm 0.01)\,\mathrm{PE/e.} \end{aligned} \tag{3.12}$$

After factoring out the double photoelectron effect $p_\mathrm{DPE} = 0.219$ from the best-fit in XENON1T [71], the "naked" $g1$, i.e. the average photon detection efficiency, is ∼11.7% in SR1, which is consistent with the designed value of XENON1T [77].

3.4 Backgrounds

We discuss four class of backgrounds in WIMP searches. The ER and NR backgrounds are presented in Sec. 3.4.1 and Sec. 3.4.2, respectively, while two non-standard backgrounds, accidental coincidence and surface backgrounds are described in Sec. 3.4.3 and Sec. 3.4.4, respectively.

3.4.1 Electronic Recoil Backgrounds

ER backgrounds in the ROI of DM search consists of β decays of ^{214}Pb and ^{85}Kr, Compton scattered electrons from materials, and solar neutrino elastic scattering off the electrons. More details can be found in Sec. 5.3. Despite the excellent ER rejection power in the signal reference region, ER backgrounds still contribute significantly in the DM search in XENON1T due to its large amount.

3.4.2 Nuclear Recoil Backgrounds

NR backgrounds are comprised of three components: (1) radiogenic neutrons, (2) muon-induced neutrons, and (3) coherent elastic neutrino nuclear scattering (CEνNS).

The dominant contribution is from the radiogenic neutrons, which are produced by the radioactivity of the materials via the (α, n) reaction. This background can be mitigated by selecting radio-free materials, e.g. using radio-free SiPMs instead of PMTs, the base of which is radioactive. The muon-induced neutrons, i.e. cosmogenic neutrons, which are induced by the interaction of cosmic muons with surrounding rock and concrete near the detector, are already greatly suppressed by the shielding of the mountain for the muons. This background is further reduced by the water tank outside the XENON1T detector, which can shield both neutrons and γs. Additionally, the water tank was able to tag the muons and the induced showers to *actively* shield the cosmogenic neutron background [78], which is known as the muon veto. Last but not least, neutrons are possible to scatter off the xenon nuclei multiple times and produce multi-site signals, whereas WIMP is only expected to deposit energy once due to its extremely feeble interaction. Therefore, neutron backgrounds and WIMP signals can be distinguished by the multiplicity of events. Nine candidates of multiple scattered neutron events were found in the 1.3T fiducial volume (FV) in SR0 and SR1, consistent with the expectation of (6.4 ± 3.2) events [71]. The position and energy distribution of these nine events are shown in Fig. 3.16.

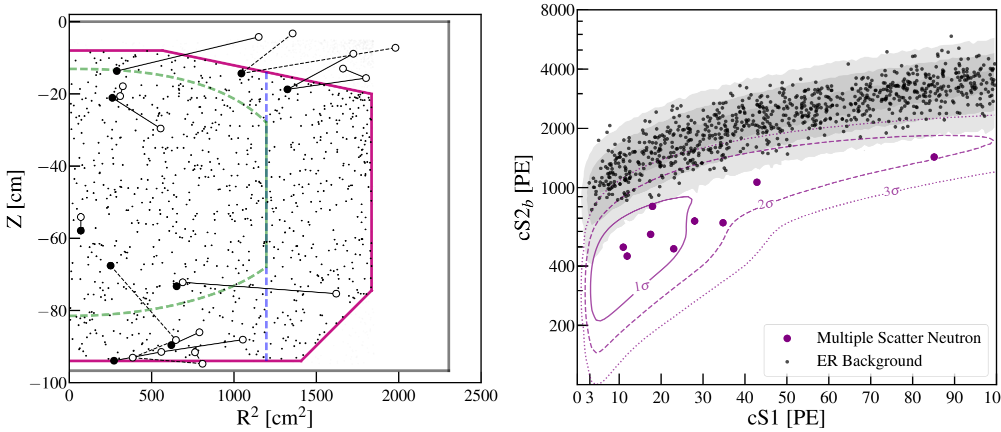

Figure 3.16: Multiple scattered events in XENON1T. Left: Spatial distribution of events after FDC. Solid and empty circles represent energy depositions from neutrons, and the solid circle has the largest $S2$ size. Depositions induced by the same neutron are connected by either dashed or solid line. The small black dots are the ER backgrounds. The 1.3T, 0.9T, and 0.6T FV are indicated by magenta, blue, and green lines, respectively [23]. Right: Energy distribution of events with energy corrections. The black and magenta dots are the ER backgrounds and neutron multiple scatter backgrounds, respectively. The 1σ, 2σ, and 3σ of expected distribution of multiple scatter neutron events are represented by the solid, dashed, and dotted magenta lines, respectively. Figure published in Ref. [71].

CEνNS is a process where a neutrino interacts coherently with a nucleus with low momentum transfer and induces a NR [79], which has been observed by the Coherent Collaboration with CsI [80] and recentlyliquid argon (LAr) [81] but is not observed in LXe yet. The CEνNS background is virtually indistinguishable from the WIMP signals in the ($S1$, $S2$) discrimination space, in particular for low-mass WIMPs. The CEνNS background in XENON1T is mainly from ^{8}B solar neutrinos [82] and is still subdominant compared to radiogenic neutrons. As DM direct detection detectors become larger and larger, they will inevitably hit the so-called "solar neutrino floor" [83], where the CEνNS contributes a substantial amount of irreducible backgrounds. However, even then the CEνNS background can still be distinguished by the phase difference, as the CEνNS background peaks in the winter due to the Sun-Earth distance change while the WIMP signal has exactly the opposite phase peaking in the summer (see Sec. 2.2.2).

3.4.3 Accidental Coincidences

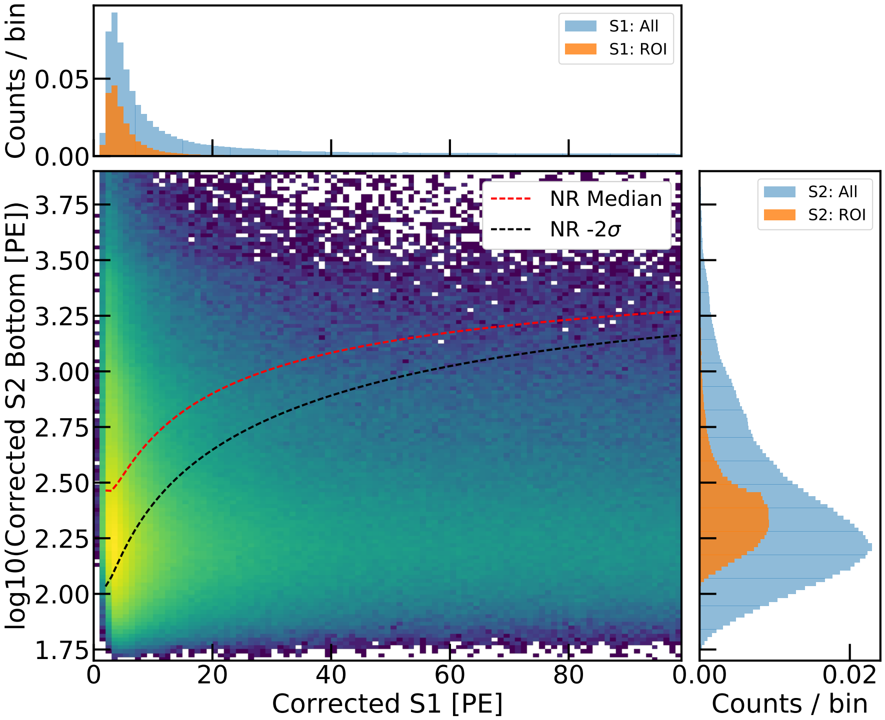

Figure 3.17: The energy distribution of AC background. The ROI of DM search is between NR band median and NR band -2σ that are denoted by the red and black dashed lines, respectively. The projections in S1 and S2 directions are also provided. Figure published in Ref. [71].

Accidental coincidence (AC) is a result of randomly pairing of lone S1 and lone S2 signals. Lone S1 mainly comes from the dark count in PMTs [84] as well as regions that are not sensitive to S2 signals, such as the region below the cathode where produced electrons cannot drift up, or the surface events with diminished

S2 signals (Sec. 3.4.4). Lone S2 signals, on the other hand, mostly originate from single electrons [62, 85], e.g. photoionization from electrodes and electronegative impurities with electron attachment, electrons that are trapped at the liquid-gas interface, etc. Sometimes single electrons are misidentified as lone S1 signals.

The AC background is modeled by randomly sampling and pairing lone S1 and lone S2 samples. Lone S1 samples are selected from the small S1s before the main S1, while lone S2 samples are obtained from low-energy events with only S2 signals (S2-only events) or S2 signals that are beyond the maximum drift time. The correction of $S1$ and $S2$ size, as well as the field distortion correction, were then applied to the combined sample. The event selection criteria were also imposed. The final spatial distribution is rather uniform as expected while the energy distribution is shown in Fig. 3.17. The AC background model was verified in ^{220}Rn data as well as a sideband in DM search data, together with surface background model (see Sec. 3.4.4.3).

3.4.4 Surface Background

Events that lost some of their S2 electrons at close proximity or on the TPC surface might “leak” into the NR band and get mis-reconstructed inwards to reside inside the FV, ending up in our signal region. Moreover, when an α emitter on the TPC surface produces an α towards external direction, the spontaneously recoiled nucleus might induce a NR signal in LXe. Those events are referred to as surface events. The observation and modeling of this background are discussed in this section.

3.4.4.1 Charge Ljoss on the TPC Surface

Events happening close to or on the TPC surface are likely to lose electrons to the surface. This so-called charge loss phenomenon were observed in several data. One of the most convincing observation is from $^{83\mathrm{m}}$Kr calibration data, see Fig. 3.18 (top). $^{83\mathrm{m}}$Kr events were selected based on its unique two-$S1$ signature — which is resulted from its two-decay scheme with the half-life of the second decay as 154 ns [63] — to ensure the purity. The events in the middle of detector have a constant $\mathrm{c}S2_{\mathrm{b}}/\mathrm{c}S1$ value, whereas events near the TPC edge have much smaller values. The events with significant charge loss, i.e. $\mathrm{Log10}(\mathrm{c}S2_{\mathrm{b}}/\mathrm{c}S1) < 1$, coincide with the spikes in the observed $^{83\mathrm{m}}$Kr positions, as illustrated in Fig. 3.18 (bottom). As mentioned in Sec. 3.2.2.1, the spike of $^{83\mathrm{m}}$Kr event distribution also coincide with the 24 fixed PTFE reflector; thus it is very possible that events happening near or on the fixed PTFE reflector lose charge to the surface, leading to a smaller $S2$ for the event itself and an increasing charge accumulation on the fixed PTFE reflectors.

The charge loss was also observed in ^{210}Po events in the background data, another notable surface events, which will be presented in Sec. 3.4.4.2. Similarly, the same phenomenon was found in the low-energy background data, which was used for the WIMP search. Depending on the extent of the lost charge, surface events can have a very different $\mathrm{c}S2_{\mathrm{b}}/\mathrm{c}S1$ and may reside in the NR band, where we search for WIMP signals. Furthermore, events with smaller $S2$ tend to have a worse position reconstruction (Eq. (3.7)) and thus is more likely to get reconstructed inside the FV. Therefore, surface events severely challenge WIMP search in the two-phase LXe detectors as they can leak into our signal region and cannot be easily rejected by fiducialization.

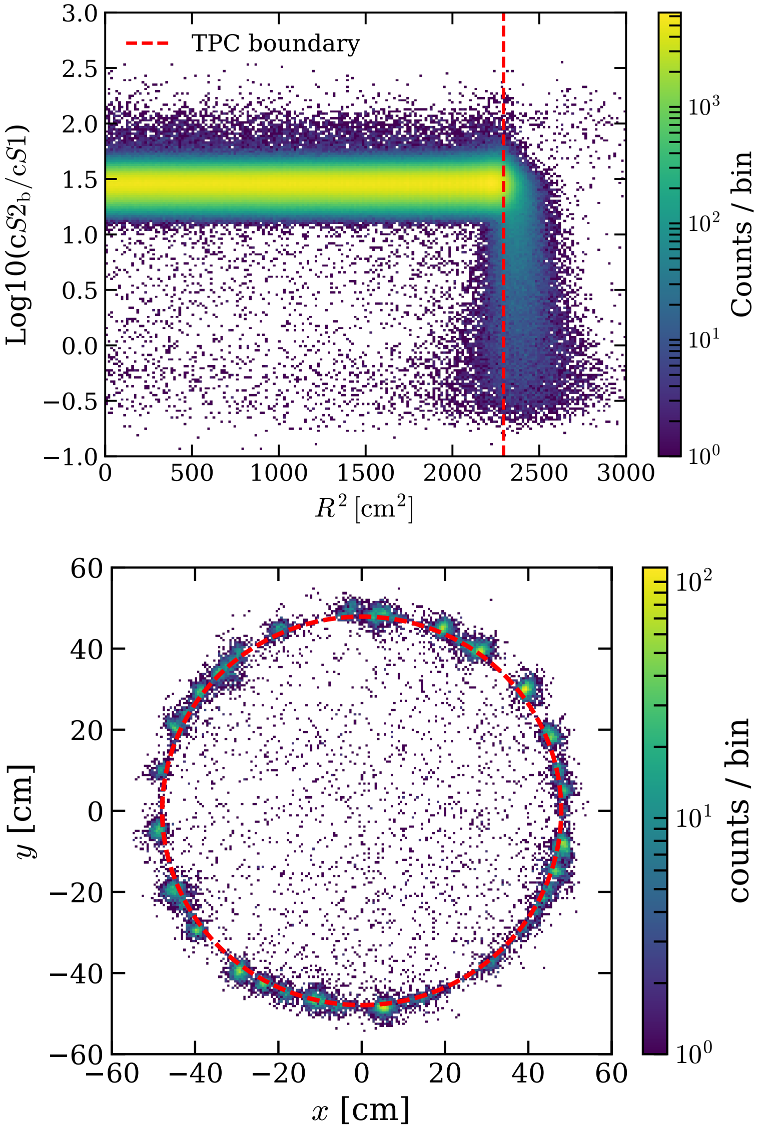

Figure 3.18: Charge loss in $^{83\mathrm{m}}$Kr calibration data, which are selected based on the unique two-S1 signature to ensure purity. Top: The c$S2_\mathrm{b}$/c$S1$ ratio is close to constant for the mono-energetic $^{83\mathrm{m}}$Kr events in the middle, but those near the TPC boundary (red dashed line) have significantly smaller ratios, indicating charge loss in $^{83\mathrm{m}}$Kr data. Bottom: The spatial distribution of charge-loss events (Log10(c$S2_\mathrm{b}$/c$S1$) $<$ 1) is discrete and in coincidence with the 24 fixed PTFE reflectors in Fig. 3.6.

3.4.4.2 Surface Background Rates

^{222}Rn chain plays an important role in WIMP search for LXe detectors. ^{222}Rn originates from the long-lived ^{226}Ra in the primordial ^{238}U chain, the trace of which are present in all materials. The main background in WIMP search is from the β decay of ^{214}Pb, daughter of ^{222}Rn. In addition, the main contributor of surface events also potentially come from this decay chain. The ^{222}Rn decay chain is illustrated in Fig. 3.19, where each isotope decays relatively fast until ^{210}Pb that has a half-life of $\sim$ 22 years. Therefore, events from this decay chain can fall into two categories: (1) events before ^{210}Pb decay. Due to their short lifetime, the isotopes are still mixed homogeneously in LXe, such as ^{214}Pb events. (2) Events after ^{210}Pb decay (including ^{210}Pb decay events). Due to its long half-life, most ^{210}Pb plate out on the PTFE surface, electrodes, etc, and so does its daughter.

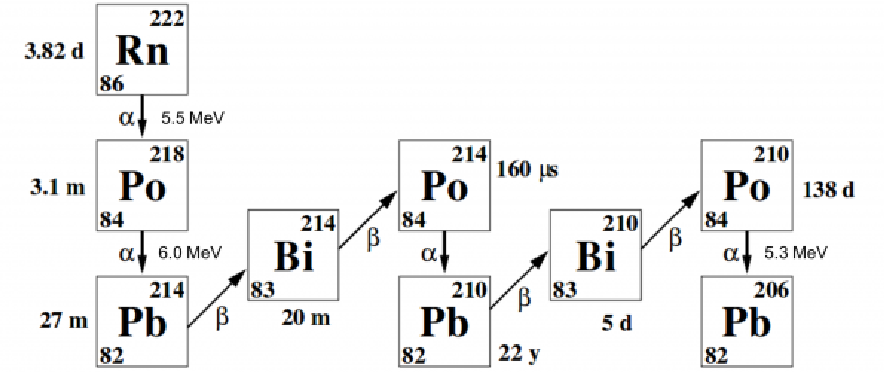

Figure 3.19: ^{222}Rn decay chain. The β decay of ^{214}Pb, a ^{222}Rn daughter, is the main background for XENON1T WIMP search.

A more detailed decay scheme starting from ^{210}Pb can be found in Fig. 3.20. The Q-value of ^{210}Pb decay is 63.5 keV. Since the half-life of ^{210}Pb is also longer than its daughters, we expect ^{210}Pb decay rate is the same as its daughters based on secular equilibrium, including the α emitter, ^{210}Po.

^{210}Po decays via emitting an α particle of 5.3 MeV with 100% branching ratio

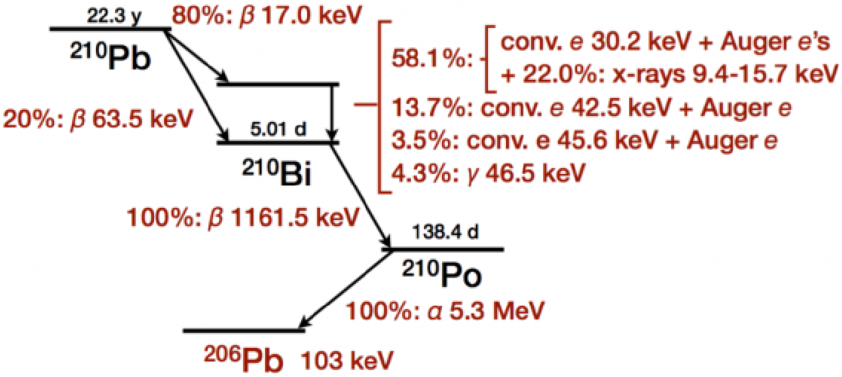

Figure 3.20: The decay scheme of ^{210}Pb and its daughters. Figure from Ref. [86].

(BR). It is easy to be identified as $\mathcal{O}$(MeV) α events have particularly large S1 signals, $\mathcal{O}(10^4)$ PE. S1 signals have $\mathcal{O}(100)$ ns duration and such a large signal would saturate PMTs, especially bottom PMTs that receive the majority of S1 signals. An $S1$ α correction map was made to account for the PMT saturation effect following the methods in Ref. [67]; the $S1$ size after this correction is denoted as c$S1_\alpha$.

Three α emitters — ^{222}Rn, ^{218}Po, and ^{210}Po — are illustrated in (c$S1_\alpha$, c$S2_\mathrm{b}$) in Fig. 3.21. Despite that all three emit mono-energetic α particles, ^{222}Rn and ^{218}Po have a well localized population in (c$S1_\alpha$, c$S2_\mathrm{b}$) parameter space as expected, whereas ^{210}Po events have spread distribution of c$S2_\mathrm{b}$ due to the charge loss. ^{210}Po events are selected by the orange rectangle, the upper limit of which is to avoid including ^{222}Rn events inside but inevitably misses some ^{210}Po events. More importantly, this selection method also requires a valid S2 signal, which also underestimates the number of ^{210}Po events as a large fraction lost the entire S2 signals. Consequently, the estimation of surface background rate from ^{210}Po should be considered as a lower limit. The selected ^{210}Po events are distributed close to the TPC surface as expected, see Fig. 3.22.

Assuming all the events within 63.5 keV and reconstructed outside TPC are

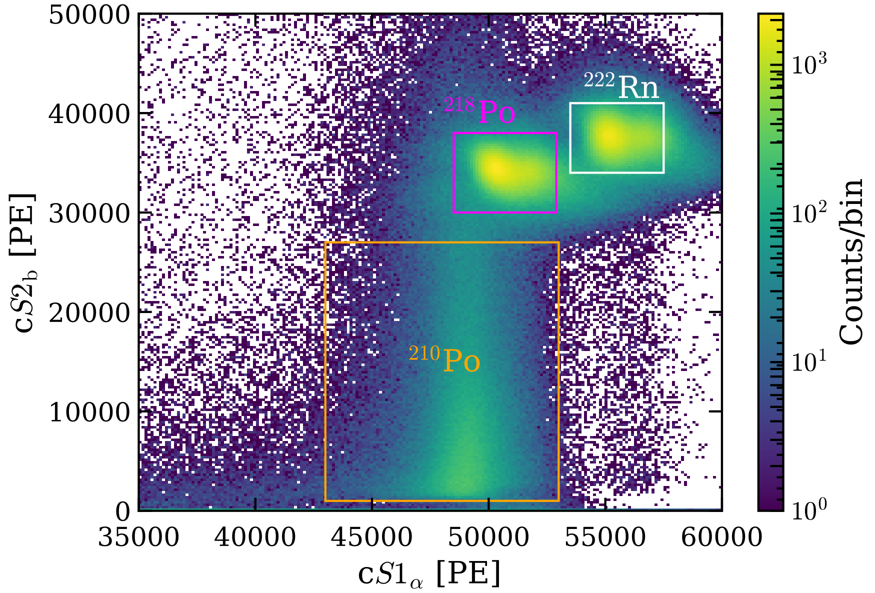

Figure 3.21: Three α emitters in ^{222}Rn decay chain with notation on each population. The large spread of $cS2_b$ for ^{210}Po events is due to charge loss. $cS1_\alpha$ is $S1$ signal after correction to account for its saturation in some PMTs.

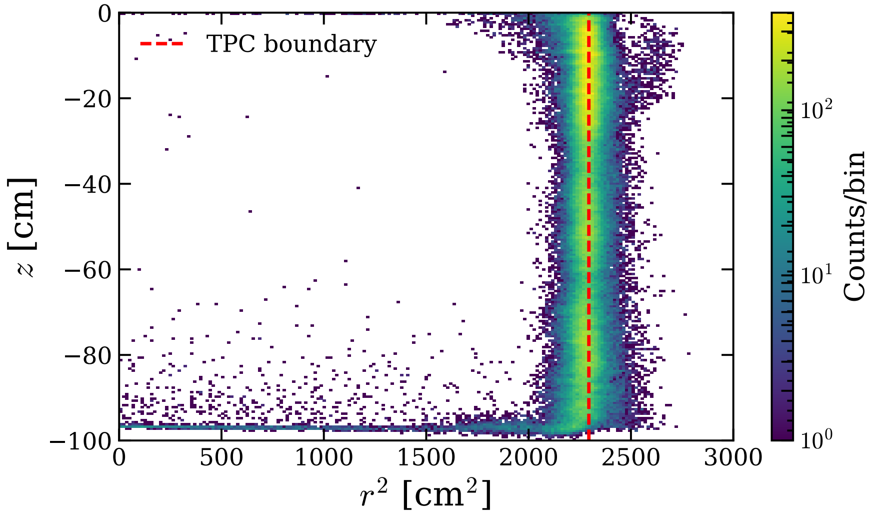

Figure 3.22: Spatial distribution of ^{210}Po events selected from the orange rectangle in Fig. 3.21. The reconstructed positions are after the 3D FDC.

from ^{210}Pb decay, we can have a rough estimation of ^{210}Pb events in SR1. A quantitative result can be found in Tab. 3.2. This is the average decay rates throughout SR1 for ^{210}Pb and ^{210}Po. We note that, the estimated ^{210}Pb rate could contain other event rate such as Compton scattering near PTFE, so we should only trust the order of magnitude. From Tab. 3.2, estimations from ^{210}Pb and ^{210}Po only differ by a factor of 2. Using the $15\,\mathrm{mBq/m^2}$ activity from ^{210}Pb, the total activity on the TPC surface is $\sim$11 mBq; this is comparable to the total ^{214}Pb activity, which is $\sim$ 32 mBq based on the nominal $10\,\mu\mathrm{Bq/kg}$ and 3200 kg LXe in total utilized in XENON1T. The ^{214}Pb rate is higher than ^{210}Pb rate, probably because the secular equilibrium has not established for ^{210}Pb. Tab. 3.2 also lists surface background rates from other noble liquid based DM experiments. LUX experiment, another LXe DM experiment, has similar surface background rate as XENON1T. DarkSide-50, a LAr DM detector, has lower surface background rate thanks to the radon-free cleanroom where the detector was assembled [87].

Table 3.2: Surface background rates in several noble liquid detectors inferred from either ^{210}Pb or ^{210}Po isotopes. One of the rate in the LUX experiment is for the cathode surface events, which is indicated in the table.

Detector	Isotope	Rate [mBq/m^2]
XENON1T	^{210}Pb	$\sim$ 15 (this work)
	^{210}Po	$>$ 7.8 (this work)
LUX	^{210}Pb	$>$ 13.5±0.8 [88]
	^{210}Po	$>$ 18.2 [89] $>$ 9.2 (cathode) [89]
DarkSide-50	^{210}Po	2.306±0.011 [90]

3.4.4.3 Surface Background Modeling

Since the surface background has a strong radial dependence, it is possible to distinguish the WIMP signal from the surface background from the radial distribution, even though they have an overlap in (c$S1$, c$S2_{\mathrm{b}}$) space. Therefore, the surface background modeling is required to model the radial distribution besides the traditional (c$S1$, c$S2_{\mathrm{b}}$) distribution; in addition, the z position is also required to optimize the FV.

The position resolution of surface events is provided in Eq. (3.7); however, the Gaussian distribution of surface events tends to underestimate events that get reconstructed far inwards, i.e. events on the tail, which are exactly the events that challenge the WIMP search. A better model is necessitated to predict non-gaussian distributed "tail" events.

Two different and complementary methods were used to obtain the $f(r|S2)$ relation for the surface background. The tail fitting method relies on an array of functions fitted to data, while the Adaptive Kernel Density Estimation (AKDE) model uses a Probability Density Function (PDF) of the data themselves to obtain the distribution of surface events inside the TPC.

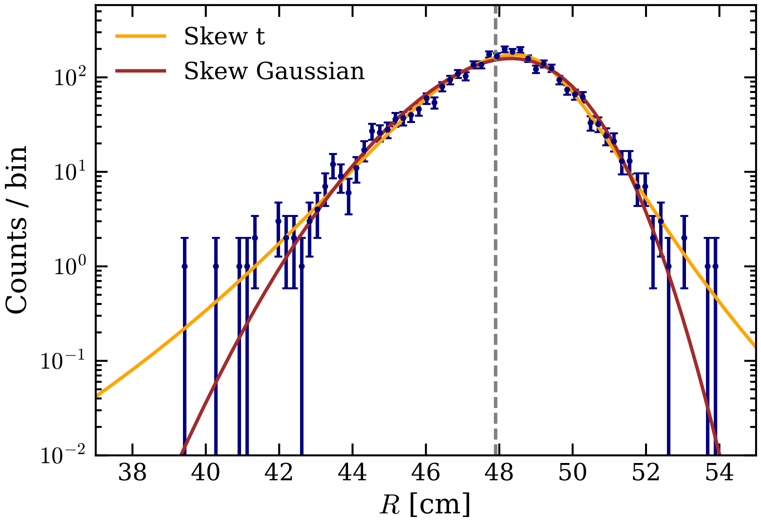

Figure 3.23: Radial distribution of surface events within a specific $S2$ range (257, 283) PE fitted by skew Gaussian (brown) and skew t (orange) functions, respectively.

In the tail fitting method, surface sample data are divided into multiple $S2$ slices, and in each $S2$ slice the radial distribution is fitted by two functions: skew Gaussian function and skew t function, see Fig. 3.23. These two functions were chosen for the following reasons: (1) the radial distribution of surface background data is not symmetric about the TPC edge, and (2) the two functions behave differently at the tail regions. The skew Gaussian drops faster and tends to be more conservative, while skew t function has a longer tail. This difference helped us to address and quantify the uncertainty from the unknown shape of radial distribution.

The 2D AKDE method relies on non-parametric multivariate ROOT based AKDE to generate an $S2$ dependent prediction for the radial distribution of the surface background. Contrary to fixed kernel KDE, in the AKDE approach the width of the kernel is adaptively recalculated from the local density of events, assigning narrow kernels to regions with high density to preserve details and wide kernels to regions with low density to promote smoothness. Details of this method can be found in Ref. [91].

The $S2$, $\mathrm{c}S2_\mathrm{b}$, $\mathrm{c}S1$, and z distribution for surface events reconstructed inside and outside the TPC are found to be similar in ^{220}Rn and background data, respectively. The comparison in background data is illustrated in Fig. 3.24 as an example. Both data are below the NR band -4.5 σ line, where the data was never blinded as it is below the signal region. Based on the similarities, surface events reconstructed outside TPC could be utilized to infer those inside the TPC; the data reconstructed outside TPC could be unblinded first as it is largely irrelevant to the WIMP search. The KDE method was employed on the surface events reconstructed outside the TPC to increase statistics.

The surface background distribution in ($\mathrm{c}S1$, $\mathrm{c}S2_\mathrm{b}$, r and z) can then be ex-

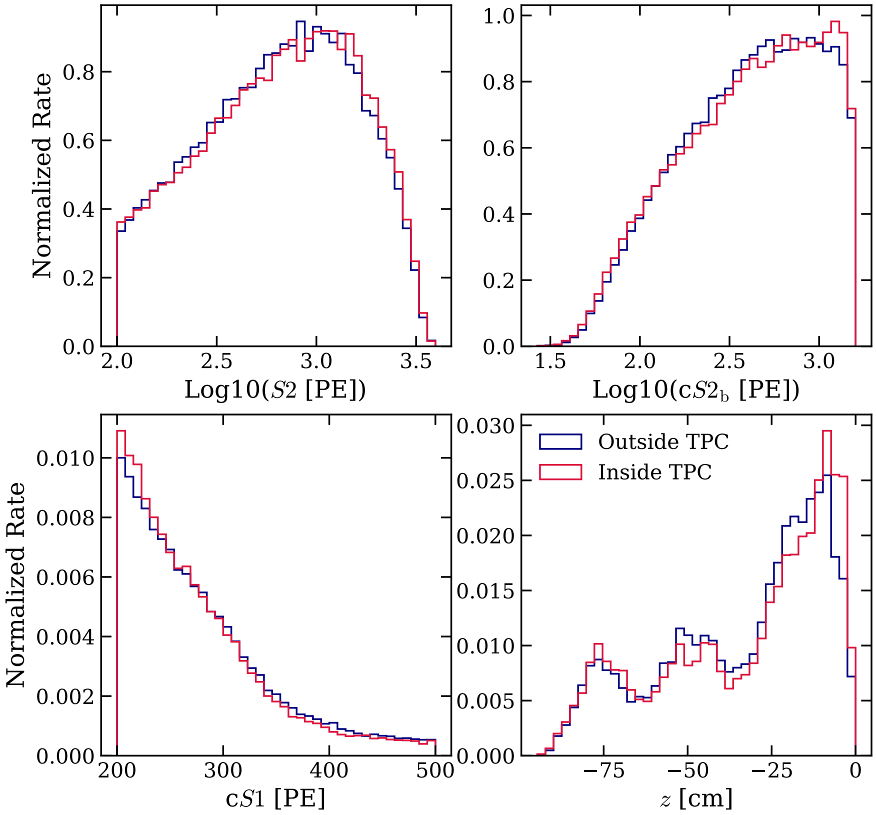

Figure 3.24: The distributions in $S2$, c$S2_\mathrm{b}$, c$S1$, and z for surface events *reconstructed* inside (red) and outside (blue) the TPC in background data share similar shapes. The rates are normalized so as to compare the spectral shape.

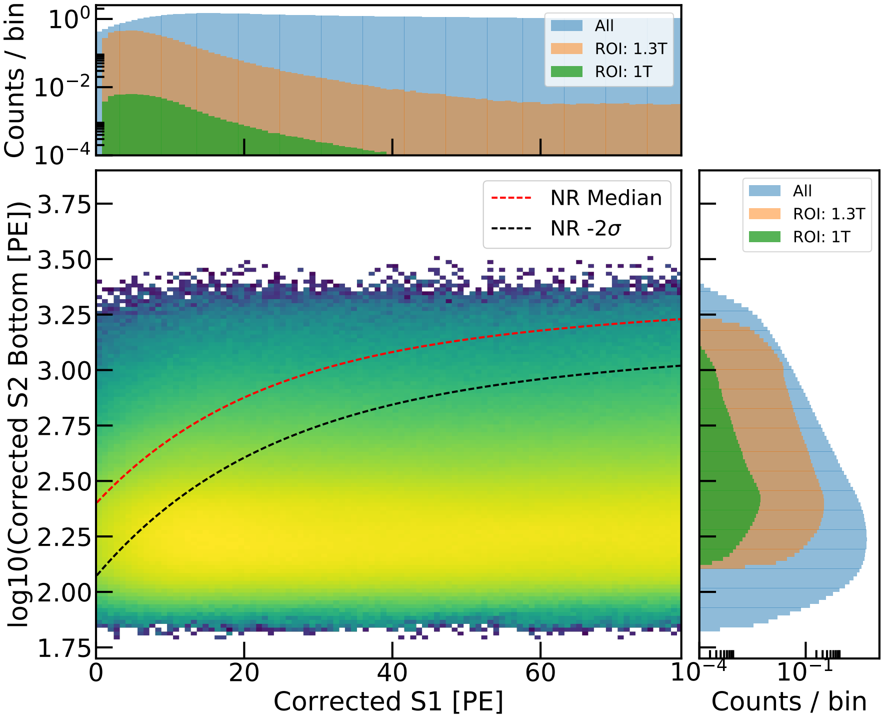

Figure 3.25: Surface background event distribution in (c$S1$, c$S2_\mathrm{b}$) parameter space with probability density indicated by the color in the logarithm scale. The projections to c$S1$ and c$S2_\mathrm{b}$ axes show surface events in the entire analysis region (blue), events in the reference region in 1.3T FV (brown) and 1T FV (green), respectively. Figure published in Ref. [71].

pressed as:

$$g(\mathrm{c}S1, \mathrm{c}S2_{\mathrm{b}}, r, z) = \int_{S2_{\min}}^{S2_{\max}} f(r|S2) \cdot \mathrm{KDE}(\mathrm{c}S1, S2, r, z) \mathrm{d}S2, \tag{3.13}$$

where both $f(R|S2)$ and $\mathrm{KDE}(\mathrm{c}S1, S2, r, z)$ are already obtained. $S2_{\min} = 100\,\mathrm{PE}$ and $S2_{\max} = 20000\,\mathrm{PE}$ so that it covers the entire ROI for WIMP search with a little extra to avoid the underestimation from the smearing at the edge (edge effect). The surface background model template can be obtained by randomly sampling from the distribution $g(\mathrm{c}S1, \mathrm{c}S2_{\mathrm{b}}, R, Z)$, and its projection in ($\mathrm{c}S1$, $\mathrm{c}S2_{\mathrm{b}}$) parameter space is shown in Fig. 3.25. The main population of surface events is below the NR band but are heavily overlapped with NR band at small $\mathrm{c}S1$, where light WIMP signals are expected to populate. However, the light WIMPs and surface backgrounds are still distinguishable due to the different radial distribution, which was added to the likelihood in the WIMP search in XENON1T [23] (see Sec. 4.1.1).

The surface background model was tested in sidebands before being applied in the final reference, together with AC background model. The sideband includes several regions in background data and ^{220}Rn data. The result showed a good agreement between the data and model, thus we used this surface background model in the final reference.

3.5 Acknowledgements

Chapter 3, in part, includes material from the following publications. (1) XENON Collaboration, “The XENON1T dark matter experiment”, Eur. Phys. J. C 77, 881 (2017). (2) XENON Collaboration, “XENON1T Dark Matter Data Analysis: Signal Reconstruction, Calibration and Event Selection”, Phys. Rev.

D 100, 052014 (2019). (3) XENON Collaboration, “XENON1T dark matter data analysis: Signal and background models and statistical inference”, Phys. Rev. D 99, 112009 (2019). The dissertation author is an author of those publications.

Chapter 4

XENON1T WIMP Results

The primary goal of XENON1T is to search for WIMP DM. Due to the unprecedented low background and the large exposure, XENON1T has set world-leading constraints on WIMP with a large range of masses and different types of interactions. This chapter is structured as follows. In Sec. 4.1, we present the search results for heavy WIMPs with different interactions, including the spin-independent, spin-dependent, and a coupling between WIMP and pion. The light WIMP results are described in Sec. 4.2, where the S2-only approach and the Migdal and Bremsstrahlung effects are taken into account.

4.1 Heavy WIMP Search Results

All heavy WIMP searches were performed with SR0 and SR1 data with a similar background model used in the searches are detailed in Sec. 3.4. However, the signal is different in each case due to different interactions from WIMP.

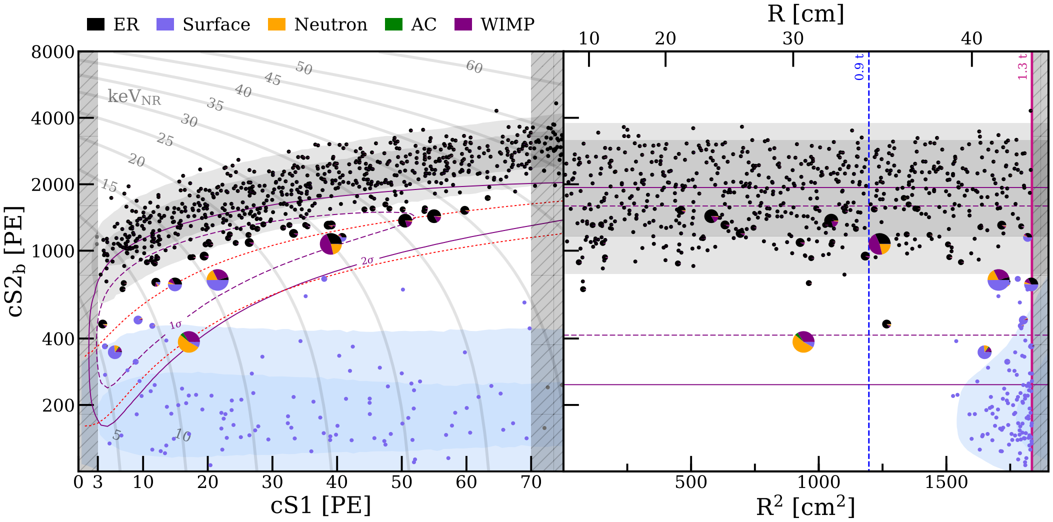

Figure 4.1: The best-fit of background plus a 200 GeV/c^2 WIMP to the data under the 3D (c$S1$, c$S2_\mathrm{b}$, R) likelihood. The observed events in ROI are denoted with pie charts, which are larger for those with relatively larger WIMP possibilities. The relative probability of being each component (background + signal) are indicated by the color code on the top of the left figure. The 1 (2)σ region for surface background and ER background are denoted with darker (lighter) blue and gray regions, respectively. Left: Distribution in (c$S1$, c$S2_\mathrm{b}$) parameter space. The 1 (2)σ contour of a 200 GeV/c^2 WIMP signal is shown by the dashed (solid) purple line. The NR signal reference region for the 200 GeV/c^2 WIMP is between the two red dotted lines. The ROI is between the two vertical gray shaded regions, i.e. (3, 70) PE for c$S1$. The isoenergy contours in NR energy are illustrated by the gray lines. Right: Distribution in (R^2, c$S2_\mathrm{b}$) parameter space. The maximum radii of the 0.9T and 1.3T FV are shown by the blue dashed line and the magenta solid line, respectively. Figure published in Ref. [23].

4.1.1 SI WIMP-nucleon Scattering

The SI WIMP-nucleon elastic scattering signal model is presented in Sec. 2.2.1. To utilize the strong radial dependence of surface background, the radius information was added to the likelihood to discriminate this background from WIMP signals. The 3D profile likelihood runs over all the events in ROI ($3 < cS1 < 70\,\mathrm{PE}$) in the 1.3T FV and is discussed in detail in Ref. [71]. The best-fit of backgrounds plus a $200\,\mathrm{GeV}/c^2$ WIMP signal to the data is illustrated in Fig. 4.1 and is also listed in Tab. 4.1.

Table 4.1: The best-fit to data under the hypothesis of a $200\,\mathrm{GeV}/c^2$ WIMP in 1.3T FV in the full ROI. The fit results for each background components and the $200\,\mathrm{GeV}/c^2$ WIMP are listed for the full ROI in 1.3T FV, but also are detailed for the $200\,\mathrm{GeV}/c^2$ WIMP reference region in 1.3T, 0.9T, and 0.6T FV, respectively. The number of observed events in each region is also shown in the last row. Table published in Ref. [23].

Mass (tonne) ($cS1$, $cS2_\mathrm{b}$)	1.3 Full	1.3 Reference	0.9 Reference	0.6 Reference
ER	627±18	1.62±0.30	1.12±0.21	0.60±0.13
neutron	1.43±0.66	0.77±0.35	0.41±0.19	0.14±0.07
CEνNS	0.05±0.01	0.03±0.01	0.02	0.01
AC	$0.47^{+0.27}_{-0.00}$	$0.10^{+0.06}_{-0.00}$	$0.06^{+0.03}_{-0.00}$	$0.04^{+0.02}_{-0.00}$
Surface	106±8	4.84±0.40	0.02	0.01
Total BG	735±20	7.36±0.61	1.62±0.28	0.80±0.14
$\mathrm{WIMP}_\text{best-fit}$	3.56	1.70	1.16	0.83
Data	739	14	2	2

Since no significant excess was observed, the 90% confidence level (C.L.) upper limit of the SI elastic scattering cross section σ_SI between WIMP and nucleon is reported. As shown in Fig. 4.2, the reported result set the most stringent upper limits for WIMP mass above $6\,\mathrm{GeV}/c^2$ and put an upper limit of $4.1 \times 10^{-47}\,\mathrm{cm}^2$

for a mass of 30 GeV/c^2.

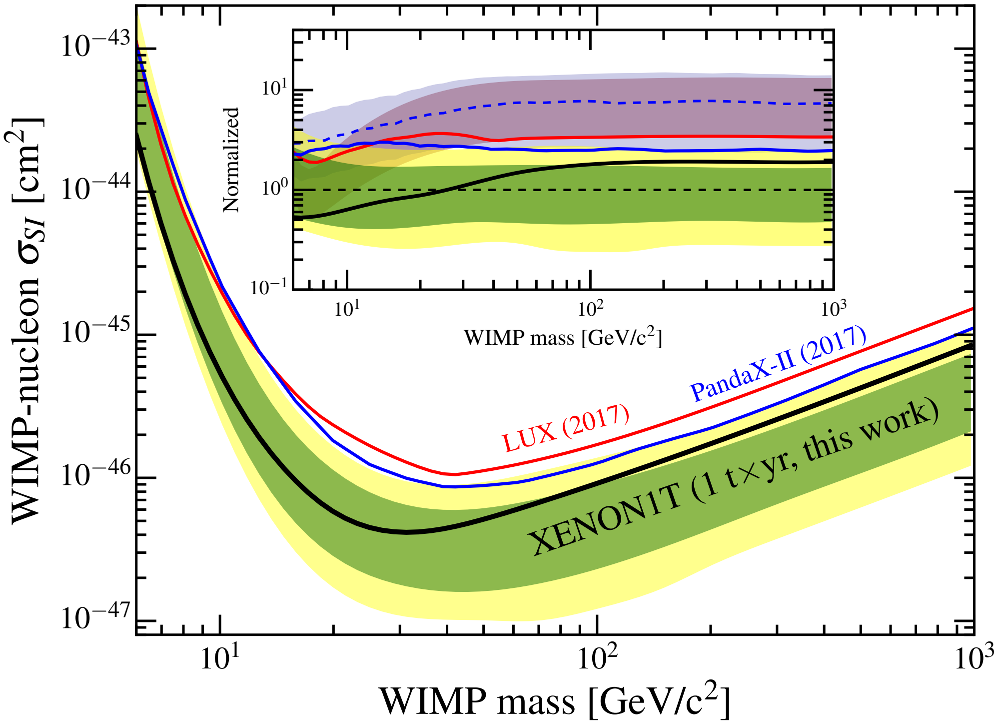

Figure 4.2: 90% confidence level upper limit on σ_{SI} from this work (thick black line) with the 1σ (green) and 2σ (yellow) sensitivity bands. Previous results from LUX [25] and PandaX-II [24] are shown for comparison. The inset shows these limits and corresponding $\pm 1\sigma$ bands normalized to the median of the sensitivity band in this work. The normalized median of the PandaX-II sensitivity band is shown as a dotted line. Figure published in Ref. [23].

4.1.2 SD WIMP-nucleon Scattering

As mentioned in Sec. 2.2.1, the WIMP-nucleon cross section consists of two parts: one is spin-independent σ_{SI} that was discussed in Sec. 2.2.1 and the other one is the SD part σ_{SD}. For the latter, the different rate of NR induced by WIMP can be written as:

$$\frac{dR}{dE_{\mathrm{r}}} = \frac{2\rho_0}{m_\chi} \int \frac{\sigma_{\chi N}^{\mathrm{SD}}}{3\mu_N^2 v^2} \frac{\pi}{2J+1} S_N(q) v f(\boldsymbol{v}) d^3\boldsymbol{v}, \tag{4.1}$$

where ρ_0 is the local WIMP density, m_χ is the WIMP mass, $f(\boldsymbol{v})$ is the WIMP velocity relative to the detector, μ_N is the reduced mass of the WIMP-nucleon system, $S_N(q)$ is the axial-vector structure factor for a proton or neutron ($N = \{n, p\}$) in xenon, and $\sigma^{\mathrm{SD}}_{\chi N}$ is the scattering cross section between a WIMP and a single proton or neutron, at zero momentum transfer [14, 92]. Since the differential rate of NR spectrum scales with $\sigma^{\mathrm{SD}}_{\chi N}$, this unknown parameter is used to set limits as a function of WIMP mass.

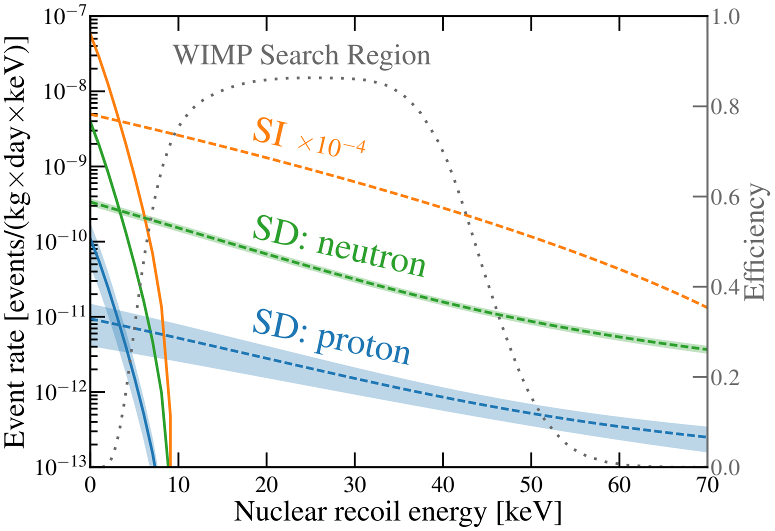

Figure 4.3: Comparison of the WIMP-nucleus recoil spectra in the SD neutron-only (green), SD proton-only (blue), and SI (orange, scaled by 10^{-4}) cases in LXe for a 10 GeV/c^2 (solid curve) and 100 GeV/c^2 (dashed curve) WIMP with a WIMP-nucleon cross section of 10^{-45} cm^2. The bands on the SD spectra come from uncertainties in the contribution to SD scattering from interactions involving the exchange of a pion between two nucleons (two-body currents). The WIMP search region in XENON1T is depicted by the total efficiency curve (gray dotted). Figure published in Ref. [93].

Two natural xenon isotopes, ^{129}Xe and ^{131}Xe, have nonzero spin of 1/2 and 3/2, respectively. The expectation values of total neutron and proton spin operators in the nucleus, $\langle S_{\mathrm{n}} \rangle$ and $\langle S_{\mathrm{p}} \rangle$, are quite different. For ^{129}Xe, $\langle S_{\mathrm{n}} \rangle = 0.329$ and $\langle S_{\mathrm{p}} \rangle = 0.010$, while for ^{131}Xe, $\langle S_{\mathrm{n}} \rangle = -0.272$ and $\langle S_{\mathrm{p}} \rangle = -0.009$ [94]. As $\langle S_{\mathrm{n}} \rangle \gg \langle S_{\mathrm{p}} \rangle$ for both xenon isotopes with nonzero spin, it follows that XENON1T is more sensitive to $\sigma_{\chi\mathrm{n}}^{\mathrm{SD}}$ than $\sigma_{\chi\mathrm{p}}^{\mathrm{SD}}$. The signal spectra for neutron-only ($\sigma_{\chi\mathrm{n}}^{\mathrm{SD}}$) and proton-only ($\sigma_{\chi\mathrm{p}}^{\mathrm{SD}}$) cases are shown in Fig. 4.3.

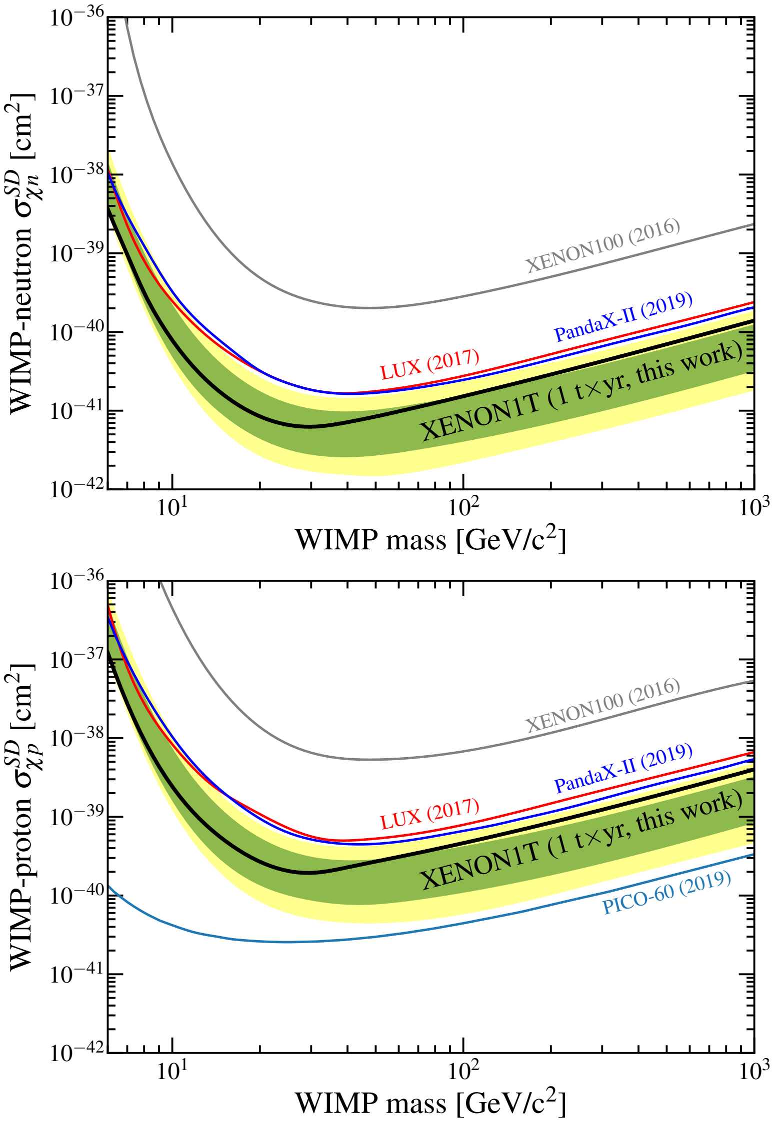

Figure 4.4: The neutron-only (top) and proton-only (bottom) cases for spin-dependent WIMP-nucleon cross section. The green (yellow) band is the 1 (2)σ sensitivity band for XENON1T and the black line is the corresponding limit. Limits from other experiments are also provided [95–98]. Figure published in Ref. [93].

Since no significant excess is observed using the same background and likelihood in Sec. 4.1.1, the 90% C.L. upper limits are reported in neutron-only and proton-only cases. In Fig. 4.4 (top), the reported WIMP-neutron cross section $\sigma_{\chi\mathrm{n}}^{\mathrm{SD}}$ in this work sets the most stringent constraints for WIMP masses between 6 and $1000\,\mathrm{GeV}/c^2$ in direct detection experiments with a minimum of $6.3 \times 10^{-42}\,\mathrm{cm}^2$ for a $30\,\mathrm{GeV}/c^2$ WIMP. In Fig. 4.4 (bottom), the WIMP-proton cross section $\sigma_{\chi\mathrm{P}}^{\mathrm{SD}}$ from this work also gives the best upper limit among direct detection experiments based on LXe; the best limit for proton-only case, however, has been consistently led by fluorine-based superheated liquid experiments such as PICO-60 [98, 99].

4.1.3 Scalar WIMP-Pion Coupling

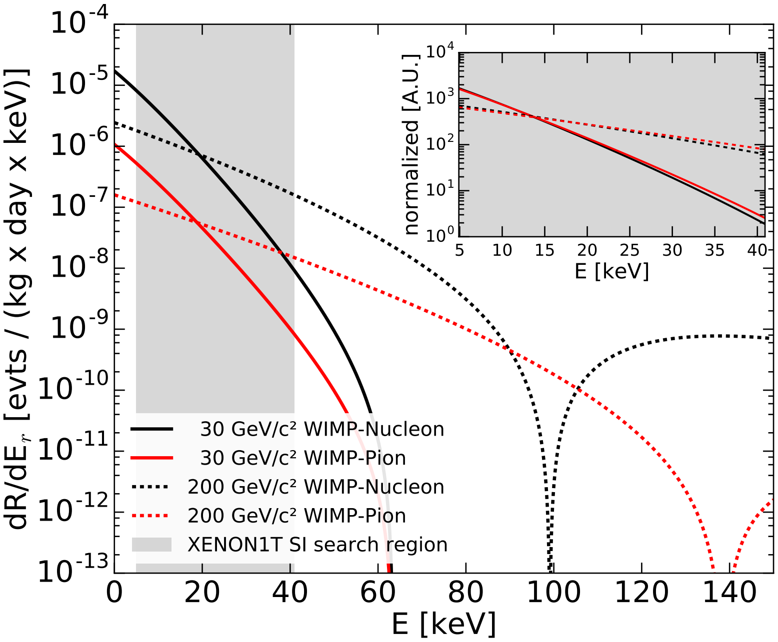

Figure 4.5: Comparison of the differential recoil spectrum for WIMP–nucleon (black) $\mathcal{F}_{+}^{M}$ versus WIMP–pion interactions (red) $\mathcal{F}_{\pi}$. Exemplarily shown are WIMP masses of $30\,\mathrm{GeV}/c^2$ (full line) and $200\,\mathrm{GeV}/c^2$ (dashed line) for the most abundant isotope ^{132}Xe. The cross section in both cases is set to $10^{-46}\,\mathrm{cm}^2$ for illustration. The gray band shows the energy range for the XENON1T SI search. The inset compares the spectral shapes in this region. Figure published in Ref. [92].

Besides the standard channels of SI and SD WIMP-nucleon elastic scattering, we also explored the possiblity of a scalar coupling between WIMPs and Pions, which was never considered before. In this case, the interaction is generated when the WIMP couples to a virtual pion exchanged between nucleons in the nucleus. The differential rate for the WIMP-Pion coupling can be written as

$$\frac{dR}{dE_{\mathrm{r}}} = \frac{2\rho_0\sigma_{\chi\pi}^{\mathrm{scalar}}}{m_\chi\mu_\pi^2} \times \left|\mathcal{F}_\pi(q^2)\right|^2 \times \int \frac{f(\boldsymbol{v},t)}{v} d^3\boldsymbol{v}, \tag{4.2}$$

which is quite similar to the SI WIMP-nucleon scattering differential rate (Eq. (2.7)), with only the difference as μ_π the reduced mass of WIMP-Pion system, $\mathcal{F}_\pi(q^2)$ the form factor for Pion coupling, $\sigma_{\chi\pi}^{\mathrm{scalar}}$ the scalar WIMP-Pion cross section. The NR recoil spectra shapes for SI WIMP-nucleon and WIMP-pion scattering are quite similar, shown in Fig. 4.5, as both spectral shapes are mainly affected by form factors.

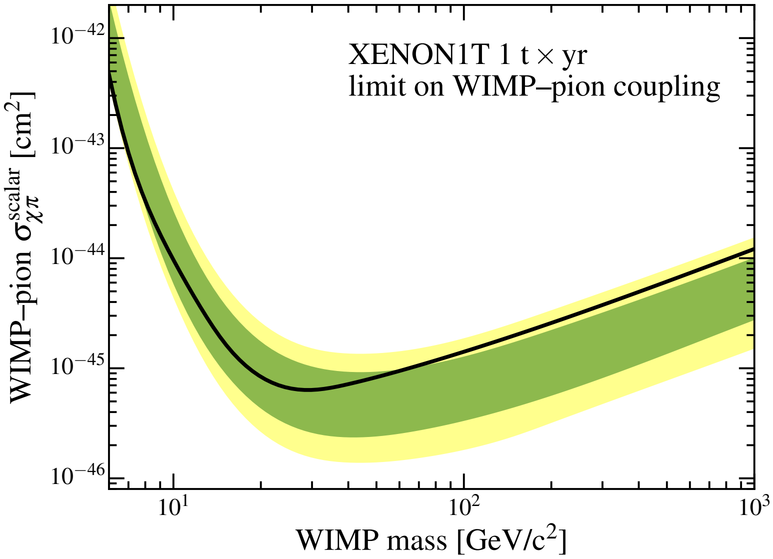

Figure 4.6: Result on scalar WIMP-pion coupling from XENON1T. The green (yellow) band is the 1 (2)σ sensitivity band and the black is the 90% C.L. upper limit. Figure published in Ref. [92].

Similar to the aforementioned WIMP searches, no significant signal-like excess was found over the background. As shown in Fig. 4.6, a 90% C.L. upper limit is placed on the scalar WIMP-pion coupling with a minimum of $6.4 \times 10^{-46}\,\mathrm{cm}^2$ for a WIMP mass of $30\,\mathrm{GeV}/c^2$.

4.2 Light WIMP Search Results

4.2.1 S2-only Approach

The standard S1S2 analysis approach has a limited detection efficiency at $\sim 1\,\mathrm{keV_{ee}}$ due to the 3-fold requirement of S1 signal (see Sec. 5.2.1). Therefore, the detection threshold can be significantly lower if the requirement of S1 signal is lifted, which motivates the search with ionization signals only, known as the S2-only approach.

The S2-only approach in XENON1T is extended down to 150 PE $S2$. In LXe experiments, the lowest measurement for charge yield were at the energies of $0.7\,\mathrm{keV_{nr}}$ and $0.186\,\mathrm{keV_{ee}}$ for NRs and ERs, respectively [100, 101], at the time of the work.[1] As S2-only approach in XENON1T was designed to set upper limits only (see below), both background and signal models were cutoff at the aforementioned energies to be conservative.

The S2-only data was divided into training data (30%) and search data (70%). Several selections were imposed to remove backgrounds based on the training data, as detailed in Ref. [103]. Here we only introduce two selections that can be considered as FV selection but are targeted at different backgrounds. The first selection makes a strict requirement on the width of S2 signals. Since most events in this analysis lack S1s, the z positions cannot be easily reconstructed from the drift time; however, it can still be inferred from the width of S2 signals, which is correlated to the depth of event interaction due to diffusion. The strict width cut can remove two backgrounds: events produced in the GXe (gas events) and from the cathode (cathode events), both of which have large S2 width. The other cut is

---

[1] At the time of the thesis writing (August 2020), the NR charge yield measurement is down to $\sim 0.3\,\mathrm{keV_{nr}}$ [102].

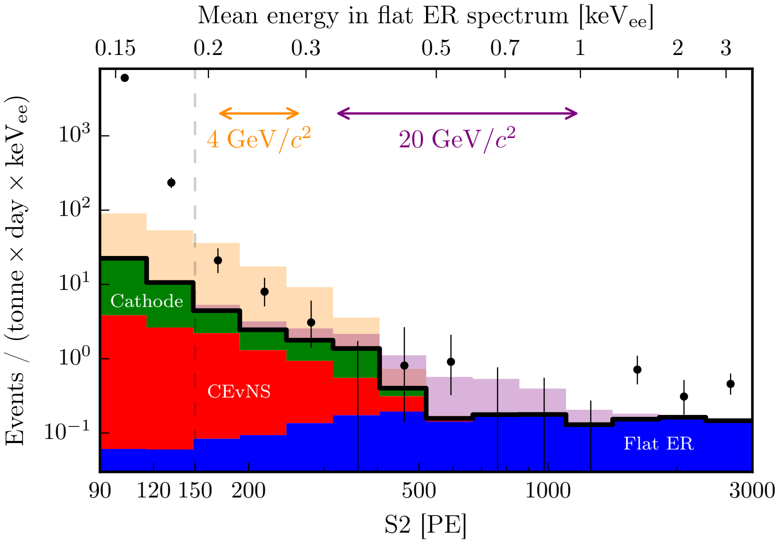

Figure 4.7: Event rate in $S2$-only analysis. Several background components are denoted, including the regular ER background (blue), cathode events (red), and CEνNS (red). The signal spectrum of a 4 (20) GeV/c^2 WIMP with cross section excluded by 90% C.L in this work is overlaid in yellow (purple). The $S2$ ROI for 4 (20) GeV/c^2 WIMP is indicated by the yellow (purple) arrow. Figure published in Ref. [103].

the radius cut that primarily aims for the surface events described in Sec. 3.4.4. The restriction on r is much more strict than that in Ref. [23] for two reasons: (1) position reconstruction gets worse with smaller $S2$ size (Eq. (3.7)), thus surface events here are more likely to be reconstructed at smaller r. (2) Due to the lack of z information, the 3D FDC discussed in Sec. 3.2.2.2 cannot be applied; therefore, the surface events get more inwards due to the field distortion. After all the cuts described in Ref. [103], the event rate is < 1 events/(tonne·day·keV$_{ee}$) for $S2 \gtrsim 300$ PE, which is $\mathcal{O}(10^3)$ lower than the previous S2-only analyses [104–106], see Fig. 4.7.

Both surface and gas events are considered to be removed completely, whereas the cathode background is included in the background model, along with CEνNS background (see Sec. 3.4.2) and the regular ER backgrounds (see Sec. 5.3). The background model is illustrated in Fig. 4.7. We do emphasize, however, the background model is incomplete; therefore, we conservatively used the lower bound from the background model prediction and only aimed to set upper limits for signal models in this analysis.

Six DM models were used to interpret the data in Fig. 4.8. The signal models of SI DM-nucleus scattering (Sec. 2.2.1), SD DM-neutron scattering (Sec. 4.1.2), and the absorption of axion-like particle (Sec. 2.3.3) and dark photon DM (Sec. 6.2), i.e. the bosonic DM are covered in this thesis. The other two scenarios, one where light DM can scatter off electrons is detailed in [117] and the other one where the interaction between DM and matter is mediated by a light particle is discussed in Refs. [111, 120, 121]. The upper limits are inferred using the Poisson statistics based on the observed count in the predefined $S2$ ROI, not from the binned event rates in Fig. 4.7 that is only for visualization. The $S2$ ROIs were optimized using the training data to get the most stringent constraint and is thus dependent on the signal model and mass. Due to the variation of ROI and the discrete nature of counting experiment, there are several jumps in the limit curves. For example, the limit curve (thick black) in Fig. 4.8 (a) has a sharp drop at $\sim 17.5\,\mathrm{GeV}/c^2$ because the observed count changes from 10 to 3 in the ROIs left and right of the drop.

In summary, benefiting from the low backgrounds achieved in XENON1T, this analysis exclude new regions for all DM models considered. Moreover, this approach was also carried out in the searches for other signals, see Secs. 4.2.2 and 5.6.5.

4.2.2 Migdal and Bremsstrahlung Effects

When the WIMP elastically scatters with xenon nucleus, the recoil of nucleus can polarize the atom as well as give a sudden kinematic boost to the orbital electrons. The depolarization process can lead to a bremsstrahlung (BREM) emission

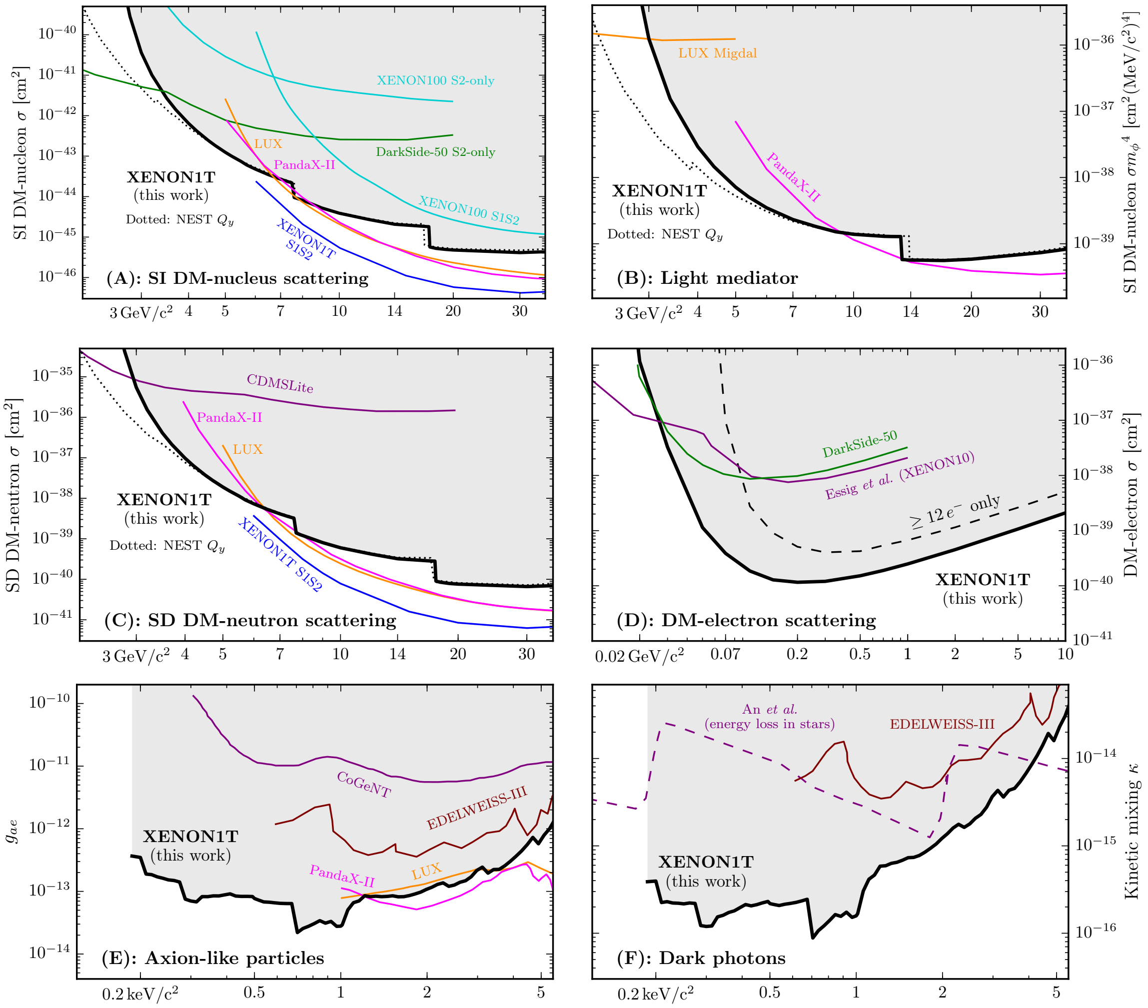

Figure 4.8: The 90% C.L. upper limits (black lines with gray shading above) on DM-matter scattering or bosonic DM absorption for the models discussed in the text, with the DM mass m_χ on the horizontal axes. Dotted lines in (a)–(c) show our limits when assuming the Qy from NEST v2.0.1 [107] cut off below 0.3 keV. The dashed line in (d) shows the limit without considering signals with < 12 produced electrons. Also shown are other constraints from experiments or astrophysics observations [23–25, 34, 93, 96, 104, 108–119]. Figure published in Ref. [103].

of a photon [122], while the kinematic boost can ionize or excite the electrons, which results in detectable secondary radiation. The second case is called the Midgal effect (MIGD) [123, 124]. Both MIGD and BREM effects bring in extra ER signals which are easier to detect compared to NR signals and thus enhance XENON1T's sensitivity to low-mass WIMPs.

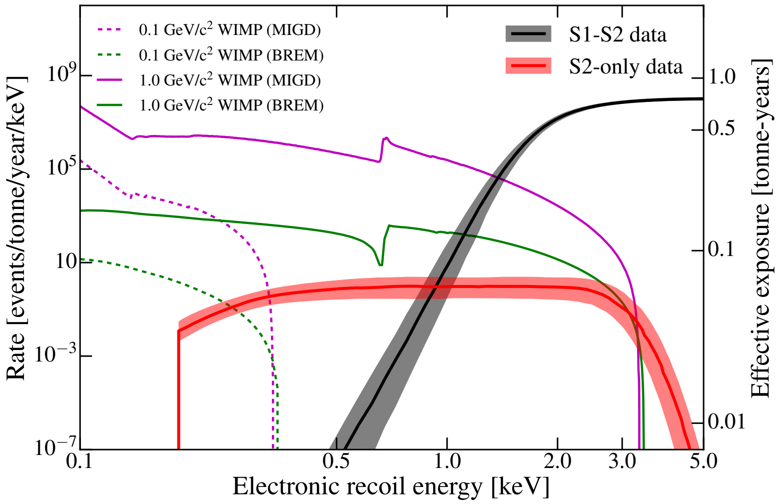

Figure 4.9: Median effective exposures of ER signals after event selections as a function of recoil energy for the S1S2 data (black line) and S2-only data (red line). The 68% credible regions of the effective exposures are also shown as the shaded regions. The expected event rate of DM-nucleus scattering from MIGD (BREM) for DM masses of 0.1 and $1.0\,\mathrm{GeV}/c^2$ are overlaid as well, in magenta (green) dashed and solid lines, respectively, assuming a SI DM-nucleon interaction cross section of $10^{-35}\,\mathrm{cm}^2$. Figure published in Ref. [125].

The ER spectra for BREM and MIGD processes with two WIMP masses are shown in Fig. 4.9. In general, the signal rate from MIGD is typically 3–4 orders of magnitude higher than that from BREM. For MIGD process, we focused on ionization as excitation of electrons are subdominant. Only electrons in M and N shells were considered, as inner electrons cannot be ionization due to the large binding energies and outer electrons have negligible contributions in the ROI. The sharp increase ∼0.85 keV is due to the M shell electrons. Since S1S2 approach has limited detection efficiency at $\mathcal{O}(1)$ keV, the S2-only approach was also employed to further probe these two channels.

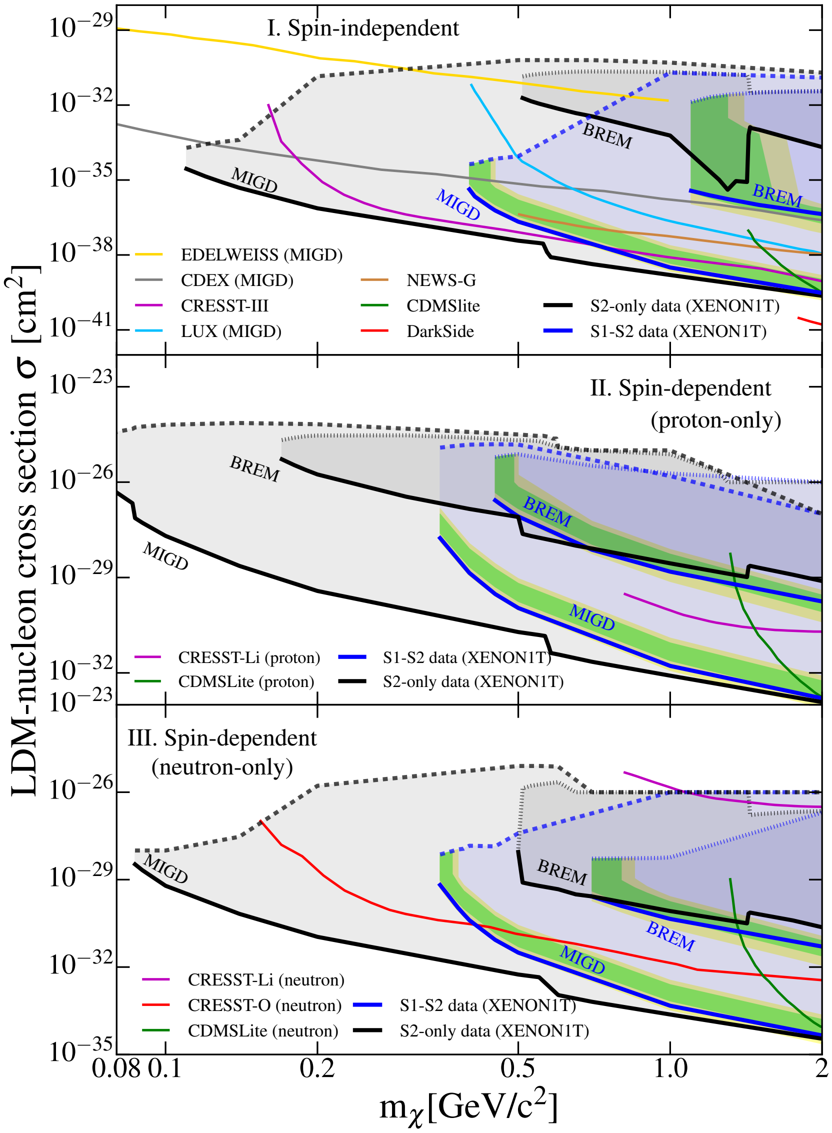

Figure 4.10: Limits on the SI (upper panel), SD proton-only (middle panel), and SD neutron-only (lower panel) DM-nucleon interaction cross sections at 90% C.L. using signal models from MIGD and BREM in the XENON1T experiment with the S1S2 data (blue contours and lines) and S2-only data (black contours and lines). The solid and dashed (dotted) lines represent the lower boundaries (also referred to as upper limits) and MIGD (BREM) upper boundaries of the excluded parameter regions. Green (yellow) shaded region gives the 1 (2)σ sensitivity contour for upper limits derived using the S1S2 data, respectively. Also shown are limits from Refs. [108, 112, 118, 126–131]. Figure published in Ref. [125].

The S1S2 approach still used the unbinned likelihood in (c$S1$, c$S2_\mathrm{b}$, r) as in Sec. 4.1.1 and S2-only approach followed the simple counting method described in Sec. 4.2.1. The data is interpreted as BREM or MIGD effect with SI WIMP-nucleon interaction (see Sec. 4.1.1), SD WIMP-proton or WIMP-neutron interaction (see Sec. 4.1.2), respectively. Since no excess was found in S1S2 data while S2-only approach was designed to set upper limits only, both approaches give 90% C.L. upper limits on these physics models. By looking for MIGD effect with S2-only approach, XENON1T experiment was able to probe WIMP mass down to 85 MeV/c^2. Furthermore, another upper boundary of excluded region is provided assuming all the WIMPs are scattered or stopped by the Earth, i.e, the Earth shielding effect.

4.3 Acknowledgements

Chapter 4, in full, is a summary of the following publications. Sec. 4.1 contains results from (1) XENON Collaboration, Dark matter search results from a one ton-year exposure of XENON1T, Phys. Rev. Lett. 121, 111302 (2018), (2) XENON Collaboration, Constraining the Spin-Dependent WIMP-Nucleon Cross Sections with XENON1T, Phys. Rev. Lett. 122, 141301 (2019), and (3) XENON Collaboration, First Results on the Scalar WIMP-Pion Coupling, Using the XENON1T Experiment, Phys. Rev. Lett. 122, 071301 (2019). Sec. 4.2 includes materials from (1) XENON Collaboration, Light Dark Matter Search with Ionization Signals in XENON1T, Phys. Rev. Lett. 123, 251801 (2019), and (2) XENON Collaboration, Search for Light Dark Matter Interactions Enhanced by the Migdal Effect or Bremsstrahlung in XENON1T, Phys. Rev. Lett. 123, 241803 (2019). The dissertation author is an author of those work.

Chapter 5

Search for Solar Axions with XENON1T

This chapter describes the solar axion search in XENON1T. As discussed in Sec. 2.3.2, solar axions would induce ERs in XENON1T detector, thus it is not necessary to perform the analysis in the (c$S1$, c$S2_{\mathrm{b}}$) parameter space to discriminate ER and NR Events. To simply the analysis, analysis space of this work is the energy of the event, which can be reconstructed from c$S1$ and c$S2_{\mathrm{b}}$ using Eq. (3.11). The chapter is structured as follows. Sec. 5.1 describes the data quality selection, the efficiency evaluation, as well as the determination of FV. The detector response modeling, including efficiency and energy resolution specific to XENON1T, is presented in Sec. 5.2. The background model, which includes ten ER components, is detailed in Sec. 5.3. Statistics method is given in Sec. 5.4. In Sec. 5.5, a hypothesis of a new background is introduced upon the observation of an excess, and the solar axion search result is reported. Sec. 5.6 provides a variety of scrutiny checks on the excess, as well as a discussion on the tension with astrophysical constraints.

5.1 Data Selection

5.1.1 Effective Time of Data

This search employs the SR1 science data, i.e. data taken between February 2017 to February 2018 with XENON1T. The data are quite similar to the SR1 part in the WIMP search [23] with a few additional requirements. Events within 24 hours from the end of calibration campaigns using injected radioactive sources were removed due to residual source activity, including $^{83\mathrm{m}}$Kr and ^{220}Rn calibrations. Additionally, several event selections remove events regardless of the properties of the events and thus are deemed as a reduction for the effective live time, which is the time that the detector accumulates science data for signal searches, excluding the calibration time, data acquisition dead time, etc. Three of the four live time selections in Ref. [59] were used except for the MuonVeto that is targeted at muon-induced neutron events (Sec. 3.4.2), which is negligible compared to the ER events was thus unused in this search. The final effective SR1 live time is 226.9 days, as illustrated in Fig. 5.1.

5.1.2 Event Selection Critefria

The event selection criteria can be classified into 4 categories: (1) noise rejection, (2) S1S2 pairing requirements, (3) single scatter requirements, as well as (4) the livetime reduction selection discussed in Sec. 5.1.1. Those selections are largely the same as the ones detailed in Ref. [59] with a few exceptions that are described below.

- A more stringent threshold of 500 PE was imposed on $S2$ size to reduce the surface background (Sec. 3.4.4). Compared to the $S2$ threshold (200 PE)

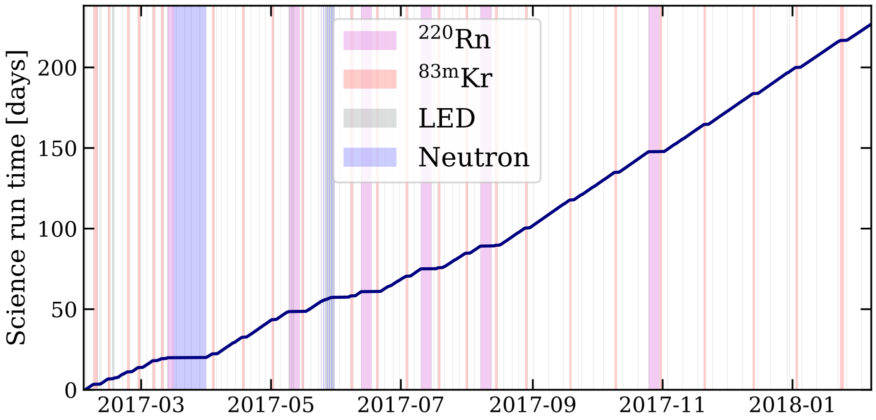

Figure 5.1: Science data in SR1 used in this analysis. The accumulated live time of data used is indicated by the blue curve, amounting to a total of 226.9 days. The while region is the science data taking period, while the magenta, pink, gray, blue regions are the ^{220}Rn, $^{83\mathrm{m}}$Kr, LED, and neutron calibration data taking periods, respectively.

in WIMP searches, the surface background rate in the ROI in the 1T FV (Sec. 5.1.4) is reduced by a factor of ~ 60.[1]

- As part of the noise rejection criteria, one event will be removed if the pattern in top PMT array illuminated by its S2 signal does not match well with its reconstructed position, which is referred to as S2 hit pattern selection. The updated cut used in this search accounts for the PMT after pulse effect for events with $S2$ larger than 10000 PE and, thus mitigates the time dependence of this event selection from the increasing after pulse over time.

- The single scatter requirement for S1 channel is also similar to that in the WIMP search, with an improvement of taking into account the case that PMT after pulses are sometimes misidentified as secondary S1s, resulting in an increased selection efficiency.

- The single scatter requirement for S2 channel has relatively large change.

---

[1] This stringent cut cannot be applied to WIMP searches as it will significantly reduce NR signals; however, ER signals have much larger $S2$ and thus are not affected.

The previous selection criterion was based on the sizes of the primary and secondary S2s, whereas the updated version utilizes the hit pattern in top PMT for the secondary S2, i.e. imposing the S2 hit pattern criterion on the secondary S2. One event will be removed if its secondary S2 can pass the S2 hit pattern criterion as it indicates the secondary S2 is a valid S2. Since some "fake" secondary S2s, such as those with origins from PMT after pulse, or single electron pile up, cannot be told by size but is differentiable by the S2 hit pattern, this parameter space is more suitable and improves selection efficiency.

- The $^{83\mathrm{m}}$Kr events, one of the backgrounds in this search (Sec. 5.3.2.2), can have single- or multi-site energy depositions. The majority of $^{83\mathrm{m}}$Kr multi-site events is already rejected by the aforementioned two single scatter requirements; however, the S1s of some multiple scatters are misidentified as S2s and escaped the removal. A new cut was developed to further reject the multi-site $^{83\mathrm{m}}$Kr backgrounds with both high removal efficiency and signal acceptance.

- Aside from the modifications and additions, several selections were removed from the event selection criterion. Besides the MuonVeto, a selection used to reduce AC background (Sec. 3.4.3) was not employed in this search as AC backgrounds are negligible in this search compared to the ER events (see Sec. 5.3).

5.1.3 Event Selection Efficiency

Although the event selection criteria aim to reject backgrounds, noisy events, or events with poor quality, inevitably they would remove a fraction of good events.

The acceptance of good events from the event selections are referred to as the selection efficiency. Two methods were used to evaluate the selection efficiency in this work.

The first method uses an analytic way to compute the efficiency. The stringent $S2$ threshold falls into this category. The newly added cut, the one aiming to remove multi-site $^{83\mathrm{m}}$Kr with misidentified S1, was evaluated to have unity acceptance analytically by its definition, which was verified by checking the background data in the parameter space.

The efficiencies of most selections were derived based on the control sample from ^{220}Rn calibration data. In this case, the ^{220}Rn calibration data are applied with all other selections except for the examined cut. This processed data are considered to be a sample of good events, therefore the pass through of the examined cut on this sample is considered to be the selection efficiency. Since the analysis space of this work is the reconstructed energy, the cut acceptance was calculated over the energy of events. The uncertainty of cut acceptance derived from ^{220}Rn data was estimated using a method based on Bayes' Theorem [132].

The cumulative selection efficiency is the product of each selection efficiency, where we conservatively assumed no correlation between each selection. Two selections were evaluated using both methods; the analytical value is supposed to be unity but the efficiency inferred from ^{220}Rn data is slightly less. Therefore, two different cumulative efficiencies were acquired depending on the method to evaluate those two selections. The two cumulative results were then fitted by two analytical functions, and the difference is treated as systematic uncertainty. The statistical uncertainties from two fittings are similar, therefore the one from analytical method was used as the statistical uncertainty. The final uncertainty includes both systematic and statistical uncertainties by error propagation. The

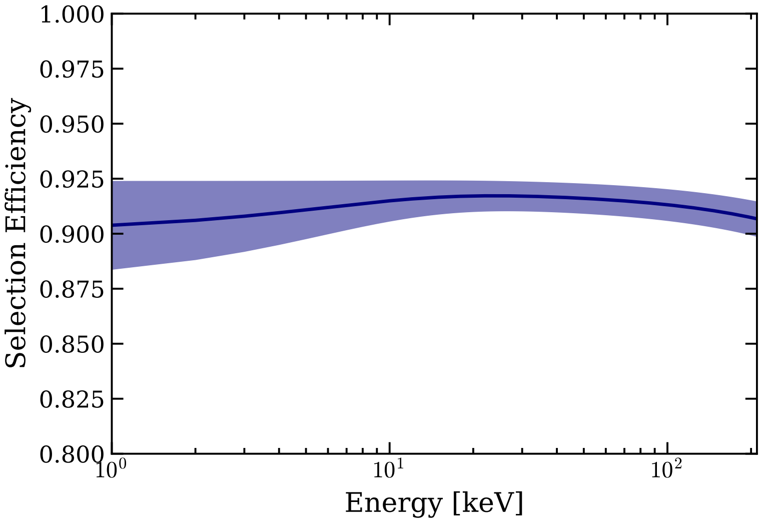

Figure 5.2: The cumulative selection efficiency in this analysis. The efficiency uncertainty includes both systematic and statistical uncertainty and is indicated by the band.

cumulative efficiency of aforementioned selections is illustrated in Fig. 5.2. The average cumulative selection efficiency over the (1, 210) keV ROI is $(91.2 \pm 0.3)\%$.

5.1.4 Fiducial Volume

The same 1042 kg cylindrical FV, i.e. the 1T FV, as in Ref. [133] was used to reduce the surface and material backgrounds. To verify this conservative FV does not significantly lower our sensitivities, we compare the sensitivity in 1T FV and the most optimized FV. The solar axion search was done together with the bosonic DM search (Sec. 6.2) in Ref. [134], the signature of which is a mono-energetic peak around its rest energy; therefore the optimized FVs in fact consider many different bosonic DM masses. However, the sensitivity of solar axion search is not much impacted as shown later.

The whole active volume of ~ 2000 kg was divided into 10 kg bins with equal interval in z and r^2. For each bosonic DM mass, which is between 1–210 keV/c^2, only events within energy region of $\pm 3\sigma$ were taken into account.[2] The optimized FV was then determined by maximizing the figure of merit given by

$$f = \frac{\sum_{i<n} S_{i,E}}{\sqrt{\sum_{i<n} B_{i,E}}}, \tag{5.1}$$

$S_{i,E}$ is the expected signal in each binned volume within the $\pm 3\sigma$ energy region around the bosonic DM rest energy E, $B_{i,E}$ is the background count in each binned volume in the same energy region, i is the index of one binned volume ranked by $S_{i,E}/\sqrt{B_{i,E}}$ in a descending order, and n is the total number of ranked indices in a certain FV. Due to the fact that the sensitivity gets better with larger signal rate and worse with background Poissonian fluctuation which can be approximated as the square root of background events, a large figure of merit can be an indicator of good sensitivities. Since signal scales linearly with exposure, $S_{i,E}$ is proportional to the mass in each binned volume, which is fixed at 10 kg. Therefore, Eq. 5.1 can be written as:

$$f(m, E) \propto \frac{m}{\sqrt{\sum_{i<n} B_{i,E}}}, \tag{5.2}$$

where m is the fiducial mass. Consequently, the optimized FV for each bosonic DM mass is the one can that maximizes Eq. (5.2) with the fixed E. The maximized figure of merit, f_{best}, as well as the one for 1T FV, f_{1T} are illustrated as function of bosonic DM rest energy in Fig. 5.3. Compared to the best figure of merit, 1T FV still maintains 80–90% sensitivity. Moreover, it is advised to avoid using mass-dependent FV for signal searches if there is no strong motivation behind. For solar axion search, the most relevant part is ~ 2 keV, which also retains a decent sensitivity (>80%). To summarize, as a balance between simplicity of analysis and

---

[2] The energy resolution used in this search can be found in Sec. 5.2.2.

sensitivity of target signals, the 1T FV was employed in this search. Combined with the effective live time of 226.9 days (Sec. 5.1.1), the SR1 data utilized in this search yields an exposure of 0.65 tonne-years.

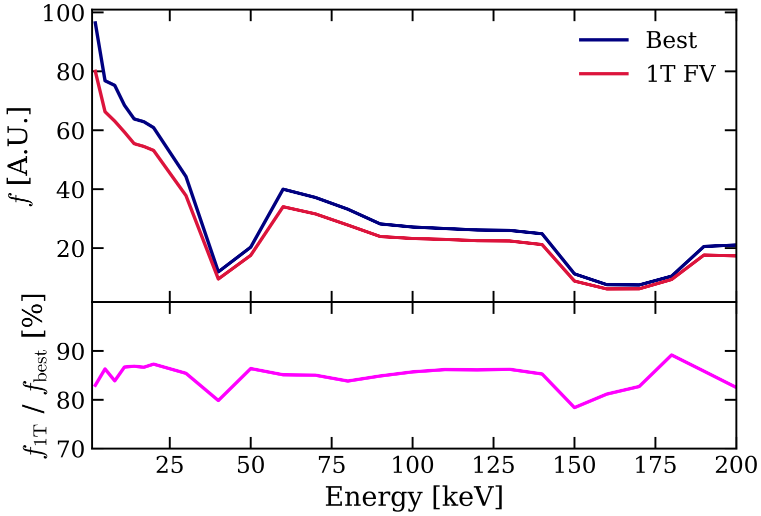

Figure 5.3: Top: The figure of merit (Eq. (5.2)) of 1T FV (red) and the best FV (red) that maximize it. Both are in arbitrary units (A. U.). Bottom: The ratio between figure of merit in 1T FV and the one in the optimized FV. Both plots show the figure of merit as function of bosonic DM rest energy.

5.2 Detector Response Modeling

Since the analysis space of this work is the reconstructed energy, two key factors that are desired to convert the true energy to the reconstructed energy — which is experimentally expected — are the efficiency and energy resolution in one specific detector. This section describes the determination of these two factors and the subsequent conversion of true energy spectrum to reconstructed energy spectrum in XENON1T.

5.2.1 Efficiency

The efficiency contains two parts, the detection and selection efficiencies. The determination of latter is discussed in detail in Sec. 5.1.3, which yields a relatively flat efficiency curve.

The detection efficiency is dominated by the 3-fold coincidence requirement of S1s, which can greatly suppress the coincidence of PMT dark counts and ensure valid S1s. That efficiency was estimated using both a data-driven method of sampling PMT hits from S1s in the 20–100 PE range and an independent study based on simulation of low-energy S1 waveforms [59]. The difference between the two methods ($\sim 3\%$ average relative difference in the drop-off region) was considered as a systematic uncertainty. This efficiency was then converted from $S1$ to reconstructed energy using the detector-response model described in Ref. [71], accounting for additional uncertainties such as the photon yield. The S2 efficiency can be assumed to be unity for the energies considered here [59].

The combined efficiency of detection and event selection with uncertainties is shown in Fig. 5.4. Events with energies between (1, 210) keV are selected for this search, with the lower bound determined by requiring the total efficiency be larger than 10%, and the upper bound limited by an increasing $\gamma-$ray background from detector materials, which is difficult to model due to large uncertainties on its spectral shape. While extending the ROI to 210 keV is primarily motivated by the bosonic DM search (see Sec. 6.2), all profile likelihood fits use this full energy range, as it also allows for better constraints on the background components.

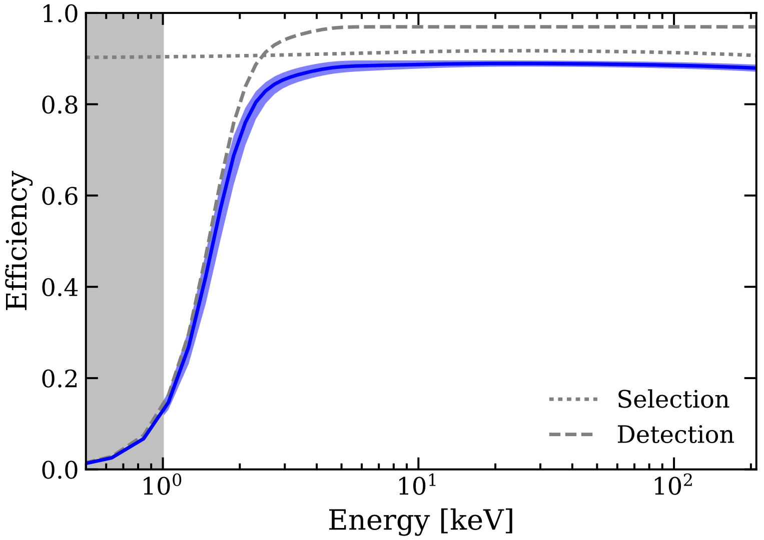

Figure 5.4: Efficiency as a function of energy. The dashed (dotted) line refers to detection (selection) efficiency, while the blue curve and band illustrate the total efficiency and the associated 1-σ uncertainty, respectively. The detection threshold is indicated by the right bound of the gray shaded region. Figure from Ref. [134].

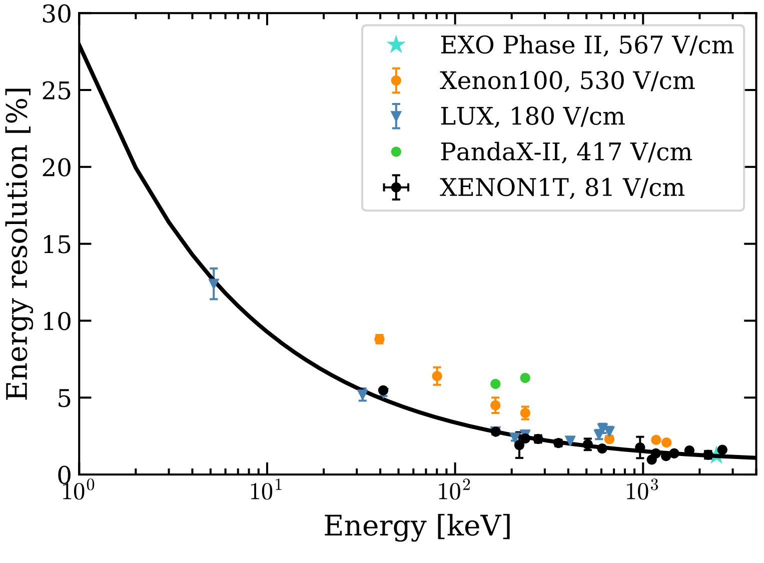

Figure 5.5: Relative energy resolution $\sigma(E)/E$ as a function of energy. The energy resolution from mono-energetic peaks in XENON1T (black dots) with energies below 1500 keV are fitted with an empirical function given in Eq. (5.3) (black line). Also shown are the energy resolutions from EXO-100 Phase II [135], XENON100 [68], LUX [136], and PandaX-II [137].

5.2.2 Energy Resolution

The energy resolution can be determined by fitting the energy resolutions obtained from these multiple mono-energetic peaks with the following empirical function:

$$\sigma(E) = a\sqrt{E} + bE, \tag{5.3}$$

where the first term $a\sqrt{E}$ accounts for the statistical fluctuation that is dependent on the energy and the second term bE includes instrumental uncertainties that are independent of the energy. The fit is illustrated in Fig. 5.5. Only peaks with energies below 1500 keV were used in the fit so as the energy resolution is more suitable for low energies. The fit result gives $a = (0.310 \pm 0.004)\sqrt{\text{keV}}$ and $b = 0.0037 \pm 0.0003$.

5.2.3 Modeling

With the detector energy resolution and efficiency ready, the true signal spectra of solar axions in Fig. 2.8 can be converted into the experimentally expected spectrum specific to the XENON1T detector. The true spectrum is smeared by a Gaussian distribution with resolution given by Eq. (5.3) and then is scaled by the combined efficiency in Fig. 5.4. The solar axion spectra that takes the XENON1T features into account are shown in shaded curves in Fig. 5.6. The "spikes" in the ABC axion true spectrum from the atomic deexcitation and recombination are smeared out by the energy resolution. Both the ABC and Primakoff signal spectra in reality have the "double-peak" features, which is due to the σ_{ae} increase at $\sim$5 keV due to the xenon L-shell, as mentioned in Sec. 2.3.2.2. The same procedure is also applied to the energy spectra of background components, which are discussed in the next section.

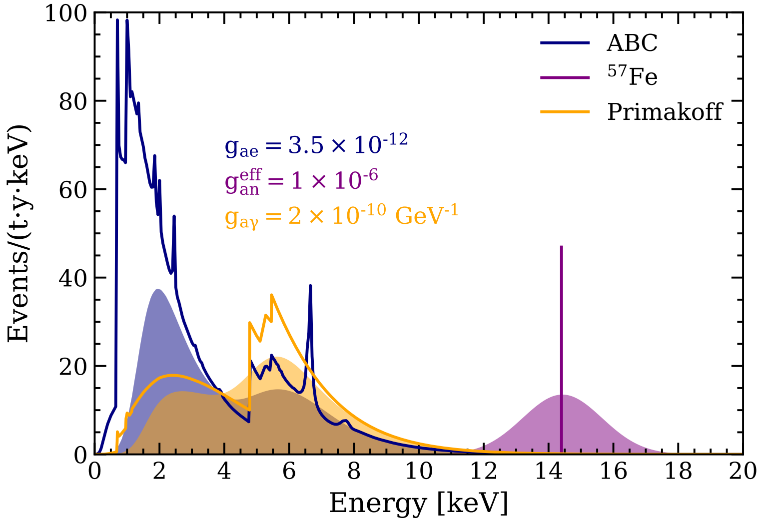

Figure 5.6: The ABC (blue), Primakoff (orange), and ^{57}Fe (purple) spectrum before (unshaded) and after (shaded) considering the energy resolution and efficiency specific to XENON1T. The assumed axion couplings are indicated in the plot. Figure adapted from Ref. [134].

5.3 Backgrounds

This section gives a detailed discussion of the background model B_0 used in this search, which includes a total of 10 ER background components. After event selection and strict fiducialization, the non-ER backgrounds, i.e. the surface backgrounds (Sec. 3.4.4), accidental coincidences (Sec. 3.4.3), and radiogenic neutrons (Sec. 3.4.2) make up less than 0.003% of the total events ($< 0.3\%$ below 7 keV), and thus are negligible for this search. The result of background-only fit to data is presented in Sec. 5.5.1.

5.3.1 β decay of ^{214}Pb

The β decays from ^{214}Pb, daughter of ^{222}Rn, is the dominant continuous background in this analysis throughout the full ROI. ^{214}Pb decays to the ground state with a BR of 11% [138]. The lowest excited state it decays to is 295 keV, the emitted γ of which is unresolved with β and thus does not enter the ROI [138]; the possibility that the accompanied γ escapes and only the β deposits energy in LXe is also rejected by the strict 1T FV. The energy spectrum of ^{214}Pb decay to the ground state is usually approximated as flat; however, the unprecedented low background achieved in the XENON1T experiment necessitated a more dedicated treatment, which is discussed in Sec. 5.6.2 and detailed in the appendix of Ref. [134].[3] ^{214}Pb rate can be constrained by its parent and daughter in the ^{222}Rn chain, which is illustrated in Fig. 3.19. ^{218}Po, parent of ^{214}Pb, is an α-emitter with a energy of 6 MeV, which is easy to identify with the large S1 signals and thus place an upper limit for ^{214}Pb. On the other hand, ^{214}Bi and ^{214}Po, daughters of ^{214}Pb, can place a lower limit for ^{214}Pb rate by its unqiue coincidence signature, where the β decay of ^{214}Bi is followed closely by the α decay of ^{214}Po ($t_{1/2} = 163.6\,\mu$s [141]). The so-called ^{214}BiPo tagging can tag the β decay of ^{214}Bi with a high efficiency, which is thus not included in the background model. As a result, the upper and lower limits on ^{214}Pb in SR1 were determined to be $(12.6 \pm 0.8)\,\mu$Bq/kg and $(5.1 \pm 0.5)\,\mu$Bq/kg, respectively. Due to its relatively loose constraints and the dominance it has in the background model, the ^{214}Pb rate was left unconstrained during the fit. Both coincident ^{214}BiPo and ^{218}Po suggest a constant rate in time in SR1, thereby we conclude that ^{214}Pb rate was also constant throughout SR1.

---

[3] Updated β decay spectra, including that from ^{214}Pb, ^{85}Kr, and ^{212}Pb, were available in Ref. [139] after the work was out; therefore, this thesis sticks to the β spectra provided in the appendix in Ref. [134]. The analysis with updated β decay spectra can be found in Ref. [140].

5.3.2 Time-dependent Backgrounds

Due to different reasons, the rates of several backgrounds exhibit time-dependent patterns, which can be utilized to predict and constrain the background rate.

5.3.2.1 $^{131\mathrm{m}}$Xe, ^{133}Xe, and ^{125}I

Three time-dependent backgrounds in SR1 are induced by neutron activation. $^{131\mathrm{m}}$Xe and ^{133}Xe are neutron-activated xenon isotopes with a half-life of $\mathcal{O}(10)$ days. Another background, ^{125}I, is produced from the β decay of ^{125}Xe, which is also from a neutron reaction ^{124}Xe(n,γ)^{125}Xe. Therefore, the time information for these three backgrounds are all related to the neutron activation in XENON1T.

There were three neutron activation periods in SR1, including two neutron calibrations, a ^{241}AmBe calibration in March 2017 and NG calibration in May 2017, and one neutron safety test in the beginning of May 2017. There was one ^{241}AmBe calibration in SR0 in November 2016, which led to a residual activated rate in the beginning of SR1. Given the similarity between the modelings of time evolution for $^{131\mathrm{m}}$Xe and ^{133}Xe, the modeling of $^{131\mathrm{m}}$Xe rate is explained as an example.

$^{131\mathrm{m}}$Xe produces a mono-energetic peak at 163.9 keV via IC [64], thereby events within $\pm 3\sigma$ energy resolution region around 163.9 keV are selected to model $^{131\mathrm{m}}$Xe rate evolution. From the energy resolution in XENON1T (Eq. (5.3)), the selected region is (145.6, 182.2) keV. All the event selections mentioned in Sec. 5.1.2 were applied. The selected events were binned with the 5 calendar days; the center of each bin is the weighted live time in the bin, while the rate in each bin considers the live time and is without efficiency loss. The binned event rate evolution is

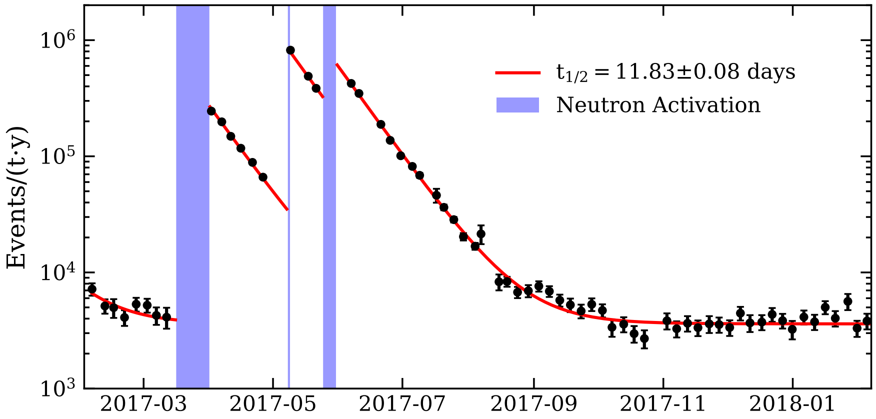

Figure 5.7: Rate evolution of events within ±3σ region centered around 163.9 keV, which is dominated by $^{131\mathrm{m}}$Xe events. The red line is the best-fit of a constant offset plus multi-exponential decay functions sharing the same half-life, which is determined to be (11.83 ± 0.08) days and is consistent with $^{131\mathrm{m}}$Xe half-life in literature. The blue region indicates the neutron activation periods.

shown in Fig. 5.7.

The rate evolution of $^{131\mathrm{m}}$Xe event is modeled by a sum of multiple exponential decay functions. Other backgrounds in this energy region, dominated by β decays of ^{214}Pb, were inevitably included and was modeled by a constant. The total rate evolution is then modeled by

$$f(t) = \sum_{i}^{n} A_i * \exp\left(-\frac{t - t_i}{t_{1/2}/\ln(2)}\right) + b, \tag{5.4}$$

where n is the number of neutron activations ($n = 4$), A_i and t_i is the number of increased $^{131\mathrm{m}}$Xe atoms and time of each neutron activation, respectively, $t_{1/2}$ is the half-life of $^{131\mathrm{m}}$Xe, and b is the constant background rate in the selected energy region. Eq. (5.4) was fit to the binned rate using χ^2 minimization with all the parameters allowed to vary freely. The best-fit $t_{1/2}$ is (11.83 ± 0.08) days and is in good agreement with the half-life in literature ($t_{1/2} = 11.84$ days [64]), shown in Fig. 5.7. The $^{131\mathrm{m}}$Xe rate in a given period of science data can be predicted by the best-fit values. The uncertainty of prediction is dominated by statistical uncertainty, which was assessed by toyMC simulations with wiggling each parameters around the best-fit values with the fitted uncertainties. An example is illustrated for the whole period in SR1 in Fig. 5.8, from which we predict the average $^{131\mathrm{m}}$Xe rate to be (42310 ± 840) events/(t·y) in SR1 without efficiency loss. The total uncertainty is 2.5%, with ∼2.0% from this statistical fluctuation.

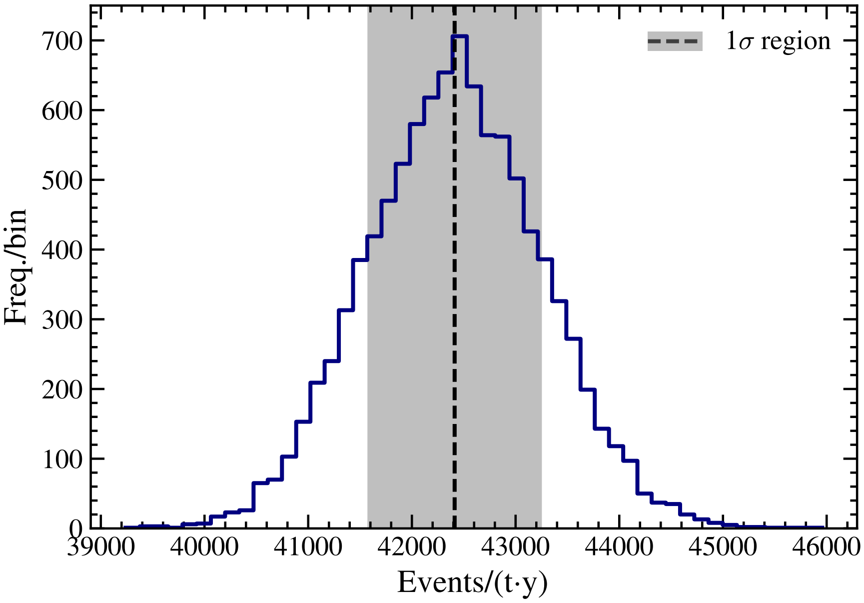

Figure 5.8: Distribution of predicted $^{131\mathrm{m}}$Xe rates in SR1 from toyMC simulations is shown in the blue curve. The 1σ region (gray) predicts the $^{131\mathrm{m}}$Xe rate to be (42310 ± 840) events/(t·y) without efficiency loss.

Similarly, the β decay rate of ^{133}Xe can be predicted in this way. ^{133}Xe decays to an excited state with a dominant BR of 98.5% and emits an 81 keV prompt γ upon de-excitation [142], resulting in a continuous spectrum starting at ∼75 keV after the energy smearing. The rate evolution of events within (80, 100) keV, where ^{133}Xe events are most visible, was modeled in the same way as for $^{131\mathrm{m}}$Xe. Afterwards, the rate is scaled from (80, 100) keV to (1, 210) keV based on the fraction of smeared spectrum in each energy region, so is the rate uncertainty.

Both ^{133}Xe and $^{131\mathrm{m}}$Xe rates are constrained in the likelihood fit.

^{125}I decays via electron capture (EC) of K-shell, L-shell, and M-shell with decreasing probabilities and produces peaks at 67.3 keV, 40.4 keV, and 36.5 keV, respectively [143]. ^{125}I background modeling is a bit complicated as there are two steps involved.[4] Details of ^{125}I modeling used in this analysis can be found in Ref. [144].

5.3.2.2 $^{83\mathrm{m}}$Kr

During SR1, a background from $^{83\mathrm{m}}$Kr (IC) was present due to a trace amount of ^{83}Rb (IC, $t_{1/2}$ ~86 days [145]) in the xenon recirculation system, which presumably was caused by a momentary malfunction of the source valve and confirmed using half-life measurements. $^{83\mathrm{m}}$Kr decays via a two-step scheme (second step $t_{1/2} \sim 154$ ns) [63] resulting in many of these events being removed by the multi-site selections mentioned in Sec. 5.1.2; however, due to the short half-life of the second step, these decays are often unresolved in time and hence contribute as a mono-energetic peak at 41.5 keV. This component was also constrained using a time-evolution model from a similar method as the $^{131\mathrm{m}}$Xe model in Sec. 5.3.2.1.

5.3.2.3 ^{85}Kr

The β decay of ^{85}Kr was greatly suppressed by the cryogenic distillation [146, 147]. The remaining ^{85}Kr decay rate was then inferred from dedicated measurements of the isotopic abundance of ^{85}Kr/$^{\mathrm{nat}}$Kr (2×10^{-11} mol/mol) and the $^{\mathrm{nat}}$Kr concentration evolution in LXe [148]. The same measurements also allow for the time-dependence of the ^{85}Kr decay rate to be taken into account. The average expected rate of ^{85}Kr is (7.4 ± 1.3) events/(t·y·keV) over the ROI in SR1 without

---

[4] The isotope ^{125}I is the daughter of ^{125}Xe that is generated through neutron activation.

efficiency loss.

5.3.3 Solar Neutrino Electron Elastic Scattering

Elastic scattering of solar neutrinos off electrons is expected to contribute subdominantly over the entire ROI. The expected energy spectrum was obtained using the standard neutrino flux in the Large Mixing Angle Mikheyev-Smirnov-Wolfenstein (LMA-MSW) model and cross section given by the SM [149, 150]. Based on rate calculations of neutrino-electron scattering in xenon as given in Ref. [151], a 3% uncertainty was assigned and used to constrain the solar neutrino rate in the fit.

5.3.4 Compton Scattering from Materials

An additional background arises from γ emissions from radioimpurities in detector materials that induce Compton-scattered electrons; however, this background is subdominant in the ROI due to the strict fiducial volume selection. The rate from materials was constrained by radioassay measurements [152] and predicted by simulations [77] to be (2.7 ± 0.3) events/(t·y·keV) in the 1T FV. This background was modeled by a fixed, flat component in the fit.

5.3.5 Double β decay of xenon isotopes

5.3.5.1 $2\nu\beta\beta$ of ^{136}Xe

One of the continuous backgrounds considered was ^{136}Xe, a two-neutrino double β decay ($2\nu\beta\beta$) emitter intrinsic to xenon. This component has an increasing rate as a function of energy over the ROI. It was constrained in the fit according to the predicted rate and associated uncertainties on (1) a ^{136}Xe isotopic abundance of

$(8.49 \pm 0.04_{\mathrm{stat}} \pm 0.13_{\mathrm{sys}})\%$ as measured by a residual gas analyzer [153], (2) the reported half-life [154], and (3) the calculated theoretical spectrum [155, 156].

5.3.5.2 2νECEC of ^{124}Xe

The first observation of 2νECEC of ^{124}Xe was recently reported using mostly the same SR1 dataset (but different selection cuts) as used in this analysis [144] and was treated as a background here.[5] In Ref. [144] we considered the dominant BR of 2νECEC, the capture of two K-shell electrons inducing a peak at 64.3 keV. It is also possible to capture a K-shell and L-shell electron (36.7 keV) or two L-shell electrons (9.8 keV) with decreasing probabilities, as calculated in Ref. [157]. For this analysis, the event selection and consideration of time dependence allow us to include all three peaks in the background model. The predicted rates of the peaks are taken from an updated half-life [158] with fixed BRs from Ref. [157]; the overall rate was not constrained in the fit since the half-life was derived from the same data set.

5.4 Statistics Method

An unbinned profile likelihood method is employed in this analysis. The likelihood is constructed as

---

[5] A summary can be found in Sec. 6.4.

$$
\begin{aligned}
\mathcal{L}(\mu_s, \boldsymbol{\mu_b}, \boldsymbol{\theta}) &= \mathrm{Poiss}(N|\mu_{\mathrm{tot}}) \\
&\quad \times \prod_i^N \left(\sum_j \frac{\mu_{b_j}}{\mu_{\mathrm{tot}}} f_{b_j}(E_i, \boldsymbol{\theta}) + \frac{\mu_s}{\mu_{\mathrm{tot}}} f_s(E_i, \boldsymbol{\theta}) \right) \\
&\quad \times \prod_m C_{\mu_m}(\mu_{b_m}) \times \prod_n C_{\theta_n}(\theta_n), \qquad (5.5) \\
\mu_{\mathrm{tot}} &\equiv \sum_j \mu_{b_j} + \mu_s,
\end{aligned}
$$

where μ_s and $\boldsymbol{\mu_b}$ are the expected numbers of signal and background events, respectively. Both $\boldsymbol{\mu_b}$ and $\boldsymbol{\theta}$ are nuisance parameters, where $\boldsymbol{\theta}$ includes shape parameters for the efficiency spectral uncertainty (see Fig. 5.4), as well as peak location uncertainties, specifically for ^{124}Xe (3 peaks), $^{83\mathrm{m}}$Kr, and $^{131\mathrm{m}}$Xe. Having largely subdominant event rates, the 3 peak locations from ^{125}I EC are fixed at their expected positions to save computation time. Index i runs over all observed events with the total number of N (=42251 events), and E_i corresponds to the energy of the ith event. f_b and f_s are the background and signal probability density functions, and index j runs over all the background components. C_μ and C_θ are constraints on the expected numbers of background events and the shape parameters. Index m runs over backgrounds including ^{85}Kr, solar neutrino, ^{136}Xe, $^{83\mathrm{m}}$Kr, ^{125}I, ^{133}Xe, and $^{131\mathrm{m}}$Xe, while index n is for all six shape parameters.

Due to time-dependent backgrounds, the SR1 data set was divided into two partitions: $\mathrm{SR1_a}$ consisting of events within 50 days following the end of neutron calibrations and $\mathrm{SR1_b}$ containing the rest, with effective live times of 55.8 and 171.2 days, respectively. Including this time information allows for better constraints on the time-independent backgrounds and improves sensitivity to bosonic DM, especially as the time-dependent background from ^{133}Xe impacts a large fraction of its search region. The full likelihood is then given by

$$\mathcal{L} = \mathcal{L}_\mathrm{a} \times \mathcal{L}_\mathrm{b}, \tag{5.6}$$

where $\mathcal{L}_\mathrm{a}$ and $\mathcal{L}_\mathrm{b}$ are evaluated using Eq. (5.5) in each partition. Nuisance parameters that do not change with time, along with all of the signal parameters, are shared between the two partitions. The constant nuisance parameters are:

- the efficiency parameter, which is dominated by detection efficiency and does not change with time.
- The ^{214}Pb component, which was determined to have a constant rate in time using detailed studies of the α-decays of the ^{222}Rn and ^{218}Po as well as the coincidence signature of ^{214}Bi and ^{214}Po.
- The solar neutrino rate, which would vary by ~3 % between the two partitions on account of Earth's orbit around the Sun. This is ignored due to the subdominant contribution from this source.
- The decay rates of the intrinsic xenon isotopes ^{136}Xe and ^{124}Xe, as well as the Compton continuum from materials.

The remaining parameters all display time dependencies that are modeled in the two partitions.

The test statistic used for the inference is defined as

$$q(\mu_s) = -2\ln\frac{\mathcal{L}(\mu_s, \hat{\hat{\boldsymbol{\mu}}}_b, \hat{\hat{\boldsymbol{\theta}}})}{\mathcal{L}(\hat{\mu}_s, \hat{\boldsymbol{\mu}}_b, \hat{\boldsymbol{\theta}})}, \tag{5.7}$$

where $(\hat{\mu}_s, \hat{\boldsymbol{\mu}}_b, \hat{\boldsymbol{\theta}})$ is the overall set of signal and nuisance parameters that maximizes $\mathcal{L}$, while $\mathcal{L}(\mu_s, \hat{\hat{\boldsymbol{\mu}}}_b, \hat{\hat{\boldsymbol{\theta}}})$ is the maximized $\mathcal{L}$ by profiling nuisance parameters with a specified signal parameter μ_s. The statistical significance of a potential signal is determined by $q(0)$. For the neutrino magnetic moment and bosonic dark matter searches, a modified Feldman-Cousins method in Ref. [159] was adopted in order to derive 90% C.L. bounds with the right coverage. An interval instead of an upper limit is reported if the global significance exceeds $3\,\sigma$. For bosonic DM this corresponds to $4\,\sigma$ local significance on account of the look-elsewhere effect, which is not present for the neutrino magnetic moment search. The $3\,\sigma$ significance threshold only serves as the transition point between reporting one- and two-sided intervals, and was decided prior to the analysis to ensure correct coverage. A two-sided interval does not necessarily indicate a discovery, which in particle physics generally demands a 5σ significance and absence of compelling alternate explanations.

Since the solar axion search is done in the space of g_{ae}, $g_{\mathrm{ae}}g_{\mathrm{a}\gamma}$, and $g_{\mathrm{ae}}g_{\mathrm{an}}^{\mathrm{eff}}$, we extend its statistical analysis to three dimensions. For this search, we use a standard profile likelihood construction where the true 90th-percentile of the test statistic (Eq. (5.7)) was evaluated at several points on a three-dimensional grid and interpolated between points to define a 3D ‘critical’ volume of true 90-percent threshold values. By construction, the intersection of this volume with the test statistic $q(g_{\mathrm{ae}}, g_{\mathrm{ae}}g_{\mathrm{a}\gamma}, g_{\mathrm{ae}}g_{\mathrm{an}})$ defines a three-dimensional 90% C.L. volume in the space of the three axion parameters. In Sec. 5.5.3 we report the two-dimensional projections of this volume, found by profiling over the third respective signal component.

5.5 Results

5.5.1 Excess at Low Energies

The background model B_0 (see Sec. 5.3) was fit to the data by maximizing the likelihood defined in Eq. (5.6). The expected and fitted results are consistent over the ROI, which is summarized in Tab. 5.1. The best fit of B_0 in SR1 is illustrated in Fig. 5.9, with the best fits in $\mathrm{SR1_a}$ and $\mathrm{SR1_b}$ shown in Fig. 5.10 (top) and (bottom), respectively. The fitted background rate in (1, 30) keV without efficiency loss is (76±2) events/(t·y·keV), which is the lowest background rate ever achieved in a DM direct detection experiment.

Table 5.1: Summary of components in the background model B_0 with expected and fitted number of events in the 0.65 tonne-year exposure of SR1. Both numbers are within the (1, 210) keV ROI and with efficiency loss. See Sec. 5.3 for details on the various components.

No.	Component	Expected Events	Fitted Events
i	^{214}Pb	(3450, 8530)	7480 ± 160
ii	^{85}Kr	890 ± 150	773 ± 80
iii	Materials	323 (fixed)	323 (fixed)
iv	^{136}Xe	2120 ± 210	2150 ± 120
v	Solar neutrino	220.7 ± 6.6	220.8 ± 4.7
vi	^{133}Xe	3900 ± 410	4009 ± 85
vii	$^{131\mathrm{m}}$Xe	23760 ± 640	24270 ± 150
viii	^{125}I (K)	79 ± 33	67 ± 12
	^{125}I (L)	15.3 ± 6.5	13.1 ± 2.3
	^{125}I (M)	3.4 ± 1.5	2.94 ± 0.50
ix	$^{83\mathrm{m}}$Kr	2500 ± 250	2671 ± 53
x	^{124}Xe (KK)	125 ± 50	113 ± 24
	^{124}Xe (KL)	38 ± 15	34.0 ± 7.3
	^{124}Xe (LL)	2.8 ± 1.1	2.56 ± 0.55

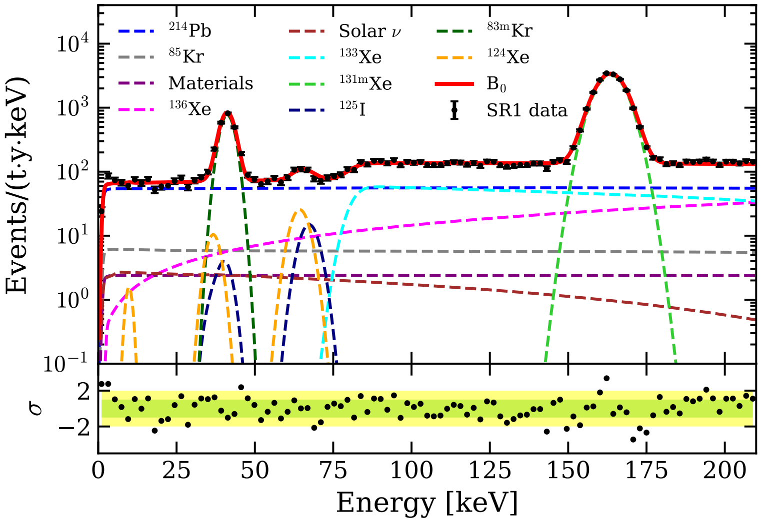

Figure 5.9: Fit to the SR1 data set using the likelihood framework described in Sec. 5.4 and the background model B_0 in Sec. 5.3. The plot shows the entire SR1 spectrum, while the best fit in each partition is shown in Fig. 5.10. The light green (yellow) band indicates the 1-σ (2-σ) residuals. The fit results are listed in Tab. 5.1. Adapted from Ref. [134].

When compared to the background model B_0, the data display an excess at low energies, as shown in Fig. 5.11. The excess departs slightly from the background model near 7 keV, rises with decreasing energy with a peak near 2–3 keV, and then subsides to within $\pm 1\,\sigma$ of the background model near 1–2 keV. Within this reference region of 1–7 keV, there are 285 events observed in the data compared to an expected (232 ± 15) events from the background-only fit, a $3.3\,\sigma$ Poissonian fluctuation. Events in this energy region are uniformly distributed in the 1T FV. The temporal distribution of these events and a more detailed discussion on spatial dependence can be found in Sec. 5.6.6.

Two low-energy backgrounds that might in principle be present in trace amounts were considered. First, low-energy X-rays from ^{127}Xe EC, as seen in Refs. [109, 110], are ruled out for a number of reasons. ^{127}Xe is produced from cosmogenic activation at sea level; given the short half-life of 36.4 days and the fact that the

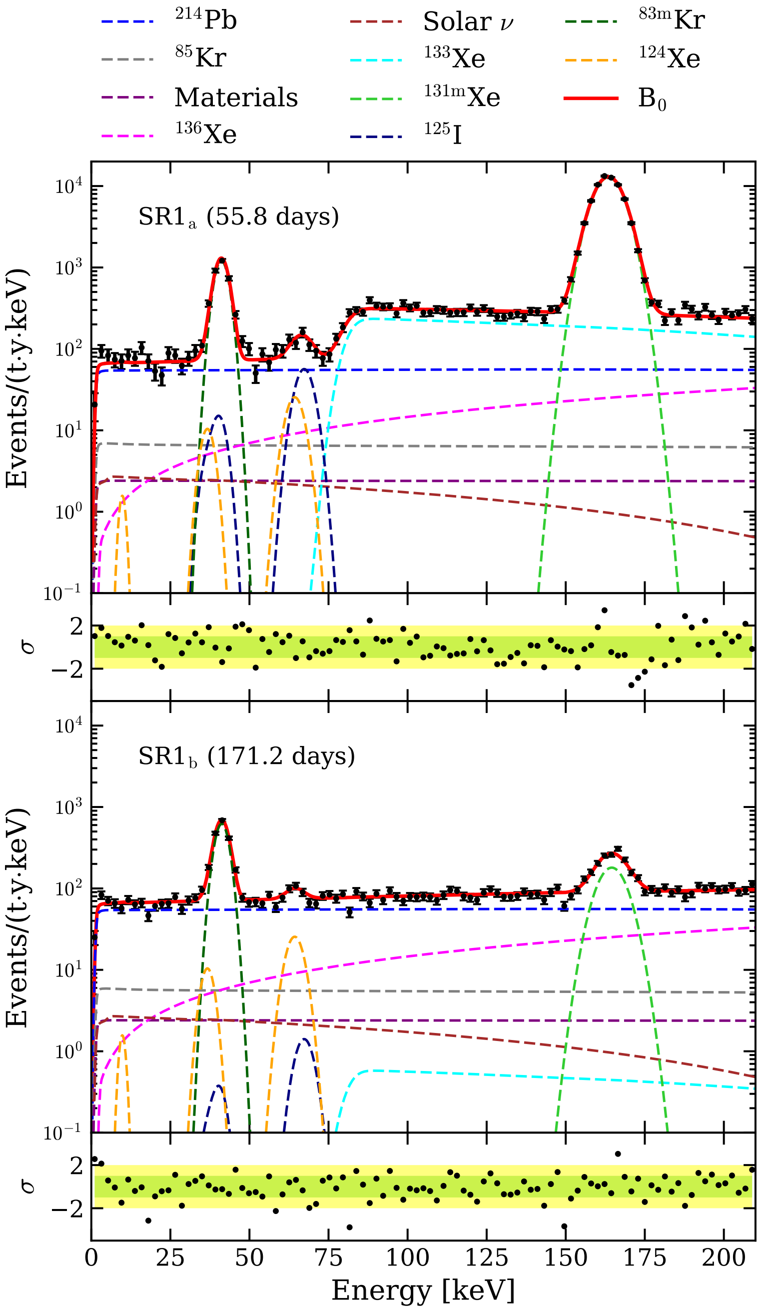

Figure 5.10: Fit to the SR1 data set using the likelihood framework described in Sec. 5.4 and the background model B_0 in Sec. 5.3. The top (bottom) panel shows SR1$_\mathrm{a}$ (SR1$_\mathrm{b}$), which contains more (less) neutron-activated backgrounds. SR1$_\mathrm{a}$ and SR1$_\mathrm{b}$ are fit simultaneously. The sum of the two spectra is illustrated in Fig. 5.9. The light green (yellow) band indicates the 1-σ (2-σ) residuals. The summed fit results are listed in Tab. 5.1. Figure adapted from Ref. [134].

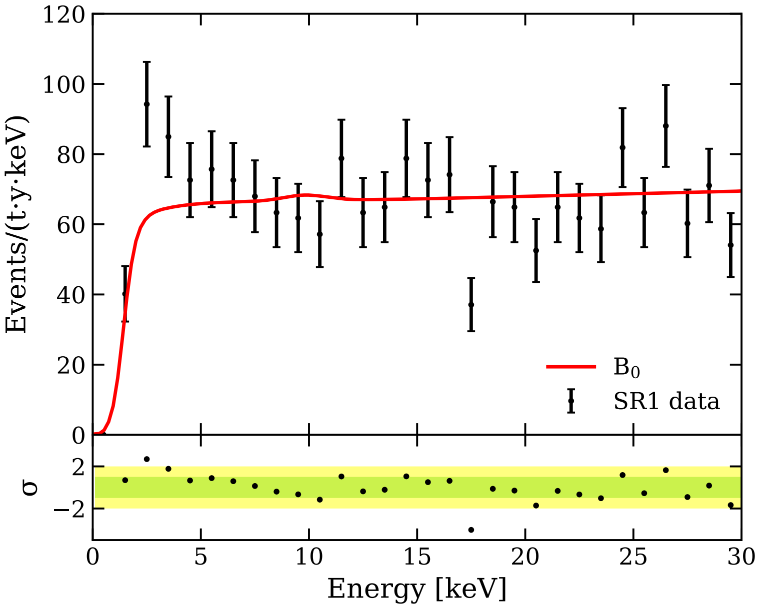

Figure 5.11: A zoomed-in and re-binned version of Fig. 5.9, where the data display an excess over the background model B_0. Figure from Ref. [134].

xenon gas was underground for $\mathcal{O}$(years) before the operation of XENON1T, ^{127}Xe would have decayed to a negligible level. Indeed, high-energy γs that accompany these X-rays were not observed, and with their $\mathcal{O}$(cm) mean free path in LXe they could not have left the $\mathcal{O}$(m)-sized TPC undetected. For these reasons, we conclude that ^{127}Xe was no longer present during SR1.

Another potential background is ^{37}Ar, which decays via EC to the ground state of ^{37}Cl, yielding a 2.82 keV peak with a BR of 90% [160]. It was considered by the LUX collaboration as a background to explain a possible excess rate at ~3 keV in their data [161]. Its ingress was hypothesized to come from either from an initial amount in the xenon gas or from an air leak during operations; however, no definitive conclusion was drawn based on measurements of both the leakage rate and the ^{37}Ar concentration in air at the experimental site [162]. We consider the two aforementioned possibilities for the introduction of ^{37}Ar into the xenon target and place quantitative constraints on each source.

^{37}Ar has a half-life of 35.0 days [160] and a typical abundance in $^{\mathrm{nat}}$Ar of $\sim 10^{-20}$ mol/mol [163]. Given an initial measured $^{\mathrm{nat}}$Ar concentration of < 5 ppm in the xenon inventory [164], ^{37}Ar decayed to a negligible level, < 1 events/(t·y), by the start of the XENON1T commissioning phase (> 400 days). As with krypton, argon is not removed by the getter in the purification system, although it is removed by online ^{85}Kr distillation (Sec. 5.3.2.3). This further suppresses its presence prior to SR1. These factors conclusively rule out the presence of ^{37}Ar from its initial concentration in the xenon inventory.

With respect to an ^{37}Ar component from a constant air leak, the similarities between krypton and argon noble gases allow us to use $^{\mathrm{nat}}$Kr to constrain the concentration of ^{37}Ar in the detector. The natural krypton was observed to increase by <1 ppt/year in the LXe using the periodical rare gas mass spectrometry (RMGS) measurements [148]; with the krypton concentration in the air [165], the air leak rate is estimated to be < 0.9 L/year in SR1, accounting for the different volatility of krypton in LXe and GXe [147]. We make a conservative assumption that the $^{\mathrm{nat}}$Kr increase is due entirely to a leak (neglecting emanation).

Table 5.2: Key quantities for the estimation of ^{37}Ar rate due to a constant leak.

Quantity	$^{\mathrm{nat}}$Kr	^{37}Ar
Viscosity at 25 °C [Pa·s]	25.5×10^{-6} [166]	22.8×10^{-6} [166]
Concentration in the air	1.14×10^{-6} [165]	$< 5\,\mathrm{mBq/m^3}$
Relative volatility in GXe over LXe	60 [147]	50 [147]

The air inside the experimental hall at LNGS, supplied from outside of the laboratory and fully exchanged within 2.5 hours, has an ^{37}Ar concentration of < 3.2 mBq/m^3, as determined from measurements taken in July 2020 following the methods in Refs. [167, 168]. A robust upper limit of 5 mBq/m^3 for the ^{37}Ar equilibrium concentration is set as the constraint to account for possible seasonal variations [169, 170]. The ^{37}Ar rate estimation further considers the viscosity difference between krypton and argon [166] and the argon volatility difference in LXe and GXe [147]; assuming that ^{37}Ar reached an equilibrium activity by the start of SR1, the ^{37}Ar rate is expected to be at most 5.2 events/(t·y) due to a constant leak. The key quantities for the rate estimation, such as the viscosity, relative volatility, and the concentration in the air, are listed in Tab. 5.2.[6] To explain the excess in XENON1T, the ^{37}Ar rate is required to be $\sim$ 65 events/(t·y), implying that the deduced upper limit is a factor of 13 too low to account for the excess. This conservative constraint on its presence in SR1 therefore excludes ^{37}Ar from a constant air leak as an explanation for the excess.

The time dependence of a potential ^{37}Ar background is discussed further in Sec. 5.6.6; however no clear trend is observed due to low statistics, and any temporal fluctuations are still constrained by the measured krypton concentrations throughout SR1. Given its short half-life, low measured concentration, and strong constraints from the leak hypothesis, we conclude that ^{37}Ar cannot make up the excess, although it may be present in the detector at a negligible level.

An additional background that was never observed in the two-phase LXe TPC as a natural source was considered: the β emission of tritium,[7] which has a Q-value of 18.6 keV and a half-life of 12.3 years [172]. Tritium may be introduced from predominantly two sources: cosmogenic activation of xenon during above-ground exposure [173] and emanation of tritiated water (HTO) and hydrogen (HT)

---

[6] One may find that the relative volatility of krypton in GXe and LXe is taken as 60, a factor of 6 larger than the nominal value of $\sim$ 10. This value comes from a fit to model the krypton evolution trend in XENON1T, which is supposed to be more reliable than a single theoretical distillation stage as it accounts for more reality factors, such as the additional bottle filling after distillation and several steps of filling and recuperation during the commission that could introduce residual krypton [147].

[7] Tritium in the form of tritiated methane has been used for calibration of LXe TPCs [24, 70, 171] including XENON100, but was not used as a calibration source in XENON1T. Following the XENON100 tritium calibration, neither the xenon gas nor the materials that came into contact with the tritiated methane were used in XENON1T.

from detector materials due to its cosmogenic and anthropogenic abundance. In contrast to ^{127}Xe and ^{37}Ar, the tritium hypothesis cannot be ruled out. In Sec. 5.5.2 we consider several possible mechanisms for the introduction of tritium into the detector and the uncertainties involved in its production and reduction processes in an attempt to estimate its concentration.

5.5.2 Tritium Hypothesis

In order to determine the hypothetical concentration of tritium required to account for the excess, we search for a ^{3}H "signal" on top of the background model B_0. When compared to B_0, the tritium hypothesis is favored at $3.2\,\sigma$ and the fitted rate is (159 ± 51) events/(t·y) (68% C.L.), which would correspond to a ^{3}H/Xe concentration of $(6.2 \pm 2.0) \times 10^{-25}$ mol/mol. As tritium is expected to be removed by the xenon purification system, this concentration would correspond to an equilibrium value between emanation and removal. The spectral fits under this hypothesis are illustrated in Fig. 5.12.

Due to its minute possible concentration, long half-life with respect to the SR1 exposure, and the fact that it decays through a single channel, we are unable to confirm the presence of tritium from SR1 data directly. We therefore try to infer its concentration from both initial conditions and detector performance parameters.

A tritium background component from cosmogenic activation of target materials has been observed in several dark matter experiments at rates compatible with predictions [174], although it has never before been detected in xenon. From exposure to cosmic rays during above-ground storage of xenon, we estimate a conservative upper limit on the initial ^{3}H/Xe concentration of $< 4 \times 10^{-20}$ mol/mol, based on GEANT4 activation rates [173] and assuming saturation activity. At this stage, tritium will predominantly take the form of HTO, given the measured ppm

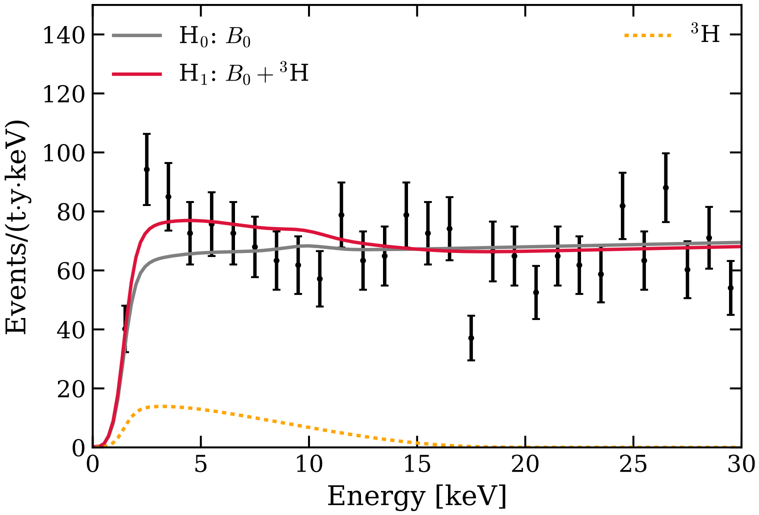

Figure 5.12: Hypothesis test for tritium. The red and gray curves are the best-fits under alternate and null hypotheses, respectively. The tritium component under alternate hypothesis is denoted by the orange dashed line. Figure adapted from Ref. [134].

water impurities in the xenon gas and equilibrium conditions [164, 175]. Through xenon gas handling prior to filling the detector (i.e., condensation of H_2O/HTO on the walls of the cooled xenon-storage vessel) and purification via a high-efficiency getter with a hydrogen removal unit [56, 176], we expect the concentration to be reduced to $< 10^{-27}$ mol/mol, thus reaching negligible levels with respect to the observed excess.

Tritium may also be introduced as HTO and HT via their respective atmospheric abundances. Water and hydrogen, and therefore tritium, may be stored inside materials, such as the TPC reflectors and the stainless steel of the cryostat. This type of source is expected to emanate from detector and subsystem materials at a rate in equilibrium with its removal via getter purification. Tritium can be found in water at a concentration of $(5 - 10) \times 10^{-18}$ atoms of ^{3}H for each atom of hydrogen in H_2O [177–179]. Here we assume the same abundance of ^{3}H in atmospheric H_2 as for water.[8] Using the best-fit rate of tritium and the HTO atmospheric abundance, a combined (H_2O + H_2) impurity concentration of 30–60 ppbin the LXe target would be required to make up the excess. Since water impurities affect optical transparency, the high light yield in SR1 indicates an $\mathcal{O}(1)$-ppb H_2O concentration [77, 182], thus implying a maximum contribution from HTO to the ^{3}H/Xe concentration of $\sim 1 \times 10^{-26}$ mol/mol. With respect to H_2, we currently have no direct or indirect measurements of its concentration in the detector. Instead, we consider that O_2-equivalent, electronegative impurities must reach sub-ppb levels in SR1, given the achieved electron lifetime of $\sim 650\,\mu$s (at 81 V/cm) [23, 183]. Thus for tritium to make up the excess requires a factor ~ 100 higher H_2 concentration than that of electronegative impurities. Under the above assumptions, tritium from atmospheric abundance appears to be an unlikely explanation for the excess. However, we do not currently have measurements of the equilibrium H_2 emanation rate in XENON1T, and thus the HT concentration cannot be sufficiently quantified.

In conclusion, possible tritium contributions from cosmogenic activation or from HTO in SR1 appear too small to account for the excess, while it is not possible to infer the concentration of HT. In addition, various factors contribute further to the uncertainty in estimating a tritium concentration within a LXe environment, such as its unknown solubility and diffusion properties, as well as the possibility that it may form molecules other than HT and HTO. Since the information and measurements necessary to quantify the tritium concentration are not available, we can neither confirm nor exclude it as a background component. Therefore, we report results using the background model B_0, and then summarize how our results

---

[8] Although geographical and temporal HT abundances in the atmosphere vary due to anthropogenic activities, HT that reaches the Earth's surface undergoes exchange to HTO within 5 hours [180, 181].

would change if tritium were included as an unconstrained background component. All reported constraints are placed with the validated background model B_0 (i.e., without tritium).

5.5.3 Solar Axions

We search for ABC, ^{57}Fe, and Primakoff axions simultaneously. Under this signal model, B_0 is rejected at $3.4\,\sigma$, a value determined using toy MC methods to account for the three parameters of interest in the alternative hypothesis, as shown in Fig. 5.13. A comparison of the best fits under the alternative hypothesis ($B_0 + \text{axion}$) and null hypothesis (B_0) can be found in Fig. 5.14.

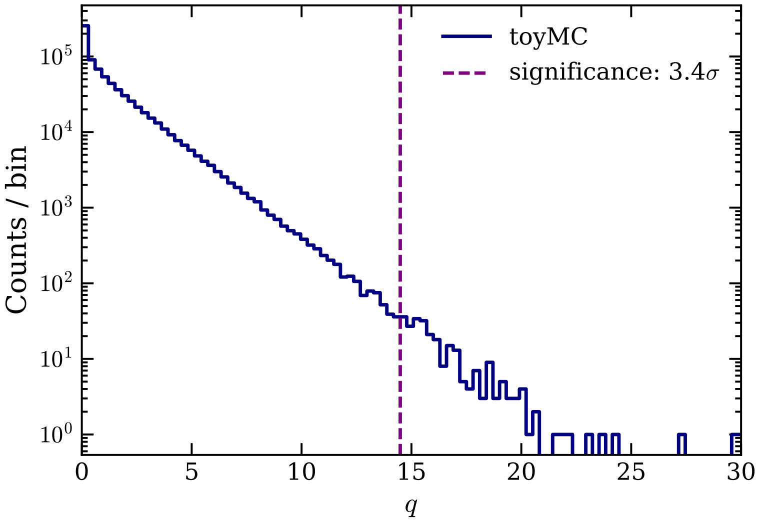

Figure 5.13: Significance of the solar axion hypothesis. The blue curve is the null distribution of log-likelihood ratio q of solar axion hypothesis fit to simulated data from toyMC simulations using background model B_0. The purple dashed line represents the log-likelihood ratio that solar axion hypothesis is favored over B_0 in the data, which gives a significance of 3.4σ when compared to the null distribution. A total of 8.2×10^5 toyMCs were simulated to obtain the null distribution.

A three-dimensional confidence volume (90% C.L.) was calculated in the space

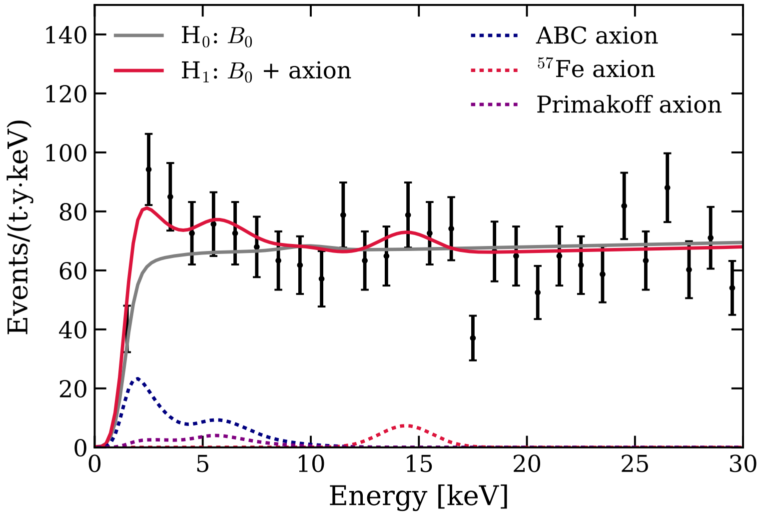

Figure 5.14: Hypothesis test for solar axions. The red and gray curves are the best-fits under alternate and null hypotheses, respectively. Each component of solar axion under alternate hypothesis is denoted with corresponding colored dashed line. Figure adapted from Ref. [134].

of g_{ae} vs. $g_{\mathrm{ae}}g_{\mathrm{a\gamma}}$ vs. $g_{\mathrm{ae}}g_{\mathrm{an}}^{\mathrm{eff}}$. This volume is inscribed in the cuboid given by

$$\begin{aligned} g_{\mathrm{ae}} &< 3.8 \times 10^{-12} \\ g_{\mathrm{ae}}g_{\mathrm{an}}^{\mathrm{eff}} &< 4.8 \times 10^{-18} \\ g_{\mathrm{ae}}g_{\mathrm{a\gamma}} &< 7.7 \times 10^{-22}\ \mathrm{GeV}^{-1}. \end{aligned}$$

While easy to visualize, this cuboid is more conservative (it displays over-coverage) than the 3D confidence volume it encloses and does not describe the correlations between the parameters. The correlation information can be found in Fig. 5.15 and 5.16, which shows the 2D projections of the surface. For the ABC–Primakoff and ABC–^{57}Fe projections (Fig. 5.15 and Fig. 5.16 (top), respectively), g_{ae} can be easily factored out of the y-axis to plot $g_{\mathrm{a\gamma}}$ vs. g_{ae} and $g_{\mathrm{an}}^{\mathrm{eff}}$ vs. g_{ae}. This is not as straightforward for the ^{57}Fe-Primakoff projection, shown in Fig. 5.16 (bottom). Also shown in these two plots are constraints from other axion searches [109, 110, 184–188] as well as predicted values from the benchmark QCD models DFSZ and KSVZ.

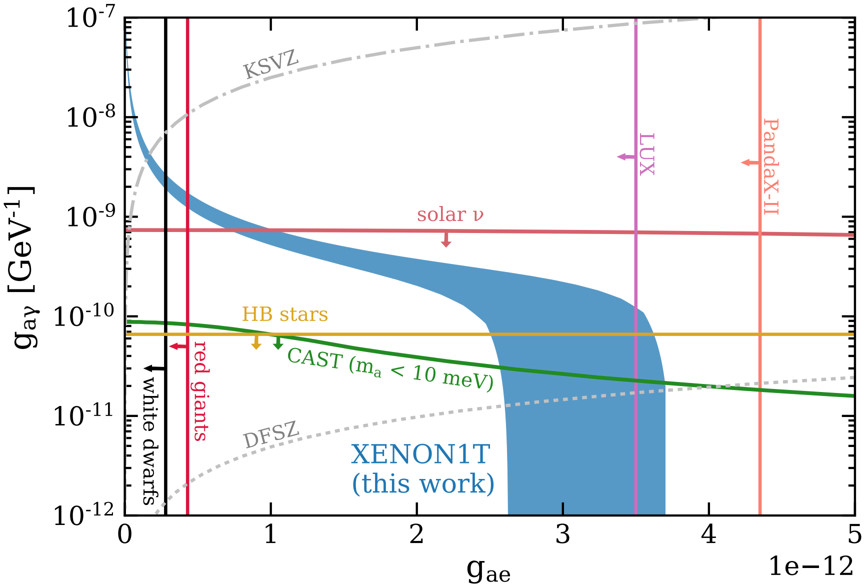

Figure 5.15: Constraints on the axion-electron g_{ae} and axion-photon $g_{\mathrm{a}\gamma}$ couplings from a search for solar axions. The shaded blue regions show the two-dimensional projections of the three-dimensional confidence surface (90% C.L.) of this work, and hold for $m_{\mathrm{a}} < 100\,\mathrm{eV/c^2}$. See text for more details on the three individual projections. It include constraints (90% C.L.) from other axion searches, with arrows denoting allowed regions, and the predicted values from the benchmark QCD axion models DFSZ and KSVZ. Figure adapted from Ref. [134].

Fig. 5.15 is extracted from the projection onto the ABC–Primakoff plane. Since the ABC and Primakoff components are both low-energy signals, the 90% confidence region is anti-correlated in this space and — due to the presence of the low-energy excess — suggests either a non-zero ABC component or non-zero Primakoff component. Since our result gives no absolute lower bound on g_{ae}, the limit on the product $g_{\mathrm{ae}}g_{\mathrm{a}\gamma}$ cannot be converted into a limit on $g_{\mathrm{a}\gamma}$ on its own; i.e., with $g_{\mathrm{ae}}g_{\mathrm{a}\gamma}$=$7.6 \times 10^{-22}\,\mathrm{GeV}^{-1}$, $g_{\mathrm{a}\gamma} \to \infty$ as $g_{\mathrm{ae}} \to 0$, as shown in Fig. 5.15.

Fig. 5.16 (top) is taken from the projection onto the ABC–^{57}Fe plane. Unlike the ABC-Primakoff case, these two signals are not degenerate; however, they still

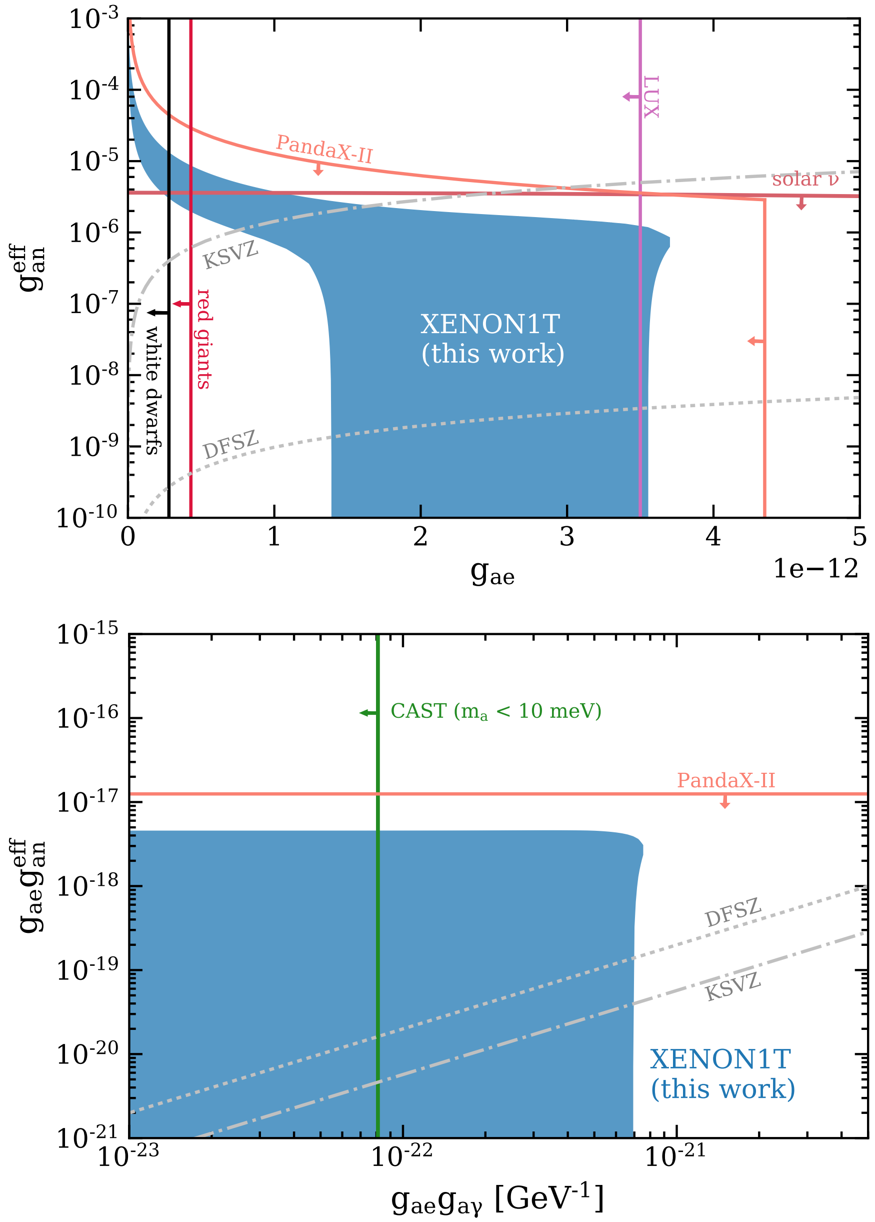

Figure 5.16: Constraints on the axion-electron g_{ae}, axion-photon $g_{\mathrm{a}\gamma}$, and effective axion-nucleon $g_{\mathrm{an}}^{\mathrm{eff}}$ couplings from a search for solar axions. The shaded blue regions show the two-dimensional projections of the three-dimensional confidence surface (90% C.L.) of this work, and hold for $m_{\mathrm{a}} < 100\,\mathrm{eV}/c^2$. See text for more details on the three individual projections. All three plots include constraints (90% C.L.) from other axion searches, with arrows denoting allowed regions, and the predicted values from the benchmark QCD axion models DFSZ and KSVZ. Figure adapted from Ref. [134].

display anti-correlated behavior. The reason for this is that the test statistic q (Eq. (5.7)) is relatively large with small g_{ae}, meaning small changes in the ^{57}Fe rate about the best-fit make q cross the 90% threshold value and thus be excluded by our 90% confidence volume. There is no statistical significance ($< 1\,\sigma$) for the presence of a 14.4 keV peak from ^{57}Fe axions.

Lastly, Fig. 5.16 (bottom) shows the projection onto the Primakoff-^{57}Fe plane, where no correlation is observed. The Primakoff and ^{57}Fe components are both allowed to be absent as long as there is a non-zero ABC component. This means that, of the three axion signals considered, the ABC component is the most consistent with the observed excess.

The three projections can be used to reconstruct the 3D 90% confidence volume for g_{ae}, $g_{\mathrm{ae}}g_{\mathrm{a\gamma}}$, and $g_{\mathrm{ae}}g_{\mathrm{an}}^{\mathrm{eff}}$. Due to the presence of an excess at low energy, this volume would suggest either a non-zero ABC component or a non-zero Primakoff component. However, the coupling values needed to explain this excess are in strong tension with stellar cooling constraints [186–190], with the exception of a minute region in the 3D coupling space which corresponds to small g_{ae} and large $g_{\mathrm{an}}^{\mathrm{eff}}$, $g_{\mathrm{a\gamma}}$. The CAST constraints [184] as shown are valid for axion masses below $10\,\mathrm{meV}/c^2$ while those from XENON1T and similar experiments hold for all axion masses up to $\sim 100\,\mathrm{eV}/c^2$ (Sec. 2.3.2). For an axion mass below $10\,\mathrm{meV}/c^2$, the CAST result prefers the region with large g_{ae} and small $g_{\mathrm{a\gamma}}$; however, there is no tension between the CAST result and this result for higher axion masses ($m_a > 250\ \mathrm{meV}/c^2$) due to the limited sensitivity of CAST for high-mass axions.[9]

As described above, we cannot exclude tritium as an explanation for this excess. Thus, we report on an additional statistical test, where an unconstrained tritium component was added to the background model B_0 and profiled over alongside

---

[9] The conversion probability from an axion to a photon is suppressed with a large mass, see Eq. (2.8).

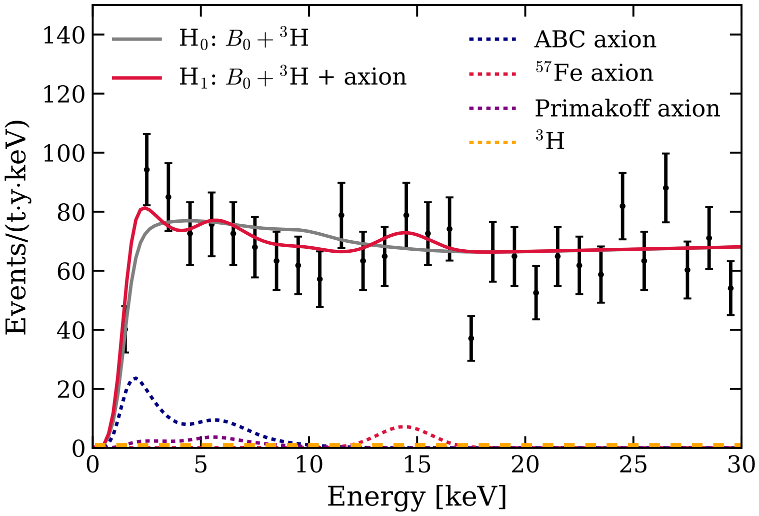

Figure 5.17: Hypothesis test for solar axions, with an unconstrained tritium component added in both alternate and null hypotheses. The red and gray curves are the best-fits under alternate and null hypotheses, respectively. Each component of solar axion as well as tritium under alternate hypothesis is denoted with corresponding colored dashed line. Although the tritium component is unconstrained in the alternate hypothesis, its contribution is still zero, which indicates that solar axion is more favored than tritium by data. Figure adapted from Ref. [134].

the other nuisance parameters. In this case, the null hypothesis is the background model plus tritium ($B_0 + {}^3\mathrm{H}$) and the alternative includes the three axion signal components ($B_0 + {}^3\mathrm{H} + \mathrm{axion}$), where tritium is unconstrained in both cases. The solar axion signal is still preferred in this test, but its significance is reduced to 2.0σ. The fits for this analysis are shown in Fig. 5.17. The tritium component is negligible in the alternate best-fit, but its presence allows for a better fit under—and thus a reduced significance of rejecting—the null hypothesis.

5.6 Additional Checks and Discussion

5.6.1 Check on Science Run 2

We also checked data from SR2, an R&D science run that followed SR1, in an attempt to understand the observed excess. Many purification upgrades were implemented during SR2, including the replacement of the xenon circulation pumps with units that (1) are more powerful, leading to improved purification speed, and (2) have lower ^{222}Rn emanation, leading to a reduced ^{214}Pb background rate in the TPC [191, 192], which was further decreased by online radon distillation. The resulting increased purification speed and reduced background make SR2 useful to study the tritium hypothesis. If the excess were from tritium (or another non-noble contaminant), we would expect its rate to decrease due to the improved purification; on the other hand, the rate of the signal hypotheses would not change with purification speed.

While the SR2 purification upgrades allowed for an improved xenon purity and a reduced background level, the unavoidable interruption of recirculation for the upgrades also led to less stable detector conditions. Thus, in addition to a similar event selection process as SR1 in Sec. 5.1.2, we removed several periods of

SR2 for this analysis to ensure data quality. Periods where the electron lifetime changed rapidly due to tests of the purification system were removed to reduce uncertainty in the energy reconstruction. We also removed datasets during which a $^{83\mathrm{m}}$Kr source was left open for calibration. Data within 50 days of the end of neutron calibrations were also removed to reduce neutron-activated backgrounds and better constrain the background at low energies. After the other selections, this data would have only added ~ 10 days of live time; thus, for simplicity, it was removed rather than fit separately like the SR1 dataset. With these selections, the effective SR2 live time for this analysis is 24.4 days, with an average ER background reduction of ∼20% in (1, 30) keV as compared to SR1.

A profile likelihood analysis was then performed on SR2 with a similar background model as SR1, denoted as B_{SR2}. Since we are primarily interested in using this data set to test the tritium hypothesis, we focus on the tritium results.

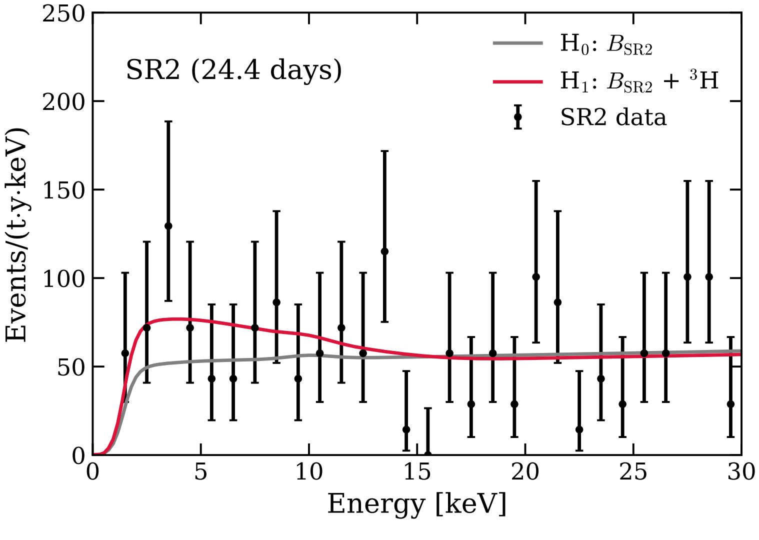

Figure 5.18: A fit to SR2 data if tritium is treated as a signal. The red (gray) line is the fit with (without) tritium in the background model. Figure from Ref. [134].

Similarly to SR1, we search for a tritium signal on top of the background model B_{SR2}, and find that the background-only hypothesis is slightly disfavored at

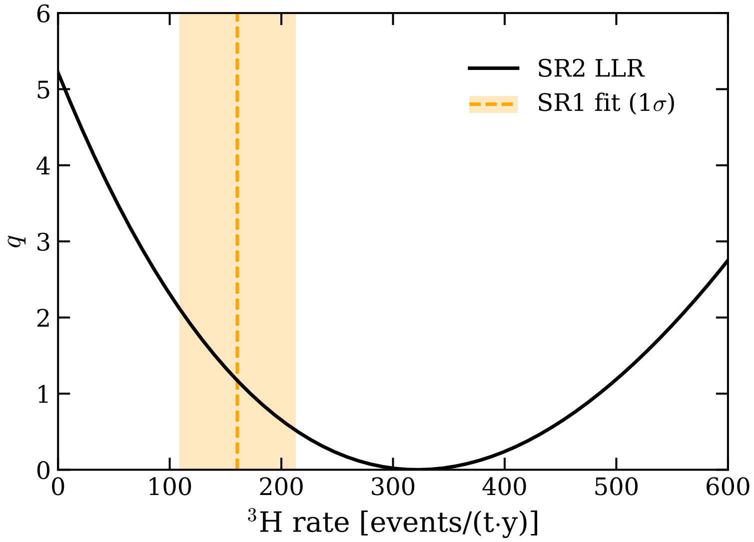

Figure 5.19: The log likelihood ratio curve for the tritium rate in SR2. The orange line and band indicate the best-fit and $1\,\sigma$ uncertainty for the tritium rate in SR1. The SR2 fit result is consistent with SR1, but with a large uncertainty due to limited statistics. Figure from Ref. [134].

$2.3\,\sigma$. The SR2 spectrum, along with the fits for the null (B_{SR2}) and alternative ($B_{\mathrm{SR2}} + {}^{3}\mathrm{H}$) hypotheses, can be found in Fig. 5.18. A log-likelihood ratio curve for the tritium component is given in Fig. 5.19, which shows that the fitted tritium rate is (320 ± 160) events/(t·y), higher than that from SR1 but consistent within uncertainties. The rate uncertainty in SR2 is much larger than that in SR1 due to limited statistics. The solar axion and magnetic moment hypotheses give similar results, with significances $\sim 2\,\sigma$ and best-fit values larger than, but consistent with, the respective SR1 fit results. Thus these SR2 studies are largely inconclusive.

5.6.2 Impact from β Spectral Shape

Since the dominant background is the β decay of ^{214}Pb, the β decay spectral shape uncertainty, especially that at low energies, can play a role in the low-energy excess. In addition, the β decay spectral of ^{85}Kr can also have an impact. The shape of these spectra, particularly at low energies, can be affected by atomic screening and exchange effects, as well as by nuclear structure [193, 194]. The β decays of ^{214}Pb and ^{85}Kr are first forbidden non-unique and first forbidden unique transitions, respectively; however spectra from the IAEA LiveChart (Nuclear Data Services database) [195] are based on calculations of allowed and forbidden unique transitions, neither of which includes exchange effects [196]. Likewise, models from GEANT4 [197] include only the screening effect; however, its implementation displays a non-physical discontinuity at low energies [196, 198]. For this work, we performed dedicated theoretical calculations to account for possible low-energy discrepancies from these effects in ^{214}Pb and ^{85}Kr spectra.[10] These calculations are described in detail in the appendix in Ref. [134]. The comparison of aforementioned spectra for ^{214}Pb are illustrated in Fig. 5.20. The data for the ground-state to ground-state β decay spectra of ^{214}Pb, ^{85}Kr, and ^{212}Pb, which is used in calibration (Sec. 3.3.1) and also involves the first forbidden non-unique transition, are available in Ref. [200] over the ROI.

Uncertainties in the theoretical background models were considered, particularly for the dominant ^{214}Pb component. More details can be found in the appendix in Ref. [134], but a brief summary is also given here. A steep rise in the spectrum at low energies could potentially be caused by exchange effects in β-decay emission; however, this component is accurate to within 1% and therefore negligible with respect to the observed excess. The remaining two components, namely the endpoint energy and nuclear structure, tend to shift the entire β distribution, rather than cause steep changes over a range of $\sim$ 10 keV. Conservatively, the combined uncertainty from these two components is +6% in the 1–10 keV region.

---

[10] Two recent studies [139, 199] on the β spectrum of ^{214}Pb were available after the work in Ref. [134]; in this thesis, we will limit our discussion to the β spectrum calculated in Ref. [134] only.

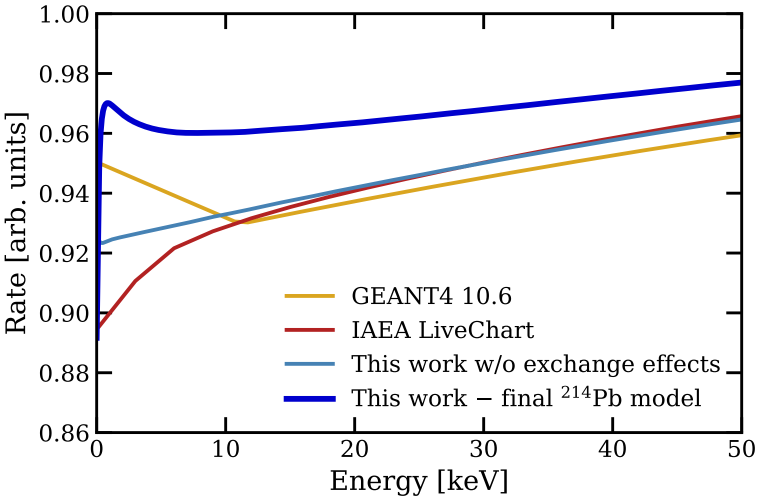

Figure 5.20: Low energy part of the β spectral shape of the ground-state to ground-state transition in ^{214}Pb decay. This first forbidden non-unique transition was calculated as allowed in every case but with different levels of approximations, as described in the text. The four spectra are normalized by area over the full energy range. Figure from Ref. [134].

In comparison, a +50% uncertainty at 2–3 keV on the calculated ^{214}Pb spectrum, as constrained by the higher energy component, would be needed to make up the excess. Therefore, we conclude that the β decay spectral shape of ^{214}Pb in low energies cannot explain the observed excess.

5.6.3 Efficiency Check with ^{220}Rn Calibration Data

The detection and selection efficiencies were verified using ^{220}Rn calibration data. The β decay of ^{212}Pb, a daughter of ^{220}Rn, was used to calibrate the ER response of the detector (Sec. 3.3.1), and thus allows us to validate the efficiency modeling with a high-statistics data set. Similarly to ^{214}Pb, the model for ^{212}Pb was calculated to account for atomic screening and exchange effects, as detailed in appendix in Ref. [134]. A fit to the ^{220}Rn data with this model and the efficiency parameter described in Sec. 5.4 is shown in Fig. 5.21 for a 1T FV, where

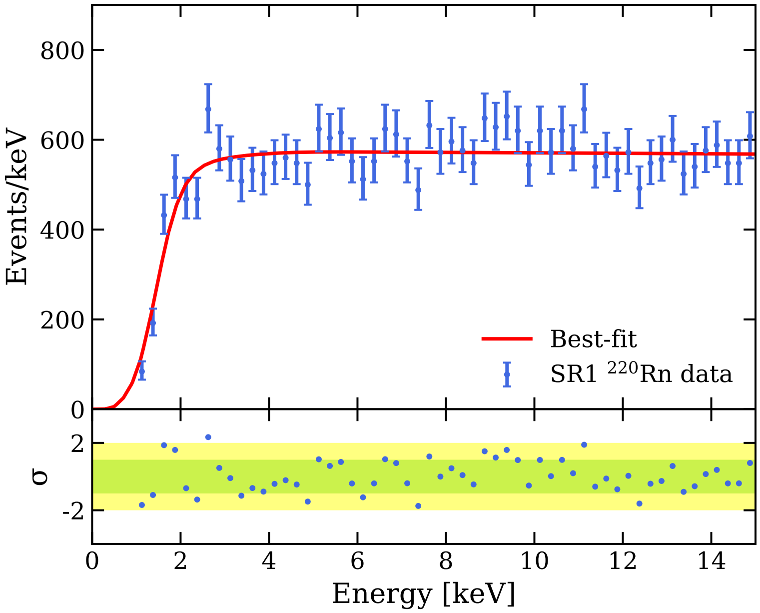

Figure 5.21: Fit to ^{220}Rn *calibration* data with a theoretical β-decay mode (see the appendix in Ref. [134]) and the efficiency nuisance parameter, using the same unbinned profile likelihood framework described in Sec. 5.4. This fit suggests that the efficiency shown in Fig. 5.4 describes well the expected spectrum from ^{214}Pb, the dominant background at low energies. Figure from Ref. [134].

good agreement is observed (p-value = 0.50). Consequently, we conclude that the efficiency used in this search is validated and cannot explain the excess.

5.6.4 Detection Threshold

The energy threshold (1 keV) and efficiency (along with uncertainty) are illustrated in Fig. 5.4. Since the total efficiency at the threshold is only ∼10%, it is motivated to validate the observed excess with thresholds of better efficiencies. Four different energy thresholds were chosen in this study, including 1.6, 2, 3, and 4 keV. The latter three were selected from even spacing, while the 1.6 keV threshold has ∼ 50% total efficiency. Efficiency at each energy can be found in Tab. 5.3. Three cases were tested: (1) solar axion, (2) tritium, and (3) solar axion vs. tritium. For simplicity, ABC solar axion will be used in lieu of the full three-component solar axion model.

Table 5.3: Total efficiencies, including detection and event selection efficiency, at several energies that were used as energy thresholds in this threshold study.

Energy [keV]	Efficiency
1	12%
1.6	52%
2	73%
3	85%
4	87%

The same background model and likelihood was used for each threshold. The results for solar axion and tritium hypotheses are shown in Tab. 5.4. The significance of solar axion increases with threhshold at 1.6 and 2 keV, no matter whether an unconstrained tritium is added in the background model. Tritium, on the other hand, decreases with a higher energy threshold.

The various hypothesis tests are also illustrated in Fig. 5.22. ABC axion fit

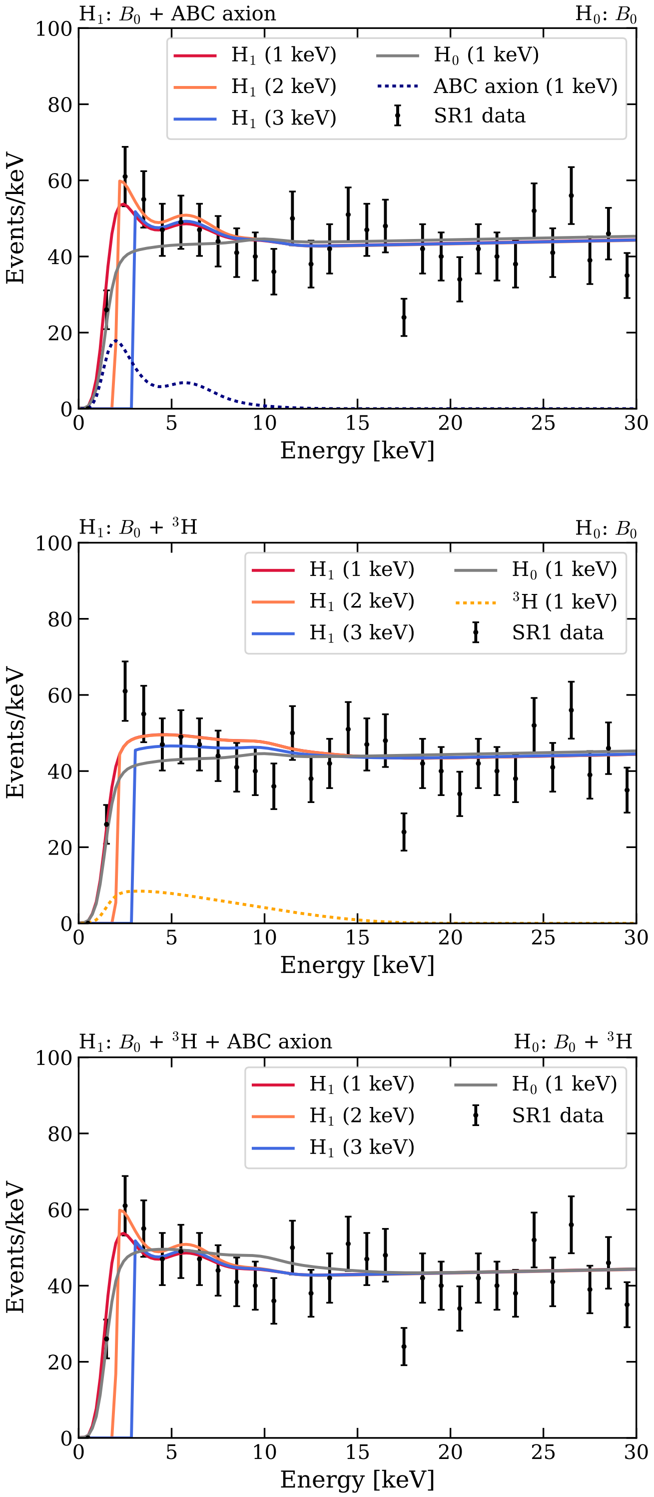

Figure 5.22: Fitting of different hypotheses under different energy thresholds indicated inside the parenthesis. Top: ABC axion. Middle: Tritium. Bottom: ABC axion vs. Tritium. See text for more details.

Table 5.4: Significances of solar axion and tritium hypotheses with different energy thresholds.

Energy threshold [keV]	ABC axion	ABC axion vs. ^{3}H	^{3}H
1	3.75	2.33	2.93
1.6	3.98	2.71	2.92
2	4.09	2.97	2.81
3	2.35	1.69	1.64
4	1.10	1.24	0.85

(Fig. 5.22 (top)) was partly constrained by (1, 2) keV bin, where data is about the same as fit. Without this bin, H_1 (coral) just shoots up with 2 keV as the energy threshold. Background-only fits are largely the same with all given thresholds, since it is mostly constrained by the whole ROI. When we use 3 keV as energy threshold, most of the excess is excluded and thus the significance begins to decrease. However, it is a bit different for tritium. Unlike ABC axion, tritium (Fig. 5.22 (middle)) has a relatively flat spectral shape and extends to 18 keV; thus, tritium fit with a 2 keV threshold (coral) does not tend to go higher even starting with the highest bin of (2, 3) keV. In addition, tritium fit with 1 keV threshold (crimson) is already higher than data around 10 keV, which further prevents the fit from being pulling higher with 2 keV threshold. When an unconstrained tritium is added to both null and alternate hypotheses (Fig. 5.22 (bottom)), the ABC axion component completely outperforms tritium, as the best-fit of tritium in the alternate hypothesis is zero, which holds for threshold up to 3 keV (3 keV included).[11] This is also good evidence that ABC axion is preferred than tritium. Thus, in this scenario, the

---

[11] One can find it by the fact that square of significance in the second column in Tab. 5.4 is the sum of squares of third and forth columns. This is because when T(^{3}H) contributes nothing in the alternate fit, the best-fit of (B_0+axion+T) is the same as (B_0+axion), i.e. the axion hypothesis, therefore the comparison of (B_0+axion+T) vs. (B_0+T) is equivalent to (B_0+axion) vs. (B_0+T); as the significance is computed assuming asymptotic distribution of the test statistic, the significance of axion vs. T is $\sqrt{q_{\text{axion}} - q_{\text{T}}}$ (q from Eq. (5.7)), whereas the significance of axion and T, σ_{axion} and σ_{T}, are calculated as $\sqrt{q_{\text{axion}}}$ and $\sqrt{q_{\text{T}}}$, respectively.

best-fit actually comes from axion best-fit while background-only fit comes from tritium best-fit; thus, we would expect an increase of significance at 2 keV energy threshold.

This study proves that the excess still exists with higher thresholds of better efficiencies, and that the solar axion hypothesis is always favored over tritium. The signal significances with an unconstrained tritium component in the background model even increase with higher threshold until a 3 keV threshold where most of the excess is gone.

5.6.5 S2-only Check

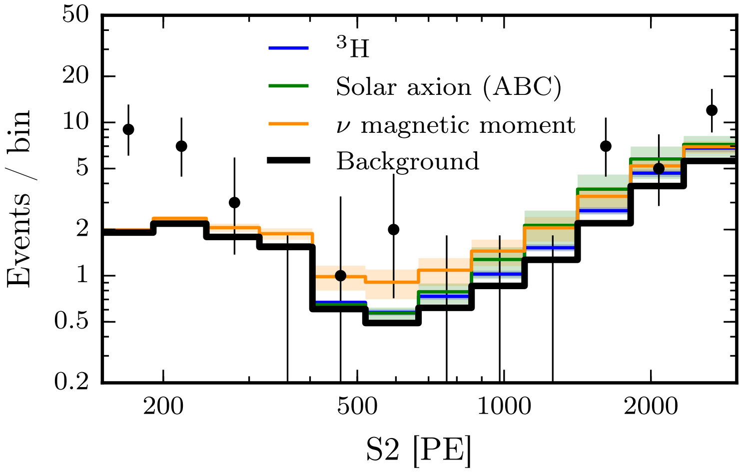

Figure 5.23: Using S2-only approach in [103] to probe the main hypotheses for the excess, including solar axion (ABC), tritium, and neutrino magnetic moment (Sec. 6.1). The balck line is the background model in S2-only approach [103]. The best-fits of ABC solar axion (green), tritium (blue), and neutrino magnetic moment (orange) from *the S1S2 analysis* are overlaid over the background to compare to with S2-only data (black dots) in XENON1T.

As mentioned in Sec. 4.2.1, S2-only approach has a lower threshold than this S1S2 analysis.[12] Therefore, it is beneficial to use S2-only to check the excess in

---

[12] S1S2 analysis refers to the utilization of both S1 and S2 signal, but not necessarily in ($S1$, $S2$) space.

the context of each main hypothesis; if the result of one hypothesis from S1S2 analysis contradicts with the upper limit placed by the S2-only approach, then this hypothesis can be ruled out.

Here we focus on three hypotheses: (1) ABC solar axion, (2) tritium, and (3) neutrino magnetic moment, which is detailed in Sec. 6.1. The ABC solar axion is used instead of the full solar axion model for simplicity. The best-fit of each signal in S1S2 analysis is overlaid over the background model in S2-only approach and is compared to the S2-only data, as shown in Fig. 5.23. From the plot, both ABC axion and tritium are apparently lower than the data, while the neutrino magnetic moment signal is lower by a smaller difference. For one, all the signals are lower than the data largely due to the fact that the background model in S2-only is quite conservative and thus S2-only search in XENON1T is designed as a limit-only analysis [103] (see Sec. 4.2.1); for another, neutrino magnetic moment has the least difference with the data as its spectrum rises the most rapidly towards low energies, making it the most sensitive signal for the S2-only approach.

The S2-only results are listed in Tab. 5.5. Each result is larger than the upper bound of result from S1S2 analysis, which is understandable as discussed above. Therefore, we conclude that all the hypotheses are compatible with S2-only approach.

Table 5.5: 90% C.L. upper limit for each hypothesis using S2-only method, including the avarage tritium activity over SR1, the axion-electron coupling g_{ae} inferred from ABC solar axion only, and the neutrino magnetic moment μ_ν. The S1S2 results are also listed for comparison; all the results there are of 90% C.L. except for ^{3}H that gives a 68% confidence region. μ_{B} is the Bohr magneton.

Method	^{3}H [events/(t·y)]	g_{ae}	μ_ν [μ_{B}]
S2-only	< 2256	$< 4.84 \times 10^{-12}$	$< 3.07 \times 10^{-11}$
S1S2	159 ± 51	$(2.75, 3.63) \times 10^{-12}$	$(1.4, 2.9) \times 10^{-11}$

5.6.6 Time and Spatial Dependence

The time dependence of events with energies in (1, 7) keV reference region in SR1 was investigated and found to be inconclusive. The event rate is slightly higher in the beginning of SR1, but the rate evolution is statistically consistent with (1) a constant rate, (2) a constant background rate (B_0) plus a subtle $\sim 7\,\%$ (peak-to-peak) rate modulation from the change in Earth-Sun distance, and (3) a constant background rate (B_0) plus an exponentially decreasing component with a fixed half-life of 35 days (^{37}Ar half-life) or 12.3 years (^{3}H half-life). As another test of time dependence, we split SR1 into three periods with equal exposure and fit the data in each period with the ABC solar axion signal model. Similarly to the (1,7) keV rate evolution, the best-fit signal rate is the highest in the first period of SR1, but is not statistically significant as the signal rate is consistent within uncertainty between the three periods. We therefore conclude that, due to limited statistics, at this time we cannot use time dependence to exclude any of the hypotheses discussed in this work. More detailed time dependence studies will be presented in a forthcoming publication [201].

The events of energies within the (1, 7) keV reference region are spatially uniform inside the 1T FV, as illustrated in Fig. 5.24. The distribution of excess-like events is also checked, which is visualized by using the solar axion hypothesis as an example. In this case, one event is deemed as excess-like if the relative probability of being solar axions is larger than 25%. Since the analysis is done in the space of reconstructed energy and solar axion signal is most prominent ~ 2 keV, most excess-like events under solar axion hypothesis are in fact around that energy. From the same plot, the excess-like events are also quite homogeneous in spatial distributions.

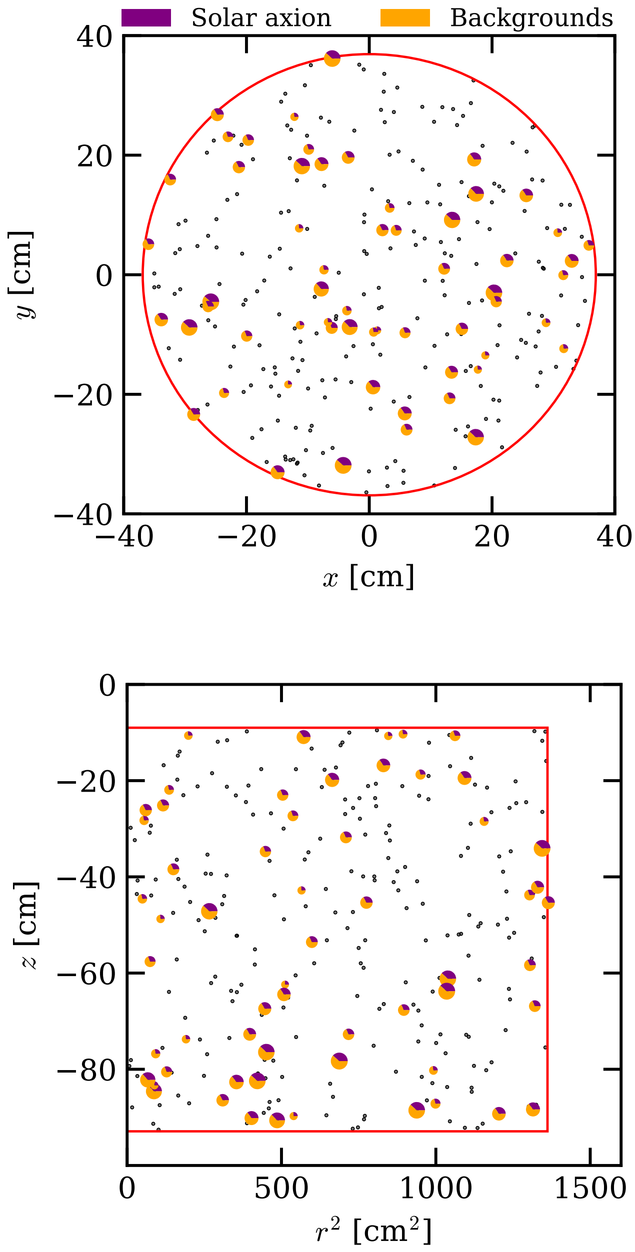

Figure 5.24: The spatial distribution of events with energies between 1–7 keV. Events with relative probabilities of being solar axions larger than 25% are indicated with pie charts, the sizes of which increase with the relative probabilities. The relative probabilities of being solar axions and backgrounds are represented by the orange and purple portion in pie charts, respectively. The 1T FV used in this search is denoted by the red curve.

The excess was also checked in different FVs. Two cylindrical FVs, 0.7T and 1.3T FV were selected for this check. The 0.7T FV and 1.3T FV have a radius of 30.3 cm and 41.3 cm, respectively, and share the same z definition as 1T cylindrical FV (-92.9 $< z <$ -9 cm). The significance of the excess in the (1, 7) keV reference region in each FV was calculated as a counting experiment to avoid model dependence. For the reference, the Poissonian significance of the excess in the reference region in 1T FV is 3.3σ (Sec. 5.5.1).

The background rate prediction is slightly dependent on the FV due to the spatial dependence of material and surface backgrounds. The material background rate decreases by $\sim 5.8\times10^{-6}$ events/(kg·day·keV) from 1T to 0.7T FV [77], leading to a difference of 5.5 events in (1, 7) keV. The surface background, on the other hand, only amounts to 0.4 events inside 1T FV thanks to the strict $S2$ cut ($S2$ $>$ 500 PE), thus the surface background difference between 0.7T and 1T FV can be safely neglected. By accounting for the rate change of materials background and scaling the rate of the rest backgrounds, a total of 150 events are expected in (1, 7) keV inside 0.7T FV. Since 192 events were observed, the significance of the excess in 0.7T FV was evaluated to be 3.3σ.

The predicted number of background events in 1.3T FV are subject to changes from both material and surface backgrounds. The material background increases by 5.3 events/(t·y·keV) from 1T to 1.3T FV [77]; the surface background increases by 5.9 events, i.e., 6.3 events in 1.3T, from the updated surface background template. Therefore, after scaling to 1.3T FV, we expect in total 323 events in the (1, 7) keV. With 382 events observed, the significance excess in the reference region is found to be 3.2σ. In a summary, the excess events are uniformly distributed and do not rely on a specific FV.

5.6.7 Tension with Astrophysical Constraints

If this excess were a hint of a solar axion, our result would suggest either (1) a non-zero rate of ABC axions or (2) a non-zero rate of both Primakoff and ^{57}Fe axions. If we interpret the excess as an ABC axion signal (i.e., take $g_{\mathrm{a}\gamma}$ and $g_{\mathrm{an}}^{\mathrm{eff}}$ to be zero), the required value of g_{ae} is smaller than that ruled out by other direct searches but has a clear discrepancy with constraints from indirect searches [202, 203], a brief introduction of which can be found in Sec. 1.2.2. These constraints are a factor of $\sim$ 5–10 lower than reported here, although subject to systematic uncertainties. It is noteworthy that some of these astrophysical analyses, while their constraints are still stronger than direct searches, do in fact suggest an additional source of cooling compatible with axions [189, 202]. If the indirect hints and the XENON1T excess were indeed explained by axions, the tension in g_{ae} could be relieved by underestimated systematic uncertainties in, e.g., stellar evolution theory [203] or white dwarf luminosity functions [204], or by a larger solar axion flux than that given in Ref. [18].

Although not considered in this work, XENON1T is also directly sensitive to the axion-photon coupling $g_{\mathrm{a}\gamma}$ via the inverse Primakoff effect, whereby a solar axion coherently scatters off the effective electric field of the xenon atom, thus producing an outgoing photon and inducing an electronic recoil. This detection channel was considered only recently for xenon-based detectors in Refs. [40, 41], which demonstrated that the tension of axion-photon coupling between the XENON1T excess and stellar constraints can be significantly reduced. Since Refs. [40, 41] were both after this work, this channel was not included.

5.7 Acknowledgements

Chapters 5, in part, is accepted for publication as it should appear soon in Phys. Rev. D, 2020, XENON Collaboration and Xavier Mougeot, Excess Electronic Recoil Events in XENON1T. The dissertation author is the primary investigator and one of the corresponding authors of this publication.

Chapter 6

Searches for Other New Physics and Rare Processes

This chapter describes searches for other physics and rate processes in ER events and is organized as follows. Sec. 6.1 discusses the search for an anomalously large neutrino magnetic moment, which is also a plausible explanation for the excess observed in Chap. 5. The search for bosonic DM is presented in Sec. 6.2, where the most favored mass is $2.3\,\mathrm{keV}/c^2$ and is also a viable interpretation for the excess. Lastly, Sec. 6.3 hunts for the leptophillic DM that has an axial-vector coupling with electrons; unlike the other two candidates of new physics, the leptophillic DM cannot explain the excess and thus an upper limit of the interaction strength is given as a function of DM mass. Sec. 6.4 describes the first observation of two-neutrino double electron capture of ^{124}Xe, which is a SM process but had remained elusive for years to detect due to the extremely long half-life.

6.1 Neutrino Magnetic Moment

In the SM, eutrinos are massless and therefore without a finite magnetic dipole moment. However, the observation of neutrino oscillation tells us that neutrinos have mass and the SM must be extended, implying a magnetic moment of $\mu_\nu \sim 10^{-20}\,\mu_\mathrm{B}$ [205–208], where μ_B is the Bohr magneton. Larger values of μ_ν have been considered theoretically and experimentally [208–210]. Interestingly, in addition to providing evidence of beyond-SM physics, the observation of a $\mu_\nu \gtrsim 10^{-15}\,\mu_\mathrm{B}$ would suggest that neutrinos are Majorana fermions [208]. Currently the most stringent direct detection limit is $\mu_\nu < 2.8 \times 10^{-11}\,\mu_\mathrm{B}$ from Borexino [210], and indirect constraints based on the cooling of globular cluster and white dwarfs are an order of magnitude stronger at $\sim 10^{-12}\,\mu_\mathrm{B}$ [203, 211, 212].

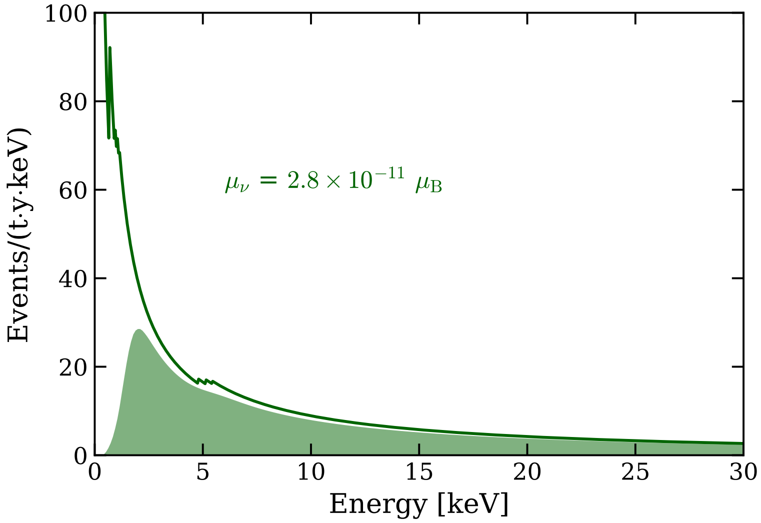

Figure 6.1: Electronic recoils induced by solar neutrino assuming finite magnetic moment $\mu_\nu = 2.8 \times 10^{-11}\,\mu_\mathrm{B}$, excluding the contribution from neutrino elastic scattering off the electrons. The curve and shaded region are before and after accounting for the efficiency and energy resolution specific in the XENON1T detector. Figure adapted from Ref. [134].

An enhanced magnetic moment would increase the neutrino scattering cross-sections at low energies (on both electrons and nuclei), and thus could be observable by low-threshold detectors such as XENON1T. Here we only consider the enhancement to elastic scattering on electrons, given by [213]

$$\frac{d\sigma_\mu}{dE_\mathrm{r}} = \mu_\nu^2 \alpha \left(\frac{1}{E_\mathrm{r}} - \frac{1}{E_\nu} \right), \tag{6.1}$$

where E_r is the electronic recoil energy, E_ν is the energy of the neutrino, and α is the fine structure constant. Note that Eq. (6.1) assumes free electrons; small corrections need to be made for the electron binding energies at $\mathcal{O}$(keV) energies.

We search for an anomalous magnetic moment using solar neutrinos, predominantly those from the proton-proton (pp) reaction [149]. The expected energy spectrum for $\mu_\nu = 2.8 \times 10^{-11}\,\mu_\mathrm{B}$ is shown in Fig. 6.1, which was calculated by folding the expected solar neutrino flux [149] with Eq. (6.1) and applying a step-function approximation to account for the electron binding energies. In the energy range considered here, this approximation agrees well with more detailed calculations [214]. Note that this signal would be added to the SM neutrino elastic scattering spectrum, which we treat as a background as described in Sec. 5.3.3.

When compared to the neutrino magnetic moment signal model, the background model B_0 is rejected at $3.2\,\sigma$. The best-fits of the null (B_0) and alternative ($B_0 + \mu_\nu$) hypotheses for this search are shown in Fig. 6.2.

The 90% confidence interval for μ_ν from this analysis is given by

$$\mu_\nu \in (1.4,\ 2.9) \times 10^{-11}\,\mu_B,$$

and is shown in Fig. 6.3 along with the constraints from other searches. The upper boundary of this interval is very close to the limit reported by Borexino [210], which is currently the most stringent direct detection constraint on the neutrino

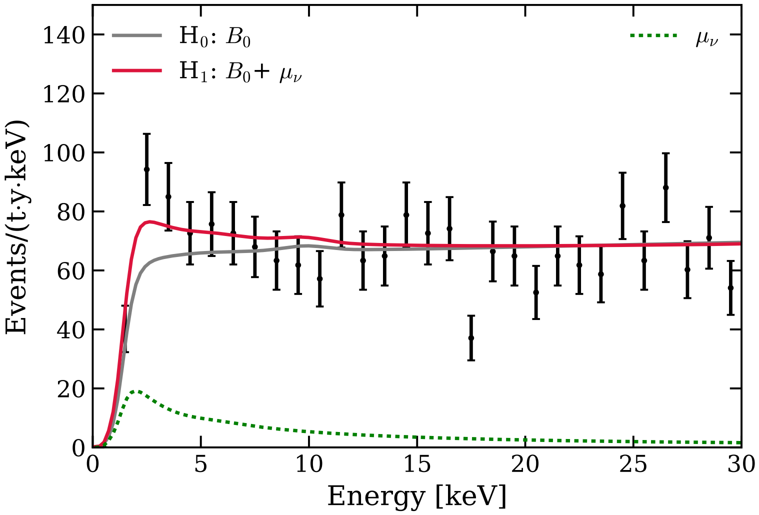

Figure 6.2: Hypothesis test for neutrino magnetic moment. The red and gray curves are the best-fits under alternate and null hypotheses, respectively. The green dashed line is the best-fit of the neutrino magnetic moment contribution to ER spectrum. Figure adapted from Ref. [134].

magnetic moment. Similar to the solar axion analysis, if we infer the excess as a neutrino magnetic moment signal, our result is in strong tension with astrophysical constraints from analyses of white dwarfs [216] and globular clusters [203]. The result is also compatible with the constraint from XENON1T using the S2-only method, which is able to probe a lower energy region and is further discussed in Sec. 5.6.5. It is important to note that the neutrino flavor does impact the interaction involving the magnetic moment, which in reality is a 3 × 3 matrix due to neutrino mixing. Our result, based on a flavor-insensitive detection of solar neutrinos, is thus directly comparable to Borexino's, but not necessarily to Gemma's (reactor electron anti-neutrinos) or the astrophysical limits (electron neutrinos).

As in Sec. 5.5.3, we report on an additional statistical test where an unconstrained tritium component was included in both null and alternative hypotheses. In this test the significance of the neutrino magnetic moment signal is reduced to

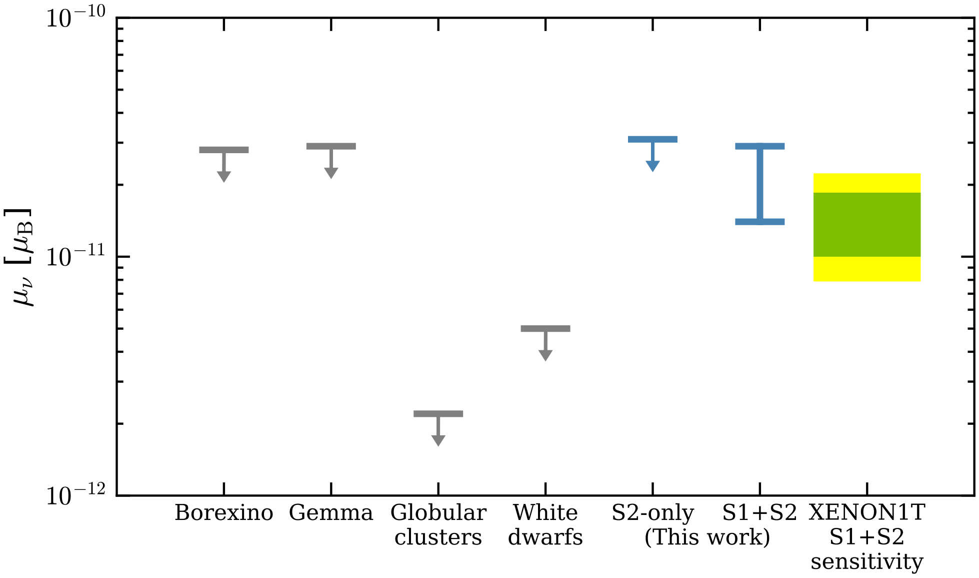

Figure 6.3: Constraints (90% C.L.) on the neutrino magnetic moment from this work using both S1 and S2 signals compared to experiments Borexino [210] and Gemma [215], along with astrophysical limits from the cooling of globular clusters [203] and white dwarfs [216]. The 1 (2)σ sensitivity band is indicated in the green (yellow) region. The constraint from XENON1T using ionization signal only (S2-only) is also shown (see Sec. 5.6.5). Arrows denote allowed regions. The upper boundary of the interval from this work is about the same as that from Borexino and Gemma. If we interpret the low-energy excess as a neutrino magnetic moment signal, its 90% confidence interval is in strong tension with the astrophysical constraints. Figure adapted from Ref. [134].

$0.9\,\sigma$ with the presence of a tritium background.

This is the most sensitive search to date for an enhanced neutrino magnetic moment with a DM detector, and suggests that this beyond-the-SM signal be included in the physics reach of other dark matter experiments.

6.2 Bosonic Dark Matter

Bosonic DM can be classified into pseudoscalar and vector bosons. In addition to the pseudoscalar ALPs that are discussed in Sec. 2.3.3, XENON1T is also sensitive to vector bosonic DM, of which dark photons are a common example. Dark photons can couple weakly with SM photons through kinetic mixing [217] and be absorbed with cross section σ_{V} given by [119]

$$\sigma_{\mathrm{V}} \simeq \frac{\sigma_{\mathrm{pe}}}{\beta}\kappa^2, \tag{6.2}$$

where σ_{pe}, α, and β are the same as in Eq. (2.15), and κ parameterizes the strength of kinetic mixing between the photon and dark photon. Similarly to Eq. (2.18), by following the calculation in Ref. [50], the rate for non-relativistic dark photons in a detector reduces to

$$\mathrm{Rate} \simeq \frac{4.7\times 10^{23}}{A}\kappa^2\left(\frac{\mathrm{keV}/c^2}{m_{\mathrm{V}}}\right)\left(\frac{\sigma_{\mathrm{pe}}}{\mathrm{b}}\right)\mathrm{kg}^{-1}\mathrm{d}^{-1}, \tag{6.3}$$

where m_{V} is the rest mass of the vector boson. The detection rate dependency on mass is illustrated in Fig. 6.4 for both ALP and dark photon DM. Compared to dark photon, ALP DM rate has a slower decreasing trend over mass as its cross section involves an extra dependency on m_{a}^2 (Eq. (2.15)).

For bosonic DM, we iterate over (fixed) masses between 1 and $210\,\mathrm{keV}/c^2$ to

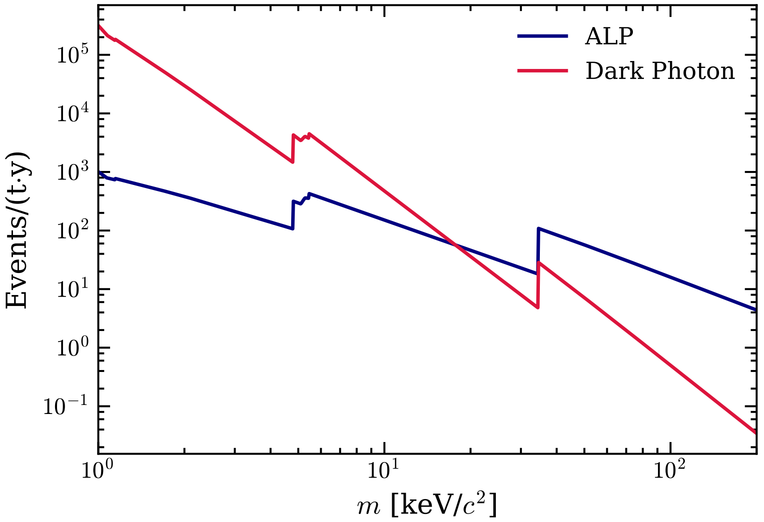

Figure 6.4: The detection rates for ALPs and Dark photon as function of mass, assuming all the local DM are made of them, respectively. The assumed axion-electron coupling $g_{\mathrm{ae}} = 1 \times 10^{-13}$ and the kinetic mixing parameter $\kappa = 1 \times 10^{-14}$. Detector features, such as detection efficiency and energy resolution, are not included.

search for peak-like excesses. The trial factors to convert between local and global significance were extracted using toyMC methods. While the excess does lead to looser constraints than expected at low energies, we find no global significance over $3\,\sigma$ for this search under the background model B_0. We thus set an upper limit on the couplings g_{ae} and κ as a function of particle mass.

These upper limits (90% C.L.) are shown in Fig. 6.5, along with the sensitivity band in green (1σ) and yellow (2σ). The losses of sensitivity at 41.5 keV and 164 keV are due to the $^{83\mathrm{m}}$Kr and $^{131\mathrm{m}}$Xe backgrounds, respectively, and the gains in sensitivity at around 5 and 35 keV are due to increases in the photoelectric cross section σ_{pe} in xenon from M-shell and L-shell electrons, respectively, see Fig. 2.6. The fluctuations in the limit are due to the photoelectric cross section, the logarithmic scaling, and the fact that the signal energy spectra differ significantly across the range of masses. For most masses considered, XENON1T sets the most

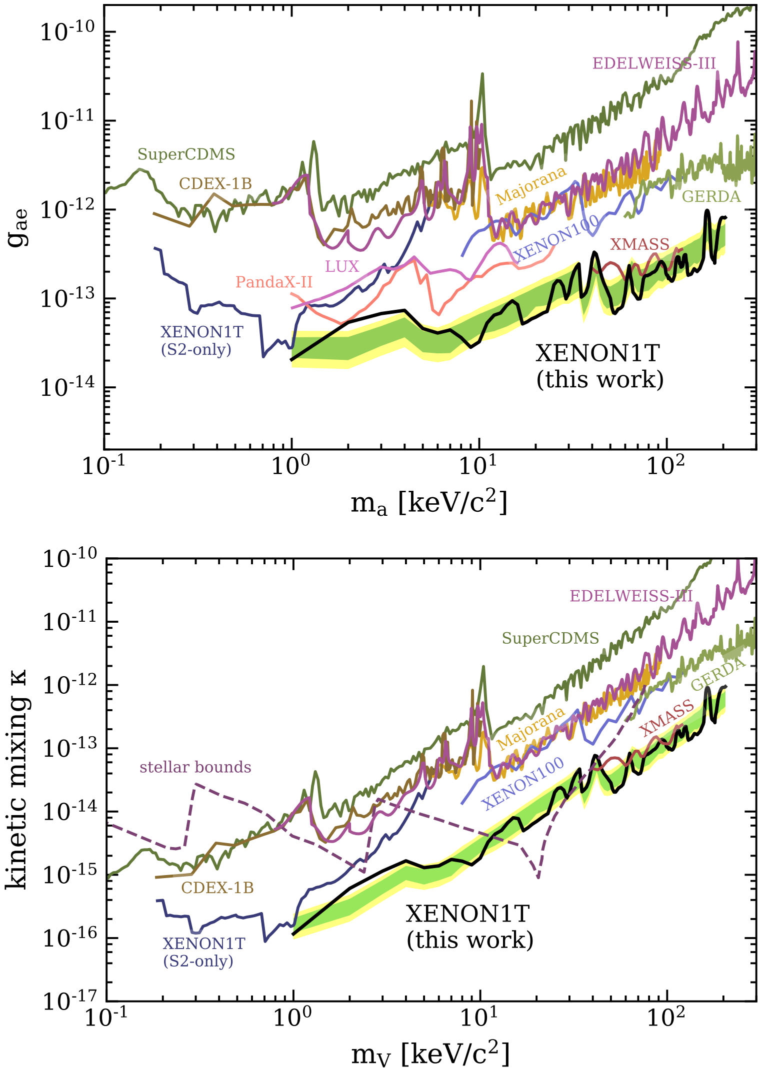

Figure 6.5: Constraints on couplings for bosonic pseudoscalar ALP (top) and vector (bottom) dark matter, as a function of particle mass. The XENON1T limits (90% C.L.) are shown in black with the expected 1 (2) σ sensitivities in green (yellow). Limits from other detectors or astrophysical constraints are also shown for both the pseudoscalar and vector cases [103, 109, 110, 116, 119, 218–223]. Figure from Ref. [134].

stringent direct-detection limits to date on pseudoscalar and vector bosonic DM couplings.[1]

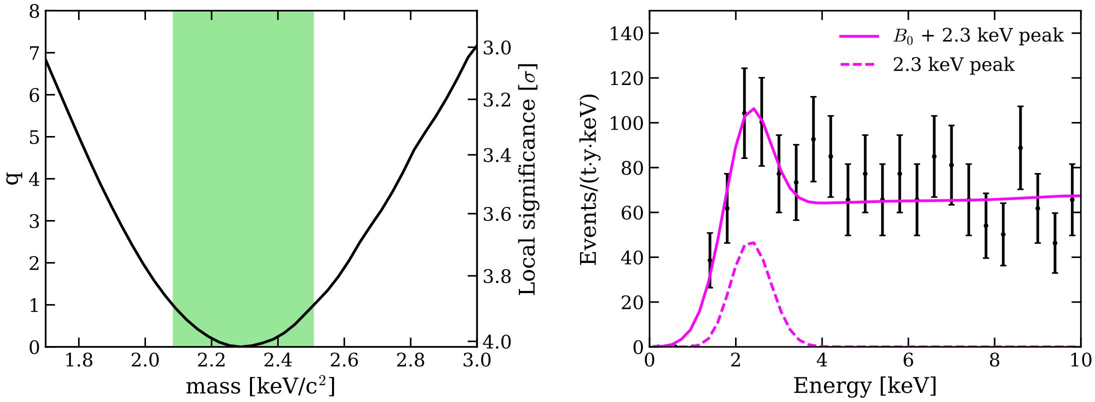

Figure 6.6: Left: The log-likelihood ratio for different bosonic dark matter masses with respect to the best-fit mass at 2.3 keV/c^2. At each mass, we show the result for the best-fit coupling at that mass. The green band shows an asymptotic 68% C.L. confidence interval on the bosonic dark matter mass. The local significance for each mass is also indicated. Right: Best-fit of a 2.3 keV peak and B_0 to the data. A 0.4 keV binning is used for better visualization. Figure from Ref. [134].

Due to the presence of the excess, we performed an additional fit using the bosonic DM signal model, with the particle mass allowed to vary freely between 1.7–3.3 keV/c^2. The result gives a favored mass value of $(2.3 \pm 0.2)\,\mathrm{keV}/c^2$ (68% C.L.) with a $3.0\,\sigma$ global ($4.0\,\sigma$ local) significance over background. A log-likelihood ratio curve as a function of mass is shown in Fig. 6.6 (left), along with the asymptotic 1-σ uncertainty. The spectral fit of the 2.3 keV peak is illustrated in Fig. 6.6 (right). Since the energy reconstruction in this region is validated using ^{37}Ar calibration data, whose distribution has a mean value within $< 1\%$ of the expectation at 2.82 keV [160], this analysis can also be used to compare the data to potential mono-energetic backgrounds in this region.

---

[1] The astrophysical constraint is not added to Fig. 6.5 (top) because those constraints are usually derived under the massless assumption; the calculation itself does not present much difficulties though, e.g. the stellar bound [119] considers the dark photon mass in Fig. 6.5 (bottom). See more detail in Sec. 2.3.3.

6.3 Leptophillic Dark Matter

WIMPs interact with electrons in leptophilic DM models. One specific model [224] assumes the interaction is via the axial-vector coupling with a differential rate given by:

$$\begin{aligned}\frac{dR}{dE_\mathrm{r}} \simeq \frac{3\rho_0}{4m_\chi m_\mathrm{Xe} m_\mathrm{e}} \sigma^0_{\chi e} \sum_{nl} \sqrt{2m_\mathrm{e}(E_\mathrm{r} - E_{\mathrm{B},nl})}(2l+1) \times 2 \\ \times \int \frac{dpp}{(2\pi)^3} |\chi_{nl}(p)|^2 I(v_\mathrm{min}),\end{aligned} \tag{6.4}$$

where $\sigma^0_{\chi\mathrm{e}}$ is cross section for WIMPs coupling to electrons through axial-vector interactions, $E_{\mathrm{B},nl}$ is the binding energy for xenon shell with principal and azimuthal quantum number of n and l, respectively [225, 226], and $\chi_{nl}(p)$ is the momentum wave function of the nl shell. The velocity term is calculated as

$$I(v_\mathrm{min}) = \int d^3\boldsymbol{v} \frac{f(\boldsymbol{v})}{v} \theta(v - v_\mathrm{min}), \tag{6.5}$$

where $f(\boldsymbol{v})$ is the distribution function of WIMP velocity relative to the detector (Eq. (2.2)), and the minimum velocity v_min to induce an ER with an energy of E_r is

$$v_\mathrm{min} \sim \frac{E_\mathrm{r}}{p} + \frac{p}{2m_\chi}. \tag{6.6}$$

The numerical expression of $\chi_{nl}(p)$ is given in Ref. [224] and its expansion coefficients calculated by Roothaan-Hartree-Fock method are available in Ref. [227]. Momentum wave functions from different xenon shells are shown in Fig. 6.7.

Since E_r is detectable above 1 keV in XENON1T, only large momentum transfer

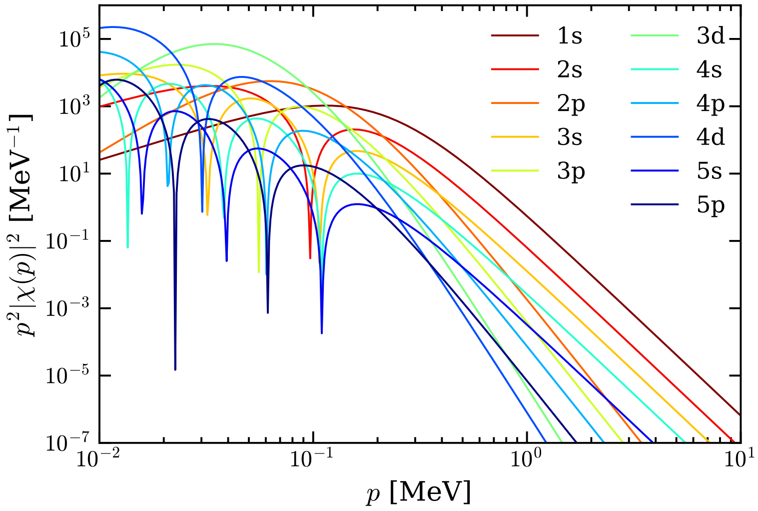

Figure 6.7: Momentum space wave functions in different xenon shells.

($p \gtrsim \mathcal{O}$(MeV)) contributes, otherwise the minimum required velocity v_{min} would exceed the DM escape velocity v_{esc} ($v_{\mathrm{esc}} < 2 \times 10^{-3}\,c$), see Eq. (6.6).

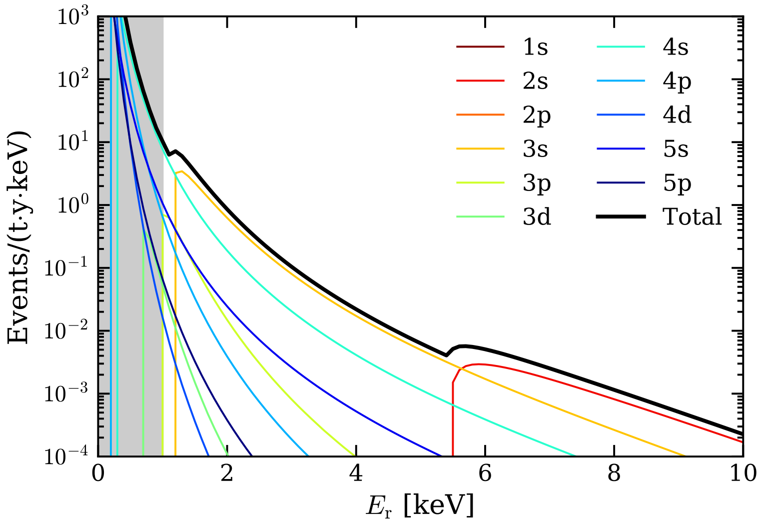

Figure 6.8: Energy spectrum for a 200 GeV/c^2 WIMP coupled with electrons through axial-vector coupling of $\sigma^0_{\chi \mathrm{e}} = 1 \times 10^{-34}\,\mathrm{cm}^2$. The thick black curve is the total energy spectrum while the various thin curves represent the contribution from different xenon shells.

The signal spectrum of a $200\,\mathrm{GeV}/c^2$ WIMP is calculated as an example. In Fig. 6.8, the main contribution between (1, 5) keV is from 3s shell as its electrons can be scattered off (E_b ~1.15 keV [225, 226]) and the large momentum wave function shown in Fig. 6.7. It is noteworthy that this calculation does not consider the relativistic effect, which could enhance the WIMP-electron scattering rate as pointed by Ref. [228].

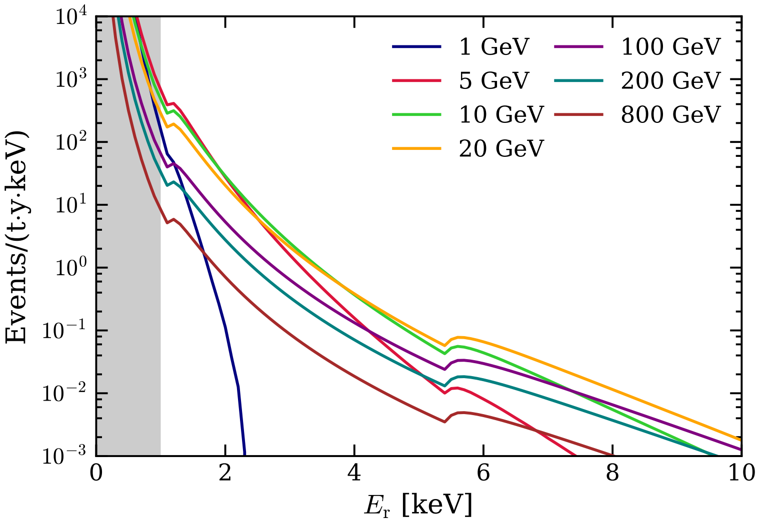

Figure 6.9: Spectra for WIMP-electron scattering via axial-vector coupling for different WIMP masses with $\sigma^0_{\chi\mathrm{e}} = 1 \times 10^{-34}\,\mathrm{cm}^2$. The detection threshold (1 keV) in XENON1T is indicated by the right bound of the shaded region.

Fig. 6.9 shows signal spectra with different WIMP masses. The signal spectrum is affected by WIMP mass m_χ in two ways: (1) change WIMP number density. This only scales the signal spectrum up and down. (2) Change required minimum velocity v_min to get a detectable signal, see Eq. (6.6). For relatively heavy WIMPs ($m_\chi \gtrsim 20\,\mathrm{GeV}/c^2$), the first term in Eq. (6.6) dominates and thus the minimum velocity will be independent of WIMP mass m_χ. For WIMPs with $m_\chi \lesssim 20\,\mathrm{GeV}/c^2$, the second term in Eq. (6.6) also play a role; therefore, a smaller m_χ will lead to a larger v_min, resulting in a lower signal rate. As a consequence, for light WIMPs, spectrum with lower mass drops faster, see the comparison between spectra for $1\,\mathrm{GeV}/c^2$ and $5\,\mathrm{GeV}/c^2$ WIMPs in Fig. 6.9; the spectral shape for the heavy WIMP is almost identical.

No excess is observed for WIMP signals with any mass, therefore an upper limit is reported. Due to the low background and large exposure, XENON1T sets the most stringent limit for WIMP-electron interaction cross section $\sigma^0_{\chi\mathrm{e}}$ with axial-vector coupling for WIMP mass ranging from 2 to 1000 GeV/c^2, as shown in Fig. 6.10. This result is about 3 orders of magnitude lower than the 3σ DAMA region [224].

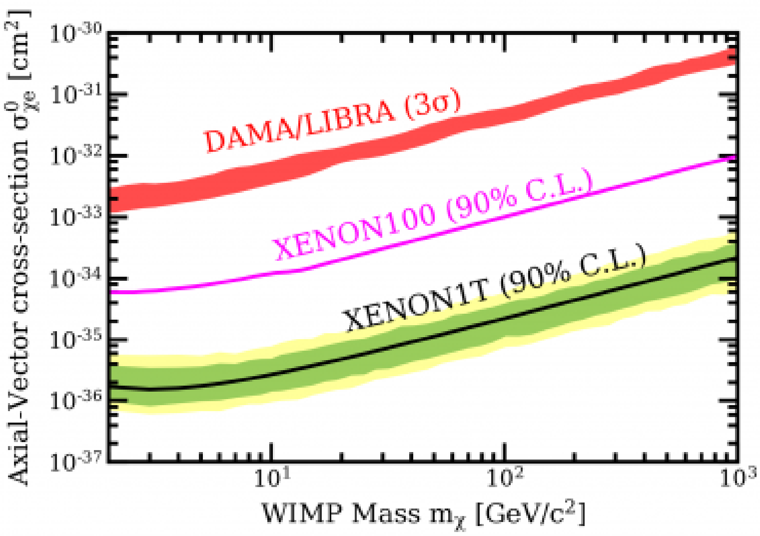

Figure 6.10: 90% C.L. upper limit on the cross section $\sigma^0_{\chi\mathrm{e}}$ for WIMPs coupling to electrons through axial-vector interactions, along with the 1 (2)σ sensitivity bands indicated by the green (yellow) region. The 3σ DAMA region [224] and XENON100 upper limit (90% C.L.) [35] are represented by the red region and magenta curve, respectively.

6.4 Double Electron Capture of ^{124}Xe

This search is different from the all the other searches mentioned in this thesis. It aims for a process predicted in SM, the 2νECEC of ^{124}Xe, other than new physics that are beyond the SM. This work [144] is earlier than the search for solar axions [134], where the 2νECEC of ^{124}Xe was treated as a background (Sec. 5.3.5.2). For this search, we only considered the capture of two K-shell electrons, which produces a peak at 64.3 keV with the dominant BR of 76.7% [229]. The analysis framework is also different from that used in the aforementioned ER signals.

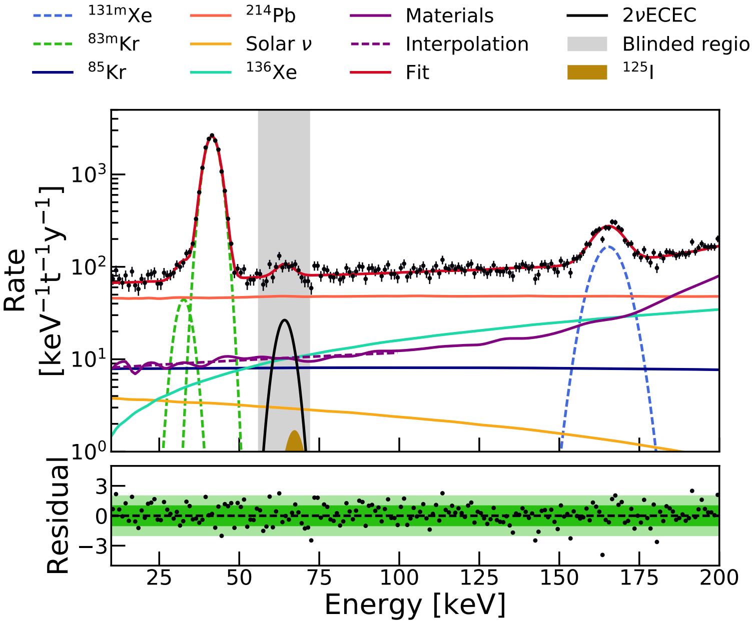

Figure 6.11: Best-fit of the background model plus the signal of 2νECEC of ^{124}Xe to the measured energy spectrum. The shaded region was blinded before the event selection and background model were finalized. Figure published in Ref. [144].

The FV was optimized for this particular signal and was determined as a 1.5T superellipsoid. The most dominant background, as shown in Fig. 6.11, is from the K-shell EC of ^{125}I. The other two peaks produced by ^{125}I was not considered here as they are subdominant and are also away from the signal region. Since ^{125}I was produced during the neutron calibrations, using a dedicated neutron calibration in SR2, the *effective* decay constant for ^{125}I was evaluated to be (9.1 ± 2.6) days, which took into account the decrease from the natural decay and the removal from the purification. This search was also done with SR1 data, a large period after the neutron calibrations was removed to reduce the ^{125}I background, resulting in a final live time of 177.7 days. The 1.5T FV was divided into an inner volume (1T) and an outer volume (0.5T) in the statistics inference with fit range of 10–200 keV and 10–300 keV, respectively; the fit range in the inner volume is allowed to extend more towards high energy due to the smaller spectral shape uncertainty of Compton scattering from the materials. The inference was done by a combined χ^2 method that accounts for inner/outer volume as well as a number of systematic constraints. The fit result in the 1.5T FVin 10–200 keV is illustrated in Fig. 6.11, where the 2νECEC of ^{124}Xe is visible in the expected energy region thanks to the unprecedented low background in XENON1T. This work gives the half-life of K-shell 2νECEC of ^{124}Xe $t_{1/2} = (1.8 \pm 0.5_{\mathrm{stat}} \pm 0.1_{\mathrm{sys}}) \times 10^{22}$ years with a significance of 4.4σ. Since the peak signal has a fixed energy, the look-else effect is irrelevant here. More detail can be found in Ref. [144].

6.5 Acknowledgements

Chapter 6, in part, contains results that are accepted for publication or have been published. Secs. 6.1 and 6.2, in part, are accepted for publication as it should appear soon in Phys. Rev. D, 2020, XENON Collaboration and Xavier Mougeot, Excess Electronic Recoil Events in XENON1T. The dissertation author is the primary investigator and one of the corresponding authors of the publication. Sec. 6.4, in full, is a summary of the following publication, XENON Collaboration, Observation of two-neutrino double electron capture in ^{124}Xe with XENON1T, Nature 568, 532-535 (2019). The dissertation author is an author of the publication.

Chapter 7

The XENONnT Experiment

This chapter describes the future aspects of the XENON project and is structured as follows. Sec. 7.1 introduces the XENONnT experiment, the next-generation experiment of XENON1T, with a focus on the expected level of ER and NR backgrounds. The projected sensitivity of SI WIMP-nucleon scattering cross section is presented in Sec. 7.2. The prospects of the investigation on the excess observed in XENON1T are briefly discussed in Sec. 7.3.

7.1 Background Predictions

The XENONnT experiment [55] is currently under commissioning in LNGS and is expected to start taking science data soon. The majority of systems outside the inner cryostat vessel in XENON1T have been reused in XENONnT, including the outer cryostat vessel, water tank, etc, which allows for a fast and stable upgrade. The detector will have 8 tonne LXe in total, 5.9 tonne of which are in the active volume. The CAD of XENONnT TPC, as well as the two cryostat vessels, are illustrated in Fig. 7.1. The TPC has a diameter and height of 1.3 m and 1.5 m, respectively, with the top (bottom) PMT array consisting of 253 (241) PMTs.

A 4 tonne cylindrical FV is chosen based on the spatial distribution of materials background [55]. Assuming a 5 year live time of science data collection, XENONnT is projected to embrace an unprecedented exposure of 20 tonne-years. Compared to the detectors of previous generations, XENONnT will not only feature a larger target, but also significantly reduce both the ER and NR backgrounds.

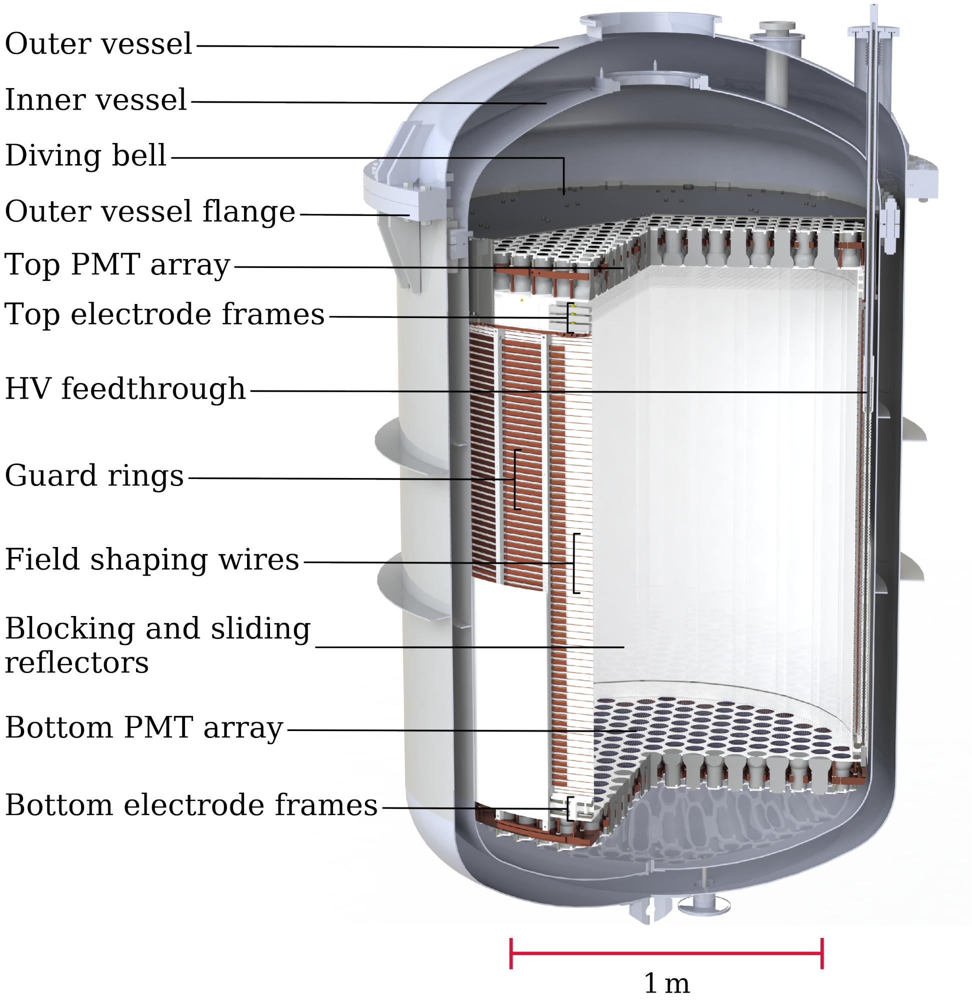

Figure 7.1: The CAD rendering of the two cryostat vessels, as well as the XENONnT TPC, which has a diameter of 1.3 m and a height of 1.5 m. A total of 253 and 241 PMTs are deployed in the top and bottom PMT arrays, respectively. Figure from Ref. [55].

The main ER background, the β decay of ^{214}Pb, will be mitigated by the rig-

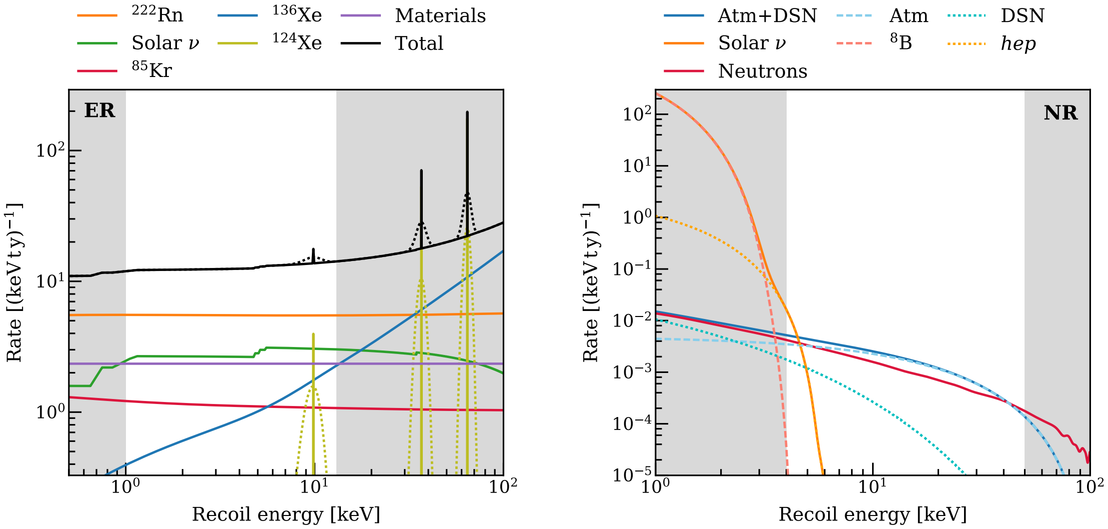

Figure 7.2: Left: Projected ER backgrounds in XENONnT. The solid lines are the true energy spectra, i.e. excluding efficiency or energy resolution. The dashed lines are ^{124}Xe peaks after considering XENON1T energy resolution [144]. Right: Projected NR backgrounds in XENONnT. The solid lines represent the three main categories of NR backgrounds, while the blue and orange non-solid lines detail the contributions from two categories, i.e. solar neutrino, and atmospheric and diffuse supernovae neutrino (Atm+DSN), respectively. The ROI for WIMP search is denoted by the white region in both plots. Figure from Ref. [55].

orous selection of low radon-emanating materials, smaller surface-to-volume ratio, and a dedicated online ^{222}Rn distillation column in XENONnT. The distillation method has been tested in the XENON100 experiment [230] and the XENON1T experiment [147, 192], respectively. It was demonstrated in the XENON1T experiment that ^{222}Rn level reached down to $4.5\,\mu$Bq/kg in SR2 [147, 192] (Sec. 5.6.1); therefore, together with other improvements, the ^{222}Rn concentration in XENONnT is assumed to be $1\,\mu$Bq/kg. This design goal predicts $5.5\,\text{events}/(\text{t}\cdot\text{y}\cdot\text{keV})$ ^{214}Pb β-decay events in the (1, 13) keV$_{\text{ee}}$ energy region, which is roughly the ROI for WIMP search in XENONnT. Another ER background, the β decay of ^{85}Kr, is also significantly mitigated by the distillation of whole xenon inventory for XENONnT in 2019 and is expected to contribute $1.3\,\text{events}/(\text{t}\cdot\text{y}\cdot\text{keV})$ in the (1, 13) keV$_{\text{ee}}$ energy region, which is even lower than the predicted contribution from the solar neutrino electron scattering rate in this energy region. The ER backgrounds in XENONnT are illustrated in Fig. 7.2 (left).

The dominant NR background in XENON1T, radiogenic neutron background, will also be greatly suppressed in XENONnT thanks to the careful materials selection, smaller surface-to-volume ratio, and more importantly the introduction of a neutron veto system. The neutron veto is outside the outer cryostat vessel and inside the water tank, which is filled with Gd-loaded water. Gd has the highest thermal neutron capture cross section among the known stable isotopes. Radiogenic neutrons from detector materials that deposit energy in LXe once and escape the detector would be moderated by water and become thermal neutrons after a typical length of ∼20 cm. Most of the thermal neutrons would be captured by Gd, which is followed by emissions of ∼8 MeV γ rays. A $150\,\mu$s window coincident with this distinct neutron signature will be tagged and vetoed, which is expected to have a ∼87% tag efficiency for single scatter radiogenic neutron events [55].

With other additional improvements, the radiogenic neutron background is only expected to contribute an average differential rate of $\sim 9\times10^{-4}$ events/(t·y·keV) in (4, 50) $\mathrm{keV_{nr}}$ energy region, which is even lower than the CEνNS background. The NR backgrounds in XENONnT are shown in Fig. 7.2 (right).

7.2 Projected WIMP Sensitivity

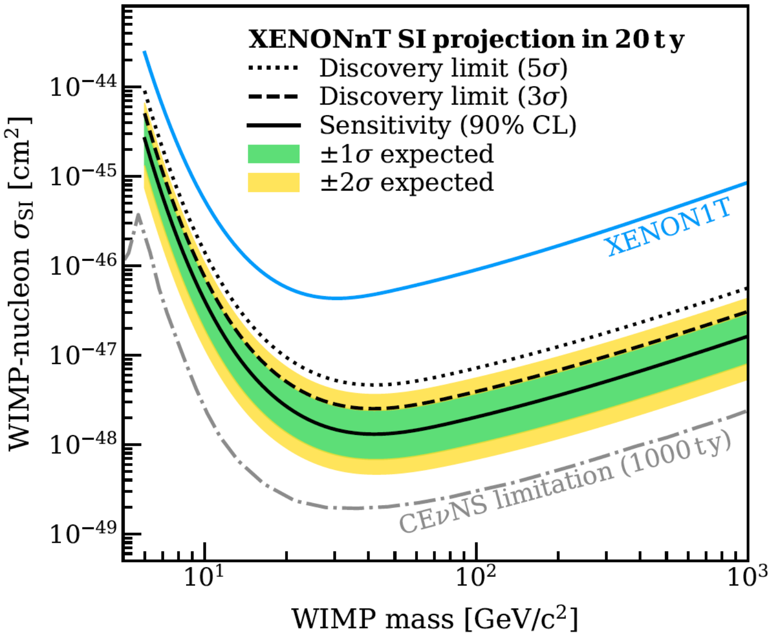

Figure 7.3: XENONnT experiment projected sensitivity of SI WIMP-nucleon cross section. The 1 (2)σ sensitivity band is shown in green (yellow) region and the median of sensitivity band is denoted with the black line. The discovery limit, at which an excess is expected to observe with 50% chance, are shown for 3 (5)σ significance with dashed (dotted) lines. The current best limit from XENON1T [23] is shown in blue curve. The limitation curve that assumes 1000 ty exposure and CEνNS as the only background [231] is illustrated by the dash-dotted gray line, below which the WIMP discovery potential is significantly slowed with increasing exposure due to the resemblance between WIMP events and CEνNS events. Figure adapted from Ref. [55].

The statistical inference for the WIMP sensitivity estimation in XENONnT is done in the (c$S1$, c$S2_{\mathrm{b}}$) parameter space, with the ER and NR backgrounds summarized in Fig. 7.2. The sensitivity projection for SI WIMP-nucleon cross section σ_{SI} in XENONnT is shown in Fig. 7.3, assuming the 20 tonne-year exposure and the designed $1\,\mu\mathrm{Bq/kg}$ ^{222}Rn activity. The projected median exclusion limit at 90% C.L. level for a $50\,\mathrm{GeV}/c^2$ WIMP is $1.4 \times 10^{-48}\,\mathrm{cm}^2$, more than 1 order of magnitude smaller than the current best limit. Additionally, the experiment has a 50% chance to observe an excess from a $50\,\mathrm{GeV}/c^2$ WIMP with 3σ (5σ) significance for a σ_{SI} of $2.6 \times 10^{-48}\,\mathrm{cm}^2$ ($5.0 \times 10^{-48}\,\mathrm{cm}^2$).

7.3 Discrimination Power on the XENON1T ER Excess

With the large exposure and low backgrounds, the XENONnT experiment can further investigate on the low-energy ER excess found in XENON1T based on the spectral shape. Here the discussion is mainly devoted to the tritium hypothesis and solar axion hypothesis, the latter of which is restricted to ABC solar axion only for simplicity. The full ROI for this investigation is temporarily chosen to be (1, 30) $\mathrm{keV_{ee}}$ in this work to get a balance between focusing on the low-energy region and maintaining a good constraint on the ^{214}Pb background which mainly relies on statistics. The fiducialization follows the same 4T cylindrical FV used in the WIMP sensitivity projection and thus all the ER backgrounds adopt the predicted values in Ref. [55] except for ^{222}Rn. Since ^{222}Rn is the dominant background in ER signal search, the study is done with different ^{222}Rn activity levels between 1 and $5\,\mu\mathrm{Bq/kg}$, the upper bound of which has been achieved in SR2 [192]. Different livetime is also assumed to explore the discrimination power over time. A statistical framework similar to that in XENON1T (Sec. 5.4) is used except for the partition, because the two time-dependent backgrounds are either too subdominant (^{85}Kr) or of negligible variation (solar neutrino; ∼ 7% peak-to-peak amplitude).

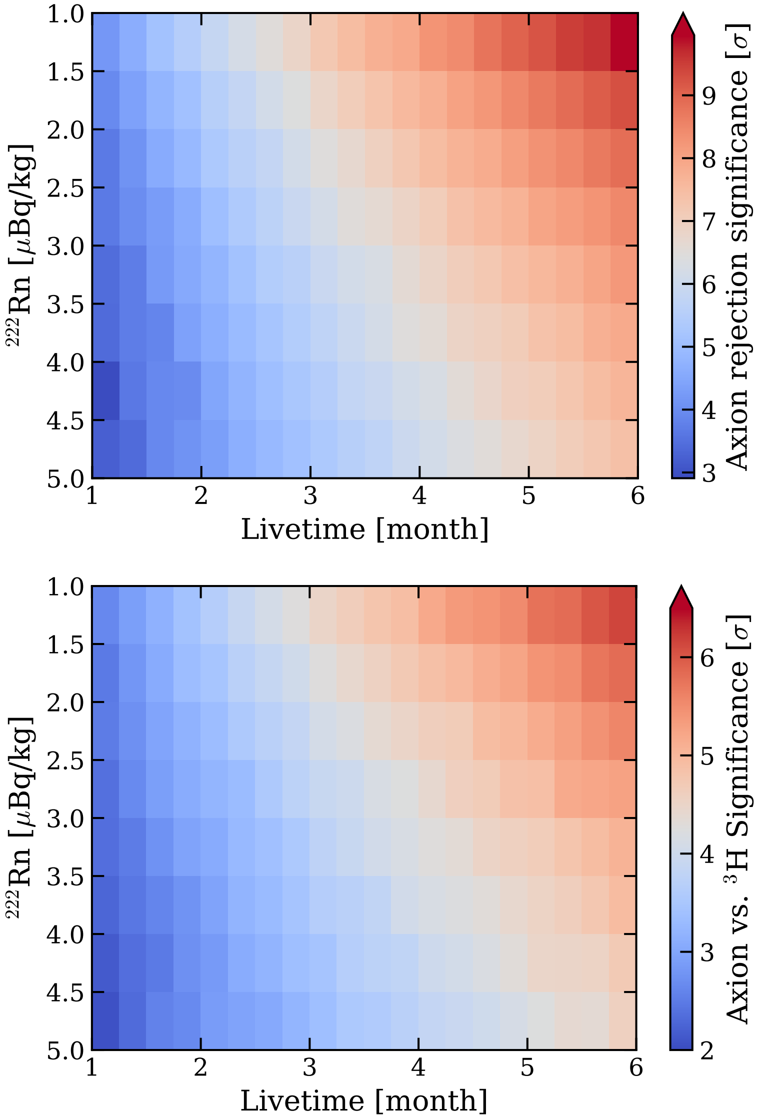

Figure 7.4: Top: The rejection power of solar axion hypothesis with coupling obtained from XENON1T [134] if the excess is completely gone in XENONnT. Bottom: The significance of solar axion hypothesis with an unconstrained tritium component in the alternate and null hypotheses in XENONnT, if the excess electronic recoils in XENONT were induced by solar axions and preserve in XENONnT. Both show the median significance with respect to different ^{222}Rn activities and livetime, assuming the 4T cylindrical FV. Only ABC component is considered in the solar axion hypothesis for simplicity. See text for more detail.

To study the discrimination power over the solar axion and tritium hypotheses, two scenarios are postulated here: (1) the excess in XENON1T was induced by tritium or some other contaminants and is completely gone in XENONnT, and (2) the excess in XENON1T was produced by solar axions and persists in XENONnT.[1] Accordingly, the first case would focus on the rejection power of solar axion with the best-fit axion-photon coupling g_{ae} from XENON1T, whereas the second case studies the solar axion significance with an unconstrained tritium in both alternate and null hypotheses. With the assumptions mentioned above, the excess discrimination power in XENONnT for the two cases are summarized in Fig. 7.4. As expected, the discrimination power improved with lower ^{222}Rn activities and larger exposure. Should the excess remain in XENONnT, it will require longer livetime and/or lower ^{222}Rn activities to distinguish tritium and solar axions, compared to the case that the excess is gone; however, it still only demands a few months of data to achieve 5σ significance depending on the ^{222}Rn level. With the next-generation LXe experiments being online soon, such as PandaX-4T [232], LZ [233], as well as XENONnT, we expect the excess observed in XENON1T to be investigated independently with better sensitivities in the near future.

7.4 Acknowledgements

Chapter 7, in part, is submitted for publication as it may appear in Journal of Cosmology and Astroparticle Physics, 2020, XENON Collaboration, “Projected WIMP Sensitivity of the XENONnT Dark Matter Experiment”. The dissertation author is an author of this material.

---

[1] The tritium-induced excess is not investigated because tritium concentration can change significantly between detectors even if the excess was from tritium. Besides, this study is intended to investigate the discrimination power over different hypotheses in XENONnT thus the axion-induced excess should suffice.

Bibliography

[1] William Thomson Baron Kelvin. *Baltimore Lectures on Molecular Dynamics and the Wave Theory of Light*. Cambridge Library Collection - Physical Sciences. Cambridge University Press, 2010. DOI: `10.1017/CBO9780511694523`.

[2] H. Poincare. "The Milky Way and the Theory of Gases". In: *Popular Astronomy* 14 (Oct. 1906), pp. 475–488.

[3] Gianfranco Bertone and Dan Hooper. "History of dark matter". In: *Rev. Mod. Phys.* 90 (4 2018), p. 045002. DOI: `10.1103/RevModPhys.90.045002`.

[4] Edvige Corbelli and Paolo Salucci. "The extended rotation curve and the dark matter halo of M33". In: *Monthly Notices of the Royal Astronomical Society* 311.2 (Jan. 2000), pp. 441–447. ISSN: 0035-8711. DOI: `10.1046/j.1365-8711.2000.03075.x`. eprint: `https://academic.oup.com/mnras/article-pdf/311/2/441/2881340/311-2-441.pdf`.

[5] Douglas Clowe, Maruša Bradač, Anthony H. Gonzalez, Maxim Markevitch, Scott W. Randall, Christine Jones, and Dennis Zaritsky. "A Direct Empirical Proof of the Existence of Dark Matter". In: *The Astrophysical Journal* 648.2 (2006), pp. L109–L113. DOI: `10.1086/508162`.

[6] Chandra Collaboration. *1E 0657-56: NASA Finds Direct Proof of Dark Matter*. 2006.

[7] Pieter van Dokkum, Shany Danieli, Yotam Cohen, Allison Merritt, Aaron J. Romanowsky, Roberto Abraham, Jean Brodie, Charlie Conroy, Deborah Lokhorst, Lamiya Mowla, Ewan O'Sullivan, and Jielai Zhang. "A galaxy lacking dark matter". In: *Nature* 555.7698 (2018), pp. 629–632. ISSN: 1476-4687. DOI: `10.1038/nature25767`.

[8] Planck Collaboration. *Planck 2018 results. VI. Cosmological parameters*. 2018. arXiv: `1807.06209 [astro-ph.CO]`.

[9] R.H. Dicke, P.J.E. Peebles, P.G. Roll, and D.T. Wilkinson. "Cosmic Black-Body Radiation". In: *Astrophys. J.* 142 (1965), pp. 414–419. DOI: `10.1086/148306`.

[10] D. J. Fixsen, E. S. Cheng, D. A. Cottingham, Jr. Eplee R. E., R. B. Isaacman, J. C. Mather, S. S. Meyer, P. D. Noerdlinger, R. A. Shafer, R. Weiss, E. L. Wright, C. L. Bennett, N. W. Boggess, T. Kelsall, S. H. Moseley, R. F. Silverberg, G. F. Smoot, and D. T. Wilkinson. "Cosmic microwave background dipole spectrum measured by the COBE FIRAS". In: *Astrophys. J.* 420 (1994), p. 445. DOI: `10.1086/173575`.

[11] WMAP Collaboration. "NINE-YEAR WILKINSON MICROWAVE ANISOTROPY PROBE (WMAP) OBSERVATIONS: FINAL MAPS AND RESULTS". In: *The Astrophysical Journal Supplement Series* 208.2 (2013), p. 20. DOI: `10.1088/0067-0049/208/2/20`.

[12] Raymond T. Co and Keisuke Harigaya. "Axiogenesis". In: *Phys. Rev. Lett.* 124 (11 2020), p. 111602. DOI: `10.1103/PhysRevLett.124.111602`.

[13] Edward W. Kolb and Michael S. Turner. *The Early Universe.* Vol. 69. 1990. ISBN: 978-0-201-62674-2.

[14] Gerard Jungman, Marc Kamionkowski, and Kim Griest. "Supersymmetric dark matter". In: *Physics Reports* 267.5 (1996), pp. 195 –373. ISSN: 0370-1573. DOI: `https://doi.org/10.1016/0370-1573(95)00058-5`.

[15] R. D. Peccei and Helen R. Quinn. "CP Conservation in the Presence of Pseudoparticles". In: *Phys. Rev. Lett.* 38 (25 1977), pp. 1440–1443. DOI: `10.1103/PhysRevLett.38.1440`.

[16] Markus Kuster, Georg Raffelt, and Berta Beltran. *Axions. Theory, Cosmology, and Experimental Searches.* Springer-Verlag Berlin Heidelberg, 2008.

[17] Richard Bradley, John Clarke, Darin Kinion, Leslie J Rosenberg, Karl van Bibber, Seishi Matsuki, Michael Mück, and Pierre Sikivie. "Microwave cavity searches for dark-matter axions". In: *Rev. Mod. Phys.* 75 (3 2003), pp. 777–817. DOI: `10.1103/RevModPhys.75.777`.

[18] Javier Redondo. "Solar axion flux from the axion-electron coupling". In: *Journal of Cosmology and Astroparticle Physics* 2013.12 (2013), p. 008.

[19] "Introduction". In: *Noble Gas Detectors.* John Wiley & Sons, Ltd, 2006. Chap. 1, pp. 1–5. ISBN: 9783527610020. DOI: `10.1002/9783527610020.ch1`. eprint: `https://onlinelibrary.wiley.com/doi/pdf/10.1002/9783527610020.ch1`.

[20] E. Hogenbirk, J. Aalbers, P.A. Breur, M.P. Decowski, K. van Teutem, and A.P. Colijn. "Precision measurements of the scintillation pulse shape for low-energy recoils in liquid xenon". In: *Journal of Instrumentation* 13.05 (2018), P05016–P05016. DOI: `10.1088/1748-0221/13/05/p05016`.

[21] N.G. Basov, E.M. Balashov, O.V. Bogdankevitch, V.A. Danilychev, G.N. Kashnikov, N.P. Lantzov, and D.D. Khodkevitch. “Luminescence of condensed Xe, Kr, Ar and their mixtures in vacuum region of spectrum under excitation by fast electrons”. In: *J. Lumin.* 1-2 (1970), pp. 834 –841. DOI: `https://doi.org/10.1016/0022-2313(70)90095-5`.

[22] M. Althüser. “Light collection efficiency simulations of the XENON1T experiment and comparison to data”. MA thesis. Westfälische Wilhelms-Universität Münster, 2017.

[23] XENON Collaboration. “Dark Matter Search Results from a One Ton-Year Exposure of XENON1T”. In: *Phys. Rev. Lett.* 121 (11 2018), p. 111302. DOI: `10.1103/PhysRevLett.121.111302`.

[24] PandaX-II Collaboration. “Dark Matter Results from 54-Ton-Day Exposure of PandaX-II Experiment”. In: *Phys. Rev. Lett.* 119 (18 2017), p. 181302. DOI: `10.1103/PhysRevLett.119.181302`.

[25] LUX Collaboration. “Results from a Search for Dark Matter in the Complete LUX Exposure”. In: *Phys. Rev. Lett.* 118 (2 2017), p. 021303. DOI: `10.1103/PhysRevLett.118.021303`.

[26] J. Lindhard, V. Nielsen, M. Scharff, and P. Thomsen. “RANGE CONCEPTS AND HEAVY ION RANGES”. In: *Mat. Fys. Medd. K. Dan. Vidensk. Selsk* 33.1 (1963). DOI: `10.1088/1361-6471/ab8e93`.

[27] XENON Collaboration. “Search for WIMP inelastic scattering off xenon nuclei with XENON100”. In: *Phys. Rev. D* 96 (2 2017), p. 022008. DOI: `10.1103/PhysRevD.96.022008`.

[28] Richard H. Helm. “Inelastic and Elastic Scattering of 187-Mev Electrons from Selected Even-Even Nuclei”. In: *Phys. Rev.* 104 (5 1956), pp. 1466–1475. DOI: `10.1103/PhysRev.104.1466`.

[29] J.D. Lewin and P.F. Smith. “Review of mathematics, numerical factors, and corrections for dark matter experiments based on elastic nuclear recoil”. In: *Astroparticle Physics* 6.1 (1996), pp. 87 –112. ISSN: 0927-6505. DOI: `https://doi.org/10.1016/S0927-6505(96)00047-3`.

[30] L. Vietze, P. Klos, J. Menéndez, W. C. Haxton, and A. Schwenk. “Nuclear structure aspects of spin-independent WIMP scattering off xenon”. In: *Phys. Rev. D* 91 (4 2015), p. 043520. DOI: `10.1103/PhysRevD.91.043520`.

[31] Francis Froborg and Alan R Duffy. “Annual modulation in direct dark matter searches”. In: *Journal of Physics G: Nuclear and Particle Physics* 47.9 (2020), p. 094002. DOI: `10.1088/1361-6471/ab8e93`.

[32] DAMA Collaboration. “First results from DAMA/LIBRA and the combined results with DAMA/NaI”. In: *The European Physical Journal C* 56.3 (2008), pp. 333–355. DOI: `10.1140/epjc/s10052-008-0662-y`.

[33] DAMA Collaboration. “First Model Independent Results from DAMA/LIBRA–Phase2”. In: *Nucl. Phys. At. Energy* 19.11 (4 2018), p. 116. DOI: `https://doi.org/10.15407/jnpae2018.04.307`.

[34] CoGeNT Collaboration. “Experimental Constraints on a Dark Matter Origin for the DAMA Annual Modulation Effect”. In: *Phys. Rev. Lett.* 101 (25 2008), p. 251301. DOI: `10.1103/PhysRevLett.101.251301`.

[35] XENON Collaboration. “Exclusion of leptophilic dark matter models using XENON100 electronic recoil data”. In: *Science* 349.6250 (2015), pp. 851–854. ISSN: 0036-8075. DOI: `10.1126/science.aab2069`.

[36] XENON Collaboration. “Search for Event Rate Modulation in XENON100 Electronic Recoil Data”. In: *Phys. Rev. Lett.* 115 (9 2015), p. 091302. DOI: `10.1103/PhysRevLett.115.091302`.

[37] XENON Collaboration. “Search for Electronic Recoil Event Rate Modulation with 4 Years of XENON100 Data”. In: *Phys. Rev. Lett.* 118 (10 2017), p. 101101. DOI: `10.1103/PhysRevLett.118.101101`.

[38] SABRE Collaboration. “The SABRE project and the SABRE Proof-of-Principle”. In: *The European Physical Journal C* 79.4 (2019), p. 363. ISSN: 1434-6052. DOI: `10.1140/epjc/s10052-019-6860-y`.

[39] Klaus Ehret, Maik Frede, Samvel Ghazaryan, Matthias Hildebrandt, Ernst-Axel Knabbe, Dietmar Kracht, Axel Lindner, Jenny List, Tobias Meier, Niels Meyer, Dieter Notz, Javier Redondo, Andreas Ringwald, Günter Wiedemann, and Benno Willke. “New ALPS results on hidden-sector lightweights”. In: *Physics Letters B* 689.4 (2010), pp. 149 –155. ISSN: 0370-2693. DOI: `https://doi.org/10.1016/j.physletb.2010.04.066`.

[40] Christina Gao, Jia Liu, Lian-Tao Wang, Xiao-Ping Wang, Wei Xue, and Yi-Ming Zhong. *Re-examining the Solar Axion Explanation for the XENON1T Excess*. 2020. arXiv: `2006.14598 [hep-ph]`.

[41] James B. Dent, Bhaskar Dutta, Jayden L. Newstead, and Adrian Thompson. “Inverse Primakoff Scattering as a Probe of Solar Axions at Liquid Xenon Direct Detection Experiments”. In: (June 2020). arXiv: `2006.15118 [hep-ph]`.

[42] CAST Collaboration. “New CAST limit on the axion–photon interaction”. In: *Nature Physics* 13.6 (2017), pp. 584–590. ISSN: 1745-2481. DOI: `10.1038/nphys4109`.

[43] IAXO collaboration. “Physics potential of the International Axion Observatory (IAXO)”. In: *Journal of Cosmology and Astroparticle Physics* 2019.06 (2019), pp. 047–047. DOI: `10.1088/1475-7516/2019/06/047`.

[44] ADMX Collaboration. “Search for Invisible Axion Dark Matter with the Axion Dark Matter Experiment”. In: *Phys. Rev. Lett.* 120 (15 2018), p. 151301. DOI: `10.1103/PhysRevLett.120.151301`.

[45] Aldo M. Serenelli, Sarbani Basu, Jason W. Ferguson, and Martin Asplund. "NEW SOLAR COMPOSITION: THE PROBLEM WITH SOLAR MODELS REVISITED". In: *The Astrophysical Journal* 705.2 (2009), pp. L123–L127. DOI: `10.1088/0004-637x/705/2/l123`.

[46] CAST Collaboration. "Search for 14.4 keV solar axions emitted in the M1-transition of ^{57}Fe nuclei with CAST". In: *Journal of Cosmology and Astroparticle Physics* 2009.12 (2009), pp. 002–002. DOI: `10.1088/1475-7516/2009/12/002`.

[47] CUORE Collaboration. "Search for 14.4 keV solar axions from M1 transition of ^{57}Fe with CUORE crystals". In: *Journal of Cosmology and Astroparticle Physics* 2013.05 (2013), pp. 007–007. DOI: `10.1088/1475-7516/2013/05/007`.

[48] S. Dimopoulos, G.D. Starkman, and B.W. Lynn. "Atomic Enhancements in the Detection of Axions". In: *Mod. Phys. Lett. A* 1 (1986), pp. 491–500. DOI: `10.1142/S0217732386000622`.

[49] Savas Dimopoulos, G.D. Starkman, and B.W. Lynn. "Atomic Enhancements in the Detection of Weakly Interacting Particles". In: *Phys. Lett. B* 168 (1986), pp. 145–150. DOI: `10.1016/0370-2693(86)91477-2`.

[50] Maxim Pospelov, Adam Ritz, and Mikhail Voloshin. "Bosonic super-WIMPs as keV-scale dark matter". In: *Phys. Rev. D* 78 (11 2008), p. 115012. DOI: `10.1103/PhysRevD.78.115012`.

[51] Wm.J. Veigele. "Photon cross sections from 0.1 keV to 1 MeV for elements Z = 1 to Z = 94". In: *Atomic Data and Nuclear Data Tables* 5.1 (1973), pp. 51 –111. ISSN: 0092-640X. DOI: `https://doi.org/10.1016/S0092-640X(73)80015-4`.

[52] `https://physics.nist.gov/PhysRefData/Xcom/Text/chap3.html`.

[53] Paola Arias, Davide Cadamuro, Mark Goodsell, Joerg Jaeckel, Javier Redondo, and Andreas Ringwald. "WISPy cold dark matter". In: *Journal of Cosmology and Astroparticle Physics* 2012.06 (2012), pp. 013–013. DOI: `10.1088/1475-7516/2012/06/013`.

[54] Itay M. Bloch, Rouven Essig, Kohsaku Tobioka, Tomer Volansky, and Tien-Tien Yu. "Searching for Dark Absorption with Direct Detection Experiments". In: *JHEP* 06 (2017), p. 087. DOI: `10.1007/JHEP06(2017)087`.

[55] XENON Collaboration. *Projected WIMP Sensitivity of the XENONnT Dark Matter Experiment.* arXiv: `2007.08796 [physics.ins-det]`.

[56] XENON Collaboration. "The XENON1T dark matter experiment". In: *The European Physical Journal C* 77.12 (2017), p. 881. ISSN: 1434-6052. DOI: `10.1140/epjc/s10052-017-5326-3`.

[57] C.H. Faham, V.M. Gehman, A. Currie, A. Dobi, P. Sorensen, and R.J. Gaitskell. “Measurements of wavelength-dependent double photoelectron emission from single photons in VUV-sensitive photomultiplier tubes”. In: *Journal of Instrumentation* 10.09 (2015), P09010–P09010. DOI: `10.1088/1748-0221/10/09/p09010`.

[58] B. López Paredes, H.M. Araújo, F. Froborg, N. Marangou, I. Olcina, T.J. Sumner, R. Taylor, A. Tomás, and A. Vacheret. “Response of photomultiplier tubes to xenon scintillation light”. In: *Astroparticle Physics* 102 (2018), pp. 56 –66. ISSN: 0927-6505. DOI: `https://doi.org/10.1016/j.astropartphys.2018.04.006`.

[59] XENON Collaboration. “XENON1T dark matter data analysis: Signal reconstruction, calibration, and event selection”. In: *Phys. Rev. D* 100 (5 2019), p. 052014. DOI: `10.1103/PhysRevD.100.052014`.

[60] L.M Barkov, A.A Grebenuk, N.M Ryskulov, P.Yu Stepanov, and S.G Zverev. “Measurement of the refractive index of liquid xenon for intrinsic scintillation light”. In: *Nuclear Instruments and Methods in Physics Research Section A: Accelerators, Spectrometers, Detectors and Associated Equipment* 379.3 (1996). Proceedings of the Sixth International Conference on Instrumentation for Experiments at e+ e- Colliders, pp. 482 –483. ISSN: 0168-9002. DOI: `https://doi.org/10.1016/0168-9002(99)00518-5`.

[61] XENON Collaboration. In preparation.

[62] XENON Collaboration. “Observation and applications of single-electron charge signals in the XENON100 experiment”. In: *Journal of Physics G: Nuclear and Particle Physics* 41.3 (2014), p. 035201. DOI: `10.1088/0954-3899/41/3/035201`.

[63] A. Manalaysay, T. Marrodán Undagoitia, A. Askin, L. Baudis, A. Behrens, A. D. Ferella, A. Kish, O. Lebeda, R. Santorelli, D. Vénos, and A. Vollhardt. “Spatially uniform calibration of a liquid xenon detector at low energies using K83mr”. In: *Review of Scientific Instruments* 81.7 (2010), p. 073303. DOI: `10.1063/1.3436636`.

[64] Yu. Khazov, I. Mitropolsky, and A. Rodionov. “Nuclear Data Sheets for A = 131”. In: *Nuclear Data Sheets* 107.11 (2006), pp. 2715 –2930. ISSN: 0090-3752. DOI: `https://doi.org/10.1016/j.nds.2006.10.001`.

[65] A. Kolmogorov. “Sulla determinazione empirica di una lgge di distribuzione”. In: *Inst. Ital. Attuari, Giorn.* 4 (1933), pp. 83–91.

[66] N. Smirnov. “Table for Estimating the Goodness of Fit of Empirical Distributions”. In: *Ann. Math. Statist.* 19.2 (June 1948), pp. 279–281. DOI: `10.1214/aoms/1177730256`.

[67] XENON Collaboration. "Results from a calibration of XENON100 using a source of dissolved radon-220". In: *Phys. Rev. D* 95 (7 2017), p. 072008. DOI: `10.1103/PhysRevD.95.072008`.

[68] XENON Collaboration. "The XENON100 dark matter experiment". In: *Astroparticle Physics* 35.9 (2012), pp. 573 –590. ISSN: 0927-6505. DOI: `https://doi.org/10.1016/j.astropartphys.2012.01.003`.

[69] LUX Collaboration. "Tritium calibration of the LUX dark matter experiment". In: *Phys. Rev.* D93.7 (2016), p. 072009. DOI: `10.1103/PhysRevD.93.072009`. arXiv: `1512.03133 [physics.ins-det]`.

[70] XENON Collaboration. "Signal yields of keV electronic recoils and their discrimination from nuclear recoils in liquid xenon". In: *Phys. Rev. D* 97 (9 2018), p. 092007. DOI: `10.1103/PhysRevD.97.092007`.

[71] XENON Collaboration. "XENON1T dark matter data analysis: Signal and background models and statistical inference". In: *Phys. Rev. D* 99 (11 2019), p. 112009. DOI: `10.1103/PhysRevD.99.112009`.

[72] M Szydagis, N Barry, K Kazkaz, J Mock, D Stolp, M Sweany, M Tripathi, S Uvarov, N Walsh, and M Woods. "NEST: a comprehensive model for scintillation yield in liquid xenon". In: *Journal of Instrumentation* 6.10 (2011), P10002–P10002. DOI: `10.1088/1748-0221/6/10/p10002`.

[73] R.F. Lang, J. Pienaar, E. Hogenbirk, D. Masson, R. Nolte, A. Zimbal, S. Röttger, M.L. Benabderrahmane, and G. Bruno. "Characterization of a deuterium–deuterium plasma fusion neutron generator". In: *Nuclear Instruments and Methods in Physics Research Section A: Accelerators, Spectrometers, Detectors and Associated Equipment* 879 (2018), pp. 31 –38. ISSN: 0168-9002. DOI: `https://doi.org/10.1016/j.nima.2017.10.001`.

[74] XENON Collaboration. "Energy resolution and linearity of XENON1T in the MeV energy range". In: *The European Physical Journal C* 80.8 (2020), p. 785. ISSN: 1434-6052. DOI: `10.1140/epjc/s10052-020-8284-0`.

[75] Carl Eric Dahl. "The physics of background discrimination in liquid xenon, and first results from Xenon10 in the hunt for WIMP dark matter". PhD thesis. Princeton U., 2009.

[76] EXO-200 Collaboration. "Measurement of the scintillation and ionization response of liquid xenon at MeV energies in the EXO-200 experiment". In: *Phys. Rev. C* 101 (6 2020), p. 065501. DOI: `10.1103/PhysRevC.101.065501`.

[77] XENON Collaboration. "Physics reach of the XENON1T dark matter experiment." In: *Journal of Cosmology and Astroparticle Physics* 2016.04 (2016), p. 027.

[78] XENON Collaboration. "Conceptual design and simulation of a water Cherenkov muon veto for the XENON1T experiment". In: *Journal of Instrumentation* 9.11 (2014), P11006–P11006. DOI: `10.1088/1748-0221/9/11/p11006`.

[79] Daniel Z. Freedman. "Coherent effects of a weak neutral current". In: *Phys. Rev. D* 9 (5 1974), pp. 1389–1392. DOI: `10.1103/PhysRevD.9.1389`.

[80] COHERENT Collaboration. "Observation of coherent elastic neutrino-nucleus scattering". In: *Science* 357.6356 (2017), pp. 1123–1126. ISSN: 0036-8075. DOI: `10.1126/science.aao0990`. eprint: `https://science.sciencemag.org/content/357/6356/1123.full.pdf`.

[81] COHERENT Collaboration. *First Detection of Coherent Elastic Neutrino-Nucleus Scattering on Argon*. 2020. arXiv: `2003.10630 [nucl-ex]`.

[82] Aldo M. Serenelli, W. C. Haxton, and Carlos Peña-Garay. "SOLAR MODELS WITH ACCRETION. I. APPLICATION TO THE SOLAR ABUNDANCE PROBLEM". In: *The Astrophysical Journal* 743.1 (2011), p. 24. DOI: `10.1088/0004-637x/743/1/24`.

[83] M. C. Gonzalez-Garcia, Michele Maltoni, Yuber F. Perez-Gonzalez, and Renata Zukanovich Funchal. "Neutrino discovery limit of Dark Matter direct detection experiments in the presence of non-standard interactions". In: *Journal of High Energy Physics* 2018.7 (2018), p. 19. ISSN: 1029-8479. DOI: `10.1007/JHEP07(2018)019`.

[84] P. Barrow, L. Baudis, D. Cichon, M. Danisch, D. Franco, F. Kaether, A. Kish, M. Lindner, T. Marrodán Undagoitia, D. Mayani, L. Rauch, Y. Wei, and J. Wulf. "Qualification tests of the R11410-21 photomultiplier tubes for the XENON1T detector". In: *Journal of Instrumentation* 12.01 (2017), P01024–P01024. DOI: `10.1088/1748-0221/12/01/p01024`.

[85] LUX Collaboration. *Investigation of background electron emission in the LUX detector*. 2020. arXiv: `2004.07791 [physics.ins-det]`.

[86] Adam Anderson. "Phonon-Based Position Determination in SuperCDMS iZIP Detectors". In: *Journal of Low Temperature Physics* 176.5 (2014), pp. 959–965. DOI: `10.1007/s10909-013-1015-2`.

[87] DarkSide Collaboration. "The veto system of the DarkSide-50 experiment". In: *Journal of Instrumentation* 11.03 (2016), P03016–P03016. DOI: `10.1088/1748-0221/11/03/p03016`.

[88] Kelsey Oliver-Mallory. *Determination of Backgrounds for the LUX Experiment*. 2018.

[89] LUX Collaboration. "Radon-related Backgrounds in the LUX Dark Matter Search". In: *Physics Procedia* 61 (2015). 13th International Conference on Topics in Astroparticle and Underground Physics, TAUP 2013, pp. 658 – 665. ISSN: 1875-3892. DOI: `https://doi.org/10.1016/j.phpro.2014.12.067`.

[90] Christopher J. Stanford. “Alphas and surface backgrounds in liquid argon dark matter detectors”. PhD thesis. Princeton University, Jan. 2017.

[91] A. Elykov. “Background Modeling & Data Acquisition for XENON Detectors”. PhD thesis. Albert-Ludwigs-Universität Freiburg, 2021.

[92] XENON Collaboration. “First Results on the Scalar WIMP-Pion Coupling, Using the XENON1T Experiment”. In: *Phys. Rev. Lett.* 122 (7 2019), p. 071301. DOI: `10.1103/PhysRevLett.122.071301`.

[93] XENON Collaboration. “Constraining the Spin-Dependent WIMP-Nucleon Cross Sections with XENON1T”. In: *Phys. Rev. Lett.* 122 (14 2019), p. 141301. DOI: `10.1103/PhysRevLett.122.141301`.

[94] P. Klos, J. Menéndez, D. Gazit, and A. Schwenk. “Large-scale nuclear structure calculations for spin-dependent WIMP scattering with chiral effective field theory currents”. In: *Phys. Rev. D* 88 (8 2013), p. 083516. DOI: `10.1103/PhysRevD.88.083516`.

[95] XENON Collaboration. “Limits on Spin-Dependent WIMP-Nucleon Cross Sections from 225 Live Days of XENON100 Data”. In: *Phys. Rev. Lett.* 111 (2 2013), p. 021301. DOI: `10.1103/PhysRevLett.111.021301`.

[96] LUX Collaboration. “Limits on Spin-Dependent WIMP-Nucleon Cross Section Obtained from the Complete LUX Exposure”. In: *Phys. Rev. Lett.* 118 (25 2017), p. 251302. DOI: `10.1103/PhysRevLett.118.251302`.

[97] PandaX-II Collaboration. “PandaX-II constraints on spin-dependent WIMP-nucleon effective interactions”. In: *Physics Letters B* 792 (2019), pp. 193 – 198. ISSN: 0370-2693. DOI: `https://doi.org/10.1016/j.physletb.2019.02.043`.

[98] PICO Collaboration. “Dark matter search results from the complete exposure of the PICO-60 C_3F_8 bubble chamber”. In: *Phys. Rev. D* 100 (2 2019), p. 022001. DOI: `10.1103/PhysRevD.100.022001`.

[99] PICO Collaboration. “Dark Matter Search Results from the PICO$-$60 C_3F_8 Bubble Chamber”. In: *Phys. Rev. Lett.* 118 (25 2017), p. 251301. DOI: `10.1103/PhysRevLett.118.251301`.

[100] LUX Collaboration. “Low-energy (0.7-74 keV) nuclear recoil calibration of the LUX dark matter experiment using D-D neutron scattering kinematics”. In: (Aug. 2016). arXiv: `1608.05381 [physics.ins-det]`.

[101] LUX Collaboration. “Ultralow energy calibration of LUX detector using ^{127}Xe electron capture”. In: *Phys. Rev. D* 96 (11 2017), p. 112011. DOI: `10.1103/PhysRevD.96.112011`.

[102] B. G. Lenardo, J. Xu, S. Pereverzev, O. A. Akindele, D. Naim, J. Kingston, A. Bernstein, K. Kazkaz, M. Tripathi, C. Awe, L. Li, J. Runge, S. Hedges, P. An, and P. S. Barbeau. "Low-Energy Physics Reach of Xenon Detectors for Nuclear-Recoil-Based Dark Matter and Neutrino Experiments". In: *Phys. Rev. Lett.* 123 (23 2019), p. 231106. DOI: `10.1103/PhysRevLett.123.231106`.

[103] XENON Collaboration. "Light Dark Matter Search with Ionization Signals in XENON1T". In: *Phys. Rev. Lett.* 123 (25 2019), p. 251801. DOI: `10.1103/PhysRevLett.123.251801`.

[104] XENON Collaboration. "Low-mass dark matter search using ionization signals in XENON100". In: *Phys. Rev. D* 94 (9 2016), p. 092001. DOI: `10.1103/PhysRevD.94.092001`.

[105] XENON Collaboration. "Erratum: Low-mass dark matter search using ionization signals in XENON100 [Phys. Rev. D 94, 092001 (2016)]". In: *Phys. Rev. D* 95 (5 2017), p. 059901. DOI: `10.1103/PhysRevD.95.059901`.

[106] DarkSide Collaboration. "Low-Mass Dark Matter Search with the DarkSide-50 Experiment". In: *Phys. Rev. Lett.* 121 (8 2018), p. 081307. DOI: `10.1103/PhysRevLett.121.081307`.

[107] NEST Collaboration. *NESTCollaboration/nest: New, flexible LXe NR yields and resolution model + G4 improvements + linear Noise + much more.* Version v2.0.1. Aug. 2019. DOI: `10.5281/zenodo.3357973`.

[108] LUX Collaboration. "Results of a Search for Sub-GeV Dark Matter Using 2013 LUX Data". In: *Phys. Rev. Lett.* 122 (13 2019), p. 131301. DOI: `10.1103/PhysRevLett.122.131301`.

[109] LUX Collaboration. "First Searches for Axions and Axionlike Particles with the LUX Experiment". In: *Phys. Rev. Lett.* 118 (26 2017), p. 261301. DOI: `10.1103/PhysRevLett.118.261301`.

[110] PandaX-II Collaboration. "Limits on Axion Couplings from the First 80 Days of Data of the PandaX-II Experiment". In: *Phys. Rev. Lett.* 119 (18 2017), p. 181806. DOI: `10.1103/PhysRevLett.119.181806`.

[111] PandaX-II Collaboration. "Constraining Dark Matter Models with a Light Mediator at the PandaX-II Experiment". In: *Phys. Rev. Lett.* 121 (2 2018), p. 021304. DOI: `10.1103/PhysRevLett.121.021304`.

[112] DarkSide Collaboration. "Low-Mass Dark Matter Search with the DarkSide-50 Experiment". In: *Phys. Rev. Lett.* 121 (8 2018), p. 081307. DOI: `10.1103/PhysRevLett.121.081307`.

[113] DarkSide Collaboration. "Constraints on Sub-GeV Dark-Matter–Electron Scattering from the DarkSide-50 Experiment". In: *Phys. Rev. Lett.* 121 (11 2018), p. 111303. DOI: `10.1103/PhysRevLett.121.111303`.

[114] DarkSide Collaboration. “DarkSide-50 532-day dark matter search with low-radioactivity argon”. In: *Phys. Rev. D* 98 (10 2018), p. 102006. DOI: `10.1103/PhysRevD.98.102006`.

[115] XENON Collaboration. “XENON100 dark matter results from a combination of 477 live days”. In: *Phys. Rev. D* 94 (12 2016), p. 122001. DOI: `10.1103/PhysRevD.94.122001`.

[116] EDELWEISS Collaboration. “Searches for electron interactions induced by new physics in the EDELWEISS-III germanium bolometers”. In: *Phys. Rev. D* 98 (8 2018), p. 082004. DOI: `10.1103/PhysRevD.98.082004`.

[117] Rouven Essig, Tomer Volansky, and Tien-Tien Yu. “New constraints and prospects for sub-GeV dark matter scattering off electrons in xenon”. In: *Phys. Rev. D* 96 (4 2017), p. 043017. DOI: `10.1103/PhysRevD.96.043017`.

[118] SuperCDMS Collaboration. “Low-mass dark matter search with CDMSlite”. In: *Phys. Rev. D* 97 (2 2018), p. 022002. DOI: `10.1103/PhysRevD.97.022002`.

[119] Haipeng An, Maxim Pospelov, Josef Pradler, and Adam Ritz. “Direct detection constraints on dark photon dark matter”. In: *Physics Letters B* 747 (2015), pp. 331 –338. ISSN: 0370-2693. DOI: `https://doi.org/10.1016/j.physletb.2015.06.018`.

[120] N. Fornengo, P. Panci, and M. Regis. “Long-range forces in direct dark matter searches”. In: *Phys. Rev. D* 84 (11 2011), p. 115002. DOI: `10.1103/PhysRevD.84.115002`.

[121] Eugenio Del Nobile, Manoj Kaplinghat, and Hai-Bo Yu. “Direct detection signatures of self-interacting dark matter with a light mediator”. In: *Journal of Cosmology and Astroparticle Physics* 2015.10 (2015), pp. 055–055. DOI: `10.1088/1475-7516/2015/10/055`.

[122] Chris Kouvaris and Josef Pradler. “Probing Sub-GeV Dark Matter with Conventional Detectors”. In: *Phys. Rev. Lett.* 118 (3 2017), p. 031803. DOI: `10.1103/PhysRevLett.118.031803`.

[123] A. B. Migdal. In: *J. Phys. (USSR)* 449 (4 1949).

[124] Masahiro Ibe, Wakutaka Nakano, Yutaro Shoji, and Kazumine Suzuki. “Migdal effect in dark matter direct detection experiments”. In: *Journal of High Energy Physics* 2018.3 (2018), p. 194. ISSN: 1029-8479. DOI: `10.1007/JHEP03(2018)194`.

[125] XENON Collaboration. “Search for Light Dark Matter Interactions Enhanced by the Migdal Effect or Bremsstrahlung in XENON1T”. In: *Phys. Rev. Lett.* 123 (24 2019), p. 241803. DOI: `10.1103/PhysRevLett.123.241803`.

[126] EDELWEISS Collaboration. "Searching for low-mass dark matter particles with a massive Ge bolometer operated above ground". In: *Phys. Rev. D* 99 (8 2019), p. 082003. DOI: `10.1103/PhysRevD.99.082003`.

[127] CDEX Collaboration. "Constraints on Spin-Independent Nucleus Scattering with sub-GeV Weakly Interacting Massive Particle Dark Matter from the CDEX-1B Experiment at the China Jinping Underground Laboratory". In: *Phys. Rev. Lett.* 123 (16 2019), p. 161301. DOI: `10.1103/PhysRevLett.123.161301`.

[128] CRESST Collaboration. "First results from the CRESST-III low-mass dark matter program". In: *Phys. Rev. D* 100 (10 2019), p. 102002. DOI: `10.1103/PhysRevD.100.102002`.

[129] NEWS-G collaboration. "First results from the NEWS-G direct dark matter search experiment at the LSM". In: *Astroparticle Physics* 97 (2018), pp. 54 –62. ISSN: 0927-6505. DOI: `https://doi.org/10.1016/j.astropartphys.2017.10.009`.

[130] SuperCDMS Collaboration. "New Results from the Search for Low-Mass Weakly Interacting Massive Particles with the CDMS Low Ionization Threshold Experiment". In: *Phys. Rev. Lett.* 116 (7 2016), p. 071301. DOI: `10.1103/PhysRevLett.116.071301`.

[131] CRESST Collaboration. "First results on sub-GeV spin-dependent dark matter interactions with ^{7}Li". In: *The European Physical Journal C* 79.7 (2019), p. 630. ISSN: 1434-6052. DOI: `10.1140/epjc/s10052-019-7126-4`.

[132] Marc Paterno. "Calculating efficiencies and their uncertainties". In: (Dec. 2004). DOI: `10.2172/15017262`.

[133] XENON Collaboration. "First Dark Matter Search Results from the XENON1T Experiment". In: *Phys. Rev. Lett.* 119 (18 2017), p. 181301. DOI: `10.1103/PhysRevLett.119.181301`.

[134] XENON Collaboration. *Observation of Excess Electronic Recoil Events in XENON1T*. 2020. arXiv: `2006.09721 [hep-ex]`.

[135] EXO-200 Collaboration. "Search for Neutrinoless Double-Beta Decay with the Upgraded EXO-200 Detector". In: *Phys. Rev. Lett.* 120 (7 2018), p. 072701. DOI: `10.1103/PhysRevLett.120.072701`.

[136] LUX Collaboration. "Signal yields, energy resolution, and recombination fluctuations in liquid xenon". In: *Phys. Rev. D* 95 (1 2017), p. 012008. DOI: `10.1103/PhysRevD.95.012008`.

[137] PandaX-II Collaboration. "Dark Matter Results from First 98.7 Days of Data from the PandaX-II Experiment". In: *Phys. Rev. Lett.* 117 (12 2016), p. 121303. DOI: `10.1103/PhysRevLett.117.121303`.

[138] S.-C. Wu. “Nuclear Data Sheets for A = 214”. In: *Nuclear Data Sheets* 110.3 (2009), pp. 681 –748. ISSN: 0090-3752. DOI: `https://doi.org/10.1016/j.nds.2009.02.002`.

[139] Scott Haselschwardt, Joel Kostensalo, Xavier Mougeot, and Jouni Suhonen. *Improved calculations of beta decay backgrounds to new physics in liquid xenon detectors*. 2020. arXiv: `2007.13686 [hep-ex]`.

[140] E. Shockley. “Study of Excess Electronic Recoil Events in XENON1T”. PhD thesis. The University of Chicago, 2020.

[141] M. Shamsuzzoha Basunia. “Nuclear Data Sheets for A = 210”. In: *Nuclear Data Sheets* 121 (2014), pp. 561 –694. ISSN: 0090-3752. DOI: `https://doi.org/10.1016/j.nds.2014.09.004`.

[142] Yu. Khazov, A. Rodionov, and F.G. Kondev. “Nuclear Data Sheets for A = 133”. In: *Nuclear Data Sheets* 112.4 (2011), pp. 855 –1113. ISSN: 0090-3752. DOI: `https://doi.org/10.1016/j.nds.2011.03.001`.

[143] M.-M. Bé, V. Chisté, C. Dulieu, X. Mougeot, V. Chechev, N. Kuzmenko, F. Kondev, A. Luca, M. Galán, A.L. Nichols, A. Arinc, A. Pearce, X. Huang, and B. Wang. *Table of Radionuclides*. Vol. 6. Monographie BIPM-5. Pavillon de Breteuil, F-92310 Sèvres, France: Bureau International des Poids et Mesures, 2011. ISBN: 92-822-2242-3.

[144] XENON Collaboration. “Observation of two-neutrino double electron capture in ^{124}Xe with XENON1T”. In: *Nature* 568.7753 (2019), pp. 532–535. DOI: `10.1038/s41586-019-1124-4`.

[145] E.A. McCutchan. “Nuclear Data Sheets for A = 83”. In: *Nuclear Data Sheets* 125 (2015), pp. 201 –394. ISSN: 0090-3752. DOI: `https://doi.org/10.1016/j.nds.2015.02.002`.

[146] XENON Collaboration. “Removing krypton from xenon by cryogenic distillation to the ppq level”. In: *The European Physical Journal C* 77.5 (2017), p. 275. ISSN: 1434-6052. DOI: `10.1140/epjc/s10052-017-4757-1`.

[147] M. Murra. “Intrinsic background reduction by cryogenic distillation for the XENON1T dark matter experiment”. PhD thesis. Westfälische Wilhelms-Universität Münster, 2019.

[148] Sebastian Lindemann and Hardy Simgen. “Krypton assay in xenon at the ppq level using a gas chromatographic system and mass spectrometer”. In: *The European Physical Journal C* 74.2 (2014), p. 2746. ISSN: 1434-6052. DOI: `10.1140/epjc/s10052-014-2746-1`.

[149] John N Bahcall and Carlos Peña-Garay. “Solar models and solar neutrino oscillations”. In: *New Journal of Physics* 6 (2004), pp. 63–63. DOI: `10.1088/1367-2630/6/1/063`.

[150] W C Haxton, R G Hamish Robertson, and Aldo M. Serenelli. “Solar Neutrinos: Status and Prospects”. In: *Annual Review of Astronomy and Astrophysics* 51.1 (2013), pp. 21–61. DOI: `10.1146/annurev-astro-081811-125539`.

[151] Jiunn-Wei Chen, Hsin-Chang Chi, C.-P. Liu, and Chih-Pan Wu. “Low-energy electronic recoil in xenon detectors by solar neutrinos”. In: *Physics Letters B* 774 (2017), pp. 656 –661. ISSN: 0370-2693. DOI: `https://doi.org/10.1016/j.physletb.2017.10.029`.

[152] XENON Collaboration. “Material radioassay and selection for the XENON1T dark matter experiment”. In: *The European Physical Journal C* 77.12 (2017), p. 890. ISSN: 1434-6052. DOI: `10.1140/epjc/s10052-017-5329-0`.

[153] A. Fieguth. “First observation of double electron capture in Xe-124 and detection prospects for underlying nuclear interaction mechanisms in direct dark matter search”. PhD thesis. Westfälische Wilhelms-Universität Münster, 2018.

[154] EXO Collaboration. “Improved measurement of the $2\nu\beta\beta$ half-life of ^{136}Xe with the EXO-200 detector”. In: *Phys. Rev. C* 89 (1 2014), p. 015502. DOI: `10.1103/PhysRevC.89.015502`.

[155] J. Kotila and F. Iachello. “Phase-space factors for double-β decay”. In: *Phys. Rev. C* 85 (3 2012), p. 034316. DOI: `10.1103/PhysRevC.85.034316`.

[156] `http://nucleartheory.yale.edu`.

[157] Masaru Doi and Tsuneyuki Kotani. “Neutrino Emitting Modes of Double Beta Decay”. In: *Progress of Theoretical Physics* 87.5 (May 1992), pp. 1207–1231. ISSN: 0033-068X. DOI: `10.1143/ptp/87.5.1207`.

[158] Christian Wittweg, Brian Lenardo, Alexander Fieguth, and Christian Weinheimer. *Detection prospects for the second-order weak decays of ^{124}Xe in multi-tonne xenon time projection chambers.* 2020. arXiv: `2002.04239 [nucl-ex]`.

[159] K.D. Morå. “Harmonizing discovery thresholds and reporting two-sided confidence intervals: a modified Feldman & Cousins method”. In: *Journal of Instrumentation* 14.02 (2019), P02003–P02003. DOI: `10.1088/1748-0221/14/02/p02003`.

[160] V. I. Barsanov, A. A. Dzhanelidze, S. B. Zlokazov, N. A. Kotelnikov, S. Yu. Markov, V. V. Selin, Z. N. Shakirov, D. N. Abdurashitov, E. P. Veretenkin, V. N. Gavrin, V. V. Gorbachev, T. V. Ibragimova, A. V. Kalikhov, I. N. Mirmov, A. A. Shikhin, V. E. Yants, Yu. S. Khomyakov, and B. T. Cleveland. “Artificial neutrino source based on the Ar-37 isotope”. In: *Phys. Atom. Nucl.* 70 (2007), pp. 300–310. DOI: `10.1134/S1063778807020111`.

[161] LUX Collaboration. "Improved Limits on Scattering of Weakly Interacting Massive Particles from Reanalysis of 2013 LUX Data". In: *Phys. Rev. Lett.* 116.16 (2016), p. 161301. DOI: `10.1103/PhysRevLett.116.161301`. arXiv: `1512.03506 [astro-ph.CO]`.

[162] LUX Collaboration. "Search for annual and diurnal rate modulations in the LUX experiment". In: *Phys. Rev. D* 98.6 (2018), p. 062005. DOI: `10.1103/PhysRevD.98.062005`. arXiv: `1807.07113 [astro-ph.CO]`.

[163] R. Saldanha, H. O. Back, R. H. M. Tsang, T. Alexander, S. R. Elliott, S. Ferrara, E. Mace, C. Overman, and M. Zalavadia. "Cosmogenic production of ^{39}Ar and ^{37}Ar in argon". In: *Phys. Rev. C* 100 (2 2019), p. 024608. DOI: `10.1103/PhysRevC.100.024608`.

[164] C. Hasterok. "Gas Purity Analytics, Calibration Studies, and Background Predictions towards the First Results of XENON1T." PhD thesis. Ruprecht-Karls-Universität, Heidelberg, 2017.

[165] H. R. Byers, H. E. Landsberg, H. Wexler, Haurwitz B., A. F. Spilhaus, H. C. Willett, and H. G. Houghton. *Compendium of meteorology.* American Meteorological Society, 1951, p. 5. DOI: `10.1007/978-1-940033-70-9`.

[166] Hans Rottländer, Walter Umrath, and Gerhard Voss. "Fundamentals of leak detection". In: *Leybold GMBH (ed) Cat* 199 (2016), p. 37.

[167] Robin A. Riedmann and Roland Purtschert. "Separation of argon from environmental samples for Ar-37 and Ar-39 analyses". In: *Separation and Purification Technology* 170 (2016), pp. 217 –223. ISSN: 1383-5866. DOI: `https://doi.org/10.1016/j.seppur.2016.06.017`.

[168] R. Riedmann. "Separation of Argon from atmospheric air and Measurements of ^{37}Ar for CTBT purposes." PhD thesis. University of Bern, Switzerland, 2011.

[169] H. W. Gäggeler. "Radioactivity in the Atmosphere". In: *Radiochimica Acta* 70-71.s1 (1995), pp. 345 –354. DOI: `https://doi.org/10.1524/ract.1995.7071.s1.345`.

[170] Robin A Riedmann and Roland Purtschert. "Natural ^{37}Ar concentrations in soil air: implications for monitoring underground nuclear explosions". In: *Environ. Sci. Technol* 45.20 (2011), pp. 8656–8664. ISSN: 0013-936X. DOI: `10.1021/es201192u`.

[171] LUX Collaboration. "Tritium calibration of the LUX dark matter experiment". In: *Phys. Rev. D* 93 (7 2016), p. 072009. DOI: `10.1103/PhysRevD.93.072009`.

[172] L L Lucas and M P Unterweger. "Comprehensive Review and Critical Evaluation of the Half-Life of Tritium". In: *Journal of research of the National Institute of Standards and Technology* 105.4 (Aug. 2000), pp. 541–549. DOI: `10.6028/jres.105.043`.

[173] C. Zhang, D.-M. Mei, V.A. Kudryavtsev, and S. Fiorucci. “Cosmogenic activation of materials used in rare event search experiments”. In: *Astroparticle Physics* 84 (2016), pp. 62 –69. ISSN: 0927-6505. DOI: `https://doi.org/10.1016/j.astropartphys.2016.08.008`.

[174] J. Amaré, J. Castel, S. Cebrián, I. Coarasa, C. Cuesta, T. Dafni, J. Galán, E. García, J.G. Garza, F.J. Iguaz, I.G. Irastorza, G. Luzón, M. Martínez, H. Mirallas, M.A. Oliván, Y. Ortigoza, A. Ortiz de Solórzano, J. Puimedón, E. Ruiz-Chóliz, M.L. Sarsa, J.A. Villar, and P. Villar. “Cosmogenic production of tritium in dark matter detectors”. In: *Astropart. Phys.* 97 (2018), pp. 96–105. DOI: `10.1016/j.astropartphys.2017.11.004`. arXiv: `1706.05818 [physics.ins-det]`.

[175] Takanobu Ishida. “Isotope Effect and Isotope Separation: A Chemist’s View”. In: *Journal of Nuclear Science and Technology* 39.4 (2002), pp. 407–412.

[176] A. Dobi, D. S. Leonard, C. Hall, L. Kaufman, T. Langford, S. Slutsky, and Y. R. Yen. “Study of a zirconium getter for purification of xenon gas”. In: *Nucl. Instrum. Meth.* A620 (2010), pp. 594–598. DOI: `10.1016/j.nima.2010.03.151`.

[177] W. Plastino, G. F. Panza, C. Doglioni, M. L. Frezzotti, A. Peccerillo, P. De Felice, F. Bella, P. P. Povinec, S. Nisi, L. Ioannucci, P. Aprili, M. Balata, M. L. Cozzella, and M. Laubenstein. “Tritium in water electrolytic enrichment and liquid scintillation counting”. In: *Radiat. Meas.* 42 (Jan. 2007), pp. 68–73. DOI: `10.1016/j.radmeas.2006.07.010`.

[178] Wolfango Plastino, Iosif Chereji, Stela Cuna, Lauri Kaihola, Pierino De Felice, Nicolae Lupsa, Gabriela Balas, Valentin Mirel, Petre Berdea, and Calin Baciu. “Uranium groundwater anomalies and active normal faulting”. In: *Journal of Radioanalytical and Nuclear Chemistry* 288 (Apr. 2011), pp. 101–. DOI: `10.1007/s10967-010-0876-y`.

[179] IAEA/WMO. *Global Network of Isotopes in Precipitation. The GNIP Database.* `https://nucleus.iaea.org/wiser`. 2015.

[180] James D. Happell, Göte Östlund, and Allen S. Mason. “A history of atmospheric tritium gas (HT) 1950-2002”. In: *Tellus* 56(3).3 (2004), pp. 183–193. DOI: `10.1111/j.1600-0889.2004.00103.x`.

[181] J. Mishima and C. M. Steele. *Oxidation of Tritium Gas Under Accident and Transport Conditions.* Report LA-UR-02-3803. U.S.. Department of Energy Los Alamos, NM, 2002.

[182] E. Aprile and T. Doke. “Liquid xenon detectors for particle physics and astrophysics”. In: *Rev. Mod. Phys.* 82 (3 2010), pp. 2053–2097. DOI: `10.1103/RevModPhys.82.2053`.

[183] E. Aprile, R. Mukherjee, and M. Suzuki. “Measurements of the lifetime of conduction electrons in liquid xenon”. In: *Nucl. Instrum. Meth.* A300 (1991), pp. 343–350. DOI: `10.1016/0168-9002(91)90446-W`.

[184] CAST Collaboration. “CAST constraints on the axion-electron coupling”. In: *Journal of Cosmology and Astroparticle Physics* 2013.05 (2013), pp. 010–010. DOI: `10.1088/1475-7516/2013/05/010`.

[185] Paolo Gondolo and Georg G. Raffelt. “Solar neutrino limit on axions and keV-mass bosons”. In: *Phys. Rev. D* 79 (10 2009), p. 107301. DOI: `10.1103/PhysRevD.79.107301`.

[186] M.M. Miller Bertolami, B.E. Melendez, L.G. Althaus, and J. Isern. “Revisiting the axion bounds from the Galactic white dwarf luminosity function”. In: *Journal of Cosmology and Astroparticle Physics* 2014.10 (2014), pp. 069–069. DOI: `10.1088/1475-7516/2014/10/069`.

[187] Adrian Ayala, Inma Domínguez, Maurizio Giannotti, Alessandro Mirizzi, and Oscar Straniero. “Revisiting the Bound on Axion-Photon Coupling from Globular Clusters”. In: *Phys. Rev. Lett.* 113 (19 2014), p. 191302. DOI: `10.1103/PhysRevLett.113.191302`.

[188] N. Viaux, M. Catelan, P. B. Stetson, G. G. Raffelt, J. Redondo, A. A. R. Valcarce, and A. Weiss. “Neutrino and Axion Bounds from the Globular Cluster M5 (NGC 5904)”. In: *Phys. Rev. Lett.* 111 (23 2013), p. 231301. DOI: `10.1103/PhysRevLett.111.231301`.

[189] Maurizio Giannotti, Igor G. Irastorza, Javier Redondo, Andreas Ringwald, and Ken’ichi Saikawa. “Stellar Recipes for Axion Hunters”. In: *Journal of Cosmology and Astroparticle Physics* 2017.10 (2017), 010–010. ISSN: 1475-7516. DOI: `10.1088/1475-7516/2017/10/010`.

[190] Luca Di Luzio, Maurizio Giannotti, Enrico Nardi, and Luca Visinelli. “The landscape of QCD axion models”. In: (Mar. 2020). arXiv: `2003.01100 [hep-ph]`.

[191] E. Brown, A. Buss, A. Fieguth, C. Huhmann, M. Murra, H.-W. Ortjohann, S. Rosendahl, A. Schubert, D. Schulte, D. Tosi, G. Gratta, and C. Weinheimer. “Magnetically-coupled piston pump for high-purity gas applications”. In: *The European Physical Journal C* 78.7 (2018), p. 604. ISSN: 1434-6052. DOI: `10.1140/epjc/s10052-018-6062-z`.

[192] XENON Collaboration. “^{222}Rn emanation measurements for the XENON1T experiment”. In preparation.

[193] M. R. Bhat. *Evaluated Nuclear Structure Data File (ENSDF)*. Ed. by S. M. Qaim. Nucl. Data Sci. Tech. Data extracted using the NNDC On-Line Data Service from the ENSDF database, files revised as of October, 2019. Berlin, Germany: Springer-Verlag, 1992, p. 817.

[194] M. R. Harston and N. C. Pyper. “Exchange effects in β decays of many-electron atoms”. In: *Phys. Rev. A* 45 (1992), p. 6282. DOI: `10.1103/PhysRevA.45.6282`.

[195] M. Verpelli and L. Vrapcenjak. *LiveChart of Nuclides*. `https://www-nds.iaea.org/livechart/`. IAEA, Nuclear Data Section, 2020.

[196] X. Mougeot. “Reliability of usual assumptions in the calculation of β and ν spectra”. In: *Phys. Rev. C* 91 (5 2015), p. 055504. DOI: `10.1103/PhysRevC.91.055504`.

[197] GEANT4 Collaboration. “GEANT4: A Simulation toolkit”. In: *Nucl. Instrum. Meth.* A506 (2003), pp. 250–303. DOI: `10.1016/S0168-9002(03)01368-8`.

[198] S. Hauf, M. Kuster, M. Batič, Z. W. Bell, D. H. H. Hoffmann, P. M. Lang, S. Neff, M. G. Pia, G. Weidenspointner, and A. Zoglauer. “Radioactive Decays in Geant4”. In: *IEEE Trans. Nucl. Sci.* 60.4 (2013), pp. 2966–2983. DOI: `10.1109/TNS.2013.2270894`.

[199] Leendert Hayen, Stefano Simonucci, and Simone Taioli. *Detailed β spectrum calculations of ^{214}Pb for new physics searches in liquid Xenon.* 2020. arXiv: `2009.08303 [nucl-th]`.

[200] XENON Collaboration. *Data from: Observation of Excess Electronic Recoil Events in XENON1T.* June 2020. DOI: `10.5281/zenodo.3924406`.

[201] XENON Collaboration. In preparation.

[202] Alejandro Corsico, Leandro Althaus, Marcelo Bertolami, and S. Kepler. “Pulsating white dwarfs: new insights”. In: *The Astronomy and Astrophysics Review* 27 (Dec. 2019). DOI: `10.1007/s00159-019-0118-4`.

[203] Santiago Arceo Díaz, Klaus-Peter Schröder, Kai Zuber, Dennis Jack, and Elena Elsa Bricio Barrios. “Constraint on the axion-electron coupling constant and the neutrino magnetic dipole moment by using the tip-RGB luminosity of fifty globular clusters”. In: (). arXiv: `1910.10568`.

[204] M.M. Miller Bertolami, B.E. Melendez, L.G. Althaus, and J. Isern. “Revisiting the axion bounds from the Galactic white dwarf luminosity function”. In: *Journal of Cosmology and Astroparticle Physics* 2014.10 (2014), pp. 069–069. DOI: `10.1088/1475-7516/2014/10/069`.

[205] Kazuo Fujikawa and Robert E. Shrock. “Magnetic Moment of a Massive Neutrino and Neutrino-Spin Rotation”. In: *Phys. Rev. Lett.* 45 (12 1980), pp. 963–966. DOI: `10.1103/PhysRevLett.45.963`.

[206] J. E. Kim. “Neutrino magnetic moment”. In: *Phys. Rev. D* 14 (11 1976), pp. 3000–3002. DOI: `10.1103/PhysRevD.14.3000`.

[207] Jihn E. Kim. “Effects of the Transition Magnetic Moment of the Neutrino”. In: *Phys. Rev. Lett.* 41 (6 1978), pp. 360–363. DOI: `10.1103/PhysRevLett.41.360`.

[208] Nicole F. Bell, Mikhail Gorchtein, Michael J. Ramsey-Musolf, Petr Vogel, and Peng Wang. “Model independent bounds on magnetic moments of Majorana neutrinos”. In: *Physics Letters, Section B: Nuclear, Elementary Particle and High-Energy Physics* 642.4 (2006), 377–383. DOI: `10.1016/j.physletb.2006.09.055`.

[209] Nicole F. Bell, V. Cirigliano, M. J. Ramsey-Musolf, P. Vogel, and Mark B. Wise. “How magnetic is the dirac neutrino?” In: *Physical Review Letters* 95.15 (2005), 1–4. DOI: `10.1103/PhysRevLett.95.151802`.

[210] Borexino Collaboration. “Limiting neutrino magnetic moments with Borexino Phase-II solar neutrino data”. In: *Phys. Rev. D* 96 (9 2017), p. 091103. DOI: `10.1103/PhysRevD.96.091103`.

[211] S. Arceo-Díaz, K. P. Schröder, K. Zuber, and D. Jack. “Constraint on the magnetic dipole moment of neutrinos by the tip-RGB luminosity in Centauri”. In: *Astroparticle Physics* (2015). DOI: `10.1016/j.astropartphys.2015.03.006`.

[212] Particle Data Group. “Review of Particle Physics”. In: *Phys. Rev.* D98.3 (2018), p. 030001. DOI: `10.1103/PhysRevD.98.030001`.

[213] P. Vogel and J. Engel. “Neutrino electromagnetic form factors”. In: *Phys. Rev. D* 39 (11 1989), pp. 3378–3383. DOI: `10.1103/PhysRevD.39.3378`.

[214] Chung-Chun Hsieh, Lakhwinder Singh, Chih-Pan Wu, Jiunn-Wei Chen, Hsin-Chang Chi, C.-P. Liu, Mukesh K. Pandey, and Henry T. Wong. “Discovery potential of multiton xenon detectors in neutrino electromagnetic properties”. In: *Phys. Rev. D* 100 (7 2019), p. 073001. DOI: `10.1103/PhysRevD.100.073001`.

[215] A. G. Beda, V. B. Brudanin, V. G. Egorov, D. V. Medvedev, V. S. Pogosov, E. A. Shevchik, M. V. Shirchenko, A. S. Starostin, and I. V. Zhitnikov. “Gemma experiment: The results of neutrino magnetic moment search”. In: *Physics of Particles and Nuclei Letters* 10.2 (2013), 139–143. ISSN: 1547-4771, 1531-8567. DOI: `10.1134/S1547477113020027`.

[216] A.H. Córsico, L.G. Althaus, M.M. Miller Bertolami, S.O. Kepler, and E. García-Berro. “Constraining the neutrino magnetic dipole moment from white dwarf pulsations”. In: *Journal of Cosmology and Astroparticle Physics* 2014.08 (2014), pp. 054–054. DOI: `10.1088/1475-7516/2014/08/054`.

[217] Peter Galison and Aneesh Manohar. “Two Z’s or not two Z’s?” In: *Physics Letters B* 136.4 (1984), pp. 279 –283. ISSN: 0370-2693. DOI: `https://doi.org/10.1016/0370-2693(84)91161-4`.

[218] CDEX Collaboration. "Improved limits on solar axions and bosonic dark matter from the CDEX-1B experiment using the profile likelihood ratio method". In: *Phys. Rev. D* 101 (5 2020), p. 052003. DOI: `10.1103/PhysRevD.101.052003`.

[219] SuperCDMS Collaboration. "Constraints on dark photons and axionlike particles from the SuperCDMS Soudan experiment". In: *Phys. Rev. D* 101 (5 2020), p. 052008. DOI: `10.1103/PhysRevD.101.052008`.

[220] XMASS Collaboration. "Search for dark matter in the form of hidden photons and axion-like particles in the XMASS detector". In: *Physics Letters B* 787 (2018), pp. 153 –158. ISSN: 0370-2693. DOI: `https://doi.org/10.1016/j.physletb.2018.10.050`.

[221] XENON Collaboration. "Search for bosonic super-WIMP interactions with the XENON100 experiment". In: *Phys. Rev. D* 96 (12 2017), p. 122002. DOI: `10.1103/PhysRevD.96.122002`.

[222] GERDA Collaboration. "The first search for bosonic super-WIMPs with masses up to 1 MeV/c^2 with GERDA". In: (May 2020). arXiv: `2005.14184 [hep-ex]`.

[223] Majorana Collaboration. "New Limits on Bosonic Dark Matter, Solar Axions, Pauli Exclusion Principle Violation, and Electron Decay from the Majorana Demonstrator". In: *Phys. Rev. Lett.* 118 (16 2017), p. 161801. DOI: `10.1103/PhysRevLett.118.161801`.

[224] Joachim Kopp, Viviana Niro, Thomas Schwetz, and Jure Zupan. "DAMA/LIBRA data and leptonically interacting dark matter". In: *Phys. Rev. D* 80 (8 2009), p. 083502. DOI: `10.1103/PhysRevD.80.083502`.

[225] J. A. BEARDEN and A. F. BURR. "Reevaluation of X-Ray Atomic Energy Levels". In: *Rev. Mod. Phys.* 39 (1 1967), pp. 125–142. DOI: `10.1103/RevModPhys.39.125`.

[226] M Cardona and Ley. L. *Photoemission in Solids I: General Principles.* Vol. 69. Springer, 1978. ISBN: 978-0-201-62674-2.

[227] C.F. Bunge, J.A. Barrientos, and A.V. Bunge. "Roothaan-Hartree-Fock Ground-State Atomic Wave Functions: Slater-Type Orbital Expansions and Expectation Values for Z = 2-54". In: *Atomic Data and Nuclear Data Tables* 53.1 (1993), pp. 113 –162. ISSN: 0092-640X. DOI: `https://doi.org/10.1006/adnd.1993.1003`.

[228] B. M. Roberts, V. A. Dzuba, V. V. Flambaum, M. Pospelov, and Y. V. Stadnik. "Dark matter scattering on electrons: Accurate calculations of atomic excitations and implications for the DAMA signal". In: *Phys. Rev. D* 93 (11 2016), p. 115037. DOI: `10.1103/PhysRevD.93.115037`.

[229] Masaru Doi and Tsuneyuki Kotani. “Neutrinoless Modes of Double Beta Decay”. In: *Progress of Theoretical Physics* 89.1 (Jan. 1993), pp. 139–159. ISSN: 0033-068X. DOI: `10.1143/ptp/89.1.139`. eprint: `https://academic.oup.com/ptp/article-pdf/89/1/139/5207768/89-1-139.pdf`.

[230] XENON Collaboration. “Online ^{222}Rn removal by cryogenic distillation in the XENON100 experiment”. In: *The European Physical Journal C* 77.6 (2017), p. 358. ISSN: 1434-6052. DOI: `10.1140/epjc/s10052-017-4902-x`.

[231] F. Ruppin, J. Billard, E. Figueroa-Feliciano, and L. Strigari. “Complementarity of dark matter detectors in light of the neutrino background”. In: *Phys. Rev. D* 90 (8 2014), p. 083510. DOI: `10.1103/PhysRevD.90.083510`.

[232] PandaX Collaboration. “Dark matter direct search sensitivity of the PandaX-4T experiment”. In: *Science China Physics, Mechanics & Astronomy* 62.3 (2018), p. 31011. DOI: `10.1007/s11433-018-9259-0`.

[233] LZ Collaboration. “The LUX-ZEPLIN (LZ) experiment”. In: *Nuclear Instruments and Methods in Physics Research Section A: Accelerators, Spectrometers, Detectors and Associated Equipment* 953 (2020), p. 163047. ISSN: 0168-9002. DOI: `https://doi.org/10.1016/j.nima.2019.163047`.